ЧЕТВЕРТЫЙ
МОСКОВСКИЙ
СИМПОЗИУМ
ПО СОЛНЕЧНОЙ СИСТЕМЕ

THE FOURTH
MOSCOW
SOLAR SYSTEM
SYMPOSIUM

14-18 ОКТЯБРЯ 2013
ИНСТИТУТ
КОСМИЧЕСКИХ
ИССЛЕДОВАНИЙ
РАН
МОСКВА

14-18 OCTOBER 2013
SPACE
RESEARCH
INSTITUTE
MOSCOW

4M-S³ SCIENTIFIC PROGRAM

	15 OCTOBER 2013		
	OPENING SESSION		**10.00-11.40**
4MS³-OS-01	Lev Zelenyi	Welcome	10.00-10.10
4MS³-OS-02	Lev Zelenyi, Vladimir Popovkin	Russian Solar system exploration program. Updated version	10.10-10.40
4MS³-OS-03	Alvaro Giménez	ESA's Space Science programme - achievements and future opportunities	10.40-11.10
4MS³-OS-04	James L. Green	NASA's Planetary Science Missions	11.10-11.40
	coffee-break		11.40-12.00
	SESSION 1: MARS		**12.00-18.00**
	conveners: Oleg Korablev, Olivier Witasse		
4MS³-MS-01	Olivier Witasse and A. Chicarro	10 years of Mars-Express **/invited talk/**	12.00-12.20
4MS³-MS-02	James Head and David Marchant	Antarctic Dry Valley Streams and Lakes: Analogs for Noachian Mars?	12.20-12.40
4MS³-MS-03	Mikhail Zolotov and M. Mironenko	Chemistry and timing of formation of Martian phyllosilicates and salts	12.40-13.00
	lunch		13.00-14.00
4MS³-MS-04	Igor Mitrofanov et al	Recent results of DAN investigation onboard Curiosity	14.00-14.20
4MS³-MS-05	Ruslan Kuzmin et al	Mars: Local morphology of the surface at the DAN measurements spots in the Gale crater	14.20-14.40
4MS³-MS-06	Tamara Gudkova et al	Construction of Martian seismic models. Free oscillations and body waves	14.40-15.00
4MS³-MS-07	Marina Michelena and Miguel Herraiz	Global scale magnetometry	15.00-15.20
4MS³-MS-08	Mikhail Ivanov et al	Evidence for possible Hesperian glaciation in Utopia Planitia on Mars	15.20-15.40
4MS³-MS-09	David Kutai Weiss and James Head	Noachian highland crater degradation on Mars: assessing the role of regional snow and ice deposits in a cold and dry early Mars	15.40-16.00
	coffee-break		16.00-16.20
4MS³-MS-10	Kathleen Scanlon and James Head	Volcano-Ice Interactions at Arsia Mons, Mars	16.20-16.40
4MS³-MS-11	Franck Lefèvre and Franck Montmessin	A polar ozone layer on Mars	16.40-17.00
4MS³-MS-12	Vladimir Krasnopolsky	Observations of the CO dayglow at 4.7 μm on Mars: Variations of temperature and CO mixing ratio at 50 km	17.00-17.20
4MS³-MS-13	Alexey Pankine and L. Tamparry	Vertical distribution of water vapor in Martian atmosphere from MGS TES day and night observations	17.20-17.40
4MS³-MS-14	Elena Vorobyova et al	Microbial communities of Earth permafrost and arid soils may persist at least 500 thousand years in the subsurface of Martian regolith and in the open space	17.40-18.00
	POSTER SESSION (all sessions)		**18.00-19.00**

16 OCTOBER 2013

	SESSION 2: MOON **convener: Igor Mitrofanov, Lev Zelenyi**		**10.00-19.00**
	SESSION 2.1. MOON. LUNAR DATA ANALYSIS AND INTERPRETATION **chair: Maxim Litvak**		**10.00-13.00**
4MS^3-MN-01	Alexander Basilevsky et al	On the history of early meteoritic bombardment of the Moon	10.00-10.20
4MS^3-MN-02	Evgeniy Lazarev et al	Comparison of impact crater populations in the lunar polar regions	10.20-10.40
4MS^3-MN-03	Hideo Hanada et al	Geodetic observations for study of interior of the Moon and the planets in SELENE-2 and future missions	10.40-11.00
4MS^3-MN-04	Jinsong Ping and X. Su	Chang'E-1 mission identified Lunar hidden BGA basins	11.00-11.20
4MS^3-MN-05	Yuri Velikodsky et al	Opposition effect of the Moon from LROC WAC data	11.20-11.40
	coffee-break		11.40-12.00
4MS^3-MN-06	Jürgen Oberst et al	Reduction and analysis of one-way laser ranging data from ILRS ground stations to LRO	12.00-12.20
4MS^3-MN-07	Anton Sanin et al	LEND mapping of water at the south pole regions: data from LRO	12.20-12.40
4MS^3-MN-08	Maya Djachkova and E. N. Lazarev	Selecting landing sites for lunar lander missions using spatial analysis	12.40-13.00
	lunch		13.00-14.00
	SESSION 2.2. MISSIONS LUNA-GLOB AND LUNA-RESOURCE **chair: Vladislav Tretyakov**		**14.00-15.20**
4MS^3-MN-09	Igor Mitrofanov and V. Tretyakov	Scientific investigations onboard Luna landers	14.00-14.20
4MS^3-MN-10	Maxim Litvak and O.Kozlov	Robotic arm and drilling element for Luna landers	14.20-14.40
4MS^3-MN-11	Stas Barabash et al	Miniaturized analyzer of energetic neutrals LINA-XSAN for the Luna-Glob mission	14.40-15.00
4MS^3-MN-12	Peter Wurz et al	In situ dating of planetary material by laser-based mass spectrometer	15.00-15.20
	SESSION 2.3. EXPLORATION OF THE MOON **chair: Lev Zelenyi**		**15.20-19.00**
4MS^3-MN-13	Lev Zelenyi et al	Russian lunar program of robotic exploration precursors	15.20-15.40
4MS^3-MN-14	Viktor Khartov et al	Missions Luna-Glob and Luna- Resource	15.40-16.00
	coffee-break		16.00-16.20
4MS^3-MN-15	Bernerdo Patti et al	Synergy of lunar program for Lunar Polar Sample Return in ESA and Roscosmos	16.20-16.40
4MS^3-MN-16	Richard Fisackerly et al	European objectives and approach to lunar exploration in cooperation with Russia	16.40-17.00
4MS^3-MN-17	Richard Fisackerly et al	Landing site characterization for future lunar exploration missions	17.00-17.20
4MS^3-MN-18	Vladislav Shevchenko	Lunar resources: possibilities for utilization	17.20-17.40
4MS^3-MN-19	Mikhail Panasuk	Lunar monitoring outpost of cosmic rays	17.40-18.00
4MS^3-MN-20	Oleg Ugolnikov	Future perspectives of optical observations on the surface of the Moon	18.00-18.20
4MS^3-MN-21	Mikhail Mogilevsky et al	Lunar low-frequency array: exploration of possible marker for exoplanets habitability	18.20-18.40
4MS^3-MN-22	Nikolay Brukhanov	Plans for manned flight to the Moon	18.40-19.00
	POSTER SESSION (all sessions)		**19.00-20.00**

17 OCTOBER 2013

	SESSION 3: DUST AND DUSTY PLASMA IN SPACE **convener: Alexander Zakharov**		**10.00-11.40**
4MS³-DP-01	Sergey Popel et al	Parameters of photoelectrons over the illuminated part of the Moon **/invited talk/**	10.00-10.20
4MS³-DP-02	Oleg Petrov and Vladimir Fortov	Structures and transport of charged dust under laboratory and microgravity conditions **/invited talk/**	10.20-10.40
4MS³-DP-03	Mark Koepke et al	Laboratory analysis of granular materials properties, size distributions, chemical and mineralogical compositions relevant to dust-grain charging investigations **/invited talk/**	10.40-11.00
4MS³-DP-04	Nikolay Borisov	The influence of the surface conductivity on the dust motion near the Moon and asteroids **/invited talk/**	11.00-11.20
4MS³-DP-05	Yaroslaw Ilyushin	Intensity and polarization of Lunar Horizon Glow: numerical simulations.	11.20-11.40
	coffee-break		11.40-12.00
	SESSION 4: SOLAR SYSTEM STUDY: SOME MILESTONES **(acad. Mikhail Marov 80th anniversary session)** **chair: Oleg Kuskov**		**12.00-19.20**
4MS³-SS-01	Mikhail Marov	Space Exploration: A Personal Historical Highlights	12.00-12.20
4MS³-SS-02	James Head et al	50 Years of Russian and American Lunar Exploration: A Roadmap for the Future **/invited talk/**	12.20-12.40
4MS³-SS-03	Ludmila Zasova	Study of Venus by space missions: from Venera-4 to Venera-D **/invited talk/**	12.40-13.00
	lunch		13.00-14.00
4MS³-SS-04	Oleg Korablev	Mars exploration at the turn of the century **/invited talk/**	14.00-14.20
4MS³-SS-05	Vladislav Shevchenko	Lunar exploration problems **/invited talk/**	14.20-14.40
4MS³-SS-06	Oleg Kuskov et al	The interior of the Moon: Thermodynamics vs seismology **/invited talk/**	14.40-15.00
4MS³-SS-07	Mikhail Nazarov et al	Spinel-enstatite Association of lunar meteorites **/invited talk/**	15.00-15.20
4MS³-SS-08	Alexander Bazilevskiy	Estimation of the age of impact craters on the Moon, Mercury, Mars and Venus based on their morphology **/invited talk/**	15.20-15.40
4MS³-SS-09	Vladimir Zharkov and Tamara Gudkova	Construction of Martian seismic models. 1. Effects of temperature, anelasticity and hydration **/invited talk/**	15.40-16.00
	coffee-break		16.00-16.20
4MS³-SS-10	Igor Mitrofanov	Water and the problems of life on Mars **/invited talk/**	16.20-16.40
4MS³-SS-11	Yury Golubev	Development of Space Research Methods in the Keldysh Institute of Applied Mathematics **/invited talk/**	16.40-17.00
4MS³-SS-12	Alexandr Kolesnichenko	To theory of vortical dynamo in astrophysical disk with a gyrotropic turbulence **/invited talk/**	17.00-17.20

4MS^3-SS-13	Valery Shematovich	Astrochemistry of the atmosphere-icy surface interface for astrophysical objects **/invited talk/**	17.20-17.40
4MS^3-SS-14	Dmitry Bisikalo	Simulation of the interaction between the exoplanet WASP-12b and its host star **/invited talk/**	17.40-18.00
4MS^3-SS-15	Vera Dorofeeva	Cosmochemical restrictions on models of evolution of outer solar nebula **/invited talk/**	18.00-18.20
4MS^3-SS-16	Leonid Ksanfomality	On Temple 1 comet's nuclei surface	18.20-18.40
4MS^3-SS-17	Vladimir Mazhukin	Mathematical modeling of pulsed laser impact on small space objects	18.40-19.00
4MS^3-SS-18	Ivan Shevchenko	Resonances in the Solar and exoplanetary systems **/invited talk/**	19.00-19.20

18 OCTOBER 2013

	SESSION 5: VENUS		**10.00-16.00**
	conveners: Ludmila Zasova, Hakan Svedhem **chair: Ludmila Zasova**		
4MS³-VN-01	Hakan Svedhem, Colin Wilson	Recent results and future activities of Venus Express / **invited talk**/	10.00-10.20
4MS³-VN-02	Vladimir Krasnopolsky	Nighttime photochemical model and nightglow on Venus / **invited talk**/	10.20-10.40
4MS³-VN-03	Francesca Altieri	Gravity wave detection in the terrestrial planets' atmosphere through O2 airglow / **invited talk**/	10.40-11.00
4MS³-VN-04	Nikolay Ignatiev et al	Upper haze on the night side of Venus from VIRTIS-M / Venus Express observations	11.00-11.15
4MS³-VN-05	Alexander Rodin et al	Non-hydrostatic general circulation simulations of the transition region in the Venus atmosphere / **invited talk**/	11.15-11.30
4MS³-VN-06	Sanjay Limaye	Towards a better understanding of the Venus atmosphere – observations needed between 65 – 110 km	11.30-11.45
	coffee-break		11.45-12.00
	chair: Alexander Bazilevskiy		
4MS³-VN-07	Gabriele Arnold et al	Surface emissivity retrieval from VIRTIS/ VEX data in the Quetzalpetlatl quadrangle on Venus based on the new MSR multi-spectrum retrieval technique / **invited talk**/	12.00-12.20
4MS³-VN-08	Mikhail Ivanov, James Head	Evolution of tectonics on Venus	12.20-12.40
4MS³-VN-09	Mikhail Ivanov, James Head	Geology of Fortuna Tessera: Insights into the beginning of the recorded history of Venus	12.40-13.00
	lunch		13.00-14.00
	chair: Hakan Svedhem		
4MS³-VN-10	Oleg Vaisberg and Artyom Shestakov	Dynamic processes in the solar wind as the cause of Venus ionosphere disturbances and loss of mass / **invited talk**/	14.00-14.20
4MS³-VN-11	Eduard Dubinin	Ionospheric magnetic fields and currents at Venus	14.20-14.40
4MS³-VN-12	Anatoly Gavrik et al	Stratified multi-layer structures of the Venus ionosphere from Venera 15 and 16 radio occultation measurements	14.40-14.55
4MS³-VN-13	Vladimir Gubenko et al	Radio occultation studies of internal gravity waves in the Earth's and planetary atmospheres	14.55-15.10
4MS³-VN-14	Vladimir Gotlib et al	Continued studies of the atmosphere of Venus on the basis of the development of long-lived balloons. / Next step for Venus investigation with long-living superpressure balloons-aerobots	15.10-15.25
4MS³-VN-15	Mikhail Ivanov et al	Selection of landing sites for the Venera-D mission	15.25-15.40
4MS³-VN-16	Leonid Ksanfomality	Hypothetical life found at the VENERA-14 landing site	15.40-16.00
	coffee-break		16.00-16.30
	SESSION 6: NEW PROJECTS		**16.30-19.00**
	convener: Oleg Korablev		
4MS³-NP-1	Olivier Witasse et al	The ExoMars programme	16.30-16.45
4MS³-NP-2	Francesca Esposito et al	The DREAMS experiment for the ExoMars 2016 mission	16.45-17.00

4MS^3-NP-3	Daniil Rodionov et al	Science investigations at the ExoMars 2018 Landing Platform	17.00-17.15
4MS^3-NP-4	Philippe Lognonne et al	Seismic exploration of Mars with VBB seismometers	17.15-17.30
4MS^3-NP-5	Imant Vinogradov et al	Diode Laser Spectroscopy for Martian studies	17.30-17.45
4MS^3-NP-6	Oleg Vaisberg et al	Investigation of atmosphere-magnetosphere connections and atmospheric losses at Mars	17.45-18.00
4MS^3-NP-7	Marina Diaz Michelena and Rolf Kilian	MOURA Magnetometer and gradiometer for planetary magnetic mineralogy	18.00-18.15
4MS^3-NP-8	Jordanka Semkova et al	Radiation investigations for ExoMars and Luna-Glob missions	18.15-18.30
4MS^3-NP-9	Jinsong Ping et al	Chang'E-3/4 Lunar Landing Missions and Lunar Radio Science Experiments	18.30-18.45
4MS^3-NP-10	Alexander Gusev and O.Titov	Moon geodetic VLBI system	18.45-19.00

POSTER SESSION

15 OCTOBER 18.00-19.00
16 OCTOBER 19.00-20.00

	MARS	
4MS³-PS-01	Sergey Voropaev et al	Raman characterization of minerals in the recently fallen Martian meteorite Tissint
4MS³-PS-02	Soile Kukkonen et al	Resurfacing events on Martian outflow channels: A case study of Harmakhis Vallis in the eastern Hellas rim region
4MS³-PS-03	Sergey Raevskiy and Tamara Gudkova	Calculation of travel times for Martian interior structure models
4MS³-PS-04	Vladimir Smirnov, O.V. Yushkova	Calibration of subsurface radar «MARSIS» with Martian ionosphere
4MS³-PS-05	David K. Weiss and James W. Head	Ejecta Mobility of Excess Ejecta Craters on Mars: Assessing the Influence of Surface Snow and Ice deposits
4MS³-PS-06	Kathleen Scanlon and James W. Head	Snowmelt Modeling for Early Mars
4MS³-PS-07	Alvaro Gimenez-Bravo et al	Tomographic Signal Analysis for the Detection of Dust-Devils in Mars Atmosphere
4MS³-PS-08	Alexey Berezhnoy et al	Altai salt lakes halophiles under simulated early Mars conditions
	MOON	
4MS³-PS-09	Christian Wöhler et al	Analysis of the lunar hydroxyl absorption depth based on simulated surface temperature data
4MS³-PS-10	Roman Zhuravlev et al	Experiment ARIES-L for investigation of lunar regolith by means of SIMS and secondary neutras mass-spectrometry
4MS³-PS-11	Albert Abdrakhimov et al	Geological review of Lunokhod 1 area
4MS³-PS-12	Alex Tye et al	Ages of crater deposits of lunar south circum-polar craters containing evidence for volatiles: Haworth, Shoemaker, and Faustini
4MS³-PS-13	Ekaterina Grishakina et al	Compiling the hypsometric map of the Moon for the atlas “Relief of terres-trial planets and their satellites”
4MS³-PS-14	Mikhail Sinitsyn et al	Analysis of lunar pyroclastic deposits using LEND spectrometer data
4MS³-PS-15	Ekaterina Kronrod et al	The temperature profile of the lunar mantle and concentrations of radioactive elements in the Moon
4MS³-PS-16	Yangxiaoyi Lu et al	New Lunar Lander Site Selection
4MS³-PS-17	Michael Shpekin, A.A. Barenbaum	Impact craters Tsiolkovsky and Aitken as objects of search for residual water on the Moon
4MS³-PS-18	Boris Ivanov	Largest impact craters at small planetary bodies – models and observations
4MS³-PS-19	Gennady Kochemasov	Two examples of non-traditional interpretation of planetary features in light of latest cosmic data: 1) Mare Orientale gravity pattern; 2) Mercury’s Northern Plains and Arctic Ocean of Earth
4MS³-PS-20	Vladimir Smirnov , O.V. Yushkova	Luna-Glob: consideration of the relief effect in solving the inverse problem of subsurface sensing
4MS³-PS-21	Natalia Kozlova et al	New technology of Lunokhod’s panoramas image processing for detail mapping and analysis of lunar surface
4MS³-PS-22	Valeriy Burmin et al	On the nature of the seismic ringing of the Moon. Analytical modeling
4MS³-PS-23	Peter Wurz et al	Prototype of the gas chromatograph – mass spectrometer to investigate volatile species in the lunar soil for the Luna-Glob and Luna-Resource missions

DUST AND DUSTY PLASMA IN SPACE

4MS^3-PS-24	Maria Blecka et al	Numerical modeling the radiation emitted and scattered from the dust in the inner coma of the Comet 67P/ Churyumov Gerasimenko - a possible basis for spectrometric searches
4MS^3-PS-25	Elena Seran et al	Dust Lifting Experiment (DLE) : Variations of electric field and electric resistivity of air caused by dust motion
4MS^3-PS-26	Alexander Volokitin and Barbara Atamaniuk	The low-frequency turbulence in an inhomogeneous dusty plasma
4MS^3-PS-27	Inna Shashkova et al	Modeling the influence of lunar dust on the physical and biological systems

SOLAR SYSTEM STUDY: SOME MILESTONES

4MS^3-PS-28	Andrei Makalkin	What determines the sizes of the regular satellite systems of Jupiter and Saturn
4MS^3-PS-29	James Head et al	A global geologic map of Ganymede
4MS^3-PS-30	Alexey Berezhnoy et al	Theoretical fluorescence spectra of pyrene in cometary comae
4MS^3-PS-31	Svetlana Pugacheva, V. V. Shevchenko	Ancient volcanic relief types at Mars, Venus, Mercury and Moon. Origin, morphology, age
4MS^3-PS-32	Gennady Kochemasov	The wave planetology: comparative tectonic granulation of Titan, Moon, and Mercury in relation to heir orbital frequencies
4MS^3-PS-33	Victor Kronrod et al	Internal structure of Titan for the model of the homogeneous accretion in the circumplanetary disk
4MS^3-PS-34	Vladimir Busarev	Detection of possible spectral signs of O2 and CH4 on Europa and O2 on Ganymede and Callisto
4MS^3-PS-35	Tagir Abdulmyanov	Simulation of the initial stages of formation of proto-planetary rings in the Solar system
4MS^3-PS-36	Tagir Abdulmyanov	Determination of the initial moments of formation of proto-planetary rings in the Solar system
4MS^3-PS-37	Oleg Khavroshkin, V.V. Tsyplakov	Sun – Earth: new channel of interaction
4MS^3-PS-38	Sergei Ipatov	Outbursts and cavities in comets
4MS^3-PS-39	Sergei Ipatov	The angular momentum of colliding rarefied preplanetesimals allows the formation of binaries

VENUS

4MS^3-PS-40	Denis Belyaev et al	Analysis of sulfur oxides content above Venus' clouds
4MS^3-PS-41	Anna Fedorova et al	Observations of the near-IR nightside windows of Venus during Maxwell Montes transits by SPICAV IR onboard Venus Express
4MS^3-PS-42	Andrea Longobardo et al	Nocturnal variations of the Venus upper cloud scale height
4MS^3-PS-43	Evgeniya Guseva	Results of comparison of morphometric parameters of the dome-shaped rises and associated rift zones on Venus (Atla, Beta-Phoebe) and Earth (East Africa)
4MS^3-PS-44	Anatoly Gavrik, Ya. Ilyushin	Structure of the multi-ray radio wave field in the Venusian ionosphere: numerical simulations with parabolic diffraction equation
4MS^3-PS-45	Elena Petrova et al	Sizes of particles in the upper clouds of Venus from the SPICAV/VEx polarimetry
4MS^3-PS-46	Alessandra Migliorini et al	Thermal structure of the Venus night side, retrieved on VIRTIS/Venus Ex-press data
4MS^3-PS-47	Evgeniy Kuleshov et al	Database of Venus-15 and Venus-16 Radio Occultation Experiments

NEW PROJECTS

4MS^3-PS-48	Ilya Kuznetsov et al	Dust Complex of the ExoMars-2018 project
4MS^3-PS-49	Ilya Kuznetsov et al	Dust instrument for the Lunar landers

4MS^3-PS-50	Andrea Longobardo et al	VISTA, a micro-thermogravimeter to measure water and organics content in planetary environment
4MS^3-PS-51	Sergey Pavlov et al	Micro-Raman spectroscopy of a particle RA-QD02-0035 from a collection of the HAYABUSA space probe to the 25143 Itokawa asteroid
4MS^3-PS-52	Luis Vazquez et al	Solar Irradiance Sensor of the DREAMS-EDM ExoMars 2016
4MS^3-PS-53	Julia Bodnarik et al	Using In Situ Neutron and Gamma-ray Spectroscopy to Characterized Asteroids
4MS^3-PS-54	William Vaughan, J. W. Head	Thermal infrared spectroscopy of Mercury from orbit: Potential of, and predictions for, BepiColombo MERTIS
4MS^3-PS-55	Vassiliy Marchuk et al	Model of 3D-GPR for space applications
4MS^3-PS-56	Oleg Khavroshkin, A.Bogdanov	Exploration of Solar system: active seismology
4MS^3-PS-57	Konstantin Luchnikov et al	Polyatomic ions mass analysis using compact laser desorption/ ionization TOF-MS
4MS^3-PS-58	Dmitry Moiseenko et al	Energy-mass spectrometer for plasma measurements at Ganymede
4MS^3-PS-59	Ivan Ilin, A.G.Tuchin	Quasi periodic orbits in the vicinity of the Sun-Earth system L2 point and their implementation in "Spectr-RG" and "Millimetron" missions
4MS^3-PS-60	Alexey Grushevskii et al	To the Orbit Designing of the Jovian's Missions Using Reducing Gravity Assist Maneuvers For The Landing
4MS^3-PS-61	Anna Dunaeva et al	Temperature change under adiabatic conditions in H2O containing interiors of Titan

RUSSIAN SOLAR SYSTEM EXPLORATION PROGRAM. UPDATED VERSION.

Lev Zelenyi[1], Vladimir Popovkin[2],
[1]Space Research Institute, RAS, Moscow, Russia, [2]Russian Federal Space Agency, Moscow, Russia

Space programs dedicated for the studies of Solar System are a part of the National programme of fundamental research in space. Until recently this program was entirely dedicated to late fulfilment of the 1980-90th plans. This in particular concerns the astrophysical missions of Spectrum series: Spectrum-R (Radioastron) is being successfully operated; Spectrum-X and Spectrum-UV (WSO) are in preparation. In the filed of Solar System the lessons learnt from the Phobos-Grunt mission led to significant strategy change: Roscosmos and the Space Council of Russian Academy are working toward implementing a more conservative step-by-step approach. The strategic line of planetary exploration is oriented on landings, the main targets being Moon and Mars. Close and equal cooperation with European Space Agency in planned missions has already become pivotal, and is continuously broadening. The newest timeline of lunar launches, its connection with ExoMars ESA-Roscosmos programme, will be presented. The plans for Solar terrestrial, and the developments toward the space missions to other planets will be also outlined.

ESA'S SPACE SCIENCE PROGRAMME – ACHIEVEMENTS AND FUTURE OPPORTUNITIES

Alvaro Gimenez,
ESA

The Science Programme of the European Space Agency has been covering a broad array of scientific topics, spanning from space astronomy to visiting a number of solar system objects, from comets - with the Rosetta mission, soon to encounter its target- to Venus and Mars -with the missions Venus Express and Mars Express- to the outer planets -with the successful landing of the Huygens probe on Titan and the recently started JUICE probe to Jupiter's icy moons. The presentation will give an overview of both the Programme and its governance, illustrating the range of successful missions implemented in the past and the ones currently under implementation, and explaining how missions are defined and decided within ESA's Science Programme. It will in particular focus on current and future opportunities offered by the Programme. In parallel ESA also has a Robotic Exploration Programme, which currently focuses on the exploration of Mars through the ExoMars mission implemented in collaboration with Roscosmos, the details of which will be highlighted in a dedicated presentation.

NASA'S PLANETARY SCIENCE MISSIONS

James L. Green
NASA, Planetary Science

The status and plans of NASA's Planetary program will be reviewed. In exploring any particular solar system object, NASA has followed a general paradigm of "flyby, orbit, land, rove, and sample return." A complete campaign may not be performed for each interesting object in the solar system, since not all our scientific questions can be studied at all objects, and there are high technological and financial hurdles to overcome for some missions and certain destinations. The National Academy of Science's Planetary Decadal document provides recommendations on critical missions answering the top science questions which are used as NASA guideline for potential future missions.

Significant recent progress on a number of solar system bodies has been made. Our first flyby or reconnaissance missions include: New Horizons, a mission to the Pluto system (encounter July 2015), the Dawn mission, is making its way to Ceres (spring July 2014) after spending a year at Vesta, both in the asteroid belt. NASA orbiting missions include: Lunar Reconnaissance Orbiter around the Moon, MESSENGER orbiting Mercury, Juno launched in August 2011 will begin to orbit Jupiter in 2017, and the Lunar Atmosphere and Dust Environment Explorer (LADEE) mission just launched in September is on its way to the Moon. The Cassini/Huygens flagship mission has been orbiting Saturn since the summer of 2004 and has been extended. NASA is also developing the OSIRIS-REx mission, a sample return mission to asteroid *Bennu*, and the InSight mission to Mars as the first geophysical seismic station, both of these missions are to be launched in 2016.

Starting in 2000 NASA embarked on a "follow the water" strategy for a string of tremendously successful missions of orbiters, landers, and rovers on Mars. Currently NASA has a number of active missions at Mars that include: Mars Reconnaissance Orbiter, Mars Odyssey, and the mid-sized rover Opportunity. These missions have made measurements that clearly show that Mars held a significant amount of water in its distant past. Even today we have indications that Mars holds significant water reserves below its surface. With the successful landing of the Curiosity rover on Mars we start a new era of missions that involve "seeking the signs of life." Curiosity is working flawlessly and has started on a two-year mission that will investigate the question of whether Mars was ever habitable. As we look further into the future, we now have started a new Mars rover, to be launched in 2020 and based on Curiosity's success, that will interrogate rock samples and store them for potential return.

Last but not least, NASA's planetary science division is proud of its participation on a number of missions originating with our foreign space agency partners. As NASA develops its strategic plans for future solar system exploration it will continue to embrace international participation and look for opportunities to contribute as appropriate.

MARS EXPRESS: 10 YEARS OF EXCITING SCIENCE

O. Witasse and A. Chicarro[1],
[1]ESA, ESTEC, PO Box 299, 2200 AG Noordwijk, the Netherlands,
contact: owitasse@rssd.esa.int

The ESA Mars Express mission was launched in June 2003 and has been orbiting the planet Mars for almost ten years. All the instruments and components of the spacecraft are still working flawlessly. This first European planetary mission has been providing exciting new scientific results on the interior of the red planet, its subsurface, its surface mineralogy, geological processes and seasonal effects, its atmospheric dynamics and chemistry, the interaction of its upper atmosphere with the solar wind, as well as a mine of unique information on the natural satellites Phobos and Deimos. Also, Mars Express is helping to pave the way of future European Mars Exploration, including the ExoMars Trace Gas Orbiter and Entry and Descent Module in 2016, the ExoMars rover in 2018 and beyond. Among the abundant Mars Express results, a selection of scientific highlights of the mission will be presented, addressing all fields of Mars investigation.

ANTARCTIC DRY VALLEY STREAMS AND LAKES: ANALOGS FOR NOACHIAN MARS?

J. W. Head, III[1] and D. R. Marchant[2],
[1]Dept. of Geological Sciences, Brown University, Box 1846, Providence, RI 02912 USA; [2]Dept. of Earth & Environment, Boston University, Boston, MA 02215 USA. Contact: james_head@brown.edu

Introduction: Recent climate models [1,2] suggest that Noachian Mars may have been characterized by a “cold and icy”, rather than a “warm and wet” climate [3]. Noachian valley networks and open basin lakes have been cited as key evidence for a “warm and wet” early Mars. Here we investigate fluvial and lacustrine processes in the Mars-like Antarctic McMurdo Dry Valleys (MDV) [4] to assess whether such processes, which take place in the absence of pluvial activity and with mean annual temperatures (MAT) well below zero, can serve as informative proxies for Noachian Mars [3].

Fluvial Processes: Fluvial processes in temperate climates dominate the evolution of the landscape due to the abundance of pluvial activity and the consequence of its drainage, chemical and physical erosion and transport, and its influence on a host of other processes. In the hyperarid, hypothermal MDV, however, there is no pluvial activity. Delivery of water to the surface environment is by direct snowfall in very small amounts (3-50 mm a^{-1} water equivalent in the MDV [5]) and from snow transported laterally off the polar plateau by katabatic winds. Snowfall can drift and be sequestered in topographic traps and wind shadows. Long-term snow and ice accumulation results in the formation of glaciers, and their seasonal melting represents the major source of liquid water for fluvial activity. Melting occurs only seasonally and all streams are ephemeral on seasonal and sometimes daily time scales. Due to localized sources and the immature topography of the MDV, stream order is very low, and streams tend to form ice-covered, closed-basin lakes.

The range of microenvironments in the MDV results in significant variation in the state and activity of water *within* the MDV [4]. In the *stable upland zone* (SUZ), temperatures are sufficiently cold both annually and seasonally that fluvial activity does not occur. In the *inland mixed zone* (IMZ), streams are minimal in number, drainage basins are by definition small, and streams are virtually all of first order. The shallow substrate is characterized by permafrost with an ice table at 15-40 cm depth beneath a regionally dry active layer. Recharge zones are limited to perennial and annual snow patches, some of which are trapped in alcoves and gully channels that undergo top-down melting. Initially, meltwater percolates vertically downward, wetting the dry active layer below, and then also migrates laterally to create a wetted zone along the margins of channels (the *hyporheic zone*).

Significant volumes of meltwater that infiltrate down from the surface may flow downslope along the top of the ice table (15-40 cm depth), wicking up and feeding the advancing hyporheic zone. Flow in the hyporheic zone along ephermal streams occurs at three scales: 1) locally in the stream bed, flux may be insufficient to overcome the infiltration capacity of the channel sediment, and meltwater percolates into the substrate only to re-emerge a few meters down-channel in springs at a topographic step caused by the presence of rocks; 2) at the bases of slopes and near valley bottoms, wet-topped polygons form in topographic lows, creating a “swampy” spongy area where patches of water can be seen to emerge to the surface; 3) water may continue to travel along the ice table in the valley floor until it can intersect the surface, forming a local pond [6].

In the *coastal thaw zone* (CTZ), seasonal temperatures exceed the melting point of snow and ice in soils. Alpine and piedmont cold-based glaciers extend down into the CTZ and can undergo significant surface melting, creating the meltwater that feeds the vast majority of ephemeral streams and associated hyporheic zones, and ultimately drains into lakes. Meltwater generation is significantly influenced by the geometry of the glacier relative to solar insolation [7,8]. There is also evidence that significant melting can take place below the solid surface in the upper meter of glacial ice by absorption of solar radiation along crystal boundaries [7]. Glacial meltwater cascades off the edge of the ice, often in waterfalls, and drains downslope in streams. Streamflow is quite variable [9], depending on melting in the source region [7], and streams are of low order. Most streams flow into closed-basin lakes [10]. Since there is no pluvial activity, streamflow is restricted to the meltwater fluvial channel and associated hyporheic zone [6]. Chemical weathering is highly concentrated, especially in stream channels [11], and the large areas of terrain between channels are largely unaffected and unmodified by fluvial activity.

In some cases, epiglacial lakes [10] can serve as the source of streams and, because of short-term storage of liquid water next to the source, these can form longer streams and even rivers that flow for most of the summer season. Meltwater from Wright Lower Glacier is impounded behind a moraine complex, forming Lake Brownsworth. Drainage from Lake Brownsworth forms the ~35 km long Onyx River that flows into Lake Vanda, a closed-basin lake toward the western end of Wright Valley. The immature nature of the Onyx River retains a memory of recent antecedent climatic events and can thus be used to compare fluvial histories between valleys [12].

In summary, in contrast to temperate climates, fluvial processes in the MDV (and thus a host of weathering, erosion and transport processes there) are severely limited by the lack of rainfall. Fluvial activity is absent in the stable upland zone, seasonal and intermittent in the inland mixed zone, and often seasonally continuous, but ephemeral in the coastal thaw zone [4]. The limited sources of meltwater provide very local streams and hyporheic zones, serving to concentrate chemical weathering processes and biological ecosystems. The horizontally stratified hydrologic system means that localized meltwater is constrained to flow in a very shallow and narrow aquifer perched on top of the ice table aquiclude (Fig. 1).

Lacustrine Processes: More than 20 permanent lakes and ponds occur in the MDV [10] and, in contrast to temperate lakes, almost all are characterized by perennial ice cover up to 6 m thick, overlying liquid lake water. Ice cover serves to: 1) limit exchange of gases between the lake and the atmosphere, 2) restrict sediment deposition in the lake, 3) reduce light penetration, and 4) minimize wind-generated currents [13]. Lake levels have been rising in the recent past at about 15 cm a^{-1} [10], a trend interpreted to be due to a corresponding increase in summertime surface air temperature [14].

Chinn [10] subdivided lakes in the Dry Valleys into several hydrological types: 1) *Wet-based* lakes do not freeze to the ground during austral winter and have either permanent, seasonal or no ice cover; summer inflow of meltwater beneath the ice cover causes lake levels to rise seasonally and they lower from sublimation of the ice cover and evaporation of the summer meltwater moat. 2) *Dry-based lakes* include ice-block lakes that are permanently frozen through to the lake bed; ice thicknesses may far exceed those in wet-based lakes and such lakes rise by addition of meltwater by flooding on top of the ice surface, and fall by ablation of the surface. Some dry-based lakes may have a thin film of highly saline water at their base. 3) *Ice-free lakes*, such as Don Juan Pond, are very highly saline, and usually do not freeze even in winter. Chinn [10] further subdivided MDV lakes on the basis of their openness and associations: 1) *Enclosed lakes* have no surface outflow (*closed-basin* lakes); summer inflow is balanced by annual sublimation and evaporation and such lakes are usually warm, saline, and meromictic. 2) *Lakes with throughflow* overflow into outlet streams (*open-basin* lakes), have relatively stable levels, and are commonly not saline. 3) *Epiglacial lakes* are on or against glaciers.

How do these lakes differ from temperate lakes? First, MDV lakes lie on top of a 200-300 m thick permafrost layer; intuitively, one might imagine that these lakes should freeze solid due to mean annual surface air temperature of ~<-20°C. However, very finely-tuned conditions lead to the present characteristics in MDV wet-based lakes. Stratfication results from saline density gradients and the ice cover prevents wind mixing of lake water.

Where does the lakewater come from and under what conditions is excess meltwater produced to cause modifications in their levels? The dominant means of supply (meltwater) and loss (ablation) are clearly seasonally and climatically controlled. Throughout their recent history it is clear that small perturbations to the climate can result in large changes in the lake systems, often in non-intuitive ways [10]. Clearly, the main source of meltwater supply in the MDV is from surface melting of glaciers and snowbanks, but this is not a simple function of increasing MDV surface air temperature [10]. The observed positive correlation between increased lake levels and streamflow is thought to represent a complex relationship with the climate-related behavior of glaciers, specifically depending on the distribution of glacier area with elevation in the watershed [10,15]. As the H_2O melting temperature rises seasonally in altitude, glaciers are encountered and melting of their fronts will begin in a complex non-linear manner [7,16], feeding streamflow. The rate of stream flow will increase as seasonal warming brings the melting temperature up to the specific elevation that represents the maximum glacier area per elevation contour in the ablation zone [7,10,15,16].

Summary: Lakes and ponds in temperate areas are largely of pluvial origin and characterized by abundant vegetation, large drainage basins and higher order streams delivering rainwater. In contrast, the hyperarid, hypothermal conditions in the MDV mean that there is no rainfall, water sources are limited primarily to meltwater from the surface of cold-based glaciers, and drainage into lakes is seasonal and highly variable, being related to changing and sluggish response to surface ice hypsometry, itself a function of changing climate. Lake surface level fluctuations are caused by imbalances between meltwater input and sublimation from the lake surface ice and this sensitive balance tends to magnify even minor climate signals. This framework of seasonal melting and fluvial/lacustrine processes in an otherwise hyperarid, hypothermal Mars-like Antarctic cold-based non-pluvial environment [4,7,8,10] provides a baseline of environmental conditions to test the hypothesis that a “cold and icy” Noachian Mars [1,2] might produce the observed fluvial and lacustrine features [e.g., 17,18] during transient warming periods [3].

References: 1. F. Forget *et al*., *Icarus* **222***,* 81 (2013). 2. R. Wordsworth *et al*., *Icarus* **222***,* 1 (2013). 3. J. Head, LPSC 44, #1523. 4. D. Marchant, J. Head, *Icarus* **192**, 187(2007). 5. A. Fountain *et al*., *Int. Jour. Climate*. doi: 10.1002/joc.1933 (2009). 6. M. Gooseff *et al*., *Hydro. Proc.* **17**, 1691 (2003). 7. A. Fountain *et al., Global Planet. Change* **22**, 1 (1999). 8. G. Dana *et al*., *Ant. Res. Ser.* **72**, AGU, 39 (1998). 9. P. Conovitz *et al. Arct. Antarct. Alp. Res.* **38**, 42 (2006) 10. T. Chinn, *Ant. Res. Ser.* **59**. AGU, 1 (1993). 11. C. Nezat *et al*., *Geol. Soc. Am. Bull.* **113**, 1401 (2001). 12. J. Shaw, T. Healy, *N. Z. J. Geol. Geophy*. **23**, 223 (1980). 13. P. Doran *et al., J. Paleolimn.* **10**, 85 (1994). 14. R. Wharton *et al*., *J. Geophys. Res*. **97**, 3503 (1992). 15. A. Fountain *et al*., *J. Glaciol.* **50**, 556 (2004). 16. G. Dana *et al., Ant. Res. Ser.* **72**. AGU, 39 (1998). 17. C. Fassett, J. Head, *Icarus* **195***,* 61 (2008). 18. C. Fassett, J. Head, *Icarus* **198***,* 37 (2008).

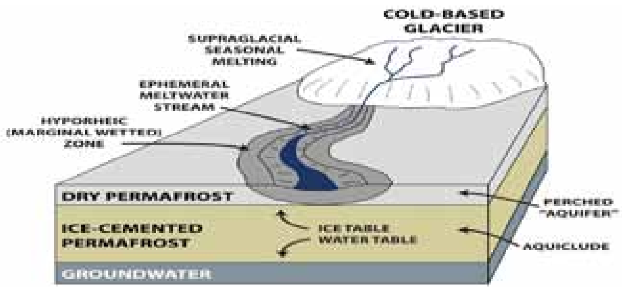

fig. 1. Antarctic MDV Hydrological System [4].

CHEMISTRY AND TIMING OF FORMATION OF MARTIAN PHYLLOSILICATES AND SALTS.

M. Yu. Zolotov[1], M. V. Mironenko[2],
[1]School of Earth and Space Exploration, Arizona State University, Tempe, AZ 85287-1404, USA; [2]Vernadsky Institute of Geochemistry and Analytical Chemistry, Russian Academy of Sciences, 19 Kosygin Str., Moscow 119991, Russia.
Contact: zolotov@asu.edu

Introduction: Orbital spectral observations of the Martian surface indicate uneven occurrences of aqueous minerals in geological formations of different ages. Secondary minerals seen in the Noachian terrains are dominated by phyllosilicates, while the Hesperian formations are characterized by massive deposits of layered sulfates seen in the Valles Marineris trough system, related depressions, and other places [1-4]. The initial interpretation of these data suggested deposition of phyllosilicates from Noachian alkaline solutions and formation of sulfates from acidic fluids related to volcanism in the Hesperian epoch [1].

Fe-Mg phyllosilicates (smectites, chlorites) are the most abundant clay minerals [2-4]. Typically, Fe-Mg phyllosilicates are located at lower stratigraphic layers than Al-rich clays such as montmorillonite and kaolinite. As an example, in the Mawrth Vallis region, minerals are observed within the following stratified sequence of layered rocks (from the top): silica and kaolinite, montmorillonite-like Al-rich clays, a Fe^{2+} phyllosilicate, Mg/Fe smectites, and sulfates [5-8]. Sulfates are also seen in the middle part of the stratigraphic sequence.

The composition and occurrence of phyllosilicates and salts could be used to constrain ancient aqueous environments. This requires understanding of effects of solution chemistry, pH, Eh, temperature, and duration of processes on composition of precipitated minerals. In addition to terrestrial analogs and laboratory data, the formation and fate of secondary minerals could be evaluated with numerical physical-chemical models. We have modeled rock alteration by percolating aqueous solutions to constrain origins of observed minerals.

Modeling of weathering profiles with clay minerals and salts: Alteration was modeled through calculation of chemical equilibria in multicomponent systems with non-ideal aqueous, solid, and gas solutions. These models consider solubilities of solids and gases in aqueous solution and constrain conditions of mineral saturation. Additional procedures quantify pH-dependent rates of mineral dissolution coupled with chemical equilibria in solution [9] and percolation of fluids. With these models, formation and compositional evolution of secondary minerals could be linked to a specific stage and/or setting of water-rock interaction. The models tie the composition and pH of solution with the mineralogical assemblage, which may contain secondary phases together with unaltered minerals.

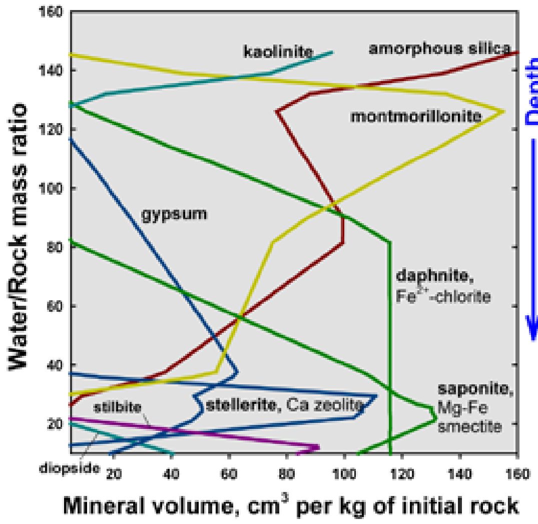

fig. 1. The water-rock (*W*/*R*) ratio as a proxy for depth in a weathering profile of Adirondack martian basalt. Upper layers are altered at higher *W*/*R* ratios. Kaolinite, montmorillonite, and amorphous silica form at high *W*/*R* ratios. Fe-Mg clays are abundant at lower *W*/*R* ratios (at depth). The results agree with observations in the Mawrth Vallis region and predict unobserved phases.

Our models demonstrate sequential formation of phyllosilicates (kaolinite then smectites), low-solubility salts (gypsum), and salt-bearing solutions through neutralization of acidic fluids interacting with martian basalt (Figs. 1-3). Modeling of percolation of acidic fluids through basalts predicts formation of the vertical sequence of dominated minerals (from the top): amorphous silica - kaolinite and/or montmorillonite - ferrous chlorite - Fe-Mg smectites. Zeolites and Fe^{2+}-chlorites occur with smectites, and Fe^{2+} chlorite-bearing rocks form between layers rich in montmorillonite and smectites. This series reflects leaching of elements and neutralization

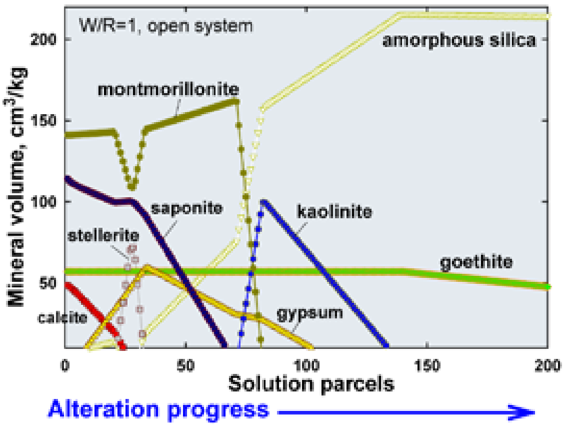

Fig. 2. The modeled evolution of the surface basalt layer affected by parcels of O_2-saturated acidic fluids. The increasing number of solution parcels corresponds to alteration progress. A moderately alerted assemblage rich in smectites evolves toward the assemblage where kaolinite, silica, and goethite dominate. Kaolinite dissolves at later stages of alteration. Silica and goethite are the only minerals in extensively leached basalt.

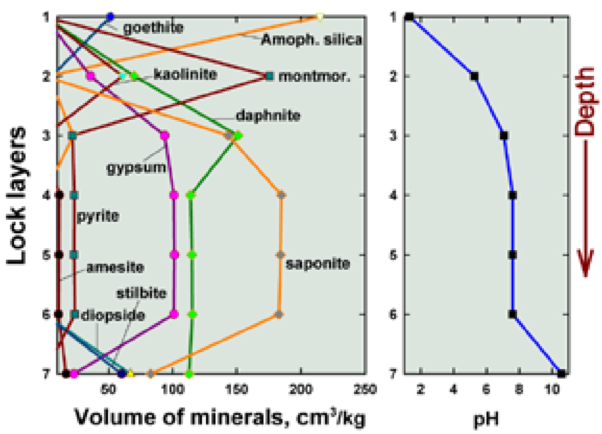

fig. 3. The modeled weathering profile of Adirondack basalt formed through percolation of acidic fluids from above. Silica and montmorillonite dominate in upper layers and Fe-Mg clays are at depth. The plot on the right shows neutralization of fluids at depth. The results agree with observations in the Mawrth Vallis region.

of fluids with depth, and is similar to the succession observed in the Mawrth Vallis region [5-8] and other areas. The minerals observed in the upper part of the martian profile (silica and ferric phases, Fig. 2) agrees with an open-system alteration in acidic conditions.

The results show that phyllosilicates could form together with sulfates, and clay-sulfate assemblages (except kaolinite-rich or jarosite-rich cases) do not indicate acidic environments. The results also suggest that alteration solutions rich in high-solubility salts could have accumulated at depth in pore spaces and subjected to freezing, evaporation or migration throughout history.

Modeled weathering by neutral fluids also leads to a stratified sequence of Al-rich (top) and Fe-Mg clays (bottom). However, formation of a 100 m weathering profile requires tremendous volumes of neutral or slightly acidic (CO_2-saturated) fluids and does not look feasible. These models do not produce abundant salts and are inconsistent with observations.

Discussion - Hesperian interior layered sulfates could be remobilized Noachian salts: The modeled formation of phyllosilicates together with salts imply formation of abundant salts in the Noachian epoch (see also [9,10]). These rock alteration models are consistent with the detection of Noachian sulfate-phyllosilicate assemblages [e.g., 11,12] and possible chloride deposits [13]. Several vol. % of sulfates could be present in Noachian clay-rich formations but may not be detected with orbital methods. A formation of interior layered sulfate deposits through acidic alteration of silicate rocks in the Hesperian epoch [1] should have led to formation of vast phyllosilicate and/or silica deposits, which are not observed. Therefore, we advocate for a scenario that includes aqueous alteration of mafic rocks by transient fluids generated by Noachian impacts related to the Late Heavy Bombardment. Acidic fluids generated by impacts [9] were neutralized through alteration of rocks followed by precipitation of phyllosilicates and low-solubility Ca sulfates. Neutralized fluids rich in high-solubility Mg and Na sulfates and chlorides have accumulated in ground waters. Subsequent freezing of subsurface fluids led to deposition of these salts in the pore space and accumulation of subfreezing brines in the megaregolith. Some cold chloride-rich brines could have released to the surface, consistent with observations [13]. A Hesperian remobilization of high-solubility sulfates and chlorides could have been caused by melting of crustal ice related to an enhanced heat flow, and by basaltic magmatism and volcanism. Subsurface drainage of neutral fluids into depressions (e.g., Valles Marineris and other chasmata) was followed by the formation and evaporation of sulfate-rich lakes. This scenario does not exclude a near-surface formation of sulfates and opaline silica by transient acidic aerosols, rains, and other fluids related to volcanic and impact events in the Hesperian and Amazonian epochs.

Acknowledgement. This work is supported by NASA Mars Fundamental Research program.

References: [1] Bibring, J.-P. *et al*. (2006) *Science* 312, 400-404. [2] Mustard, J. F. *et al*. (2008) *Nature* 454, 305-309. [3] Murchie, S. L. *et al*. (2009) *J. Geophys. Res*. 114, E00D06. [4] Carter, J. *et al*. (2013) *J. Geophys. Res.: Planets* 118, 831-858. [5] Wray, J. J. *et al*. (2008) *Geophys. Res. Lett*. 35, L12202. [6] Bishop, J. *et al*. (2008) *Science* 321, 830-833. [7] McKeown, N. K. *et al*. (2009) *J. Geophys. Res*. 114, E00D10. [8] Wray, J. J. *et al*. (2010) *Icarus* 209, 416-421. [9] Zolotov, M. Y., and Mironenko, M. V. (2007) *J. Geophys. Res*. 112, E07006. [10] Milliken, R. E. *et al*. (2009) *Geophys. Res. Lett*. 36, L11202. [11] Wray, J. J. *et al*. (2010) *Icarus* 209, 416-421. [12] Milliken, R. E. *et al*. (2010) *Geophys. Res. Lett*. 37, L04201. [13] Osterloo, M. M. *et al*. (2012) *J. Geophys. Res*. 115, E10012.

THE FIRST RESULTS OF DAN INVESTIGATIONS ONBOARD THE NASA'S CURIOSITY

Igor Mitrofanov, Maxim Litvak et al.,
Space Research Institute of RAS, Moscow, Contact: mitrofanov@l503.iki.rssi.ru

The first results will be persented of DAN active neutron measurements for probing of water content in the soil along the traverse of the Curiosity rover over the floor of the Cale crater on Mars.

MARS: LOCAL MORPHOLOGY OF THE SURFACE AT THE DAN MEASUREMENTS SPOTS IN THE GALE CRATER.

R.O. Kuzmin [1,2], I.G. Mitrofanov [1], M.L. Litvak [1], A.B. Sanin [1], A. Varenikov [1], C. Hardgrove [3], C. Tate [3], A. Behar [4], W.V. Boynton [5], L. DeFlores [4], F. Fedosov [1], D. Golovin [1], K. Harshman [5], I. Jun [4], A.S. Kozyrev [1], A. Malakhov [1], M. Mischna [4], J. Moersch [3], M. Mokrousov [1], S. Nikiforov [1], V.N. Shvetsov [6], V.I.Tret'yakov [1], A. Vostrukhin [1].

[1] Space Research Institute, RAS, Moscow, 117997, Russia, rkuzmin@yahoo.com,
[2] V. I. Vernadsky Institute for Geochemistry and Analytical Chemistry, Russia;
[3] Univeristy of Tennessee, Knoxville, TN, USA; [4] Jet Propulsion Laboratory/California Institute of Technology, Pasadena, CA, USA; [5] University of Arizona, Tucson, AZ, USA; [6] Joint Institute for Nuclear Research, Dubna, Moscow Region, Russia.

Introduction:

Along the MSL rover Curiosity traverse (from Bradbury landing site up to Yellowknife ay area) the Dynamic Albedo of Neutrons (DAN) instrument conducted measurements of the thermal and epithermal neutrons counts in active and passive modes in the top~60 cm of the Martian subsurface [1, 2]. Based on both modes of measurement it was found that the thermal and epithermal neutron counts values measured along the rover traverse show distinct variability from one rover location to another [1, 2]. Such variability in neutron counts may be caused by both inhomogeneity of the hydrogen content within the surface soil layer [1, 2] and the presence in the Martian soil of such elements as Cl and Fe, which have a higher thermal neutron absorption cross-section than other elements [3, 4]. To understand how the local surface morphology at the DAN testing spots related with observing variability in the thermal and epithermal neutron counts values, we analyzed the correlation of DAN measurements with the local diversity of surface micro-morphology and regolith texture along the rover Curiosity traverse.

Correlation of the local surface morphology with the DAN measurements:

As is well seen from HiRISE image ESP_028335_1755, the landing site area of the MSL rover represents, in general, a slightly hummocky and wavy plain inclined to the east. From the landing site (Bradbury Landing) to the point known as "Glenelg**" the elevation of the plain decreases by ~15 m. Locally, on the plain surface, spots of harder rock outcrops (with size from one to tens meters) are seen among the coarse surface regolith. This means that the thickness of the surface** clastic material layer along the rover traverse most likely varies from place to place from the first few centimeters up to one meter or more in local shallow depressions. A map of the different surface types within the rover Curiosity landing site area was compiled [5] based on the HiRISE image ESP_028335_1755. Typical examples of observing diversity of the small-scale surface morphology within some mapped surface types shown on the Figure 1.

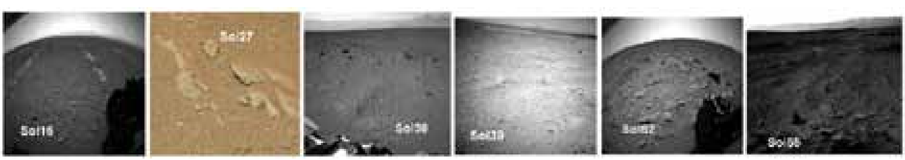

fig. 1. *Observing variability of the small-scale surface morphology at the crossing of the different surface types along the rover Curiosity traverse.*

For a correlation of the traversed surface types with the DAN measurements we used so-called "quicklook" (QL) parameters created for an initial analysis of the data: QL1- this parameter characterizes the thermal neutrons and is sensitive to both water content in the soil (more counts = more water) and content of such absorbing elements as Cl and Fe (less counts = more abundance of these elements); QL2- this parameter is more oriented towards water detection from the epithermal neutrons (lower value = more water); QL3- this parameter represents the ratio between thermal and epithermal neutrons counts. For passive mode of DAN measurements (during the rover driving) the QL5 parameter represents analog of QL3 parameter for active mode.

Observing variations of the QL1, QL2 and QL3 parameter values versus the distance along the traverse of the rover Curiosity (from Bradbury Landing to Glenelg) is shown in the Figure 2. The extent of the five surface types (5, 6, 8, 9 and 11 types) crossed by the rover during the 100 sols is shown in the lower part of the plots. As one can see from Figure 2, there is a distinct correlation between the variability of the QL1 and QL3 parameters values and the surface types: the values of the parameters are notably less within surface types 11 and 5 and higher within surface types 9, 8 and 6. During two parts of the rover Curiosity traverse (0-330 m and 420-500 m) all three quick-look parameters are characterized by a similar trend in their indication of water content variability (increasing/decreasing). Another tendency is observed at the distance range ~330-420 m of the rover traverse; here, the QL1 parameter indicates a gradual decrease of water amount in the surface regolith layer, while the QL2 parameter indicates the gradual increase of water amount. Because the parameter QL1 is also sensitive to the content of such absorbing elements as Cl and Fe in the soil, and the parameter QL2 is not sensitive to the elements, the most reasonable explanation for such a discrepancy between the parameters may be an increase in the Cl (or Fe) content in the surface regolith within this range. In places, the local differences in the degree of wind deflation result in the formation of lag deposits with a variable average size of stone fragments (gravel) as indicated by alternating places with larger and smaller gravel sizes in the lag deposits. Exactly such areal changeability of the regolith texture along the rover traverse during the Sol-48 was responsible for noticeable variability of the QL5 parameter values. It was found that during the DAN passive mode measurements when the rover Curiosity crossed different regolith structure (as well as the rocky outcrops) the QL5 parameter values noticeably changed within the distance scale in 1-5 m (Figure 3). At that, the lowest value of the QL5 parameter was related with rocky outcrop, while at the crossing of the regolith surface the parameter value was higher in the spot with finer regolith material.

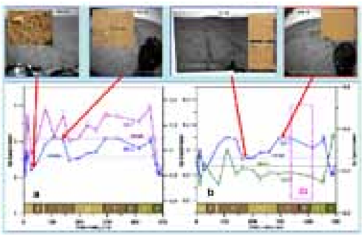

fig. 2. Variability of the DAN quick-look parameters QL1 & QL3 (a) and QL1 & QL2 (b) versus distance along the rover Curiosity traverse at active mode.

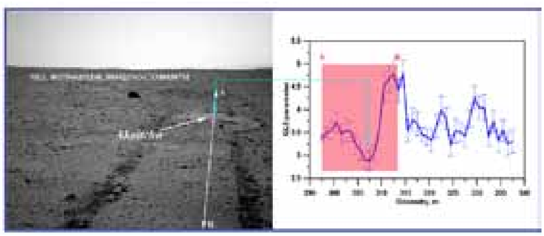

fig. 3. Dynamics of the QL5 parameter values at the DAN's passive mode measurements along 40-m path of the rover traverse during Sol-48. Blue arrow show location of the rocky outcrop Akaitcho with lowest value of the QL5.

Beginning from Sol 123 the rover Curiosity approached the region named as Yellowknife Bay representing the large-scale outcrop of the ancient and consolidated sedimentary rocks with surface broken by the polygonal set of the cracks (Figure 4). The sedimentary rocks represented by sequence of a several stratigraphic units which occupy different elevation levels and characterized by the bedded structure. The DAN measurements conducted within the region shown that the notable differences of vertical water distribution in the surface layer with ~60 cm thickness correlated well with surface morphology diversity on the distance of 1.5-2 m (Figure 5). The DAN measurements in the spot of sedimentary rocks slab (Sol-151) with polygonal cracks system are well fitted with double layer model of the water distribution (H_2O at the top=1.4 mass. %; at the depth 16 cm =3.8 mass. %), whereas it's measurements in the adjacent spot of crushed out sedimentary rocks in mixture with aeolian drift material (Sol-153) are well fitted with homogeneous model (H_2O=2.5mass. %). More detailed data will show during presentation.

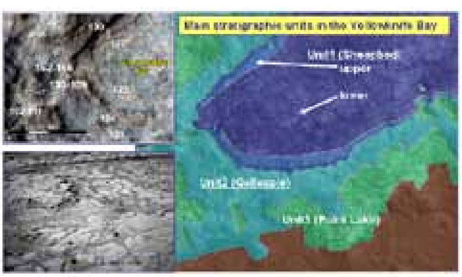

fig. 4. Targets of the DAN in the owknife Bay area.

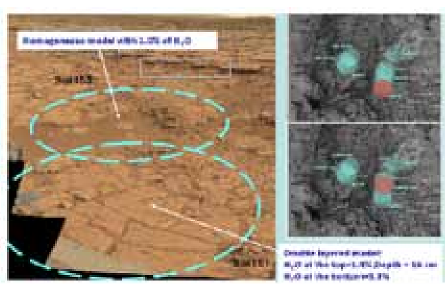

fig. 5. Variations of the water content related within the surface micro-morphology differences on the distance in 1.5-2 meters.

References: [1] Mitrofanov I.G. et al., (2013), LPSC 44 . [2] Litvak M.L. et al., (2013), LPSC 44. [3] Hardgrove et al., (2011) Nuc. Instr. Methods A, 659. [4] Hardgrove C. et al., (2013), LPSC 44. [5] Kuzmin R.O. et al. (2013), LPSC 44.

CONSTRUCTION OF MARTIAN SEISMIC MODELS. 2. FREE OSCILLATIONS AND BODY WAVES.

T. Gudkova[1], V.N. Zharkov[1], Ph.Lognonné[2], S. Raevskiy[1],
[1] *Schmidt Institute of Physics of the Earth, B.Gruzinskaya 10, Moscow 123995, Russia;* [2] *Institut de Physique du Globe de Paris, Sorbonne Paris Cité, Univ.Paris, France. Contact: gudkova@ifz.ru*

Introduction:

When constructing an interior structure model of a planet, it is common used method to describe the model by a restricted set of parameters: the thickness of the crust, the location of phase transitions, the core radius. The variation of these parameters originates from the uncertainties in temperature profile, composition, elastic and anelastic properties of relevant minerals. Olivine and its high pressure phases, wadsleyite β (Mg, Fe)$_2$SiO$_4$ and ringwoodite γ (Mg, Fe)$_2$SiO$_4$ are particularly important as they constitute about 60 wt % of the Martian mantle. Olivine, wadsleite and ringwoodite have probably large capacity for water in the Martian mantle [1]. The hydration affect seismic velocities of high pressure silicates more than the effect of Fe or temperature gradients, then water should be considered as a compositional variable in the mantle model. At present interior structure models of Mars are constrained by the recent estimates of the moment of inertia and the Love number k_2 [2]. Below we show how the admixture of water in the main minerals (olivine, wadsleite, ringwoodite) influences velocity drops at phase transition boundaries in Martian interiors and study the possibility to determine these boundaries measuring the periods of free oscillations and travel times of body waves, which could serve as additional constraints for interior structure models.

Seismic model:

Our analysis is based on a trial seismic model M7_4 from [3]. The crust is 50 km thick (with density of 2.9 g/cm^3), the molar ratio Fe/(Fe+Mg) in the mantle is 0.22, the Fe-Ni core contains 70 mol % H in addition to 14 wt % S with radius of 1775 km. The bulk Fe/Si ratio is close to chondritic. The density profile and seismic velocities are shown in Fig.1. The upper mantle extends down to 1615 km depth, The zone of phase transitions in it is of certain interest. Olivine-wadsleite transition zone is 65 km wide, it occurs at a depth of from 1115 km to 1180 km (14 GPa). The density and the velocities of P and S waves are increased by 0.22 g/cm^3, 0.6 and 0.4 km/s, respectively. The zone of wadsleite-ringwoodite transition begins at a depth of 1408 km and its width is 40 km (17 GPa). The density and the velocities of P and S waves are increased by 0.08 g/cm^3, 0.31 and 0.16 km/s, respectively. The absence of a lower mantle is related to the large core radius. The determination of the phase transition depth in the mantle is of importance, as it will fix the temperature profile in Mars.

Effects of hydration:

We use the data extrapolated for P-T conditions in Mars from Earth studies and laboratory measurements [1, 4-6]. Figure 2 shows the effects of hydration on seismic velocities of olivine, wadsleite, ringwoodite and model velocities. The compressional and shear velocities of the hydrous phase of olivine are faster than those of the anhydrous phase at 14 GPa, while hydration lowers the velocities of wadsleite. This leads to the decrease of velocity drop in the transition zone.

Free oscillations:

Free oscillations, if they are excited, is the most effective tool for sounding of deep interiors. Interpretation of data on free oscillations does not require knowledge of the time or location of the source; thus, data from a single station are sufficient. The important feature of free oscillations is that they concentrate towards the surface with increasing the degree *n*. Therefore different regions of interiors are sounded by different frequency intervals.

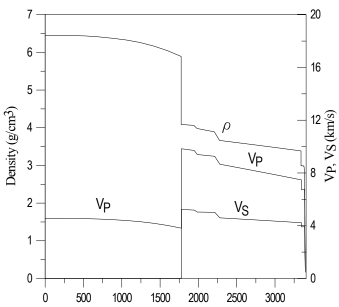

fig.1. Density ρ, compressional and shear velocities as a function of radius for a trial M7_4 model from [3].

The radial functions ${}_jW_n(l)$ of torsional oscillations are shown in Fig. 3 (l is the depth). The amplitudes of these functions are normalized to unity at the surface of Mars. The fundamental modes sound to those depth in the interiors where their displacements ≥ 0.3. The horizontal line (Fig.3 a) enables one to judge graphically which modes provide information about particular zones of the planet. Probing the transition zone begins with *n*=5-6. The internal

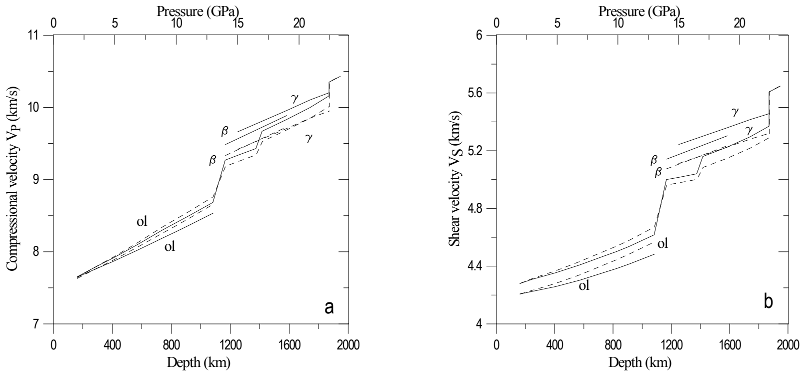

fig. 2. Compressional (a) and shear (b) velocities for olivine, wadsleite, ringwoodite and for a trial seismic M7_4 model (solid line) and the effect of hydration (dashed line). The abbreviations are ol, olivine; β, β-spinel (wadsleite); γ, γ-spinel (ringwoodite).

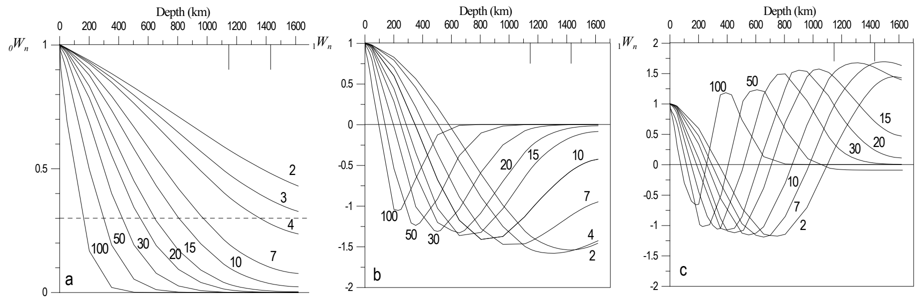

fig.3. Functions $_{l}W_{n}$ (l), proportional to the displacements of torsional oscillations for n=2 to 100 for the fundamental mode (a), the first overtone (b) and the second overtone (c). The values of $_{l}W_{n}$ are normalized to unity at the surface. The short vertical lines indicate the boundaries of the transition from olivine to wadsleite (1145 km depth) and from wadsleite to ringwoodite (1430 km depth).

regions of the planet have a greater effect on the displacements of overtones than on the fundamental tones. The oscillations with higher overtone numbers penetrate deeper into the planetary interiors. Therefore, for testing the interior of Mars, it would be interesting to record the overtones of the torsional oscillations. It was shown [7], that torsional oscillations modes with $n \geq 3$ (if a marsquake with $M_0=10^{25}$ dyne cm occurs), with $n \geq 6$ ($M_0=10^{24}$), and with $n \geq 12$ ($M_0=10^{23}$) could be detected. These modes can sound the Martian interiors down to 1600, 1100 and 700 km, respectively. The displacement amplitude for the overtones is smaller than that for the fundamental tones.

Travel times of body waves:

Differential measurements of arrival times of later-arriving phases (PcP, PcS, ScS) in comparison to P could put some restrictions on the seismic velocities in the deep mantle [8]. The difference in travel-time curves for P, PcP, S, ScS waves between a trial model M7_4 [3] and the same model with some amount of water in its mantle is up to several seconds for P and PcP, and S and ScS arrivals.

Conclusion:

Quantifying the effects of hydration on the velocities of olivine, wadsleite and ringwoodite with likely mantle Fe- content is of particular interest for accurate predictions of the seismic response of Mars. Upcoming seismic measurements [8, 9, 10] can potentially constrain mantle composition and make more precise the location of transition zone.

Acknowledgements: This work was supported by Grant No. 12-02-00378 from the Russian Fund for Fundamental Research.

References: [1] Zharkov, V.N., Gudkova, T.V. (2013) Abstract, 4M-S3. [2] Konopliv, A.S. et al. (2011) Icarus, 211, 401-428. [3] Zharkov, V.N. et al. (2009) Phys.Earth Planet.Int, 172, 324-334. [4] Mao, Z. et al. (2010) Earth Planet. Sci. Lett..293. 250-258. [5] Mao, Z. et al. (2011) Amer. Miner, 96. 1606-1612. [6] Mao, Z. et al. (2012) Earth Planet. Sci. Lett..331-332. 112-119. [7] Gudkova, T.V., Zharkov, V.N. (2004) Phys. Earth Planet. Int. 142, 1-22. [8] Dehant,V. et al. (2012) Planet. Space Sci., doi :10.1016/j.pss.2011.10.016. [9] Lognonné, P., et al. (2012) Abstract, 3MS3-1-7. [10] Gudkova, T.V. et al., (2013) Sol. Syst. Res, 47, 1.

GLOBAL SCALE PLANETARY MAGNETOMETRY

Marina Diaz-Michelena[1], Miguel Herraiz[2,3],
[1]INTA, Torrejon de Ardoz, Spain; [2] Universidad Complutense de Madrid, Spain;
[3]Instituto de Geociencias (UCM,CSIC), Madrid, Spain. Contact: diazma@inta.es

MGS magnetic data allowed obtaining a possible explanation of the sources that generate the in orbit magnetic field. The solution, though astonishing, has several deficiencies like its non-uniqueness and the space averaging due to the relatively high altitude of the spacecraft (between 100 and 400 km).

On Earth, these problems are partially solved by means of measurements at different altitudes: aeromagnetic, balloons and high resolution surveys.

Among these, aeromagnetic data are a still a dream on Mars and the Moon. However, it is achievable to have magnetic instruments both on board balloons and rovers.

In this work it is presented a reflection about the potential of this scenario in the understanding of planetary magnetic structures.

EVIDENCE FOR POSSIBLE HESPERIAN GLACIATION IN UTOPIA PLANITIA ON MARS.

M. A Ivanov[1], H. Hiesinger[2], G. Erkeling[2], and D. Reiss[2],
[1]GEOKHI, Kosygin-19 Moscow, Russia, [2]Wilhelms-Universität, Münster, Germany.
Contact: mikhail_ivanov@brown.edu;

Introduction: The southern edge of Utopia Planitia and Isidis Planitia are two major sites of thumbprint terrain (TPT) on Mars [e.g., 1] and the Hesperian-age Vastitas Borealis Formation (VBF) covers the largest portions of both regions [e.g., 2-4]. TPT is characterized by curved ridges and chains of mounds with summit pits and there is a variety of proposed models ranging from glacial to volcanic to explain formation of this terrain [5,6]. In contrast to Isidis where isolated mounds prevail [7], TPT in southern Utopia consists of more prominent ridges. This may indicate either different processes of formation of TPT in Isidis and Utopia Planitiae, or different state of preservation/ degradation of structures of TPT in these regions, or both. In our study we analyzed topographic and morphologic characteristics and age relationships of various types of ridges (including those of TPT) that are abundant near the southern edge of Utopia Planitia (20-25°N, 100-120°E). Our goal was to assess possible environments in which the ridges formed and put constraints on the range of models of TPT formation.

Characteristic features of southern Utopia: Contact between VBF (to N) and smooth plains (to S) is the main feature of the southern edge of Utopia Planitia. The contact consists of a series of lobes that are convex toward smooth plains. Numerous ridges, obviously of different origin, occur in the zone transitional from smooth plains to VBF. In our study area we have defined the following types of ridges:

(1) Ridges that have almost no morphologic signature but are topographically prominent. They form elongated rises that are a few tens of kilometers wide, several tens of kilometers long and ~80-120 m high. The ridges are oriented in NNE direction toward the center of the Utopia basin. In a few places (exclusively within smooth plains) where the ridges are exposed they appear as wrinkle ridges several kilometers wide. Within Utopia Planitia, the ridges are completely overlaid by VBF and resemble those that are observed elsewhere in northern lowlands [e.g., 8].

(2) Sinuous (winding) ridges are relatively narrow (300-500 m) structures that are ~8-10 km long. They preferentially occur within smooth plains and extend along the regional topographic slope toward VBF. The ridges usually run over the local topographic obstacles (knobs and mesas). In one locality (Fig. 1), a ridge climbs up a rim (Fig. 1, dashed line) of a degraded crater and extends along its crest.

(3) The most abundant ridges in our study area are those that define TPT. The ridges represent straight and curved chains of elongated segments and rounded mounds with the summit topographic depressions (Fig. 2). In several places there is evidence for progressive separation of the ridges into fragments (Fig. 2, arrows). These segmented ridges are a few hundred meters wide and usually ~2-5 km long. They occur exclusively within VBF in a 20-40 km wide zone near the contact with smooth plains and are more abundant eastward of ~108°E. In areas where the ridges are common, they often form dense sets of curved structures that are parallel to the margins of the VBF lobes.

(4) Narrow (a few hundred meters), single, arcuate ridges occur in association with the fronts of the VBF lobes (Fig. 3). The lobes usually consist of the higher part that is merging with the rest of VBF and is outlined by low-lying edges (the second part). The arcuate ridges are within the edges at the base of a prominent scarp between the higher and the lower parts of the lobes. The ridges occur exclusively within VBF and are convex southward conformally with the lobes.

Possible nature of ridges: The morphologic and topographic characteristics of the different types of ridges in our study area allow interpretation of their origin. Wrinkle ridges (WR) commonly characterize vast volcanic plains on Mars [e.g., 9]. Evidence for the overlapping of the ridges by materials of VBF suggests that volcanic plains covered interiors of Utopia Planitia prior to emplacement of VBF. The size-frequency distribution (SFD) of craters in the SW portion of Utopia Planitia indicates that the absolute model age of terrain underlying VBF is about 3.7 Ga [10], which coincides with the time of enhanced volcanism on Mars [8,11].

Winding ridges occur preferentially within smooth plains. The ridges overlie remnants of older terrains (mesas) and craters, which means that the ridges are neither exhumed/embayed structures nor WRs and, thus, are not related to volcanic and tectonic processes. Dimensions, morphology, shape, and topographic configuration of winding ridges are also inconsistent with their interpretation either as eolian (dunes) or coastal (berms) features. Glacial landforms, however, often represent ridges. The shapes and spatial distribution of winding ridges seem to rule out such features as drumlins and moraine suites but closely resemble the characteristics of eskers [12]. Although terrestrial eskers generally trend down the regional slopes, they are not strongly controlled by local topographic variations and can go up and down the small-scale topographic details. This is also a specific feature of winding ridges, which strongly supports their interpretation as eskers.

Segmented and arcuate ridges occur exclusively within VBF. This means that the ridges are genetically related to VBF and may provide keys to the understanding of its nature. The most characteristic feature of segmented ridges is that they represent chains of either connected or isolated fragments, each with the summit pit. In many places there is also robust evidence

for progressive segmentation of contiguous ridges. These characteristics suggest that the ridges have been heavily degraded by partial removal of their materials. HiRISE images confirm that segmented ridges consist of a mixture of finer- and coarser-grained components (Fig. 4, black and white arrows, respectively).

Another specific feature of segmented ridges is that they often occur as sets of densely spaced, curved, and nested structures. This pattern is poorly (if at all) consistent with ridges of volcanic, tectonic, or eolian origin but strongly resemble complexes of moraine ridges formed during advance/recession of debris-covered terrestrial glaciers [13-15]. The moraines (as well as segmented ridges) consist of poorly sorted materials with grain sizes from dust/sand particles to large boulders and, typically, are ice-cored [16-18].

Thus, both the spatial distribution of segmented ridges and poorly sorted material that they consist of suggest that the ridges likely represent moraines of rock glaciers. The removal of the fine-grained components by wind may have caused both the segmentation of the ridges and formation of the summit depressions. The desert pavement, however, may favor choking the blowing of the fines and prevent deep separation of ridges into fragments. The possible presence of ice in the core of segmented ridges can greatly promote the process of their degradation and formation of the pitted segments/mounds.

The arcuate ridges that often punctuate the lower edges of the VBF lobes (Fig. 3) fit nicely into the glacial hypothesis and may represent protalus ramparts that often occur at the fronts of rock glaciers on Earth [19-22].

Conclusions: Ridges near the contact of VBF with smooth plains in southern Utopia Planitia apparently present two genetic groups. The first is related to tectonic deformation and consists of wrinkle ridges of different scales. Ridges of the second group bear good evidence of their glacial origin (eskers, moraines) and suggest the presence of Hesperian ice sheets in southern Utopia ~3.5 Ga ago [10]. The spatial distribution of segmented ridges and character of their materials strongly resemble terrestrial ice-cored moraines and, thus, favor the glacial origin of TPT in southern Utopia [23-25].

The likely nature and spatial associations of the winding, segmented, and arcuate ridges may suggest that the ice sheet(s) in southern Utopia may have consisted of two facies: (1) debris-covered glaciers marked by segmented and arcuate ridges and presented now by their residue, VBF, and (2) more “clean” glaciers southward of VBF edges that are marked by the esker-like, winding ridges.

References: 1) Lockwood et al., LPSC-23, 795, 1992; 2) Scott, Tanaka, Map I-1802-A, 1986; 3) Greeley, Guest, Map I-1802-B, 1987; 4) Tanaka et al., Map 2888, 2005; 5) Lucchitta, Icarus, 45, 264, 1981; 6) Ghent et al., Icarus, 217, 169, 2012; 7) Hielscher et al., LPSC-41 #2394, 2010; 8) Head et al., JGR, 10.1029/2000JE001445, 2002; 9) Chicarro et al., Icarus, 63, 153, 1985; 10) Ivanov et al., submitted, 2012; 11) Tanaka, PLPSC-17, 1986; 12) Sreve, J.Glaciol., 11, 205, 1972; 13) Whalley, Palmer, G.Ann., 80, 221, 1998; 14) Glasser, Hambrey, Sedimentol., 49, 43, 2002; 15) Evans et al., JQS, 23, 249, 2008; 16) Ostrem, Arnold, G.Ann., 52, 120, 1970; 17) Johnson, G.Ann., 53, 198, 1971; 18) Barsch, G.Ann., v. 53, 203, 1971; 19) Blagbrough, Breed, AJS, 265, 759, 1967; 20) Ono, Watanabe, G.Ann., 68, 213, 1986; 21) Konrad, G.Ann., 80, 183, 1998; 22) Whalley, Azizi, JGR, 10.1029/2002JE001864, 2003; 23) Carr, Schaber, JGR, 82., 4039, 1977; 24) Rossbacher, Judson, Icarus, 45, 39, 1981; 25) Grizzaffi, Schultz, Icarus, 77, 358, 1989.

NOACHIAN HIGHLAND CRATER DEGRADATION ON MARS: ASSESSING THE ROLE OF REGIONAL SNOW AND ICE DEPOSITS IN A COLD AND DRY EARLY MARS.

D. K. Weiss[1], J. W. Head[1],
[1]*Department of Geological Sciences, Brown University, 324 Brook Street, Providence, RI 02912, USA. Contact: David_Weiss@brown.edu*

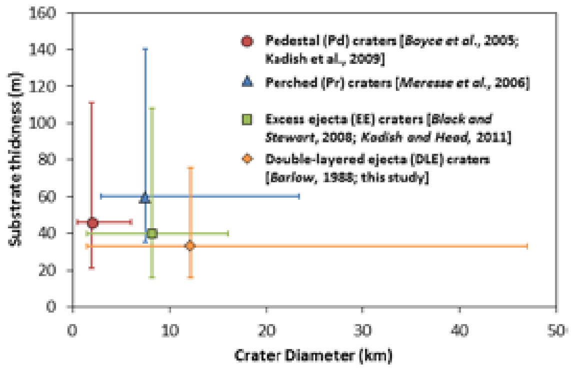

fig. 1. Icy substrate thicknesses for a variety of EE crater classes.

Introduction: The faint young sun [1,2] has led to the supposition that early Mars was cold [3-5]. The presence of valley networks, degraded state of highland craters, however, has led many investigators to suggest that the martian climate in the Noachian was warm and wet, and that precipitation and fluvial activity are the likely causes of crater degradation [6,7]. Recent climate models, however, have shown that climactic conditions in the Noachian could not have supported liquid water precipitation [8,9], and that regional snow and ice deposits, much like those inferred to be present in the Amazonian (Fig. 1) [10], pervaded the Noachian highlands [11]. Analysis of martian Noachian highland craters may give insight into conditions on early Mars. Martian Noachian highland craters (Fig 2) differ markedly from fresh martian craters (Fig 2 & 3) in that they possess 1) characteristic subdued crater rims [7,12,13], 2) flat/shallow floors [7,12,13], 3) a paucity of craters <~15 km in diameter [12,14-16], 4) channels superposing crater rims and ejecta facies [7,12,13,17], and 5) a relative absence of discernible ejecta facies [7,12,13].In this study, we reexamine the degradation state of Noachian highland craters and assess the possibility that the Noachian was characterized by a cold and dry climate.

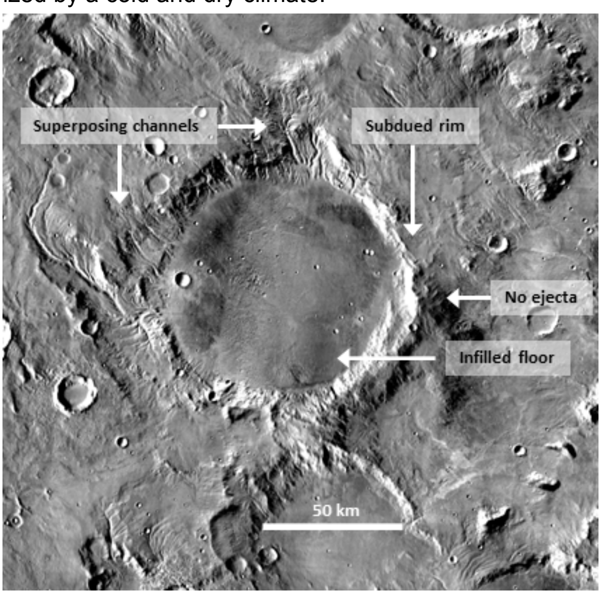

fig. 2. Typical Noachian highland crater and characteristics.

Degradation state of Noachian highland craters: The morphology of Noachian highland impact craters suggests that they have been heavily degraded [*7*], although the mode of degradation has been debated (see [7]).Although the geothermal gradient in the Noachian is relatively unconstrained [*18*], Previous investigators [5,19] have shown that it may be possible to generate basal melting of decameters thick ice and snow deposits, especially if the atmospheric temperatures are elevated. Consequently, it may have been possible for decameters thick snow and ice deposits on steep slopes to generate basal melting and thus basal erosion of the underlying bed during downward flow. Additionally, the presence of regional ice and snow deposits has been shown to affect the impact cratering process in the Amazonian (e.g. [20-24]). Could the presence of regional ice sheets, shown to potentially be present in the Noachian [8,9], account for the degraded state of Noachian impact craters?

Recent work [25] classified a large set of craters into type I (strongly degraded craters with fluvial landforms and no ejecta), type II (gently degraded craters with fluvial landforms and preserved ejecta), and type III (fresh craters with ejecta and no fluvial landforms), where type I correspond to Noachian-aged highland craters. They [25] found that there is a sharp transition at the Noachian-Hesperian boundary between type I, Noachian-aged highland craters, and type II craters, suggesting a rapid climactic shift near the Noachian-Hesperian boundary, a conclusion also reached by [*26*] when examining the ages of valley networks. If a rapid climate shift occurred near the Noachian-Hesperian boundary (e.g. [27]) it is plausible that temperature fluctuations could have influenced the modification of Noachian craters. The construction of Tharsis might have generated planet-wide warming in the Noachian [27-30], which could have potentially created a short lived “thermal pulse”, which would significantly affect Noachian highland crater morphology in the presence of regional snow and ice deposits.

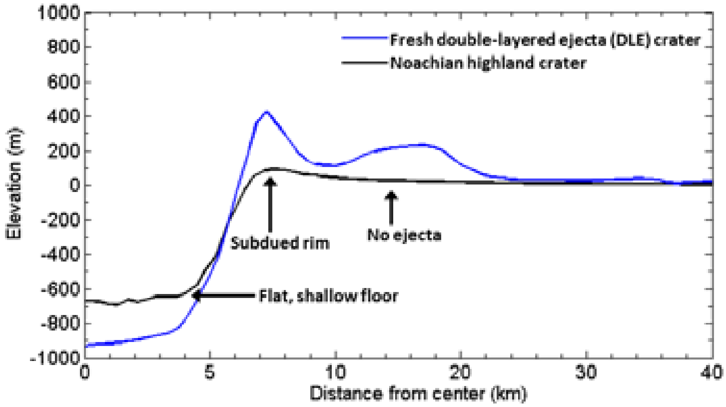

fig. 3. Altimetric profile of fresh DLE crater (blue line) and Noachian highland crater.

Testing the hypothesis: We examine the five major characteristics of Noachian highland craters enumerated above and test the hypothesis: could the degradation state of these craters be accounted for by regional snow and ice deposits, and potentially a thermal pulse, during the Noachian?

Flat/shallow floors: Noachian highland craters are characterized by shallow and flat floors (Fig. 3), and have been evidently infilled [7,12,13]. In the Amazonian, material from the rim was constantly being backwasted and infilling the crater in the absence of fluvial activity [31,32], a process evident during times of regional snow and ice deposition by the preservation of concentric crater fill (CCF) deposits (e.g. [31,32]). This process would certainly be at play during a cold and dry Noachian and could explain the characteristics flat and shallow floors of Noachian highland craters: material backwasted from the rim would fill the crater substantially [30].

Subdued rims: Noachian highland craters are characterized by subdued (lowered and rounded) rims (Fig. 3) [7,12,13]. In the *Noachian icy highlands scenario* [8,11], the process of backwasting of the rim material in the absence of fluvial activity (analogous to the CCF armoring mechanism) to infill the craters could possibly be the primary mechanism to reduce rim heights. The presence of regional snow and ice deposits, however, leads us to suggest three additional mechanisms that would reduce rim heights: 1) Impact into regional snow and ice deposits would form craters analogous to Amazonian excess ejecta (EE) craters (e.g. DLE, Pd, LARLE) (Fig. 1), which have been hypothesized to form in a decameters thick snow and ice surface layer [20-24,33]. Because some of the depth of EE craters are accommodated by the surface snow and ice layer, and some of the rim structural uplift would manifest in the snow and ice substrate, the subsequent sublimation and/or melting of the near-rim ice in a later, different climate regime may lower the observed rim height. Furthermore, numerical modeling of impacts into icy terrains have shown that the resultant crater exhibits a lower and rounded crater rim [21]. 2) Previous work [31] has shown that the outer rim crests of craters have adequate structural uplift angles to generate flow, and so enhanced glacial flow off of the structurally uplifted outer rim in a basal melting regime would enhance erosion of these craters; also, snow accumulation and flow on the crater rim interior walls could transport rim crest debris. Given sufficient ice thickness to overtop the rim crest, flow into the crater may also erode the rim. 3) If a thermal pulse occurred, fluvial erosion by the melting of snow and ice deposits, which may be both above and below the ejecta facies of EE craters, would further erode crater rims.

Paucity of small craters: The Noachian highlands have been shown to have a paucity of craters <15 km in diameter [12,15]. Due to enhanced structural uplift angles as crater diameter decreases [23,34], craters <~ 15 km in diameter are likely to be eliminated from a mixture of structural uplift-enhanced glacial basal erosion of the rim (flowing outward), infilling by backwasting, and erosion and infilling by basal melting and runoff of snow and ice deposits (e.g. [5]). Furthermore, because smaller craters have lower rim crests, ice overtopping the rim and flowing into the crater will preferentially occur for smaller craters, given a supply limited ice accumulation regime (i.e. [31]).Smaller craters that do not penetrate through a decameters thick icy substrate (i.e. pedestal craters [35] would be erased subsequent to a thermal pulse which would remove the snow and icy deposits. Craters that do penetrate through the ice will produce a smaller crater cavity in the underlying rocky substrate, and may be infilled more easily. In the scenario of a thermal pulse, the melting of the underlying snow and ice deposits would obliterate the rim, the overlying ejecta deposits, and infill craters of all sizes, given the presence of underlying and/or overlying snow and ice.

Superposed channels: Noachian highland craters often exibit channels superposed on the rim (Fig. 2). In the *Noachian icy highlands scenario* [8,11], the presence of superposing channels may result from slow runoff processes from the basal melting regional snow and ice deposits (e.g. [5]). Alternatively, if a thermal pulse occurred, the elevated temperatures could obliterate all of the snow and ice deposits in a relatively short period of time, generating the channels.

Absence of ejecta: Noachian highland crater typically lack discernible ejecta (Fig. 2 & 3). In higher atmospheric temperatures and a higher geothermal heat flux in early martian history, decameters thick snow and ice deposits may be expected to behave in a warm-based fashion, and produce basal erosion at the bed where steep slopes are present. Inner crater walls and outer crater rim structural uplift are regions of high slopes where glaciers may flow and slowly erode material given a small amount of basal melting [31], and so ejecta facies of highland craters may be preferentially eroded. In addition, if a thermal pulse occurred, the melting of ice and snow deposits underlying and/or overlying the ejecta deposits would significantly enhance the removal of the ejecta facies.

Conclusion: We find that snow and ice deposits present in the highlands during the Noachian and/or a possible subsequent thermal pulse responsible for the widespread melting of the deposits is plausible to explain 1) the flat/shallow floors, 2) subdued rims, 3) paucity of small craters, 4) superposing channels, and 5) absence of ejecta facies, and warrants further testing and analysis. Therefore, these candidate processes should be investigated further.

Acknowledgement: We gratefully acknowledge support from the NASA Mars Data Analysis Program NNX09A146G to JWH.

References: 1. Gough, Solar Physics 74, 21, 1981; 2. Newman and Rood, Science 198, 1035, 1977; 3. Kasting, Icarus 94, 1, 1991; 4. Haberle et al., LPI technical report 93, 19, 1993; 5. Carr and Head, GRL 30(24), 2003; 6. Hynek and Phillips, Geology 29, 407, 2001; 7. Craddock and Howard, JGR 107, E11, 2002; 8. Wordsworth et al., Icarus 222, 1, 2013; 9. Scanlon et al., GRL, in press, 2013; 10. Head and Marchant, LPSC XL, 1356, 2009; 11. Headm LPSC XXIII, 2137, 2012; 12. Craddock and Maxwell, JGR 98, 3453, 1993; 13. Craddock and Maxwell, JGR 102, 13321, 1997; 14. McGill and Wise, JGR 77, 2433, 1972; 15. Jones, JGR 79, 3917, 1974; 16. Craddock and Maxwell, JGR 95, 14265, 1990; 17. Masursky et al., JGR 82, 4016, 1977; 18. Solomon et al., Science 307, 1214, 2005; 19. Zent, LPSC XXX, 1803, 1999; 20. Meresse et al., MAPS 41, 1647, 2006; 21. Senft and Stewart, MAPS 43, 1993, 2008; 22. Kadish and Head, Icarus 215, 34, 2011; 23. Weiss and Head, GRL, in press, 2013a; 24. Weiss and Head, Icarus, submitted, 2013b; 25. Mangold et al., JGR 117, E4, 2012; 26. Fassett and Head, Icarus 195, 61, 2008; 27. Head and Wilson, LPSC XXII, 1214, 2012 28. Phillips et al., Science 291, 2587, 2001; 29. Johnson et al., JGR 113, E8, 2008; 30. Ehlmann et al., Nature 479, 53, 2011; 31. Fastook and Head, PSS, in review, 2013; 32. Beach and head, 2013 in prep; 33. Black and Stewart, JGR 113, E2, 2008; 34. Stewart and Valiant, MAPS 41, 1509, 2006; 35. Kadish et al., JGR 114, E10, 2009

VOLCANO-ICE INTERACTIONS AT ARSIA MONS, MARS.

K. E. Scanlon and J. W. Head,
Department of Geological Sciences, Brown University, Providence, RI, 02912 USA.
Contact: Kathleen_Scanlon@brown.edu

Introduction. It has been hypothesized that the fan-shaped deposits (FSDs) on the west or northwest flanks of the Tharsis Montes resulted from mass-wasting, volcanic, tectonic, or glacial processes (see review in [1]), but more recent evidence from the Antarctic Dry Valleys [2], climate modeling [3], and glacial flow modeling [4] has strongly validated the glacial hypothesis [5,6]. The evidence for widespread liquid water from volcano-ice interactions in the Amazonian-aged Arsia Mons FSD makes it one of the most recent potentially habitable environments on Mars. We have documented glaciovolcanic landforms in the deposit, using Mars Reconnaissance Orbiter Context Camera images, images from the High Resolution Stereo Camera (HRSC), topographic data from the Mars Orbital Laser Altimeter, and, where available, HRSC-derived [7] Digital Elevation Maps.

Glacial and glaciovolcanic features. Interaction between lava and ice on Earth creates characteristic landforms: tindar and tuyas, steep-sided ridges or plateaus that form when volcanic eruptions occur under ice cover, beginning as mounds of pillow lava and hyaloclastite tephra, and in the case of tuyas, developing flat tops when lava breaches the ice surface [8]; j**ö**kulhlaup plains, which form when glacial melt catastrophically bursts from ice vaults [8]; and steep-sided flows, which form when lava chills against ice [9]. We see evidence for each of these in the Arsia Mons fan-shaped deposit, as well as previously undescribed glacial features.

1. Northwest plateau. Towards the northwest edge of the deposit (Fig. 1A) lies a steep-sided plateau [10] ~17 km long, ~15 km wide, and ~140 m high. An elongate mound stands up to 150 m above the plateau's center. Superposed on the plateau are two sinuous ridges, 4 – 20 m high and up to 25 km long, sharply defined atop the plateau and with a more diffuse appearance downslope. The ridges continue downslope to a large moraine, where over a dozen channels coalesce into a braided streambed ~35 km long. Based on morphology and associated landforms, we interpret the plateau as a tindur and the ridges as eskers.

2. Elongate plateau. ~45 km northeast of the northwestern plateau lies an elongate plateau (Fig. 1B) ~39 km long, up to ~18 km wide, and ~140 m high. The plateau trends approximately north-south and is collinear with a curving graben to the south and a series of pit craters to the north. At its center lies an elongate mound ~140 m higher than the rest of the plateau. Overlapping, highly sinuous ridges extend ~5 km north and west from the plateau's central mound. A sharply incised channel, surrounded by smooth debris, begins near the northern terminus of the plateau and crosscuts several drop moraines. The channeled debris resembles flows from nearby cones, but for the debris to be part of the flow would require the flows to have breached several moraines, then flowed upslope and under the glacier. We therefore interpret the channels as fluvial and the plateau as a tuya.

3. L-shaped ridge. The largest plateau (Fig. 1C), ~53 km long, ~4 km wide, and over 400 m high, lies near the northern edge of the deposit. The flat-topped ridge is primarily L-shaped in plan view, with a shorter, less steep-sided, roughly triangular lobe at its upslope extent. Due to its height, steepness, and resemblance to terrestrial analogs [11], we interpret this feature as an ice-confined flow.

4. Buried plateaus. The presence of two mountains buried in the knobby facies has been noted [12], as well as one in a region we have mapped as belonging to the Smooth Lower Western Flank unit. Topographic data has revealed a third, and shows that two of the buried mountains (Fig. 1D) are similar in morphology to the northwestern plateau. Any further distinguishing features are obscured by the knobby facies, but it is probable that they were emplaced by a similar mechanism.

5. Steep-sided flows in the Smooth Lower Western Flank unit. Throughout the Smooth Lower Western Flank unit are steep-sided flows (Fig. 1E) with morphologies not seen elsewhere in the deposit. These include an exceptionally smooth-topped plateau, representing a complete tuya sequence; several flows resembling the plateaus in planform and steepness, but with sunken centers suggesting a single eruptive episode and subsequent lava retreat into the vent; and irregular, comparatively thin flows resembling terrestrial pillow mounds or sheets.

6. Steep-sided flows in the lobate facies. Pit crater chains and lava channels obscure many features in this unit, but several flows (Fig. 1F) implicate a similar eruptive sequence to the L-shaped ridge discussed above, and many flows exhibit steep sides indicative of chilling against ice..

7. Steep-sided flows in the accumulation zone. The upslope edge of the FSD is marked by numerous digitate, flat-topped, steep-sided protrusions (Fig. 1G). A typical lobe is a few kilometers wide and tens of kilometers long. Similar digitate features appear at Pavonis Mons and Ascraeus Mons, but only on the sides of their summits covered by their FSDs. On the basis of their steepness relative to nearby flows, their exclusive association with the upslope edge of the FSDs, and terrestrial analogs [13], we interpret the lobes as ice-chilled lava flows.

8. Hollowed ridges. Two landforms dispersed throughout the deposit share the morphology of an elongate ridge with a trough along its axis. Near the western edge of the fan, several of the drop moraines in the ridged facies appear to degrade into this morphology. Elsewhere, some moraines have small hollows along their crests. We interpret this morphology to result from sublimation of a remnant ice core: when some initial disturbance causes local removal of the moraine's debris armor, sublimation continues until no more ice is exposed. A class of smaller hollowed-ridge landforms behave more like dunes than moraines; they are oriented southwest-to-northeast throughout the deposit and aggregate in local lows of varying ages rather than being associated with a particular stratigraphic level. We also interpret these as resulting from sublimation of a debris-ice mixture.

9. Pit and knob terrain. Near the northern edge of the deposit (Fig. 1H) is a field of knobs up to 1 km wide and shallow pits similar in size and shape to the knobs. Moats surround many of the knobs, and some pits have what appear to be degraded knobs at their centers, implying a progression from knob to pit. The pits and knobs are aligned, concentric with a young glacier nearby [14]. We interpret the Arsia FSD pit and knob terrain as kettles and kettle blocks left during rapid retreat of the nearby glacier. The ice blocks are likely to have sublimed rather than melted to leave the pits, and they were probably covered by pyroclastic debris or dust settling from a storm rather than by glacial outwash. Since the sediment would have come from above, it could have armored some blocks from sublimation, leaving the knobs.

Evidence of local wet-based glaciation. In addition to the outflow channels near the northwestern plateau, many of the other hypothesized glaciovolcanic features in the deposit are accompanied by evidence of locally wet-based glaciation. Moraines near the plateaus, and downslope of the lobate facies, are bowed outward relative to superposed moraines, and in many of these locations boulders are streamlined or aligned along the direction of the outward glacial flow. Downslope of the lobate facies, and

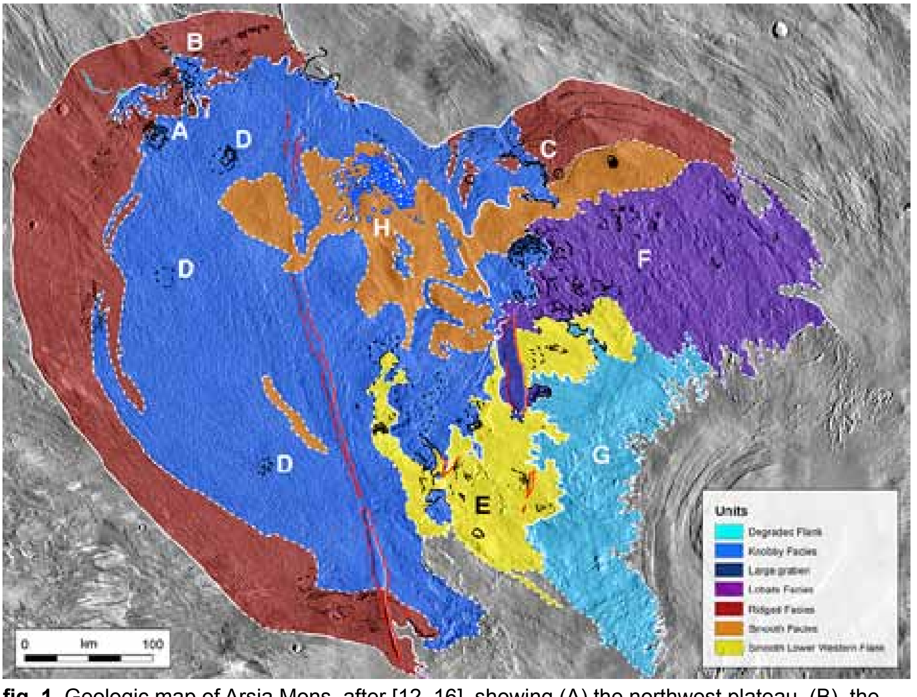

fig. 1. Geologic map of Arsia Mons, after [12, 16], showing (A) the northwest plateau, (B), the elongate plateau, (C) the L-shaped plateau, (D) buried plateaus, (E) Smooth Lower Western Flank steep-sided flows, (F) Lobate Facies steep-sided flows, (G) accumulation zone steep-sided flows, and (H) pit and knob terrain. Hollowed ridges are widespread.

near several of the plateaus, moraines are sharply defined and regularly spaced, and do not gently drape underlying topography; we interpret these as Rogen moraines, which are associated with wet-based glacial flow. Parts of the deposit's large terminal moraine have a ribbed appearance and profile consistent with a thrust-block moraine, also a wet-based glacial landform.

Preliminary conclusions. Glaciovolcanic landforms are abundant in the Arsia Mons FSD. The emplacement of these features would have melted large volumes of ice [15], potentially creating habitats. Previous work has made a strong case for cold-based glaciation, but new data also show landforms indicative of local, volcanism-induced warm-based glaciation distributed throughout the deposit. The morphology of some landforms suggests a larger extant ice inventory than previously thought.

References. [1] Shean D. E. et al. (2005), *JGR*, 110, E05001. [2] Head J. W. and D. R. Marchant (2003), *Geology*, 31, 641-644 [3] Forget F. et al. (2006), *Science*, 311, 368-371. [4] Fastook J. L. et al. (2008), *Icarus*, 198, 305–317. [5] Williams R. S. (1978), *GSA Abstr. with Programs*, 10, 517. [6] Lucchitta B.K. (1981), *Icarus*, 45, 264–303. [7] Dumke A. et al. (2008), *LPSC* 39, #1910 [8] Smellie J. L. (2009) *GSA Spec. Papers* 453, 55-76 [9] Head J. W. and L. Wilson (2007), *Ann. Glac.* 45, 1-13. [10] Head J. W. and L. Wilson (2007), *2nd Volcano-Ice Interaction on Earth and Mars Conference.* [11] Lescinsky D. T. and T. W. Sisson (1998), *Geology*, 26, 351-354 [12] Scott D. H. and J. R. Zimbelman (1995), *USGS Miscellaneous Geologic Investiga-tion Map I-2480*. [13] Edwards B. R. et al. (2002), *Bull. Vulcanol.,* 64, 254-272. [15] Wilson L. and J. W. Head (2007), *Ann. Glac.* 45, 83-86. [16] Zimbelman J. and K. Edgett (1992), *Proc. of Lun. and Planet. Sci.*, 22, 31–44. [14] Shean D. E. et al. (2007), *JGR*, 112, E03004

A POLAR OZONE LAYER ON MARS

F. Montmessin & F. Lefèvre (presenter),
CNRS LATMOS, UVSQ/UPMC, 11 bd d'Alembert, 78280 Guyancourt, France

Since its discovery by Mariner 7 ultraviolet spectrometer, our knowledge on the seasonal and spatial distribution of ozone on Mars has evolved considerably thanks to parallel efforts in observations and modeling. Martian ozone vertical distribution exhibits two main layers at low-to-mid latitudes: (1) a near-surface layer, and (2) a detached layer whose altitude is found to vary within the 30 to 60 km altitude range. Here we report evidence from the SPICAM UV spectrometer on Mars Express for the existence of a distinct ozone layer emerging at 40-60 km in the southern polar night. This layer is formed by large-scale transport and further recombination of oxygen atoms in the polar night. However, this transport-driven ozone formation is also balanced by loss reactions with HOx radicals. The seasonal dependence of hydrogen radicals (HOx) concentrations, reflecting the large seasonal variations of water vapor on Mars, creates in turn a dichotomic behavior for the two polar ozone layers, with a significantly richer layer in the southern hemisphere. This mechanism for ozone formation and seasonal evolution at the Martian poles echoes with the formation conditions of the ozone layer recently discovered on Venus.

OBSERVATIONS OF THE CO DAYGLOW AT 4.7 MM ON MARS: VARIATIONS OF TEMPERATURE AND CO MIXING RATIO AT 50 KM

Vladimir A. Krasnopolsky[1, 2],
[1]CUA, Washington, DC 20064, USA; [2] PhysTech, Moscow, Russia.
Contact: vlad.krasn@verizon.net

The CO (2-1) and (1-0) dayglow at 4.7 µm was observed on Mars at the peak of northern summer (L_S = 110°) using the CSHELL spectrograph at NASA IRTF. Six (2-1) and two (1-0) emission lines in the observed spectra are significantly affected by the solar CO lines and some martian and telluric lines. Fitting by synthetic spectra results in intensities of the dayglow lines and reflectivities of Mars at 4.7 µm. Mean reflectivity at 109°W from 50°S to 50°N is 0.15, similar to that observed by Mariner 6 and 7 in four regions on Mars. The CO (1-0) dayglow is excited by absorption of sunlight at 4.7 µm, the emission is optically thick with a non-LTE line distribution, and peaks near 87 km. The (1-0) line intensities are converted to the (1-0) band intensity using the line distribution from Billebaud et al. (1991). Mean intensity of the CO (1-0) dayglow is 1.7 MR with a weak limb darkening to 1.3 MR. This dayglow is poorly accessible for diagnostics of the martian atmosphere. The CO (2-1) dayglow is excited by absorption of the sunlight by the CO (2-0) band at 2.35 µm with minor contributions from photolysis of CO_2 and the CO (3-0) band at 1.57 µm. The dayglow is quenched by CO_2 and peaks at 50 km. Intensities of the observed six (2-1) lines result in rotational temperatures that are equal to atmospheric temperatures at 50 km. These temperatures are retrieved from 50°S to 90°N and vary in the range of 140-170 K with a mean value of 153 K. The observed intensities of the CO (2-1) dayglow are corrected for airmass and the surface reflection and give vertical intensities that are equal to 2.1 MR at 20°N to 50°N decreasing to 1.5 MR at 90°N and 1 MR at 45°S. The dayglow intensities depend on the CO mixing ratio at 50 km and cosine of the solar zenith angle. Retrieved CO mixing ratios at 50 km gradually increase from 1100 ppm at 40°S to 1600 ppm at 70°N. This behavior is very different from that observed in the lowest scale height at the same season with increase to southern polar regions because of condensation of CO_2 near the south pole (Krasnopolsky, 2003). The difference reflects complicated dynamic processes in the atmosphere. This is the first observation of CO in the middle atmosphere of Mars, and the observed behavior of CO should be further studied in both observation and theory.

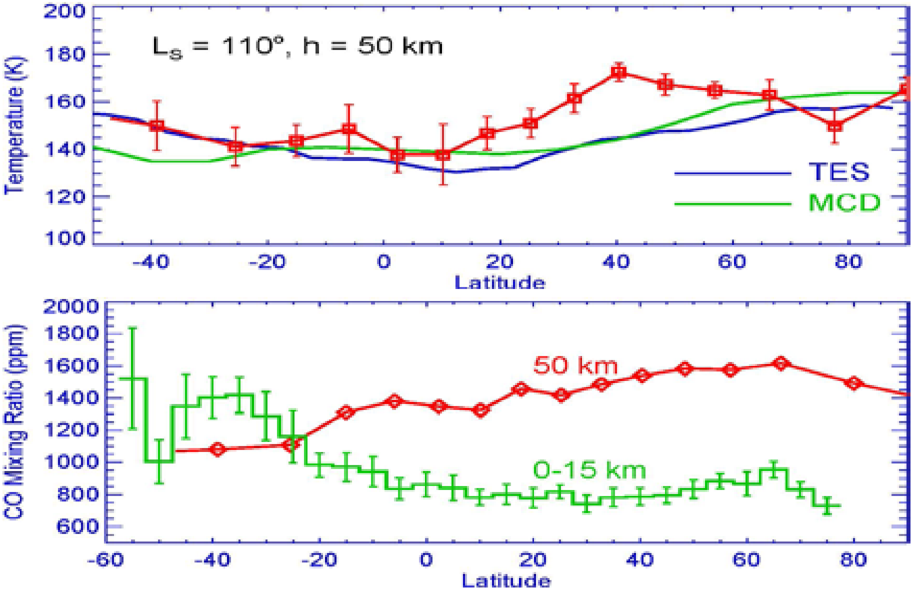

Retrieved temperatures and CO mixing ratios at 50 km.

VERTICAL DISTRIBUTION OF WATER VAPOR IN MARTIAN ATMOSPHERE FROM MGS TES DAY AND NIGHT OBSERVATIONS.

A. Pankine[1], L. Tamppari[2],
[1]Space Science Institute, Boulder, CO, USA; [2]Caltech/JPL, Pasadena, CA, USA.
Contact: apankine@spacescience.org

Introduction:

We report on new retrievals of atmospheric water vapor abundances and vertical distribution in the Martian atmosphere from combined daytime (2 pm) and nighttime (2 am) nadir observations by the Mars Global Surveyor (MGS) Thermal Emission Spectrometer (TES). The original TES water vapor retrievals used only the daytime TES data and assumed that water vapor was uniformly distributed in the atmosphere below the condensation height. If the same model is applied to the nighttime retrievals then retrieved nighttime water vapor abundances are higher than the daytime abundances, which is inconsistent with the current understanding of the martian diurnal water cycle. It is more likely that the water vapor is distributed more non-uniformly vertically than was assumed by the original model. We approximate this non-uniform distribution with a two-parameter model – with the vertical extent of vapor and its mixing ratio in the lower atmosphere as the two parameters. Assuming that the daytime vertical vapor density profile is modified at night by condensation of ice clouds at some latitude and by interaction with the surface in the lowest level of the atmosphere, the two model parameters can be retrieved from combined day and night observations for the same location. We apply this new retrieval method to the site of the Phoenix lander for the seasons of Ls=75-140° for Mars years (MY) 25 and 26. In both years the new retrieved vapor abundances vary between 30-60 precipitable microns (pr-micron), with higher abundances in MY 25. Most of the water vapor is confined below 5-8 km in MY 25 and 10-13 km in MY 26. In both years nighttime water ice clouds form at altitude 4-6 km, consistent with LIDAR observation during Phoenix mission. Mixing ratios reach values of ~600 ppmm (part-per-million by mass) also consistent with Phoenix daytime observations. Assuming that the surface adsorbs all of the water from the lowest ~0.5 km of the atmosphere at night, the diurnal change in column abundances is ~5-10 pr-micron, with ~2 pr-micron due to formation of ice clouds.

MICROBIAL COMMUNITIES OF EARTH PERMAFROST AND ARID SOILS MAY PERSIST AT LEAST 500 THOUSAND YEARS IN THE SUBSURFACE OF MARSIAN REGOLITH AND IN THE OPEN SPACE

E.A. Vorobyova[1,2], V. S. Cheptzov[2], O.A. Solovyova[2], A.K. Pavlov[3], M.A. Vdovina[3], M.V. Gorlenko[2], L.M. Polyanskaya[2], E.V. Lapygina[2] and V.N. Lomasov[4]
[1] Space Res. Inst. RAS, Profsoyuznaya str.,84/32, 117997, Moscow, Russia;
[2] Fac. Soil Sci. MSU, Leninskiye Gory 1-12, 119234, Moscow, Russia; [3] Ioffe Inst. Physics and Technology, Politechnicheskaya str.26, 195251 S.-Petersburg, Russia;
[4] SP Poitechn.Inst.: NTK "Nuclear Physics", Politechnicheskaya str.29, 195251 S.-Petersburg, Russia Contact: esautin@yandex.ru

The data on microbial resistance in Earth extreme habitats clearly show that the protective role of the natural environment can be considered as a factor which significantly corrects theoretically predicted duration of time of life support in extraterrestrial soils and in the meteorites.

The purpose of this study was to evaluate the viability of terrestrial microorganisms and native permafrost and arid soils microbial communities under conditions simulating the open space and Martian regolith with the subsequent extrapolation of data on the longevity of the possible sustaining of life in the Martian soil. We studied the influence of gamma-irradiation at a dose rate of 1Gy to 100 kGy at different temperatures (+50 C 0 C -50 C) and pressure 0,1 mbar. In addition, the impact of perchlorate in concentrations up to 5-10 wt.% on native microbial communities *in situ* was investigated, as well as the totality of all influencing factors. Accumulated doses for streams of galactic and solar cosmic rays (GCR and SCR) when exposed to different mineral analogs of Martian regolith were calculated using the latest version of the GEANT4 software package. Research was conducted in a climate chamber which allows to irradiate samples at the intensity of the absorbed dose to 0.3 Mrad/h at a stable low temperature -50oC and low pressure.

It was found that bacterial communities of xerophytic soils (Israel, Morocco) and subsurface permafrost sediments (Eastern Siberia and Antarctica) are able to sustain vitality in simulated space and Martian conditions .at ionizing radiation doses corresponding up to 500 thousand years on the Martian surface. . The presence of perchlorate in the soil reinforced the impact of radiation on microorganisms under vacuum and low temperature. However, the damage of communities as well as of bacterial cultures were not catastrophic. Despite some decrease of the total numbers of cells, bacterial communities support biodiversity, metabolic and reproductive activity.

It is experimentally established that high concentration of peroxide in soil (up to 15% weight), and in the atmosphere (saturated vapour of 30%peroxide) is not crucial for soil microorganisms. In all samples investigated resistant bacterial populations capable to reproduce were revealed. A significant part of the community provided protection from the peroxide by transition in the resting state. Adding of autostimulator of cells autolysis contributed to the partial reversal of cells ability to reproduce confirming their viability. It should be noted that microbial communities in permafrost sediments were significantly more resistant to the presence of peroxide, maintaining relatively high numbers of culturable cells.

Thus, the assumption of a high concentration of oxidants in the Martian soil or in the lower layers of atmosphere, combined with the influence of other factors: radiation, low pressure, and low temperature - doesn't contradict to the fundamental possibility of adaptation and long-term survival of Earth like microorganisms in the Martian regolith. We received experimental evidence that sublimation of the underlying ice can be the source of liquid water in the near surface deposits of Mars.

ON THE HISTORY OF EARLY METEORITIC BOMBARDMENT OF THE MOON.

A.T. Basilevsky[1,2], T. Kneissl[2], G. Michael[2], G. Neukum[2], C. Fassett[3],
[1]Vernadsky Institute of Geochemistry and Analytical Chemistry, RAS, Kosygin str., 19, 119991 Moscow, Russia; [2] Freie Universitaet Berlin, Malteserstr., 74-100, Haus D, 12249 Berlin, Germany; [3] Department of Astronomy, Mount Holyoke College, South Hadley, Massachusetts 01075, USA . Contact: atbas@geokhi.ru

Introduction:

A “lunar terminal cataclysm” is one possible scenario for the early intense bombardment of the Moon. This hypothesis suggests that at ~3.9 Ga ago, there was a strong peak in impact bombardment when most lunar highland craters and thus most lunar highland impact breccias were formed [1, 2]. Since its initial suggestion, this idea has been widely discussed with pro and contra arguments [e.g., 3-11]. Here we continue this discussion by analyzing published K-Ar ages (mostly done using Ar-Ar technique) of lunar highland rocks from the Apollo 14, 15, 16, 17 and Luna 20 missions. Furthermore, we consider the latest crater size-frequency data superposed on pre-mare lunar impact basins derived by [12] and test the resulting crater retention ages for consistency with the widely-used chronology function (CF) of [15]. More extended analysis of this problem, including considera-tion of K-Ar ages of highland rocks sampled by lunar meteorites, as well as results of modeling of the distribu-tion of ages of impact products at the surface of the Moon, is presented in [12].

Summary of K-Ar dating of lunar highland rocks:

The K-Ar clock is easily reset by thermal events, so K-Ar dating is sensitive to shock metamorphism and impact melting that results from meteoritic bombardment. We use as our major source of data the Lunar Sample Compendium (http://curator.jsc.nasa.gov/lunar/compendium.cfm), which contains information on ~360 lunar samples acquired by the Apollo astronauts and the Luna robotic sample return missions. This compendium includes a short description of the sample collection location, sample petrology, mineralogy, chemistry, isotopic dating and other characteristics. In addition, we searched for publications not included in the compendium.

Results of our search for the K-Ar data on lunar highlands rocks were compiled in the form of histograms and supporting tables based on consideration of 262 K-Ar age values: 111 values for impact melt breccias, 94 for no-melt breccias and 57 for rocks with igneous structures. For further analysis, it is important to mention that Apollo 14 and Apollo 15 landing sites are located in terrain dominated by the ejecta of Imbrium basin, Apollo 16 landed in the area of the Nectaris basin ejecta (Descartes Formation) and is at least partly affected by distant Imbrium ejecta (Cayley Formation), and Apollo 17 landed in the area of the Serenitatis basin ejecta but is also likely affected by distant Imbrium ejecta (the Sculptured Hills Formation) [e.g., 13]. Luna 20 landed in the area of the Crisium basin ejecta, superposed on the ejecta of the more ancient Fecunditatis basin, but some influence of distant Imbrium ejecta also cannot be excluded. Analysis of the data was done using ideograms, which is a type of histogram that incorporates not only the frequencies of the determined age values but the error bars as well. Below are ideograms of the K-Ar age values for all considered rocks, with subdivisions into impact melt breccias, no-melt breccias and rocks with igneous structures, all showing prominent peak at ~3.9 Ga (Fig. 1a), and ideograms for the Apollo 16 and 17 rocks among which are rather frequent varieties showing ages noticeably different from the 3.9 Ga peak (Fig. 1b).

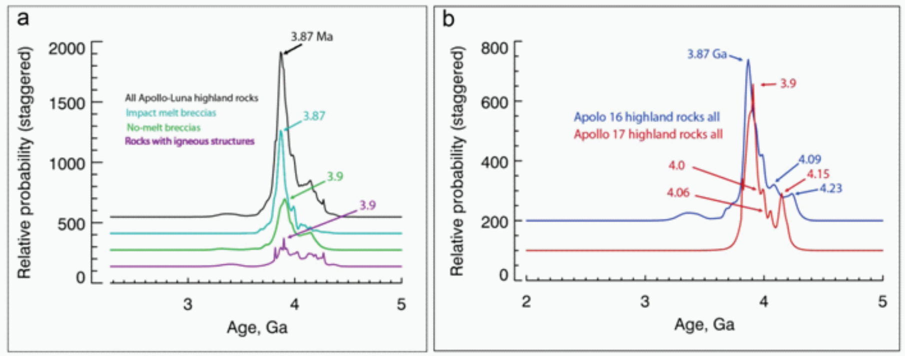

fig. 1. a) K-Ar age ideograms for all Apollo-Luna highland rocks and with subdivision them into petrologic varieties; b) K-Ar age ideograms for the Apollo 16 and 17 highland rocks.

Considering the positions of peaks on the ideograms and the geologic settings of the Apollo and Luna land-ing sites we suggest (in agreement with majority of other researchers) that the most prominent peak at ~3.87 Ga records formation of Imbrium basin. Three relatively significant secondary peaks we interpret as records of formation of Nectaris (4.09 Ga) and Serenitatis (4.15 Ga) basins and of one more basin formed ~4.23 Ga ago, which could be Fecundidatis, Australe, Tranquillitatis, or even South Pole – Aitken. Presence of these secondary peaks suggests that lunar history is not dominated by a very narrow terminal cataclysm of meteorite bombard-ment around ~3.9 Ga, and at least several basins formed at the time from ~4.1 to ~4.25 Ga ago.

Crater size-frequency distributions on lunar basins:

As second part of our efforts we consider the updated crater size-frequency data superposed on the pre-mare lunar basins by [17] in comparison with the data used for the construction of the CF by [15]. Here, we compare results of crater counts by [14, 15], [16] and [17] for three basins: Imbrium, Nectaris and Serenitatis. The Fassett et al. data are based on analysis of high-resolution data taken by the LRO Lunar Orbiter Laser Altimeter so they are independent on solar illumination conditions and thus presumably more complete. Results of this analysis are presented in Fig. 2.

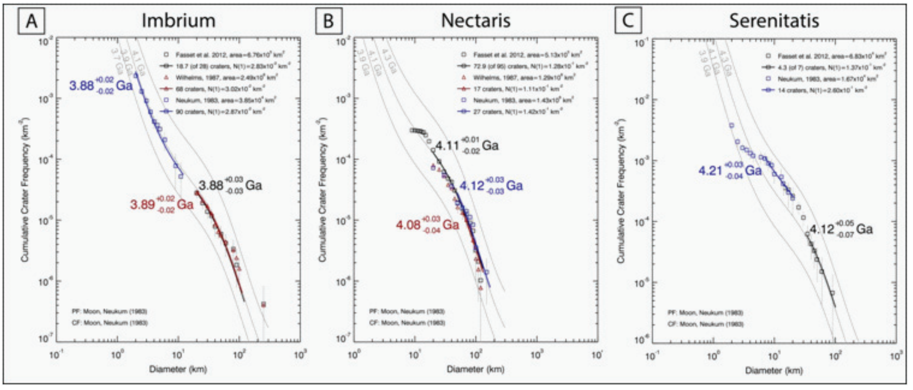

fig. 2. Reverse-cumulative plots of crater size-frequency distributions (CSFDs) superposed on Imbrium (A), Nectaris (B) and Serenitatis (C) basins. CSFDs measurements by [17] are shown in black, CSFDs by [14, 15],in blue, and CSFDs by [16], in red.

It is seen in Fig. 2 that, although the N(20) values of the measurements differ significantly, the absolute ages (N(1) values) derived by fitting the production function (PF) by [15] to the CSFDs of the three mentioned re-search groups are rather similar. Applying the CF of [15] to the measurements of Fassett et al. (2012) we received the following estimates of the basin formation ages: Imbium 3.88 ± 0.02, Nectaris 4.11 +0.01/-0.02 and Serenitatis 4.12 +0.05/-0.07 Ga. This agrees well with our age estimates for these three basins based on analysis of K-Ar data: 3.87, 4.09 and 4.15 Ga, correspondingly, and suggests that the chronology function of [15] is valid with the updated CSF data and is applicable to at least ~4.15 Ga ago.

Summary:

The above consideration of the K-Ar dating of lunar highland rocks shows that the idea of “lunar terminal cataclysm” at ~3.9 Ga ago by Tera et al. (1973, 1974) is probably not correct. Similar conclusions have been also done in some recent publications [e.g., 11, 18-21]. Our results also show that the chronology function of Neukum (1983) is applicable for analysis of crater size frequency distributions to at least 4.15 Ga ago.

Acknowledgments: Help of C. Meyer, K. Righter, L. Nyquist and J. Head is appreciated.
References: [1] Tera et al. (1973) Lunar Planet Sci. VII, 858-860; [2] Tera et al. (1974) EPSL, 22, 1-21; [3] Hartmann (1975) Icarus, 24, 181-187; [4] Grinspoon (1989) PhD Thesis, U. Arizona, 209 p; [5] Cohen et al. (2000) Science, 290, 1754-1756; [6] Stoffler & Ryder (2001) In: Chronology and Evolution of Mars. ISSI. 9-54; [7] Hartmann (2003) MPS, 38, 4, 579-593; [8] Chapman et al. (2007) Icarus, 189, 233-245; [9] Hartmann et al. (2007) Icarus, 186, 11-23, [10] Marchi et al. (2009) Astron. J. 137, 4936–4948; [11] Fernandes et al. (2013) MAPS, 48, 2, 241-269; [12] Neukum et al. (2013) PSS (in preparation); [13] Lunar Source Book.Cambridge Univ. Press, 736 p; 14] Neukum (1977) Royal Soc. London Philosoph. Trans. Series A. 285, 267-272; [15] Neukum (1983) Habilitation thesis. L-M. Universität München, 1983, p. 186; [16] Wilhelms (1987) U.S. Geol. Surv. Prof. Paper 1348; [17] Fassett et al. (2012) JGR, 117, E00H006; [18] Norman & Nemchin (2012) Third conference on early Mars, abs. 7051; [19] Marchi et al. (2012) EPSL, 325-326, 27-38; [20] Cuk (2012) Icarus, 218, 69-79. [21] Fassett & Minton (2013) Nature Geo., 6, 520-524.

COMPARISON OF IMPACT CRATER POPULATIONS IN THE LUNAR POLAR REGIONS.

Zh.F. Rodionova[1], E.N. Lazarev[1,2,3], I.P. Karachevtseva[2],
[1] Sternberg Astronomical Institute, Universitetsky pr., 13, 119991 Moscow, Russia; [2] Moscow state university of geodesy and cartography (MIIGAiK), MIIGAiK Extraterrestrial laboratory, Gorokhovskii per., 4, 105064 Moscow, Russia; [3] Lomonosov Moscow State University, Geographical Department, chair on Cartography and geoinformatics, Leninskiye gory, GSP-1, 119991 Moscow, Russia.
eugeny_lazarev@inbox.ru

Using the Morphological Catalogue of Lunar Craters [1], which lists the coordinates, sizes and main morphologic characteristics of craters with diameters from 10 to 600 km, we studied properties of lunar craters in the polar regions of the Moon. Morphological characteristics of the craters (degree of rim degradation, the presence of peaks, ridges, fissures, chains of small craters, lava on the crater flour, terraces on the inner walls) depend on the size and composition of the impactor, its velocity, and the angle of impact, as well as on the crater age and, more likely, on the nature of the surface where the crater was formed. Such features as faults and hills on the crater floor are secondary, since very often they form as a result of crater degradation. According to the degree of degradation, all the craters included in the catalog have been divided into five classes: from class 1 (the youngest craters) to class 5 (the oldest and most degraded craters).

The catalogue has been used for estimating the distribution of craters by morphological features both for the whole Moon and for individual lunar regions [2,3,4]. Analysis of this database has shown that the mean density of lunar craters of 10 km in diameter or larger is 40 per 10^5 km^2, with 44 and 7 craters for highland and mare regions, respectively. There are various values of the density of craters in the polar regions in the different papers. Some authors consider cratering rate on the lunar poles is 20% lower than on the equator, another authors calculates that latitudes within ±30º of the equator receive about 10% more impacts compared to the polar regions [5,6,7].

In this paper, we investigated the high-latitude regions from the poles down to ±60º (Fig.1). The total number of craters 10 km in diameter and larger is 950 in the Northern region and 1136 in the Southern one. We determined the areal density of craters on the Moon polar regions by calculating the number of craters in a moving circular window of 150 km in radius. The size of this moving window defines the minimum area that is effectively sampled, ~7×10^4 km^2. The resulting crater densities represent the number of craters per unit area normalized to 10^5 km^2.

In the South pole region, crater density higher than 80 craters per 10^5 km^2 is observed in the region of big craters Bailly, Lemaitre and Mutus. There are only 10 craters per 10^5 km^2 in the region of Schrödinger basin. In the Northern pole region the maximum crater density of 85 craters per 10^5 km^2 is observed in the region of crater Nansen, while the minimum 10 craters per 10^5 km^2 in the region of Mare Frigoris.

The plots of crater density for craters of different degree of degradation (Fig.2B) showed that there is the same density of craters of the third class of degradation for both poles, but there are more craters of the first, second and especially fourth and

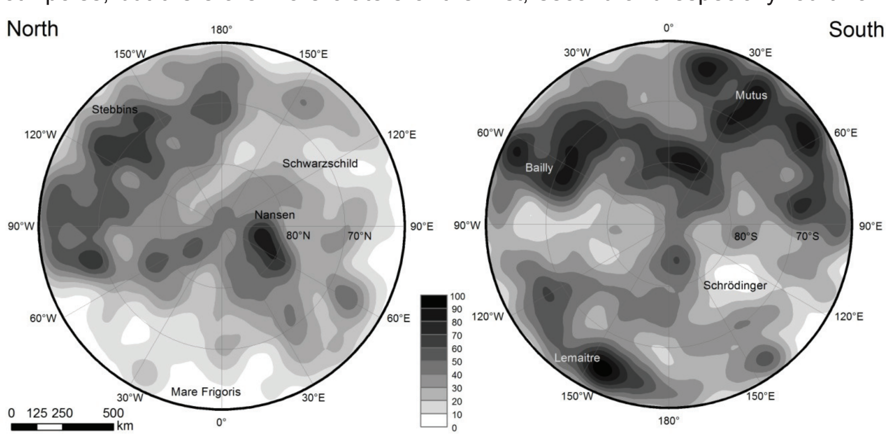

fig.1. Crater densities (number of craters per unit area, normalized to 100 000 sq.km) on the Lunar Polar regions for craters ≥10 km in diameter, calculated in neighborhoods of radius 150 km.

fifth classes in the Southern region. The number of craters of diameters from 40 km is practically the same in both Southern and Northern regions, but there are more craters of diameters from 10 to 40 km in the Southern region (Fig.2A).

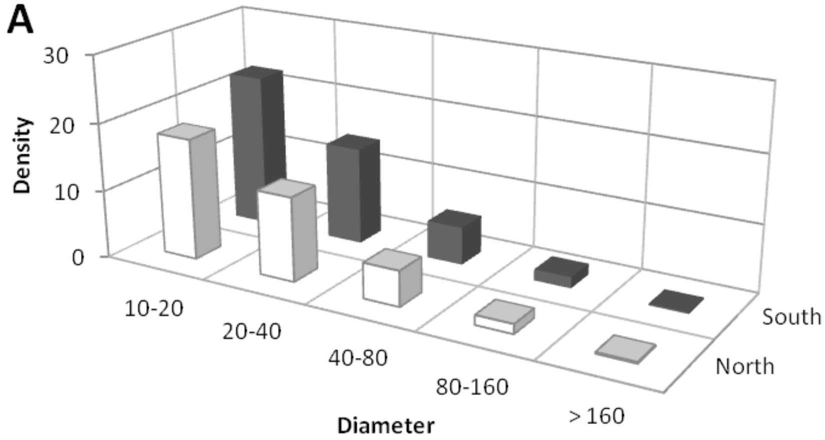

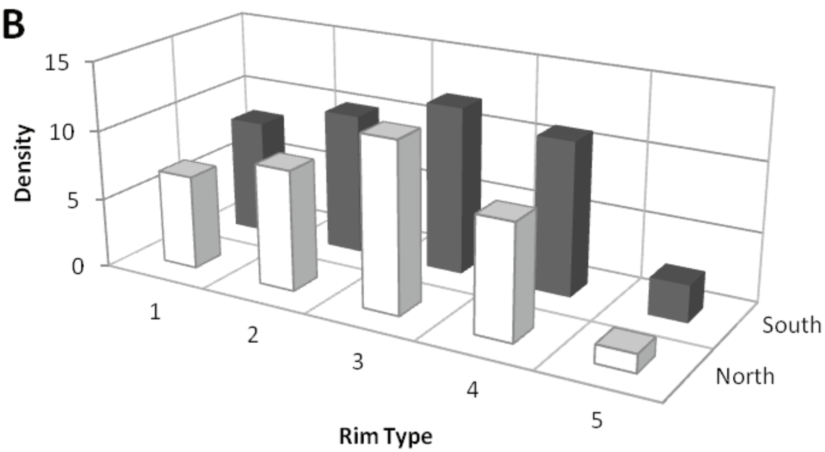

fig.2. Densities of craters (per 10^5 km^2) with different diameters in km **(A)** and degrees of rim degradation **(B)** [(1) highly pronounced rim, (2) pronounced rim, (3) smoothed rim, (4) degraded rim, and (5) ruin]

Acknowledgements: We are grateful to Misha Kreslavskiy for useful discussions and very helpful comments.

References:

1. Rodionova, Zh.F. et al. (1987) Morphological catalogue of lunar craters, Moscow University Publ.
2. Rodionova, Zh.F. et al. (1989) Analiz osobennostey raspredelenia lunnuh kraterov na osnove morphologicheskogo kataloga. Astronomicheskiy Vestnik 23, 1. 50-59.
3. Head, J.W. et al (2010) Global distribution of large lunar craters: implications for resurfacing and impactor populations. Science 329, 1504-1506.
4. Rodionova, Zh.F. et al. (2000) Morphological analysis of the cratering of the South pole–Aitken basin on the moon. Solar System Research, 34, 5, 390–397.
5. Le Feuvre, M., Wieczorek, M.A. (2011) Nonuniform cratering of the Moon and a revised crater chronology of the inner Solar System. Icarus 214, 1-20.
6. Gallant, J., Gladman, B., Ćuk, M. (2009) Current bombardment of the Earth-Moon system: Emphasis on cratering asymmetries. Icarus 202, 371-382.
7. Ito, T., Malhotra, R. (2010) Asymmetric impacts of near-Earth asteroids on the Moon. Astronomy and Astrophysics 519, A63.

GEODETIC OBSERVATIONS FOR STUDY OF INTERIOR OF THE MOON AND THE PLANETS IN SELENE-2 AND FUTURE MISSIONS.

H. Hanada[1], F. Kikuchi[1], H. Noda[1], K. Matsumoto[1], H. Kunimori[2], H. Araki[1], S. Kashima[3], S. Tsuruta[1], K. Asari[1], S. Sasaki[4],
[1]RISE Project, National Astronomical Oservatory, Oshu, Iwate 023-0861, Japan; [2] National Institute of Information and Communications Technology, Koganei, Tokyo 184-8795, Japan; [3]JASMINE/RISE Project, National Astronomical Oservatory, Mitaka,Tokyo 181-8588, Japan; [4]Graduate School of Science, Osaka University, Toyonaka, Osaka 560-0043, Japan. Contact: hideo.hanada@nao.ac.jp

Introduction: We propose geodetic observations for study of internal structure of the Moon in SELENE-2 and future missions. They are differential VLBI (Very Long Baseline Interferometer), LLR (Lunar Laser Ranging) and ILOM (In-situ Lunar Orientation Measurement). New observations will contribute to improve the lunar rotation model, and obtain new information related to properties of the lunar core and the mantle.

Differential VLBI: VLBI measures the difference in arrival time of a signal transmitted from a radio source to two ground stations. Kaguya mission employed the differential VLBI for orbit determination and gravity study, and attained the accuracy of 1 ps in the differential phase delay of the X-band signal, which is equivalent to the accuracy of the orbit of around 10 m [1]. We can expect that the differential VLBI between artificial radio sources on a lunar lander and a lunar orbiter will measure the doubly-differenced ranges more accurately than Kaguya because there are more chance of the same beam observations. Extension of two-beam system to S/X bands, which will increase the chance for the same beam, is under development. The other technical issue under development is reduction of the power consumption of the VLBI radio sources. Combination of simplification of the circuit and intermittent emission is one possible solution. We can obtain various information such as gravity coefficients and tidal Love number k2 which reflects the lunar interior through variation of the satellite orbit.

LLR: We are proposing to put a new retro-reflector on the Moon in order to expand the network of retro-reflectors and to make it possible for many ground stations to participate in the observations, and thus to improve the accuracy of LLR. A single large corner reflector not in array for LLR will improve the ranging accuracy up to 1mm order because it will not be affected by the shift of the optical center due to change of the incident angle. We should set dihedral angles which are the angles created by two intersecting surfaces slightly different (0.65-0.8 arc seconds for a reflector of 100mm diameter) for different intersections in order to receive return energy effectively [2]. Therefore the accuracy of the angles must be within 0.1 arc seconds. Manufacturing method is under development and bonding of three mirrors or integral molding are two alternatives.

ILOM: The PZT (Photographic Zenith Tube) has been used for observations of the Earth rotation, and the next usage was for observations of the deflection of the vertical by taking advantage of automatic observations. We here propose In-situ Lunar Orientation Measurement (ILOM) to study lunar rotational dynamics by direct observations of the lunar rotation from the lunar surface by using a small telescope like PZT with an accuracy of 1 milli-seconds of arc (1 mas) in a future lunar mission. Effect of large temperature change is one of the most serious problem for such a precise observation. By introducing a diffraction lens, we can loosen thermal condition by about ten times compared with the case not introducing it. We have already made a bread board model (BBM) and will use the BBM for observation of the deflection of the vertical on the ground for the time being in order to evaluate the characteristics of the total system of the telescope.

References: [1] Kikuchi, F. et al., Picosecond accuracy VLBI of the two subsatellites of SELENE (KAGUYA) using multifrequency and same beam methods, *Radio Sci.*, **44**, 1-7, doi:10.1029/2008RS003997, 2009. [2] Otsubo, T., H. Kunimori, H. Noda, and H. Hanada, Simulation of optical response of retroreflectors for future lunar laser ranging, *Adv. Space Res.*, **45**, 733–740, 2010.

CHANG'E-1 MISSION IDENTIFIED LUNAR HIDDEN BGA BASINS.

J. Ping[1] and X. Su[2]
[1]National Astronomical Observatory, CAS (20A Datun Rd., Chaoyang, Beijing, 100012, China; [2]University of Chinese Academic of Sciences ,Beijing, China. Contact: jsping@bao.ac.cn

Overview:

Lunar mascon basins have been identified using lunar topography and gravity model by means of both of the free air[1-3] and Bouguer gravity[4-5]. In an early study, we calculated the terrain correction using an average crust density of 2650kg/m^3 for lunar free-air gravity anomaly (FAGA), based on the global topography model CETM-s01 detected by the laser altimeter (LAM) on Chang'E-1 (CE-1)[6]. The obtained lunar Bouguer gravity anomaly (BGA) reveals density irregularities of the interior mass, where the South Pole-Aitken (SPA) basin was found to be the largest mascon basin on the Moon[4]. Due to the lunar impact mascon basins have been dominated by an isosdetic processing of the mantle uploading and balsalt filling at basin bottom, this evolution is directly connect with igneous activity. Identifying the mascon basins of various features will give more informations to uncover the lunar dynamical evolution history.

Chang'E-1 Lunar topography and gravity models:

We updated the lunar DEM and lunar gravity using the data of CE-1 and SELENE. To update the LAM measurements by CE-1, a short term drift in time tag was removed, s/c new orbits database with far-side gravity information was adapted[5], a long term drift in LAM counting frequency standard was calibrated. The lunar gravity model was also improved as CEGM02 by merge the tracking data of CE-1 together with historical data[7]. The updated lunar gravity model and DEM model were used to obtain the Bouguer gravity. From the BGA map, we found an early identified ancient middle scale far-side basin, Fitzgerald-Jackson by CE-1 DEM is a mascon basin[5]. An ancient mascon basin was found at southern pole area with half size impacted by Shordinger basin. Including them, some middle scale lunar ancient mascon basins were discovered[8].

Hidden impact mascon basins:

Usually, the type I~II mascon basins can be clearly identified by combining the lunar large positive FAGA with DEM depression directly[1-3]. However, some environments may hide the mascon or basin. An ancient basin is difficult to identify as an independent on using image or DEM data only, if it was destroyed by a similar size second impact, or by many small size second impacts; this ancient impacting might take place in the era of magma ocean, only mantle uploading under the impacting area happened without obvious depression and kept till now. Also for an obvious depression area, if its FAGA at center area is flat or very weak positive, it may be classified as common type depression basin. For the middle size basins of a couple hundreds kilometers in diameter, new lunar missions may give us a chance to check the DTM, DEM, FAGA and BGA of lunar surface, so as to find hidden ancient mascon depressions as basins.

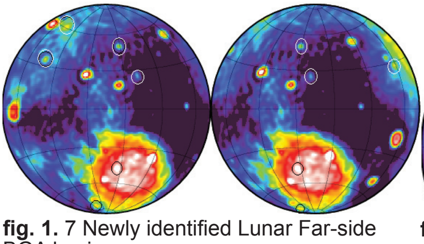

fig. 1. 7 Newly identified Lunar Far-side BGA basins.

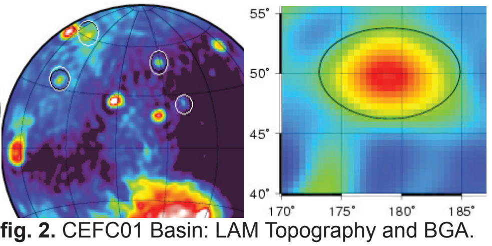

fig. 2. CEFC01 Basin: LAM Topography and BGA.

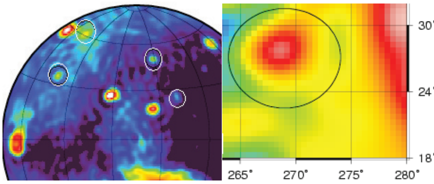

fig. 3. CEFC02 Basin: LAM Topography and BGA.

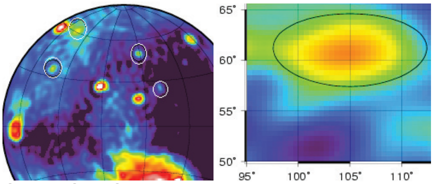

fig. 4. CEFC03 Basin: LAM Topography and BGA

New identified Mason Basins by CE-1:

CE-1 mission obtained the lunar global DTM, DEM and gravity successfully. Even without super high resolution, these data are powerful enough to support the lunar dynamical and physical studies. Taking the advantages of these CE-1 results, we obtained BGA of the moon, and compared above data degree by degree. From the results, 8 mason basins are newly identified and listed in Table 1. The basins of Fitzgerald-Jackson, Amundsen-Ganswindt and Cruger-Sirsalis have been discovered by using Clementine DTM data[10-11] as average lunar basins with large error of sizes. treated as common basins; all of these basins show strongly positive BGA; 7 basins appear at far-side, see Figure 1; 3 basins are type II FAGA mascons; 5 basins are BGA mascons; 5 basins are located at northern hemisphere and 3 basins at southern hemisphere; 6 basins are lower than average reference sphere. CEFC02 and CEFC03 show No obvious topographic depression of flat background DTM; CEFC04 and Amundsen-Ganswindt have been impacted and hidden by neighbor basins, part circle depressions and strong positive BGAs make then out as mascon basins; CEFC01 and Cruger-Sirsalis show flat or weak positive FAGA, obsvious topographic depressions in CE-1 DEM data. New identified CEFC01, CEFC02 and CEFC03 mascon basins might appear before other Pre-Nectarian basins. Combing DTM, DEM, FAGA and BGA data together, is giving us a new chance to identify the middle scale ancient mascon basins. Detail studies of these hidden ancient basins will be carried out in the near future.

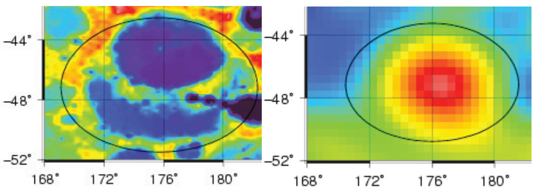

fig. 5. CEFC04 Basin broken by Von Karman Basin.

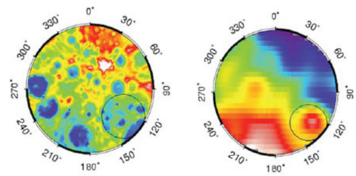

fig. 6. Amundsen-Ganswindt Basin: LAM Topography and BGA.

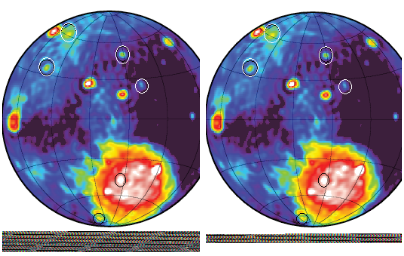

fig. 7. Cruger-Sirsalis Basin: LAM Topography, BGA and LRO image.

table 1. List of newly identified middle scale lunar BGA mascon basins by Chang'E mission

basin Name or Suggested Code	location (E°, N°)	diameter (KM)	height(KM)		BGA(mGal)		type
			RIM	bottom	RIM	bottom	
szilard	105. 7, 34.0	122	-1.1	-4.1	50	256	II
fitzgerald -Jackson	191, 25	470	3.2	-0.6	-226	84	III
CEFC01(unnamed)	178, 50	230	2.2, 0.4	-0.3	-130	220	III
CEFC02(unnamed)	269, 26	310	-0.5	-1.5	24	266	III
CEFC03(unnamed)	105, 61	290	-3.0	-4.4	140	291	III
CEFC04(unnamed)	176, -44. 8	190	-4.5	-7	560	722	III
amundsen-Ganswindt	130,-81	348	-1.0	-3.0	110	370	II
cruger-Sirsalis	293,-15.5	310	0.3	-2.5	-90	260	II

Note: type II is defined same as Namike et al. (2009), type III basin indicates strong positive BGA at center area with weak FGA and less obvious signal in image data, can be partly identified by high resolution DEM data.

References:

[1] Konopliv, A. S. et al. (2001) Icarus 150, 1-18;
[2] Namiki, N. et al. (2009) Science, 323, 900-905. DOI:10.1126/science.1168029.
[3] Matsumto, K. et al. (2010) JGR, 115, E06007, DOI: 10.1029/ 2009JE 003499.
[4]Liang, Q. et al. (2009) Sci China Phys Mech Astron,52, 1867–1875.
[5] Ping, J. et al. (2011) Sci China Phys Mech Astron, 54, 2130-2144. DOI: 10.1007/s11433-011-4561-0. [6]Huang, Q. et al. (2009) Sci China Phys Mech Astron, 52: 1815–1823.
[7]Yan, J.G. et al. (2011) Sci Sin Phys Mech Astron, 41, 870–878, doi: 10.1360/132010-868.
[8]Ping, J.S. et al. (2012), in 6th Kaguya Science Symposium.
[9] Cook, A. C. et al. (2002), LPSC XXXIII, #1281.
[10] Konopliv A.S. and Yuan D.N. (1999) LPSC XXX, #1067.

OPPOSITION EFFECT OF THE MOON FROM LROC WAC DATA.

Velikodsky Yu. I., Korokhin V. V., Shkuratov Yu. G., Kaydash V. G.,
Institute of Astronomy, Kharkiv National University, 35 Sumska St., Kharkiv 61022, Ukraine. Contact: dslpp@astron.kharkov.ua

Introduction: The lunar opposition effect is still studied insufficiently. Accuracy of existing spectrophotometric surveys does not permit to study spectral dependence of the opposition effect that is anticipated due to the coherent backscattering. Meanwhile, infrared data of Chandrayaan-1 M³ (Kaydash et al., 2013) manifest the coherent backscattering opposition spike strengthening with wavelength, which is induced by the growing albedo with wavelength.

There are new visible-light lunar data from Lunar Reconnaissance Orbiter (LRO) including the Wide Angle Camera (LROC WAC) mapping in 5 spectral bands (415–689 nm), carried out with a resolution of 100-meters. All the lunar surface have been hundreds times observed by WAC at different photometric conditions. The most of images are obtained at the incidence angle i, emergence angle e, and phase angle α in the following range: $b \le i \le 90°$, $0° \le e \le 30°$, $b \le \alpha \le 60–120°$ (where b is the selenographic latitude). So, it is possible to study phase curve near opposition for equatorial regions by comparison images containing the zero-phase point and images of the same area at larger phase angles. This method has been proposed by Kreslavsky et al. (2000) for Clementine UVVIS data and it was used for SMART-1 AMIE data (Kaydash et al., 2008) as well. We have improved this method for using a large number of images of the same area at different phase angles.

Data processing: For processing, we have downloaded all available WAC images of selected area with phase angles in the range $0° \le \alpha \le 30°$. Then, each framelet (a WAC image consists of a set of initial framelets (Robinson et al., 2010)) was corrected for distortion (Korokhin et al., 2013) and was considered as an image in the tilted perspective projection, parameters of which were calculated using the SPICE information system.

Our method of opposition surge measurement includes the solution of the system of following equations for each pixel of each image using the least square procedure:

$$I_{jk} = A_j \exp(-\mu_j \alpha_{jk})\, f(\alpha_{jk})\, D(\alpha_{jk}, i_{jk}, e_{jk})\, K_k \,, \quad (1)$$

where j is here the index of the lunar point (pixel), k is the index of the image, i is the incidence angle, e is the emergence angle, I is the radiance factor measured, μ is the phase-curve slope at large phase angles, $f(\alpha)$ is the phase curve corrected for the slope at large phase angles, A is the so-called *diffuse albedo* (the normal albedo if the opposition effect is absent: $f(\alpha)=1$), D is the disk function, K is a calibrating factor for the image. Phase curve of the *equigonal albedo* (the radiance factor in the “specular” point ($i = e = \alpha/2$)) is $\exp(-\mu\alpha)f(\alpha)$, the *disk function D* is the radiance factor normalized at the “specular” point ($D(\alpha, \alpha/2, \alpha/2)=1$) (Velikodsky et al., 2011). We use the theoretical disk function of Akimov (Akimov, 1988; Shkuratov et at., 2011).

Fitted parameters are distributions of the albedo A_j and slope μ_j, factors K_k for each image, and function $f(\alpha)$ tabulated with step 0.25° in the range 0–30° (we suppose the function $f(\alpha)$ to be the same for whole processed lunar area). This model allows us to separate the opposition curve $f(\alpha)$ and albedo pattern, because albedo affects the phase curve mainly through μ in the exponential term in Eq. (1). The influence of albedo on the opposition effect in visible light is weak; therefore it is not studied yet. Our method permits us to obtain the phase curve $f(\alpha)$ in a free form without fixation of any model functions. Then we can compare functions $f(\alpha)$ for areas with different albedo and for different wavelengths to study the albedo dependence of opposition phase curve.

Results: We have processed images of 4 lunar areas: “Mare 1” (b=−10..−2°, l=−50..−48°), “Mare 2” (b=−4..12°, l=−54.. −52°), “Highland 1” (b=−8..0°, l=−72..−70°), “Highland 2” (b=−11..4°, l=9..11°), where l is selenographic longitude. The function $f(\alpha)$ can be found from the solution of the system (1) with two free parameters: e.g., the absolute calibrating factor and mean slope of phase curve. We fixed these parameters so that in the phase-angle range 15–30° the function $f(\alpha)$ has mean value 1 and mean slope 0. Such a normalization removes a large-phase-angles trend that is supposed to be formed mainly by the shadow-hiding effect and incoherent multiple scattering in the regolith medium (Shkuratov et al., 2011). Logarithms of obtained functions $f(\alpha)$ are shown in Fig.1. We can see the opposition effect as deviation from zero at small phase angles in Fig.1. We note that another normalization of the function $f(\alpha)$ will not change qualitatively the behavior of $f(\alpha)$. In Fig.1 we can see that for maria the opposition surge slightly grows with wavelength (and therefore with albedo), and for highlands it rather becomes narrower with wavelength. This is in a qualitative accordance with the coherent backscattering theory.

For more detailed study of the opposition surge one should get rid of strong nonlinear phase trend. We use a ratio method for this. Ratios of phase curves $f(\alpha)$ at different wavelengths are shown in Fig.2. One can see that each pair of lunar areas ("1" and "2") has similar features on curves. As some color curves have a minimum at 1–5° therefore we consider our result as independent confirmation of non-monotonous dependence of color index on phase angle. This effect, also known as *color opposition effect*, was never observed with orbital lunar photometry before LRO survey (Shkuratov et al., 2011; Kaydash et al., 2013).

Curves in Fig.2 show several phase ranges with different curve slopes: they may be separated by phase angles ~2°, ~5°, ~15°. We have calculated curve slopes (a coefficient at α in the linear fitting of $\ln f(\alpha)$) for these phase ranges (Fig.3). One can see that the opposition-surge slope has different dependence on albedo for different phase ranges: at 0.25–1.25° they correlate, at 6–12° they anti-correlate, and at 2–4° albedo dependence has a maximum at 0.12–0.15. A similar maximum has been found by Velikodsky et al. (2011) using the phase ratio 1.6°/2.7°. While the anticorrelation of the global phase-curve slope μ with albedo is well known, the new result in Fig.3 reveals non-monotonous behavior of the opposition-surge slope that is corrected for global slope.

Three diagrams in Fig.3 show a good relation between a shape of the opposition surge and the albedo. There is narrowing the opposition surge with albedo growing as predicted by the mechanism of coherent backscattering enhancement. Using this relation we suggest a new parameter of the opposition surge: *effective width*. Indeed, the opposition surge has not clear boundary due to strong nonlinearity of phase curve. The surge "width" depends on the choice of a calibrating region (in our case 15–30°). Using slope–albedo diagrams like Fig.3 we can define *effective width* of the opposition surge as a maximal phase angle for which the opposition-surge slope increases with albedo growing. Fig.3 shows that the effective width of opposition surge for maria is in range 3–9°, for highlands in red light it is in range 0.75–3°, and for highlands in blue and green light (albedo 0.12–0.15) it is about 3°.

References: [1] Akimov L.A. (1988) *Kinemat. Phys. Celest. Bodies* 4 (1), 3–10, (in Russian). [2] Kaydash V. et al. (2008) *LPSC XXXIX*, No. 1391. [3] Kaydash V.G. et al. (2013) *JGR: Planets* 118, Iss.6, P.1221–1232. [4] Korokhin V.V. et al. (2013) Retrieving Lunar Topography from Multispectral LROC Images, *Planet. Space Sci.*, in press. [5] Kreslavsky M.A. et al. (2000) *JGR* 105, No.E8, P.20281–20295. [6] Robinson, M.S. et al. (2010) *Space Sci Rev*, 150, 81-124. [7] Shkuratov Y. et al. (2011) *Planet. Space Sci.* 59, 13, 1326-1371. [8] Velikodsky Yu.I. (2011) *Icarus* 214, P.30–45.

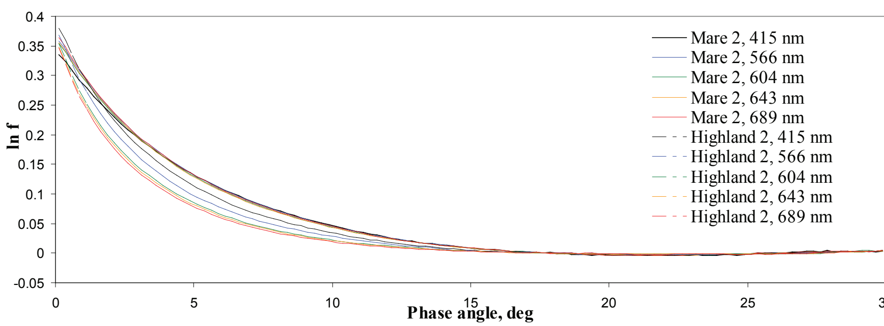

fig. 1. Phase curves of lunar equigonal albedo (corrected for slope at 15–30°)

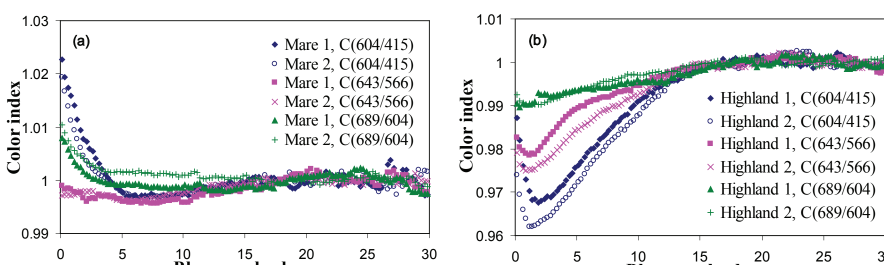

fig. 2. Phase curves of color indices (corrected for slope at 15–30°) for maria (a) and highlands (b)

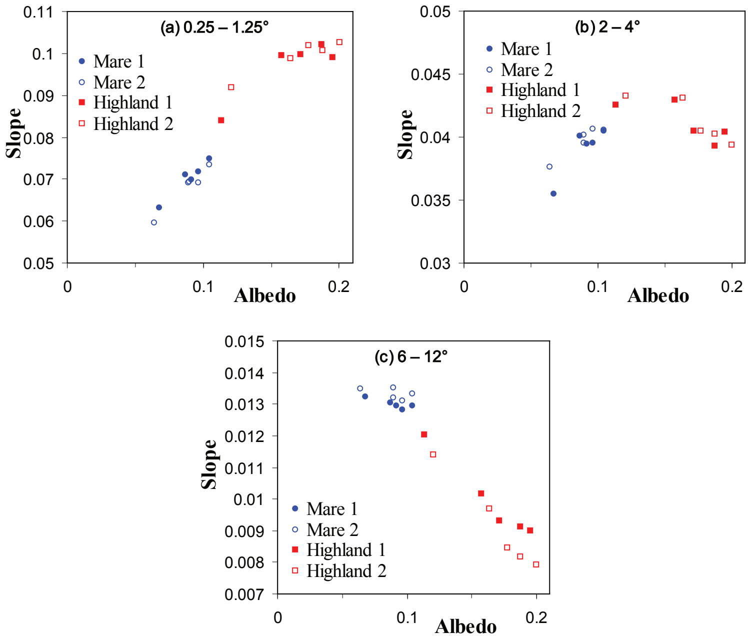

fig. 3. Correlation of opposition-surge slopes with albedo in 3 phase ranges (a – c)

REDUCTION AND ANALYSIS OF ONE-WAY LASER RANGING DATA FROM ILRS GROUND STATIONS TO LRO

S. Bauer[1], J. Oberst[1,2], H. Hussmann[1], P. Gläser[2], U. Schreiber[3], D. Mao[4], G. Neumann[5], E. Mazarico[5], M. Torrence[6], J. McGarry[5], D. Smith[7], M. Zuber[7],
[1]DLR Berlin Germany, Institute of Planetary Research, [2]TU Berlin, Germany, [3]Geodätisches Observatorium Wettzell, Germany, [4]Sigma Space Corporation, MD USA, [5]NASA Goddard Space Flight Center, MD USA, [6]SGT Inc., MD USA, [7]MIT, MA USA. Contact: sven.bauer@dlr.de

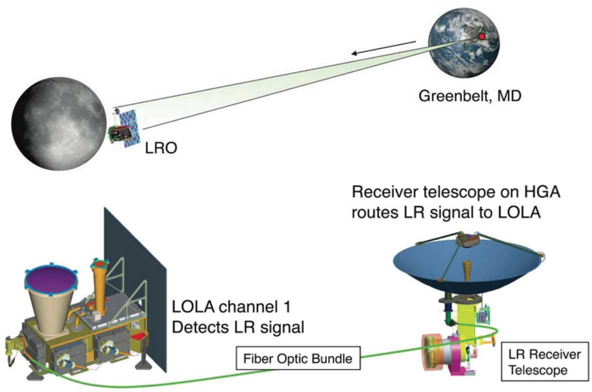

fig. 1. Laser Ranging to LRO - basic principle [1]

Background:

One-way LR (Laser Ranging) is being performed routinely from ILRS (International Laser Ranging Service) ground stations to LOLA (Lunar Orbiter Laser Altimeter), onboard NASA's LRO (Lunar Reconnaissance Orbiter). The experiment provides high accuracy spacecraft range measurements over interplanetary distances. Furthermore it can be used for laser communication**,** monitoring the LRO clock long-term behavior and referencing the MET (Mission Elapsed Time) to TDB (Barycentric Coordinated Time).

Unlike ranging experiments to reflectors or transponders, LR to LRO is a one-way measurement (Figure 1). A ground station fires a laser pulse to LRO at a certain time and the received pulse is time stamped by the satellite. An optical receiver is attached to LRO's HGA (High Gain Antenna), which is always pointed towards Earth, and incoming Laser pulses are transmitted into the LOLA laser detector by a fiber optics cable. This permits ranging measurements to LRO simultaneously while LOLA is ranging to the lunar surface [1]. By calculating the light travel time between the receiving and the firing time, a high precision range measurement is made. While current orbit determination for LRO (based on radio and the altimetric crossover data) results in uncertainties of spacecraft position of ≈ 14 m [2], Laser ranging typically achieves RMS of 10 to 30 cm [3].

Status:

Beginning with data obtained during a campaign from the ILRS station in Wettzell, Germany, we have developed a software capability for the processing of LR data. We currently develop a matching program for relating laser fire times of all ground stations to the LOLA laser receiving times automatically. We have processed most data from LRO commissioning phase through the LRO science mission (~June 2009 until June 2012). RMS values of 13.4 cm are achieved on average. We apply the observed range measurements to LRO clock characterization (offset, drift, aging), orbit determination and gravity field estimation, which will be demonstrated at the meeting.

Acknowledgements:
This work has partially been funded by the DFG (German Science Foundation) and the FP7 program of the European Union. Much of this work was carried out while the first author (S.B.) very much enjoyed a research visit at NASA Goddard Space Flight Center (GSFC).

References:
[1] Zuber, M., et al.: The Lunar Reconnaissance Orbiter Laser Ranging Investigation, Space Sci Rev, Vol. 150 No. 1-4, pp. 63 – 80, 2010. [2] Mazarico, E., et al.: Orbit determination of the Lunar Reconnaissance Orbiter, J. Geod., 86, pp. 193-207, 2012. [2] Mao, D., et al.: Laser Ranging Experiment on Lunar Reconnaissance Orbiter: Timing Determination and Orbit Constraints, http://cddis.gsfc.nasa.gov, 17th International Workshop on Laser Ranging, Bad Kötzting Germany 2011

LEND MAPPING OF WATER AT THE SOUTH POLE REGIONS: DATA FROM LRO

A. B. Sanin[1], I. G. Mitrofanov[1], M. L. Litvak[1], D. Golovin[1], R. Starr[2], W. Boynton[3], K. Harshman[3], G. Chin[4], L. G. Evans[5], J. Garvin[4], K. Harshman[3], T. P. McClanahan[4], M. I. Mokrousov[1], R. Z. Sagdeev[6], D. E. Smith[7] and M. T. Zuber[7],
[1]Space Research Institute, RAS, Moscow, 117997, Russia, [2]Catholic University of America, Washington DC, USA, [3]University of Arizona, Tucson, Arizona, USA, [4]NASA Goddard Space Flight Center, Greenbelt, Maryland, USA, [5]Computer Sciences Corporation, Lanham, Maryland, USA, [6]Space Physics Department, University Maryland, College Park, Maryland, USA, [7]Department of Earth, Atmospheric and Planetary Sciences, MIT, Cambridge, Massachusetts, USA. Contact: sanin@mx.iki.rssi.ru

We would like to present newest updated results of the LEND data gathered during the all four years of the LEND observations. Maps of thermal, epithermal and fast neutron fluxes are created using these data. Most interesting result which is found that in general case the PSRs regions are not contains a detectable amount of hydrogen but there are few large neutron suppression regions (NSRs) which there detected as a regions with statistically significant suppression of neutron flux. Three found NSRs partially overlap with the PSRs in Cabeus, Shoemaker (on South) and Rozhdestvensky U (on North) but they are spread on a sunlit vicinity of these PSRs. This means that hydrogen may be preserved for a long time or even accumulated at ~1 m layer of sunlit areas regolith. All other PSRs do not show a statistically significant suppressions of neutron flux in comparison with a sunlit areas at the same latitudes. This supposes a hypothesis what a permanent shadow is not only necessary condition for hydrogen presence at a region but an illumination conditions of this region may create a favorite for hydrogen accumulation and preserving. Such hypothesis is supported by analysis of poleward-facing and equatorial-facing slopes of craters. This analysis shows a statistically significant increasing of hydrogen concentration at poleward-facing slopes in comparison to equatorial-facing slopes.

SELECTING LANDING SITES FOR LUNAR LANDER MISSIONS USING SPATIAL ANALYSIS.

M. V. Djachkova[1], E. N. Lazarev[1,2],
[1]Department of Cartography and Geoinformatics, Faculty of Geography, Lomonosov Moscow State University, GSP-1, 1 Leninskiye Gory, Moscow, Russia. Contact: sualice@yandex.ru [2]Sternberg Astronomical Institute MSU, Universitetskiy pr., 13, Moscow, Russia. Contact: eugeny_lazarev@inbox.ru

Introduction:

Russian Federal Space Agency (Roscosmos) is planning to launch two spacecrafts to the Moon with lander missions in 2015 and 2017. [1] Here, we present an approach to create a method of landing sites selection.

We researched the physical features of the Moon using spatial analysis techniques presented in ArcGIS Desktop Software in accordance with its suitability for automatic landing.

Hence we analyzed Russian lunar program and received the technical characteristics of the spacecrafts and scientific goals that they should meet [1]. Thus we identified the criteria of surface suitability for landing. We divided them into two groups: scientific criteria (the hydrogen content of the regolith [2] and day and night surface temperature [3]) and safety criteria (surface slopes and roughness, sky view factor, the Earth altitude, presence of polar permanently shadowed regions). In conformity with some investigations [4] it's believed that the south polar region of the Moon is the most promising territory where water ice can be found (finding water ice is the main goal for Russian lunar missions [1]).

According to the selected criteria and selected area of research we used remote sensing data from LRO (Lunar Reconnaissance Orbiter) [5] as basic data, because it is the most actual and easily available.

The data was processed and analyzed using spatial analysis techniques of ArcGIS Desktop Software, so we created a number of maps depicting the criteria and then combined and overlaid them. As a result of overlay process we received five territories (fig. 1) where the landing will be safe and the scientific goals will have being met.

It should be noted that our analysis is only the first order assessment and the results cannot be used as actual landing sites for the lunar missions in 2015 and 2017, since a number of factors, which can only be analyzed in a very large scale, was not taken into account. However, an area of researching is narrowed to five territories, what can make the future research much easier. The analysis of these five areas in a large scale will be the subject of further research.

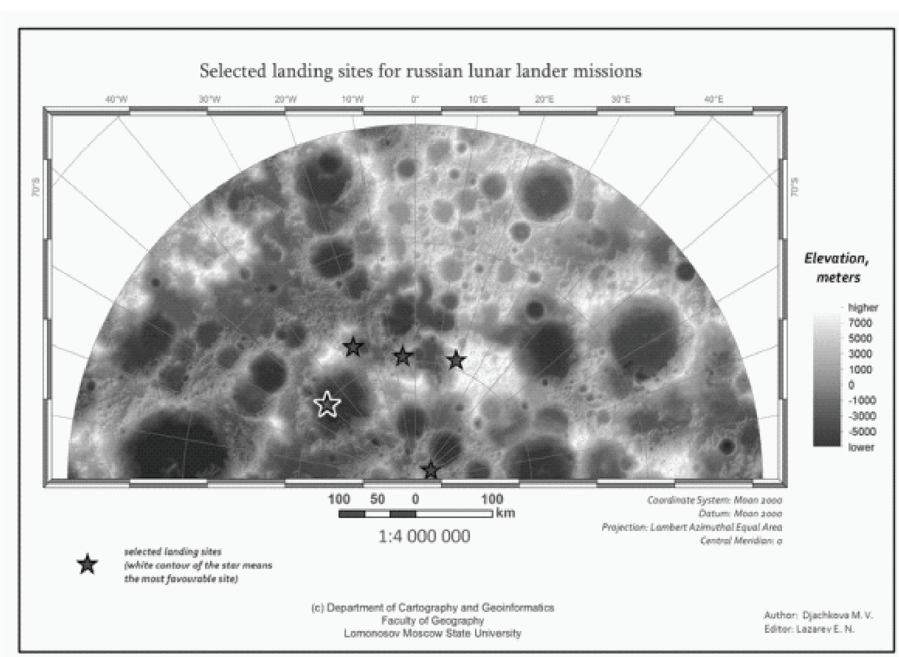

fig.1. Map of the selected landing sites

References:

[1] Mitrofanov I. G. et al. (2011) LPS XLII, Abstract #1798
[2] Mitrofanov I. G., et al. Hydrogen Mapping of the Lunar South Pole Using the LRO Neutron Detector Experiment LEND // Science vol. 330 2010, pp. 483–486
[3] Paige D.A. et al. (2011) LPS XLII, Abstract #2544
[5] De Rosa D., Bussey B., Cahill J. T., et al. Characterisation of potential landing sites for the European Space Agency's Lunar Lander project // Planetary and Space Science 74 (2012), pp. 224–246
[6] Zuber M.T. et al. (2010) Space Sci. Rev., 150, 63-80

MINIATURIZED ANALYZER OF ENERGETIC NEUTRALS LINA-XSAN FOR THE LUNA-GLOB MISSION

S. Barabash[1], M. Wieser[1], Y. Futaana[1], A. Grigoriev[2], A. Shestakov[2], O. Vaisberg[2], E. Kallio[3], W. Schmidt[3], K. Szego[4], S. Szalai[4], A. Vorburger[5], P. Wurz[5], M. Collier[6], T. Zhang[7], K. Asamura[8];
[1]Swedish Institute of Space Physics, Kiruna, Sweden; [2]Space Research Institute, Moscow, Russia; [3]Finnish Meteorological Institute, Helsinki; [4]Institute for Particle and Nuclear Physics, Winger Research Center for Physics, Budapest, Hungary; [5]University of Bern, Bern, Switzerland; [6]Goddard Space Flight Center, Greenbelt, USA; [7]Space Research Institute, Graz, Austria / University of Science and Technology of China, Hefei, China;[8]Institute of Space and Astronautical Science, Sagamihara, Japan; Contact: stas@irf.se

Introduction:

LINA-XSAN (LINA-eXtra Small Analyzer of Neutrals) is a miniaturized detector of energetic neutrals (10 eV – ~10 keV) to investigate the scattering function of neutrals originating from neutralization of the solar wind particles on the lunar regolith as well as neutrals sputtered from the surface.

Scientific background:

The Moon has neither a strong, global magnetic field, nor a dense atmosphere, thus the solar wind ions di- rectly interact with the lunar surface covered by regolith, a layer of loose, heterogeneous material of small grain size (Clark et al., 2002). It has been tacitly assumed that the solar wind plasma is almost completely absorbed in the surface material (e.g. Crider and Vondrak, 2002; Schmitt et al., 2000; Feldman et al., 2000; Behrisch and Wittmaack, 1991). However, in 2008 ion sensors onboard the SELENE spacecraft on lunar orbit detected backscattered solar wind ions and found that 0.1–1% of the solar wind protons flowing towards the lunar surface backscatter from the Moon as ions (Saito et al., 2008). The ion reflection coefficient is a strong exponential function of the solar wind velocity (Lue et al., 2013).

Neutralized solar wind protons, i.e., energetic hydrogen atoms, at the level of 10% to 20% were observed by the IBEX spacecraft (McComas et al., 2009) far away from the Moon, and in lunar orbit by the SARA instrument on Chandrayaan-1 (Wieser et al., 2009). The spectrum of backscattered neutrals turned out to be Maxwellian with a typical temperature of 80 – 160 eV proportional to the solar wind velocity (Futaana et al., 2012). The scattering function estimated with an angular resolution of few 10s degrees is approximately isotropic at small incidence angle (equatorial region) but becomes more backward at larger incidence angles (polar regions) (Schaufelberger et al., 2011). Recently, signals of sputtered oxygen and helium at energies of a few 10s eV were identified in the SARA data too (Vorburger et al., 2013).

Currently there is no comprehensive explanation of the data reported above and one needs “ground truth” to developed the required theories and models.

Scientific objectives:

The main science objective of LINA-XSAN is to investigate the scattering function of the neutralized solar wind and neutral sputtering component. These measurements are required to understand the physics of the solar wind interaction with regolith of airless bodies on the microscale. Understanding mechanisms of the interaction is the key for studies of space weathering, surface release and absorption processes, ion implantation and ultimately for establishing the origin of volatiles (water) in the lunar surface.

The main measurement requirement of LINA-XSAN is to measure the energy spectrum and composition of the neutralized solar wind from a fixed and characterized area of the lunar surface exposed by naturally varying solar wind under different incident angles.

Instrument description:

LINA-XSAN (Fig. 1) is based on miniaturized ion analyzers developed at the Swedish Institute of Space Physics, Kiruna, for Chandrayan-1, BepiColombo, Phobos-Grunt, Yinghuo, and PRISMA missions. The entrance electrostatic deflector rejects the charges particles (ions and electrons) from the incoming beam (Fig. 1a). Energetic Neutral Atoms (ENAs) then interact with the conversion surface and are converted to positive ions. The following electrostatic optics guides the ionized ENAs to the cylindrical electrostatic analyzer providing the incoming beam energy. The ions then are post-accelerated with a potential of 700 – 1000 eV and entry the time-of-flight cell (TOF). In the TOF cell ions hit the start surface and release secondary electrons guided to the start ceramic channel electron multiplier (CCEM), which provides start pulse. The reflected ions (now converted back to neutrals) hit the stop surface and generate, in the similar manner, stop pulse. The start – stop timing gives particle velocity and, for the known energy, the particle mass. Also, the coincidence of start and stop signal within the TOF window allows substantial background noise reduction and thus increasing signal-to-noise ratio.

LINA-XSAN is a stand-alone unit comprising own DC/DC converters and a data processing unit. The sensor is also equipped with a cover to protect the instrument sensors and surfaces sensitive to contamination for on-ground tests and moon landing. The instrument total mass is 650 g.

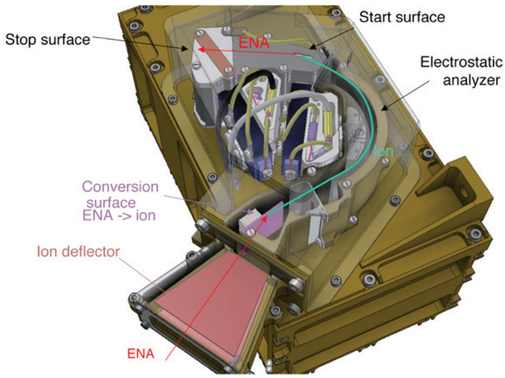

(a)

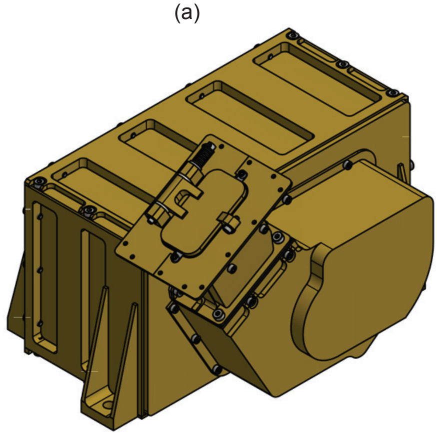

(b)

fig. 1. (a) XSAN cut-off view and operation principle, (b) XSAN view with the protective cover closed. ENA: Energetic Neutral Atoms.

Instrument performance:

Table below sums up the LINA-XSAN performance.

parameter	value
measured particles	neutrals, ions (possible but performance not optimized)
energy range	10 eV – 15 keV
resolution, $\Delta E/E$	8%
mass range, amu	1 - 70
masses resolution, M/ΔM	2..5, Mass identified M/q = 1, 2, 4, 8, >16
FoV (full)	15° x 30°
angular pixel	7°x15°
time resolution	4s
G-factor (GF)	~10^{-6} cm^2 sr eV/eV inc. efficiency (= SARA Chandrayan-1)

Synergy with other instruments:

The science return from LINA-XSAN can be significantly enhanced by synergetic measurements with LIS (Lunar IR Spectrometer) and ARIES.

LIS measures the OH/H_2O absorption line in the 2.7-3.0 mkm range and characterizes the OH/H_2O abundance in the soil. LINA-XSAN measuring simultaneously backscattered flux of neutralized solar wind characterizes the proton deposition into the surface. LINA-XSAN and LIS simultaneous measurements may help to answer the fundamental question whether or not OH/H_2O in the lunar soil originate from the solar wind.

ARIES characterizes the parent ion population resulting in the neutral signal.

IN SITU DATING OF PLANETARY MATERIAL BY LASER-BASED MASS SPECTROMETRY

P. Wurz, M. Tulej, A. Riedo, M. Neuland, and S. Meyer,
Physics Institute, University of Bern, Sidlerstrasse 5, 3012 Bern, Switzerland.
Contact: peter.wurz@space.unibe.ch

Introduction:

Developments of sensitive space instrumentation for in situ investigation of the elemental and isotopic composition of planetary surface material are of considerable interest to current space research. Not only the selection of suitable samples to be brought to Earth by a return spacecraft, but also the direct scientific investigation are of great promise. Currently, there are also three different concepts for specific application for dating of planetary materials under development: i) Sr-Rb method [8], K-Ar method [7], and the Pb isotopes [4].

Isotopes are robust tracers of element formation processes in stars. Contrary to elemental composition of planetary solids, changes of isotopic ratios are relatively small over the time of planetary evolution. A few processes that can modify isotope composition include natural decay of radiogenic elements, nuclear reactions induced by interaction with Cosmic Rays, and chemical or bio-chemical reactions. Hence, sufficiently accurate and precise isotope analysis of solid samples can deliver dating of planetary solids and insights to space weathering or possibly past or present biological activities on the planetary surface [1].

A number of mass spectrometric methods (TIMS, LA-ICP-MS, and SIMS) are applied in laboratory for measuring accurate and precise isotope composition of solid materials. Lately, laser ionisation mass spectrometry (LIMS) becomes increasingly competitive to these well-established methods [2, 3]. We will discuss perspectives of the isotope analysis in space by laser mass spectrometer.

Experimental:

The LMS instrument uses a laser ablation ion source to vaporise, atomise and ionise solid sample material and a reflectron-type time-of-flight mass spectrometer to perform mass spectrometric analyses [2, 5]. Pulsed laser radiation is focused to a spot of a few micrometres (10–40 μm) and removes and ionises surface material with high repetition rate (1–10 kHz). Ions of chemical elements produced in the ion source enter into mass analyser where they are dispersed according to their mass to charge ratio using the time-of-flight principle and detected by high performance ion detector. A sensitive and accurate element and isotope measurement can be performed within 5–50 seconds with the detection of almost all elements (and their isotopes) with concentrations larger than 10 ppb. The LMS instrument resolution is in the range of $m/\Delta m$ = 600–1500. Although this resolution is not sufficient to resolve isobaric interferences, it allows measuring well-resolved mass spectra of elements (isotopes) with concentrations larger than 10 ppb [2]. The chemical mapping of a surface by LMS was also demonstrated [6].

Isotopic Analysis:

The choice of laser parameters (e.g., pulse duration, pulse energy, laser beam characteristics: shape, wavelength), focussing condition and type of mass spectrometer is critical to achieve optimal ablation conditions for stoichiometric production of ions of chemical elements. Hence, a number of calibration measurements with a number of standard research materials are required to establish relative sensitivity factors, RSC (a deviation between actual element concentration and that determined from the measurements) to investigate samples with unknown composition. Our RSCs are close to unity indicating that efficiency of ion generation in ablation process and its detection are optimal for quantitative analysis. Among other instruments, studies conducted with LMS show that a fs-ablation ion source is highly preferable over ns-laser ionisation sources for conducting the quantitative analysis of elemental composition of solids [2,4]. The application of fs-laser ablation ion source at easily-determined experimental conditions yields quantitative elemental analysis. A choice of laser ablation ion source was found to be less critical for conducting accurate and isotope analysis. Nevertheless, the improvement to the measurement accuracy and precision by a factor of 3–5 are observed when a fs-laser ion source is used. LMS can deliver typically the measurements of isotope ratio with accuracy and precision at per mill level for isotope concentration larger than 50–100 ppm (see Figure 1). Depending on the isotopic abundances of Pb in minerals $^{207}Pb/^{206}Pb$ ages with an accuracy in the range of tens of millions of years can be achieved [4]. With an increase of the instrument dynamic range and sensitivity of measurements, also the accuracy of the isotope measurements is expected to improve accordingly [4].

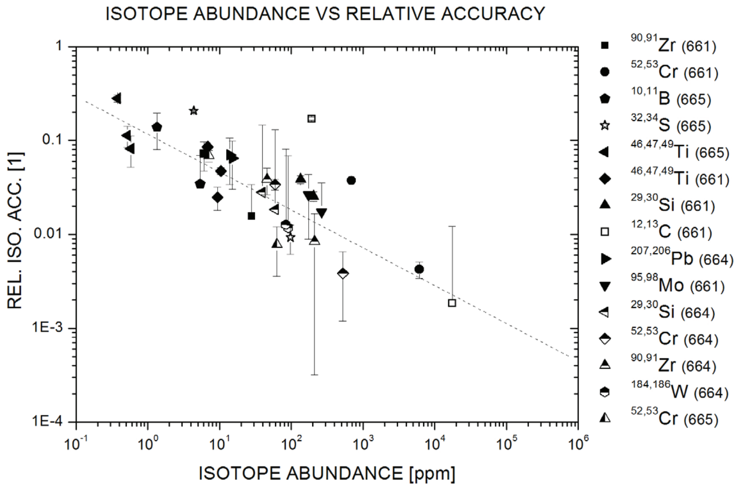

fig. 1. Accuracy of the isotope composition determination as a function of isotope concentration.

Summary and Conclusions:

Instrument performance of LMS is a subject of continued improvement in our laboratory. A fs-laser ablation ion source is very promising for further progress regarding elemental and isotopic analysis in space research and the development of standard-less instruments. By coupling of this source with LMS an increased number of elements can be now detected with high sensitivity (H, O, N, Cl, Br, J) and highly accurate and sensitive analysis of elemental and isotope composition can be conducted without additional standard materials for calibration of the measurements. Our current studies show that the sensitivity of the instrument for the detection of trace elements and accuracies of isotope measurements are sufficiently high to investigate various isotope fractionation effects (Pb-Pb isotope geochronology, C, S biomarkers, sensitive isotope analysis of upper most surface composition by space weathering).

References:

[1] Wurz, P. Abplanalp, D. Tulej, M. Iakovleva, Fernandes, V.A Chumikov, A. Managadze, G., Sol. Sys. Res. 46 (2012) 408–422
[2] Riedo, A. Bieler, A. Neuland, M. Tulej M. Wurz P., J. Mass. Spec., 48, (2013) 1–15, doi: 10.1002/jms.3157.
[3] Tulej, M. Iakovleva, M. Leya, I. Wurz, P. Anal. Bioanal. Chem., 399, (2011) 2185–2200
[4] Riedo A. et al., Planet. Sp. Sci.,, (2013), submitted.
[5] Riedo, A. et al., JAAS, 2013, in press.
[6] Neuland, M., S. Meyer, A. Riedo, M. Tulej, P. Wurz, K. Mezger, Probing the Allende meteorite with LMS, a miniature Laser-Ablation Mass Analyser for space application, 2013, Planet. Sp. Sci., submitted
[7] B. A. Cohen, Development of the potassium-argon laser experiment (KARLE) instrument for in situ geochronology, 43rd Lunar and Planetary Science Conference (2012), abstrct Nr. 1267
[8] S.F. Anderson, K. Nowicki, and T. Whitaker, In-Situ Rb-Sr Geochronology, IEEE Aerospace Conference, 2013, 1–8, doi: 10.1109/AERO.2013.6497158

EUROPEAN OBJECTIVES AND APPROACH TO LUNAR EXPLORATION IN COOPERATION WITH RUSSIA

B. Houdou[1], R. Fisackerly[1], J. Carpenter[1], D. De Rosa[1], J. Schiemann[1], B. Patti[1],
[1]*European Space Agency, Keplerlaan 1, 2201 AG, Noordwijk, Netherlands.*
Contact: Berengere.Houdou@esa.int

Introduction: The European Space Agency's approach to exploration includes three destinations: Low Earth Orbit, the Moon and Mars. The role of the Moon in this sequence is as a stepping stone for the development of cooperative robotic and human exploration capabilities, beginning with robotic precursor missions. These missions can demonstrate technologies and make measurements that enable future missions. During the buildup of these capabilities on the Moon there will also be opportunities to realise scientific benefits.

The Moon is also playing a major role in the exploration plans of ESA's international partners, in particular Russia. In the context of broader cooperation between ESA and Russia in exploration of the Solar System, agencies, industries and institutes from both sides are actively engaged in identifying and pursuing opportunities for cooperation. These opportunities focus on the Russian mission Luna-Resource (Luna-27), with a view to a Lunar Polar Sample Return (LPSR) mission (Luna-28). This paper outlines the main European objectives and approach regarding this cooperation.

Background: In the near to medium term ESA is focused on the advancement and in-flight application of existing technologies in ways which can provide an access point for Europe to cooperate in future exploration missions with international partners. In parallel the approach aims to generate research opportunities which will address the scientific challenges of exploration whilst providing opportunities for fundamental scientific research. The European Lunar Lander mission, studied by ESA and European industry to Phase B1 level, embodied this approach through its focus on key descent and landing technologies and exploration relevant scientific measurements.

Europe's experience includes precision navigation and hazard detection technologies, advanced through the European Lunar Lander development, as well as a sub-surface drilling capability developed through projects such as Rosetta and ExoMars. Together this background provides Europe with a strong foundation on which to build a long-term cooperation with Russia.

Objectives: Europe's objective is to further develop key technologies of interest and generate knowledge that will enable future human exploration of the solar system, while acknowledging that cooperation with international partners will be key to making this happen. In its efforts to achieve this objective, ESA is pursuing a cooperation with Russia on a sequence of near and medium term robotic exploration missions to the Lunar South Polar Region. Europe's priorities in this cooperation are:

1) Prepare technologies and capabilities for future exploration missions

2) Investigate lunar volatiles as a potential future resource and as a scientific repository

3) Build a robust and mutually beneficial cooperation on Lunar exploration with Russia.

Based on these objectives ESA's practical approach to cooperating on lunar exploration with Russia is driven by the following requirements. Finding means to address these requirements, jointly with Russian partners, must also take into account that the Luna-Resource lander is a Russian-led mission.

- Determine the locations at which samples of interest are likely to exist
- Access those specific locations with adequate precision and safety
- Acquire those samples of interest
- Analyse those samples
- Ensure that all contributions prepare the way for future missions

Conclusion: A European-Russian cooperation on near- and medium term lunar exploration missions, with a focus on Lunar-Resource and looking forward to Lunar Polar Sample Return, offers an opportunity for Europe to realise its own exploration objectives. Based on the significant European experience across a range of areas, and on the principle of mutual benefit, ESA and its partners in Russia are building a lunar exploration programme which offers immediate benefits to stakeholders and which paves the way for future cooperation in human exploration.

LANDING SITE CHARACTERISATION FOR FUTURE LUNAR EXPLORATION MISSIONS

D. De Rosa[1], J. Carpenter[1], R. Fisackerly[1], B. Houdou[1],
[1]European Space Agency, Keplerlaan 1, 2201 AZ Noordwijk ZH, The Netherlands,
Contact: diego.de.rosa@esa.int

Introduction: Future exploration missions to the lunar polar regions require dedicated characterisation of potential landing sites, whose specific properties can be major drivers for the design of surface systems. Charac-terisation activities must take into account the relationship between science requirements calling for access to specific areas, and driving mission and system requirements such as landing site safety, availability of solar illumination, and direct ground station visibility. In recent years a wealth of data has been generated (e.g. by the Lunar Reconnaissance Orbiter) that has enabled unprecedented investigation of landing site properties and led to an in-depth understanding of the conditions encountered at various sites.

Background: Through the European Lunar Lander mission study [1] the European Space Agency has de-veloped and applied a number of capabilities in the area of landing site characterisation. The European Lunar Lander mission targeted highly illuminated topographic highs in the Moon's South Polar region in order to per-form several weeks of surface operations without using radioactive sources. The target landing sites were shown to exhibit extended durations of illumination on spatial scales of a few hundreds of metres. Accessing these sites would therefore require a high degree of landing precision. It was also shown that a fraction of the area within these sites present steep slopes and boulders that could endanger the stability and integrity of the lander at touchdown, thus requiring the use of autonomous Hazard Detection and Avoidance (HDA).

In order to characterise the spatial and temporal distribution of the illumination, dedicated tools have been developed to simulate the Sun's visibility at a given height above the surface, using terrain models from the Lunar Orbiter Laser Altimeter. These terrain models have also been used to assess the distribution of slopes on a scale of tens of metres. Images from the Lunar Reconnaissance Orbiter Camera (LROC) have been used to characterise the distribution of craters and boulders.

More recently, ESA has funded the generation of high resolution (2 m ground sampling distance) Digital Terrain Models of the landing sites using LROC stereo products [2] and analysis of these models is underway.

In parallel, ESA is also developing a suite of web-based tools for landing site characterisation called LandSAfe [3]. LandSafe will provide end users with a means of selecting, generating and visualising different lunar and planetary products.

Landing site characterisation for future polar landers: Future missions, which target lunar polar volatiles, specifically water ice, must ensure they land at a location where such water ice can exist. It is known from the L-CROSS mission that water ice exists in certain permanently dark craters. Water may also be present in the subsurface in areas which see limited illumination. In this case, the subsurface temperature can remain low enough that water ice losses can be small on geological time scales. Such sites may also have enough illumina-tion to allow solar powered surface operations to take place. Not only do these areas have short illumination periods but they also tend to be in variable terrains, whose topography results in shadows that cause the reduced illumination. This has implications for mission design, including landing precision and HDA needs.

This paper presents an analysis of one partially illuminated site where water ice could exist, in terms of local illumination conditions and surface hazard characterization. This analysis is then used to identify major design drivers on the system such as landing precision, hazard detection and avoidance needs, and expected surface operational environment.

References: [1] De Rosa D. et al. (2012) JPSS, 74, 224–246. [2] Gläser P. et al. (2013) LPSC XLIV, Abstract #1967. [3] Schmidt R. et al. (2012) ISPRS XXXIX-B4, 505-510.

LUNAR RESOURCES: WHAT WE KNOW ABOUT IT NOW?

V. V. Shevchenko,
Sternberg State Astronomical Institute, MSU, University prospect, 13, Moscow, 119992, Russia. Contact: vladislav_shevch@mail.ru

Introduction:

Japan, China, and India, we are opening a new era of lunar studies. The International Academy of Aeronautics (IAA) has begun a study on opportunities and challenges of developing and using space mineral resources (SRM). This study will be the first international interdisciplinary assessment of the technology, economics and legal aspects of using space mineral resources for the benefit of humanity. The IAA has approved a broad outline of areas that the study will cover including type, location and extent of space mineral resources on the Moon, asteroids and others. It will be studied current technical state of the art in the identification, recovery and use of SRM in space and on the Earth that identifies all required technical processes and systems, and that makes recommendations for specific technology developments that should be addressed near term at the system and subsystem level to make possible prospecting, mineral extraction, beneficiation, transport, delivery and use of SMR. Particular attention will be dedicated to study the transportation and retrieval options available for SRM.

Lunar polar volatile:

ROSCOSMOS places a high priority on studying lunar polar volatiles, and has outlined a few goals related to the study of such volatiles. Over the course of several years, NASA's Lunar Reconnaissance Orbiter scanned the Moon's south pole using its Lunar Exploration Neutron Detector (LEND – IKI Russia) to measure how much hydrogen is trapped within the lunar soil. Areas exhibiting suppressed neutron activity indicate where hydrogen atoms are concentrated most, strongly suggesting the presence of water molecules. On Figure 1the blue areas show locations on the Moon's south pole where water ice is likely to exist (NASA/GSFC).

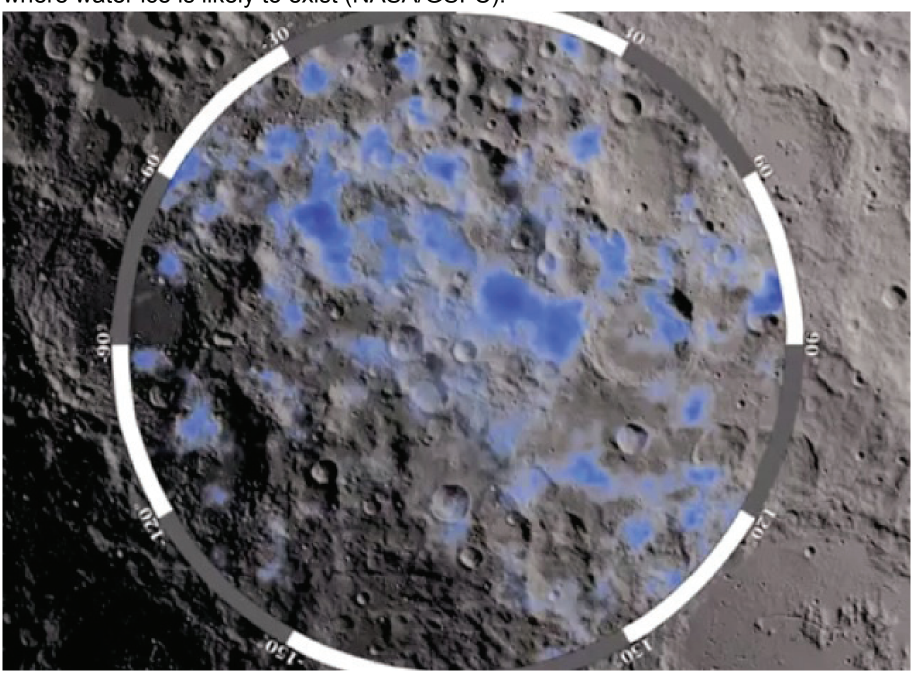

fig. 1.

Current survey of the Moon's polar regions integrated geospatial data for topography, temperature, and hydrogen abundances from Lunar Reconnaissance Orbiter, Chandrayaan-1, and Lunar Prospector to identify several landing sites near both the north and south polar regions that satisfy the stated goals.

Lunar titanium:

Objectives of the Lunar Reconnaissance Orbital (LRO) mission are to find potential safe landing sites and locate potential resources.

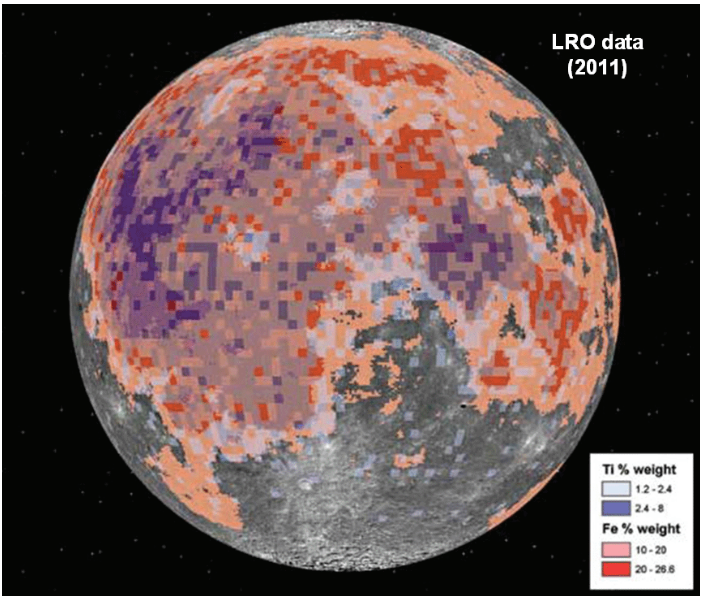

fig. 2.

New imaging from NASA' LRO has shown that the moon has areas that are rich in titanium ore. Some lunar rocks have ten times as much titanium ore as rocks on Earth. The titanium deposits were observed with the help of visible and ultraviolet imaging. The researchers scanned the lunar surface, collecting roughly 4,000 images, and compared the brightness in the range of wavelengths from ultraviolet to visible light. The scientists then cross-referenced their findings with lunar samples that were brought back to Earth from NASA's Apollo flights and the Russian Luna missions. The abundance of titanium has puzzled researchers (Fig. 2). While rocks on Earth contain around one percent titanium at most, the lunar rocks ranged from one percent all the way up to ten percent. Researchers still don't why the titanium levels are higher on the moon, but do believe it gives insight into the conditions of the Moon shortly after it formed. The titanium seems to be found primarily in the mineral ilmenite, a compound containing iron, titanium, and oxygen.

Lunar rare earth elements:

The Procellarum KREEP Terrane (PKT) dominates the nearside of the Moon. "KREEP" is an acronym for lunar rocks that are high in potassium (K), rare earth elements (REE), and phosphorous (P). The PKT is a mixture of assorted rocks, including most of the mare basalts on the Moon, and is characterized by high Th (about 5 parts per million on average). This region has also been called the "high-Th Oval Region". PKT occupies about 16% of the lunar surface (Fig. 3).

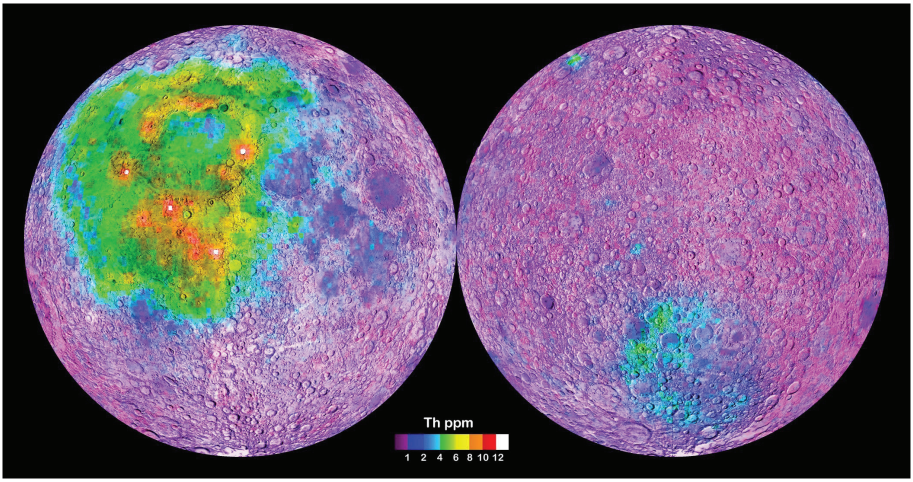

fig. 3.

PROPOSALS ON THE DEVELOPMENT OF A LUNAR-BASED SCIENTIFIC INSTRUMENT FOR STUDIES OF COSMIC RAYS CHEMICAL COMPOSITION AND SEARCH FOR DARK MATTER INTERACTION PRODUCTS.

Mikhail Panasyuk*, *Skobeltsyn Institute of Nuclear Physics (MSU SINP), panasyuk@sinp.msu.ru*

The results of development of a scientific complex for studies of cosmic rays nuclei chemical composition and search for dark matter interactions products are presented. The proposed instrument is intended for a long-term lunar station. Comparing to the Earth the Moon possesses unique possibilities for the studies of cosmic rays composition. On the Moon's surface it is possible to register partilces directly due to absence of the atmosphere where cosmic rays particles interact producing cascades of secondary particles. A possibility to determine energy of cosmic rays particles by counterflow of cascades' produced in regolith for several components: neutrons, gammas and radioemission was shown by means of preliminary simulation and analysis.

*On behalf of collaboration of SINP MSU (L.G. Sveshnikova, D.M. Podorozhny, A.N. Turundaevsky, N.N. Kalmykov, A.A. Konstantinov), INR RAS (R.A. Mukhamedshin), JINR (L.G. Tkachev), P.N. Lebedev PI RAS (A.P. Chubenko).

FUTURE PERSPECTIVES OF OPTICAL OBSERVATIONS ON THE SURFACE OF THE MOON

Ugolnikov O.S.
Space Research Institute, Russian Academy of Sciences

The talk contains the description of advantages of optical astronomical observations on the surface of the Moon. The basic advantages are:

1. Absence of the atmosphere, no extinction, clouds obscuration and less value of sky background. Observations are possible even during the local daytime. Spectral range of the observations can be included by UV- and IR-bands.

2. Angular resolution is restricted only by diffraction disk size of point-like source.

3. Small value of Moon angular rotation, possibility of very long exposures (impossible for ground-based and space observations).

4. Weak gravitation, possibility to use the equipment without heavy installation sets. It is possible to use thinner mirrors for the telescopes.

5. It is easier to maintain low temperatures for the detectors, placing them inside white or mirror cover.

LUNAR LOW-FREQUENCY ARRAY: EXPLORATION OF POSSIBLE MARKER FOR EXOPLANETS HABITABILITY

M. Mogilevsky[1], A. Skalsky[1], V. Gotlib[1], T. Romantsova[1],H. Rothkaehl[2], L. Gurvits[3]
[1]Space Research Institute RAS, (Russia), [2]Space Research Center PAN, (Poland), [3]Joint Institute for VLBI in Europe (the Netherlands), mogilevsky2012@gmail.com

The intrinsic magnetic field shielding the planetary surface from most of space radiation is one of indicator on possible habitability of exoplanet. A search of exosolar terrestrial-like planets possessing the magnetic fields and developed magnetospheres seems to be the most intriguing objective of exoplanet studies. The interaction of planetary magnetosphere with the star wind results in generation of radioemissions (similar to AKR radiation of the terrestrial magnetosphere) which allows remote sensing of exoplanet magnetic field. However, frequency range of waves expected from terrestrial-like exoplanet is below, roughly, 10 MHz and, thus, these radioemissions can be hardly investigated by ground facilities due to conducting Earth's ionosphere. The Moon possessing a week atmosphere/ionosphere around its surface seems to be a perfect base for carrying out measurements of low frequency radio emissions originated from the space. The paper presents approaches to antenna design and a scenario of radio facility deployment at Moon's surface which is aimed on terrestrial-like planet search in exosolar system.

PARAMETERS OF PHOTOELECTRONS OVER THE ILLUMINATED PART OF THE MOON.

S.I. Popel[1], A.P. Golub'[1], G.G. Dolnikov[2], Yu.N. Izvekova[1], A.V. Zakharov[2], L.M. Zelenyi[2],
[1]Institute for Dynamics of Geospheres RAS, Leninsky pr. 38, bldg. 1, 119334 Moscow, Russia; [2]Space Research Institute RAS, Profsoyuznaya 84/32, 117997 Moscow, Russia. Contact: s_i_popel@mtu-net.ru

Studies of dusty plasma near the Moon are important because of a renaissance which is currently observed in investigations of the Moon. The upcoming LADEE (Lunar Atmosphere and Dust Environment Explorer) mission will be launched in 2013 and carry an in-situ and a remote sensing instruments dedicated to the mapping of the lunar dust environment from orbit. The Russian missions Luna-Glob and Luna-Resource (the latter jointly with India) will include investigations of dust near the surface of the Moon. It is planned to equip the Luna-Glob and Luna-Resource stations with instruments both for direct detection of dust particles over the surface of the Moon (piezoelectric impact sensor (IS) and electrostatic sensor (ES)) and for optical measurements (overview camera (Cam O) and stereocamera (Cam S)). Fig. 1 shows the scheme of the location of the above instruments at the Luna-Glob and Luna-Resource stations. Measurements are planned in the **daytime** to ensure the power supply of instruments at lunar stations owing to solar energy.

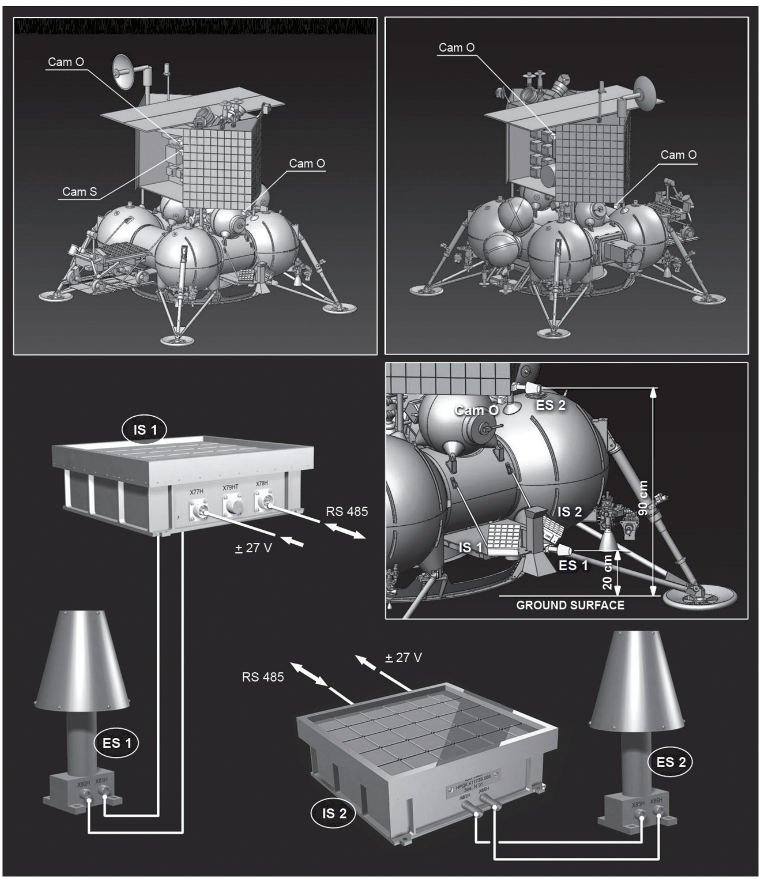

fig. 1. The scheme of the location of the instruments both for direct detection of dust particles over the surface of the Moon and for optical measurements at the Luna-Glob and Luna-Resource stations.

At the **daytime** the surface of the Moon is charged under the action of the electromagnetic radiation of the Sun, solar-wind plasma, and plasma of the Earth's magnetotail. The surface of the Moon and dusts levitating over the lunar surface interact with solar radiation. They emit electrons owing to the photoelectric effect, which leads to the formation of the photoelectron layer over the surface. Dusts located on or near the

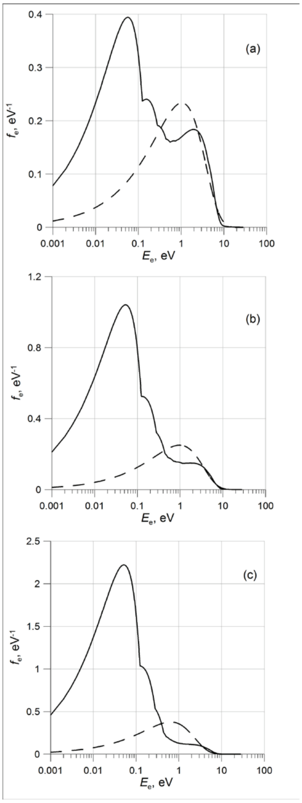

fig. 2. Photoelectron distribution functions (solid curves) near the lunar surface calculated under the conditions of solar flare (a) and two intensities of solar activity: solar maximum (b) and solar minimum (c). Dashed curves represent the Maxwellian distributions for the same averaged thermal energy (temperature) as the corresponding calculated distributions shown by the solid curves.

face of the Moon absorb photoelectrons, photons of solar radiation, electrons and ions. All these processes lead to the charging of dust particles, their interaction with the charged surface of the Moon, rise and levitation of dust [1, 2]. When determining the dusty plasma parameters over the illuminated part of the Moon, one has to find the photoelectron number density and temperature characterizing the averaged thermal energy of photoelectrons. Here, we develop the methods of calculations of the parameters of photoelectrons. We carry out our calculations for spectra of solar radiation characterizing solar flares and different solar activities. We obtain the number densities of photoelectrons and their distribution functions near the lunar surface. Fig. 2 presents the photoelectron distribution functions calculated under the conditions of solar flare (a) and two intensities of solar activity, namely, solar maximum (b) and solar minimum (c). The lunar surface work function was chosen to be 6 eV while the quantum photoemission yield was taken from [3] for lunar regolith. The values of the photoelectron number density N_0 and photoelectron temperature T_e calculated for the above data are given in Table 1.

table 1. Values of the photoelectron number density and photoelectron temperature near the lunar surface with the work function 6 eV and the quantum photoemission yield given in [3]

	solar flare	solar max	solar min
N_0, cm^{-3}	2.3×10^5	2.1×10^5	1.9×10^5
T_e, eV	0.20	0.15	0.12

table 2. Values of the photoelectron number density and photoelectron temperature near the lunar surface with the work function 5 eV and the quantum photoemission yield given in [4]

	solar flare	solar max	solar min
N_0, cm^{-3}	807	280	131
T_e, eV	2.35	2.16	1.46

The values presented in Table 1 differ from those obtained with the use of the quantum photoemission yield [4]. The values of the photoelectron number density and photoelectron temperature near the lunar surface with the work function of 5 eV and the quantum photoemission yield given in [4] are presented in Table 2. This data are in a good agreement with the data [5] which have been calculated for the same parameters as those presented in Table 2. The main factor influencing the photoelectron number density and the photoelectron temperature near the lunar surface is the quantum photoemission yield. At present, there is no adequate research concerning the quantum photoemission yield of the lunar regolith. The significance of this parameter is great because, in particular, it influences the structure of the dusty plasma system over the Moon and determines it to a great extent. In this connection the future in-situ measurements of the lunar surface quantum photoemission yield (and work functions) are of great importance, and the corresponding investigations should be planned for the future lunar missions.

This work was supported by the Presidium of the Russian Academy of Sciences (basic research program no. 22 “Fundamental Problems of Research and Exploration of the Solar System”) and by the Russian Foundation for Basic Research (project no. 12-02-00270-a).

[1] *A.P. Golub’, G.G. Dol’nikov, A.V. Zakharov, L.M. Zelenyi, Yu.N. Izvekova, S.I. Kopnin, S.I. Popel*, JETP Lett. **95**, 182 (2012).
[2] S.*I. Popel, S.I. Kopnin, A.P. Golub’, G.G. Dol’nikov, A.V. Zakharov, L.M. Zelenyi, Yu.N. Izvekova*, Solar System Research **47**, No. 6 (2013), in press.
[3] *E. Walbridge*, J. Geophys. Res. **78**, 3668 (1973).
[4] *R.F. Willis, M. Anderegg, B. Feuerbacher, and B. Fitton*, in Photon and Particle Interactions With Surfaces in Space, edited by R.J.L. Grard, D. Reidel, Dordrecht, Netherlands, 1973, p. 389.
[5] *Z. Sternovsky, P. Chamberlin, M. Horanyi, S. Robertson, and X. Wang*, J. Geophys. Res. **113**, A10104 (2008).

STRUCTURES AND TRANSPORT OF CHARGED DUST UNDER LABORATORY AND MICROGRAVITY CONDITIONS

O. F. Petrov[1] and V. E. Fortov[1],
[1]Joint Institute for High Temperatures RAS, Izhorskaya 13 bld.2, Moscow, 125412, Russia. Contact: ofpetrov@ihed.ras.ru

Introduction:

The charged dust represent a non-neutral or quasi-neutral systems (dusty plasmas) containing micron-sized particles (dust or grains) of a substance with electrical charges up to 10^2-10^5e. As a result of strong interaction of the strongly charged dust particles they may form the ordered structures of liquid and crystal types that are different from gas-like or chaotic systems.

Most of the laboratory studies of dusty plasmas are carried out in weakly ionized gas discharge plasmas. As a result, the laboratory dusty plasma is the unique object for studying the structure, phase transitions and transport properties of the systems of interacting grains on the “kinetic level”.

Dust system is affected by gravity, depending on the size of the solid particles gravity can be the dominating force. Under microgravity conditions in space much weaker forces become important and other new phenomena not achievable on Earth can be observed. In this report results are presented from the experimental studies of charged dust systems under ground bounded and microgravity conditions.

Structural and transport characteristics of dust in plasmas were measured in a set of experiments in rf gas-discharge plasmas in microgravity conditions onboard of International Space Station. The formation of ordered structures from large number (~10^4) of charged diamagnetic dust particles in a cusp magnetic trap under microgravity conditions has been studied. Dusty plasmas were also investigated in a combined dc/rf discharge under microgravity conditions in parabolic flights.

The numerical simulations of the lunar plasma-dust exosphere caused by action of solar ultraviolet radiation and the incoming solar wind on the lunar surface have been carried out. The influence of the solar wind flux on the near-surface photoelectron sheath formation as well as conditions of dust levitation above the lunar surface have been analysed.

The phase transitions in quasi-two-dimensional dust structures suspended in rf discharge were studied in experiments. The results reveal the existence of hexatic phase as well as solid-to-hexatic phase and hexatic-to-liquid transitions.

This work was supported by the Research Program of the Presidium of the Russian Academy of Sciences “Matter under High Energy Densities” and by the Russian Foundation for Basic Research (Project No. 13-02-01393-a).

LABORATORY ANALYSIS OF GRANULAR MATERIALS PROPERTIES, SIZE DISTRIBUTIONS, CHEMICAL AND MINERALOGICAL COMPOSITIONS RELEVANT TO DUST-GRAIN CHARGING INVESTIGATIONS

M. Koepke[1], J. Tucker[2], C. Freeman[3], D. Meisel[3], J. Walker[1], M. Zimmerman[4], W. Farrell[4], V. Demidov[1],
[1]West Virginia University, Morgantown, WV, USA;
[2]National Energy Technology Laboratory, Morgantown, WV, USA;
[3]Geneseo College, Geneseo, NY, USA; [4]NASA-GSFC, Greenbelt, MD, USA.
Contact: mkoepke@wvu.edu

Introduction:

A fundamental-level investigation of electrostatic charging behavior was conducted on a gas-solid multiphase fluid system in an attempt to quantify and model the influence of granular charging on fluidized-particle beds. The investigation focused on the effects of the materials properties and operating conditions on the particle charging. The impact of the charged particles on the hydrodynamics of the system was also studied. Speculation of the work functions that are presumed to govern charge magnitude are presented from the data collected.

In-depth microbeam analysis is being carried out on returned samples of meteorites, presently, and spacecraft returned cosmic dust samples, such as those provided by Stardust and Hayabusa, planned in the future, using strictly calibrated accelerator-induced neutron-activated, proton-induced, deuteron-induced, and alpha-particle-induced energetic photon emission along with nuclear reaction analysis (NRA) and Rutherford backscatter (RBS), atomic-force microscopy, phase-contrast microscopy, scanning electron microscopy (SEM), and UV and X-ray fluorescence spectroscopy, if required. Neutron activation provides the ability to study elemental composition throughout the bulk of the sample (whereas PIXE and RBS techniques are primarily limited to surface studies). The development of neutron-activation analysis microbeam techniques is considered a new and unique technology that will enable studying small returned samples with the same techniques presently used on larger objects by Mars rovers. This research supports the needs of our laboratory study and simulation of dusty plasmas throughout the solar system as the ion beam studies will provide charging information as occurs when dust particles are subjected to the solar wind.

At present, our 4-year PIXE and alpha-induced X-ray emission (AIXE) analysis experience has been mainly derived from macroscopic raw meteorite samples with good elemental detectability up to Zr (atomic number 40) and abundances as small as parts per million. With the generosity of several reliable meteorite dealers, we have been successful in developing an X-ray emission meteorite classification system that enables us with a minimum of sample damage to distinguish between meteoritic and non-meteoritic material with up to a 95% probability based on only a single 3-hour accelerator run. Three-way improvement in the accelerator-based system is expected in the near future: a) better elimination of the dominant sources of sample contamination, b) more perfect preparation of powdered thin targets from large samples to extend the PIXE/AIXE system to heavier elements Z>40, and c) the development of a neutron activation microbeam methodology that would work in conjunction with the ion microbeam capability presently available. Such a dual (neutron-activation and ion) microbeam capability will enable us to study, in a well-known, relatively non-destructive manner, very small samples including those commonly obtained via spacecraft sample returns. The Geneseo Pelletron already serves as a low-energy, nuclear, regional facility involving both undergraduate and graduate faculty and students.

THE INFLUENCE OF THE SURFACE CONDUCTIVITY ON THE DUST MOTION NEAR THE MOON AND ASTEROIDS.

N.D. Borisov,
Institute of Terrsetrial Magnetism, Ionosphere and Radio Waves Proapgation, IZMIRAN, 142190, Kaluzshskoe Hwy 4, Troitsk, Moscow, Russia.
Contact: boisov@lpi.ru

It is usually accepted that for lofting of dust grains form the surface of the Moon strong local electric fields are required. According to the theory such fields can be formed near mini-craters or mini-hills because the fluxes of solar wind electrons and protons towards the opposite slopes of such structures are quite various. As a result potential difference and local electric fields appear. Up to now the theory is worked out assuming that the surface (the regolith) is an ideal insulator. In reality the surface has small but finite conductivity due to which the magnitude of local electric fields tends to reduce. The physics behind this is that the role of electric currents in the regolith is to short-circuit potential difference near mini-craters or mini-hills. The higher the surface conductivity the stronger the effect is. We discuss theoretically the influence of finite surface conductivity on the formation of local electric fields. Our theory predicts that above the regions with high enough conductivity dust motion should be absent. This conclusion can be used to test the existence of the regions with ice under the surface of the Moon. Indeed, according to present understanding near the poles of the Moon under the surface local regions that contain frozen water are expected. Such regions have significantly higher conductivity than the neighboring ones and hence the dust motion above them is suppressed. So we suggest an independent method for detection frozen water under the surface of cosmic bodies without atmosphere. Similar results can be applied to asteroids.

INTENSITY AND POLARIZATION OF LUNAR HORIZON GLOW: NUMERICAL SIMULATIONS.

Yaroslaw A. Ilyushin[1],
[1]Moscow State University, Russia 119992 GSP-2 Moscow, Leninskie.
Contact: ilyushin@physics.msu.ru

Lunar Horizon Glow (LHG) is the glow produced by the sun light scattered by the dust particles levitating in the lunar dusty plasma mantle [1]. The mechanisms which kick the dust particles from the surface of lunar regolith an d make it levitate are not yet completely studied. Among possible candidates are the solar wind, which blows the dust off the surface, and meteoric bombardment. Electric field of charged lunar surface is supposed to suspend the dust particles at heights ranging from meters to kilometers and more. If so, dust particles, which are generally not spherically symmetric, might be preferably oriented along the electric field lines. This prevalent orientation of these particles should be manifested in the scattered light. In particular, polarization state of the scattered radiation is sensitive to the orientation of non-spherical dust grains [2].

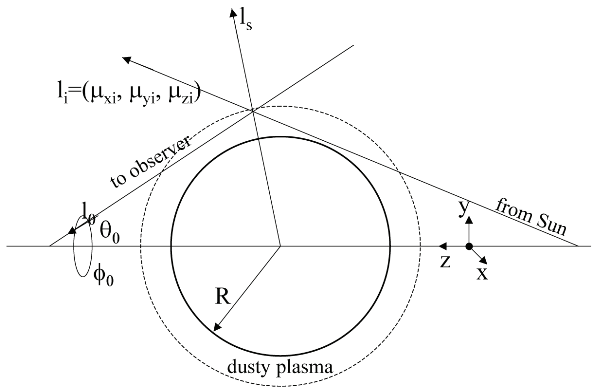

fig. 1. Schematic depiction of the observational geometry.

In the present work, Lunar Horizon Glow (LHG) has been simulated numerically. The vector radiative transfer equation (VRTE) for single-scattered solar radiation in optically thin medium [2]

$$\frac{dI(\vec{R},\vec{n})}{ds} = n_d(\vec{R})K(\vec{R},\vec{n})I(\vec{R},\vec{n}) + S,$$

where I is the vector of Stokes parameters, n_d is the volume number density of dust grains, K is the extinction matrix, S is the source term rtesponsible for the scattered solar radiation, has been evaluated. Simulation code in C++ programming language has been developed. Individual scattering properties of non-spherical dust grains have been calculated with T-matrix computer codes provided by M.I.Mishchenko for public access [3]. Angular distributions of the Stokes parameters (intensity and polarization state) have been calculated for various sets of the dusty mantle parameters (dielectric properties of the dust, shape, vertical concentration profile etc.)

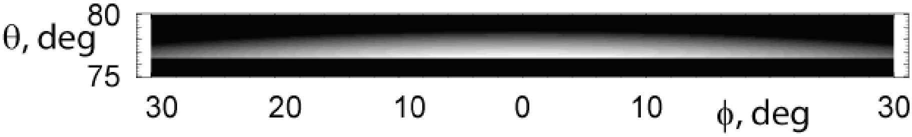

fig. 2. Simulated angular distribution of the intensity of single scattered solar radiation (arbitrary units). Rayleigh scattering particles.

References

Stubbs, T.J., D. A. Glenar, A. Colaprete, D. T. Richard. Optical scattering processes observed at the Moon: Predictions for the LADEE Ultraviolet Spectrometer, Planetary and Space Science, Volume 58, Issue 5, April 2010, pp. 830-837.
Mishchenko, M. I., 1991: Extinction and polarization of transmitted light by partially aligned non-spherical grains, *Astrophys. J.* **367**, 561-574.
http://www.giss.nasa.gov/staff/mmishchenko/t_matrix.html

SPACE EXPLORATION: A PERSONAL HISTORICAL HIGHLIGHTS

M.Ya. Marov,
Vernadsky Institute of Geochemistry and Analytical Chemistry RAS

Brief overview of space research in the former Soviet Union with the author participation is given. The main focus is is placed on the Moon, Venus, and Mars missions. Materials from the author personal archive are used.

50 YEARS OF RUSSIAN AND AMERICAN LUNAR EXPLORATION: A ROADMAP FOR THE FUTURE.

James W. Head and Apollo 15 Commander David R. Scott,
Department of Geological Sciences, Brown University, Providence, RI 02912 USA.
Contact: james_head@brown.edu

Introduction: The history of spacecraft exploration of the Earth's Moon by the Soviet Union and the United States in the 1959-1976 era provided knowledge and experience about the full range of exploration modes possible for the undertaking of scientific exploration missions to the Moon. This combined record provides fundamental insight into the most productive and scientifically rewarding modes of exploration in the future. Here we review these well-developed capabilities, summarize the most exciting and outstanding scientific questions about the origin and evolution of the Moon, and use this experience to suggest and assess how a new human-robotic exploration architecture could address these questions.

Modes of Exploration: Early lunar flybys (Luna 3-1959) led to our first synoptic views of the lunar farside; orbiters (Luna 10-12, 14, 22; Lunar Orbiter 1-5) provided synoptic views of the lunar surface to understand processes and history and plan for future surface exploration; impactors (Luna 2) with high-resolution descent imaging (Ranger 7-9) provided a perspective on the density of small craters and regolith formation; soft landers (Luna 9, 13 and Surveyor 1-7) provided clues as to the nature of the surface and chemistry of soil and rocks; robotic lunar roving vehicles (Lunokhod 1 and 2; Figure 1) traversed over 40 km of the lunar surface (Figure 2) making comprehensive magnetic, chemical, soil and geology measurements; and robotic sample return missions (Figure 2) (Luna 16, 20, 24) brought back soil and drill cores for analysis on Earth. Human exploration missions undertook walking geologic traverses (Apollo 11, 12, 14), instrument deployment, and sample collection; this capability was enhanced by the increased stay time, traverse range and mobility provided by a piloted Lunar Roving Vehicle (LRV) (Figures 5-8) (Apollo 15, 16, 17), and return of samples for laboratory analysis (Figure 4). The combined data collected from these missions provided a fundamental view of the formation and evolution of a second planetary body, and filled in many of the missing chapters of early Earth history.

The Renaissance: Following a lull in lunar exploration missions (1976-2011; Clementine and Lunar Prospector), a recent (from 2001) and current international armada of spacecraft exploring the Moon has provided a renaissance and significant new insight into the nature and evolution of the lunar crust and the structure of the lunar interior. These new data have combined high spatial and spectral resolution data together with high-resolution altimetry and gravity to reveal new minerals and rock types, as well as to help define the locations of concentrations of these types of key deposits that can help in unraveling crustal history and the nature of the geologic processes (impact cratering, volcanism, tectonism, volatile migration and sequestration) that have influenced this evolution.

Science Requirements and Legacy: These findings have permitted scientists to define basic science-engineering requirements for future lunar exploration systems: these include full lunar access, long stay times, extended surface mobility, enhanced downmass and upmass, robotic network development, communications and exploration infrastructure (communication and GPS spacecraft), orbital assets, and a mix of optimized human and robotic exploration. Furthermore, these results have clarified the focus and legacy of lunar exploration: The long-term goal is to derive an understanding of how to live and survive, and where to go, in the habitable zone of our own Solar System. On the basis of lunar exploration to date, we now know *where* to go and *what* to do to accomplish these objectives, starting with the Earth's Moon. Examples include:

1) In-Depth Exploration: Target more extensive exploration around existing exploration sites (e.g., the Apollo 15 Hadley-Apennine Landing Site) to address the new questions raised by analysis of initial data collected on Apollo 15 (Figures 4-8); What is the history of the lunar magnetic field recorded in the rille wall basalt layers? What is the source of the water-rich green pyroclastic glasses? What is the diversity of deep crustal rock types, as revealed by the 15415 anorthosite? What is the nature of the layering revealed in the Apennine Mountains Silver Spur? What is the distribution and variety of Imbrium basin ejecta as seen in the ancient 15455 shocked norite? What is the diversity of ages and compositions of the mare basalts exposed in the rille walls?

2) New Exploration Destinations: Target new sites such as the polar regions, and the floor and central peaks of Theophilus and Copernicus and ask new questions: What is the distribution and nature of shocked and unshocked rocks in central peaks? What is the distribution and origin of olivine-rich rocks in central peaks? What is the mode of occurrence and origin of spinel-rich lithologies? What is the relationships and relative abundances of shocked and unshocked anorthosite in central peaks? What does the chilled boundary layer of a melt sheet look like and how different is it from more slowly cooling melt below? How diverse are impact melt compositions and how much vertical segregation (differentiation?) is observed?

Science and Engineering Synergism: Design Reference Missions: Definition of engineering requirements is insufficient in itself for success; scientists must work hard to engage engineers in understanding their needs (and vice versa) and developing science and engineering synergism (SES) where mutual bottom-up interactions and education lead to optimized plans and exploration results. A very productive way to develop SES is in the combination of scientific goals and engineering reality in Science Design Reference Missions (DRM).

Conclusions: These types of scientific questions and Science Design Reference Missions can take advantage of 40 years of technology and operations development since the very successful Soviet and United States exploration missions to formulate new and enhanced exploration concepts. These new developments permit Lunar Human Exploration DRMs that produce longer stay times, more diverse mobility options, increased mobility and exploration radius, significantly more downmass and upmass, improved robotics to free up astronaut time for human exploration optimization, and full lunar access. We review several of these DRMs to underline this new generation of lunar exploration capabilities, and show how a program of integrated human and robotic exploration using our combined experience, can lead to fundamental new insights into living and surviving in the habitable zone for the upcoming millennia.

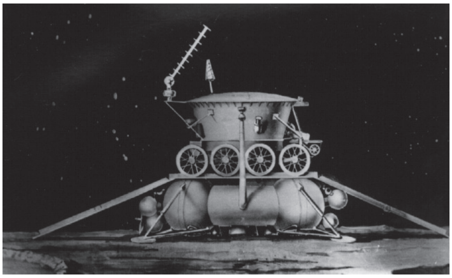

fig. 1. Soviet Lunokhod on descent stage.

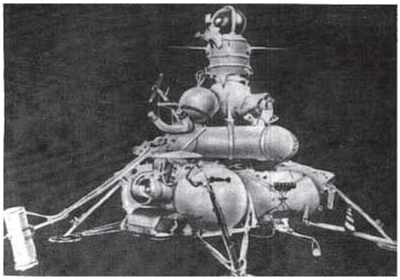

fig. 2. Soviet Luna sample return vehicle.

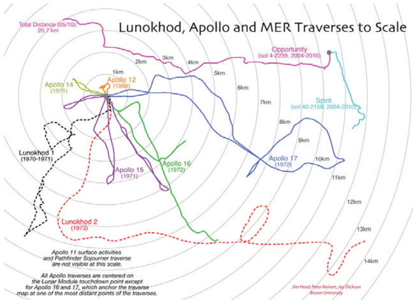

fig. 3. Combined lunar surface traverses compared to Mars rover traverses.

fig. 4. Apollo 15: Collecting rock samples at the edge of Hadley Rille.

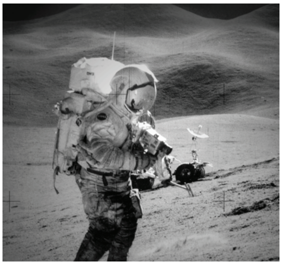

fig. 5. Apollo1 15: Documenting rock samples on Mount Hadley Delta. Note Lunar Roving Vehicle in the background.

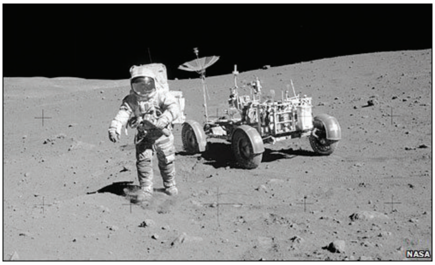

fig. 6. Apollo 15: Heading to the edge of Hadley Rille with the 500 mm telescopic lens to image layering in the far side of Hadley Rille.

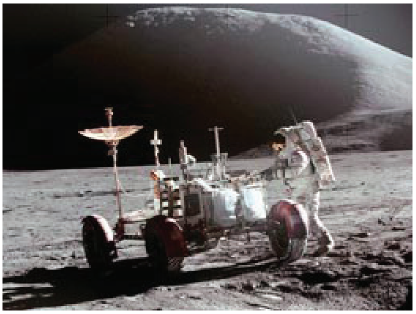

fig. 7. Apollo 15: Loading up the LRV for scientific exploration. Mount Hadley in the background.

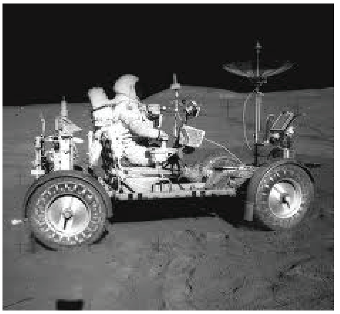

fig. 8. Apollo 15: Ready to explore the plains of Hadley with the Lunar Roving Vehicle. Note geologic traverse map just in front of steering column.

STUDY OF VENUS BY SPACE MISSIONS: FROM VENERA-4 TO VENERA-D

Zasova L.V.,
Space Research Institute, Russian Academy of Sciences, lzasova@gmail.com

Venus was often called “Russian Planet” due to series of highly successful space missions to this planet between 1965 and 1985 yrs. The Soviet Venera program remains one of the largest efforts ever undertaken to study another planet.

Ten probes from the Venera series successfully transmitted data from the Venus’ surface. In addition, thirteen Venera probes successfully transmitted scientific data from the atmosphere of Venus. The first time in a history the man-made device reached the surface of Venus (Venera-3, crashed), measured its atmosphere (Venera-4), the first time the soft landing was realized on the surface of another planet (Venera-7), and the first images of the Venus surface were obtained (Venera-9) and transmitted to Earth. High resolution radar mapping was also first carried out by Venera probe (Venera15-16). The Venera 13 mission keeps the record of survival time (127 min) at the extreme environment conditions of the planet. Another unique project is VEGA with balloons floating in the cloud layer of Venus. A basic Venera design used for all probes had largely ensured the success of the missions. Many scientific findings obtained from the data retrieved by the Venera probes keep their topicality even at the present time being a benchmark for future Venusian’ projects. Venera-D, the first of them, will continue to study Venus at a new level with modern scientific instruments, using the experience of the successful Soviet missions in the design of delivery vehicles, especially the Lander.

MARS EXPLORATION AT THE TURN OF THE CENTURY

Oleg Korablev,
Space Research Institute (IKI), Moscow, Russia. Contact: korab@iki.rssi.ru

Flights to Mars at the dawn of the space era have been combined with the development of new rockets and spaceships. In 1960-1973 Soviet Union has pursued 18 Mars launches, achieved two pioneering landings, and three partially successful orbiters. NASA score of that period was three successful fly-bys, and one long-living orbiter out of six launches aiming Mars. The first data characterizing the planet and the conditions of the surface were collected.

In the following the USSR efforts in planetary exploration were concentrated on Venus while USA completed the most successful Mars mission of the century: the Viking programme (1975-1982), which revolutionized our understanding of Mars. A combination of two landers and two orbiters, Viking delivered a wealth of global information about the planet and characterized its main climate cycles: CO_2, water, dust. However setting up the inaccessible goal of life detection, and the confusing results held further NASA exploration for 15 years. In the meanwhile the USSR prepared Phobos. The mission targeted the Mars satellite, but turned a successful Mars orbiter.

Post-Viking exploration of Mars was calling for a new level of science experiments, and both super-powers planned challenging missions: a comprehensive orbiter in the US and an unprecedented orbiter-rover-balloon-network mission in the USSR. Both efforts were a disaster. The most dramatic was Mars-96, the catastrophe, which in combination with structural change of the Russian society halted the in-country planetary exploration until recently. The most of Mars-96 orbital science survived thanks to Mars Express ESA recovery mission. The instruments of Mars Observer were launched one after another at a number of smaller orbiters in 1996-2005.

A present the Mars exploration is a massive endeavor. After Mars-96, 13 missions were launched, nine of them successful, all American, with the exception of Mars Express. A non-exhaustive list of science/exploration results is: the magnetic field (MGS); the figure, global altimetry (MGS); the climate cycles (MGS, Mars Express, etc.); subsurface water (Mars Odyssey); global cartography (Mars Express); global mineralogy (Mars Express, MRO); aquatic history (MERs, Mars Express, MRO); methane (Mars Express). At present, three orbiters and the Curiosity rover are operational on Mars.

In the talk I will try to touch the main milestones of Mars exploration balancing between the scientific results, technical and political aspects, with an emphasis on Soviet/Russian efforts, from early Mars-2 and Mars-3 to dramatic Phobos-Grunt. Russian involvement in ESA and NASA projects and joint ESA-Roscosmos ExoMars mission will be briefly described.

LUNAR EXPLORATION PROBLEMS.

V. V. Shevchenko,
Sternberg State Astronomical Institute, MSU, University prospect, 13, Moscow, 119992, Russia. Contact: vladislav_shevch@mail.ru

Introduction:

The space era of the Moon research provided such amount of new information about the Earth's natural satellite that exceeds all known of earth-based telescopic observations scores of times qualitatively and quantitatively. After an extended break, new data about the Moon are available now to science community. An international group of more complex missions received huge new data. New results were got by SMART-1 (ESA), SELENE/Kaguya (JAXA), Chang'e (CNSA), Chandrayaan-1 (ISRO), and LRO/LCROSS (NASA). It's now known that water and hydrated materials are currently widespread across the surface of the Moon, and some polar areas appear to be locations where hydrous materials are concentrated. Planetary scientists recognized that the large basins provide windows into early crustal processes.

South Pole – Aitken basin mystery:

The nature and origin of a unique formation, which is still conditionally called the South Pole – Aitken basin, remain one of the most important problems in recent studies of the Moon. The basin, which apparently belongs to the pre-Imbrian Period, is the largest ring formation not only on the lunar surface but also in the entire Solar System. Not only the basin dimensions on the absolute scale but also the fact that the basin diameter almost coincides with the lunar diameter are of interest. A similar relationship is not observed on other silicate or icy bodies in the Solar System.

Interplanetary matter on the Moon:

It is well-established that the flux of epithermal neutrons from the lunar surface with known soil composition in terms of constitutive elements depends on the hydrogen (H) content; specifically, with increasing H content the flux decreases rather sharply. The neutron emission of the lunar surface is known to be produced by the bombardment of galactic cosmic rays (GCR); energetic GCR particles produce secondary neutrons in the shallow subsurface that leak out from the surface after a random number of collisions with nuclei of constitutive elements in the soil. The energy spectrum of this neutron leakage flux depends on the efficiency of the moderation of neutrons from these collisions.

Hydrogen has been inferred to occur in enhanced concentrations within permanently shadowed regions and, hence, the coldest areas of the lunar poles. Neutron flux measurements of the Moon's south polar region from the Lunar Exploration Neutron Detector (LEND) on the Lunar Reconnaissance Orbiter (LRO) spacecraft were used for hydrogen mapping of the lunar south pole area. The final value corresponds to a water (as ice) content of ~4% by weight (Mitrofanov et al., 2010), which is in good agreement with independent estimates of the water content associated with the LCROSS Centaur impact site (Colaprete A. et al.).

The maximum total water vapor and water ice within the instrument field of view was 155 kilograms. Given the estimated total excavated mass of regolith that reached sunlight, and hence was observable, the concentration of water ice in the regolith at the LCROSS impact site is estimated to be 5.6 % by mass. In addition to water, spectral bands of a number of other volatile compounds were observed, including light hydrocarbons, sulfur-bearing species, and carbon dioxide (H_2S/H_2O, NH_3/H_2O, SO_2/H_2O, and CO/H_2O). Of interest is the indication from this preliminary analyses that some volatiles other than water are considerably more abundant (some by orders of magnitude) than the ratios found in comets, in the interstellar medium, or predicted from gas-gas reactions in the protoplanetary disk.

Current events on the Moon:

We know from practices of geology that rock material slides along a plane of structural weakness such as a bedding plane. Although they are most common on steep slopes, they can even occur on slopes of 15°. We can see such slopes from 10° to 20° on the Moon. On the Earth millions of tons of rock may plunge down slope at speeds greater than 160 km per hour in what is often the most catastrophic form of mass wasting. On Mars, similar slope failures are possibly caused by erosion from "running" water.

However, the lunar triggering mechanism of the down slope movement of the material remains unclear. It's needed to study many questions regarding the stability of natural lunar slopes else. Moreover, it's needed to note that resent studies show that new computer models simulating the creation of gullies on the surface of Mars suggest that they are in fact created by the flow of dry debris (i.e. landslides) and not by the flow of water (Kolb et al., 2010).

Now we resume one's lunar story. Debris avalanches are moving masses of rock and soil that occur when the border of the crater wall collapses and slides downslope. As the moving debris rushes down a crater, it incorporates rocks and soils. Debris avalanches may travel several kilometers before coming to rest.

Moon's Magnetism:

The study of the Moon's magnetism became practicable only using spacecraft. The first station to reach the Moon's surface – Luna-2 was launched on September 12, 1959. By readings of the station's instrumentation when approaching the Moon, it was discovered that the Moon's magnetic field having intensity within 50…100 gamm is absent (Keldysh., Marov, 1981*).* A three-component flux-gate magnetometer of the station performed measurements up to the altitude of 50 km above the Moon's surface. The subsequent analysis of the measurements showed that the Moon does not have the dipole magnetic moment that does not exceed, at least, 10^{-4} of the Earth's magnetic moment. These results were proved by measurements of the Luna-10 Moon's first artificial satellite launched in 1966. On altitudes of 350 km and over, disturbance effects and features of distribution of the magnetic field and the interplanetary plasma in the Moon's environment were explored in details. Based on the field topology observed, a conclusion was drawn that it has interplanetary nature taking into consideration the distortion by the Moon. Measurements of the residual magnetism intensity variations of the lunar rocks by means of the three-component flux-gate magnetometer, when the Lunokhod-2 self-propelled vehicle moved on the lunar surface, were of the particular interest. The magnetic survey was executed along the vehicle 30-kilometers rout with the purpose of detailed study of the local anomalies. The magnetic field in whole in the Le Monnier crater, where the measurements were executed, was weak and its intensity did not exceed 20…30 nT. However, the measurements discovered characteristic anomalies of 10…15 nT connected with craters having sizes of up to 50 m and over. At that, the magnetic field intensity increased with increase of the crater diameter crossed by the Lunokhod. That important result became the first experimental indication of possible impact nature of the magnetic anomalies on the Moon.

The next stage of study of the Moon's magnetic field was acquisition of data from subsatellites of the Apollo-15 and the Apollo-16 and Lunar Prospector magnetometric measurement results.

Moon's Gravity Field:

The external gravity field spatial structure, as a rule, is described by means of equipotential surfaces. In case of distribution uniformity of gravitating masses, the equipotential (daturence) surfaces are spherical, and the potential value depends just on remoteness of the current space point. Since real mass distribution in the Moon's body is not uniform, local excess or shortage of the material mass result in deformation of embedded equipotential surfaces modeling the system gravity field in the anomaly point environment.

Currently, the main method of study of the Moon's gravity field remains research of gravity disturbances of orbits of its artificial satellites. Grail mission — short for Gravity Recovery And Interior Laboratory — launched in September 2011. Ebb and Flow arrived at the moon about three months later, then raced around Earth's satellite in tandem, mapping out its gravity field in unprecedented detail. The probes' measurements have allowed scientists to create the best-ever gravity map of any celestial body, Grail scientists say. And that map is getting better all the time, as researchers continue to analyze the data Ebb and Flow gathered in their last weeks and months.

Meteoroid and Dust Components at Moon's Surface:

With no gas blanket on the Moon, even the smallest meteoroid particles reach the lunar surface causing intense erosion of surface strata. Estimated velocities of fall onto the lunar surface of impact particles are 13 to 18 km/s. According to evaluations of various authors, the total stream of solids falling onto the Moon is about $4 \cdot 10^{-16}$ g/cm^2·s taking into account objects with weight of 10^{-16} g (micrometeorites) to 10^{18} g (large meteorites and asteroids).

Summary:
There are probing Earth's nearest neighbor to build an understanding of the earliest events of planet evolution. On the other hand we known now that is possible to observe the nearest, current events on our "lifeless" celestial companion.

References:

Colaprete A. et al. Detection of water in the LCROSS ejecta plume // Science. 2010. V. 330 P. 463-468.
Kolb K.J., Pelletier J.D., McEwen A.S. Modeling the formation of bright slope deposits associated with gullies in Hale Crater, Mars: Implications for recent liquid water//Icarus. 2010. V. 205. P. 113–137
Keldysh M.V., Marov M.Ya. Space researches. Moscow, Nauka, 1981. 192 p. (in Russian)
Mitrofanov I. G. et al. Hydrogen mapping of the lunar south pole using the LRO Neutron Detector Experiment LEND // Science. 2010. V. 330 P. 483-486.

THE INTERIOR OF THE MOON: THERMODYNAMICS VS SEISMOLOGY

O.L. Kuskov, V.A. Kronrod, E.V. Kronrod,
Vernadsky Institute of Geochemistry and Analytical Chemistry, Moscow, Russia.
Contact: ol_kuskov@mail.ru

Introduction. To place constraints on the temperature distribution in the lunar mantle, we invert the Apollo P- and S-wave velocity models [1-4], making various assumptions regarding the lunar mantle composition. For the computation of phase equilibrium relations in the Na_2O-TiO_2-CaO-FeO-MgO-Al_2O_3-SiO_2 system, we have used a method of minimization of the total Gibbs free energy [5]. Our forward and inverse calculations include anharmonic and anelastic parameters [6].

Results. T_P and T_S inverted from the *P*- and *S*-wave velocity models for a Ca–Al-depleted Ol-bearing pyroxenite composition are shown in Figs. 1a,b and for a Ca–Al-enriched pyrolite in Figs. 1c,d (Table 1). At 50-100 km depth, $T_{P,S}$ for the pyrolite composition vary between ~700-1300°C; this is clearly unrealistic for the real rigid Moon. The T_P and T_S values calculated from G11 [4] agree with those from L05 [3] and GB06 [1] models only at depths greater than 200 km.

table 1. Bulk composition models (wt%) of the lunar mantle in the NaTiCFMAS system

Composition	1	2	3	4
MgO	32.0	37.58	34.1	37.0
FeO	11.6	8.48	10.05	12.8
Al_2O_3	2.25	4.50	6.4	2.6
CaO	1.8	3.64	5.1	2.5
SiO_2	52.0	45.25	44.0	45.1
Na_2O	0.05	0.34	0.05	0.0
TiO_2	0.3	0.21	0.3	0.0
Mg#	83.0	88.8	85.8	82-83

1- Olivine pyroxenite [6], 2 - pyrolite [6], 3 -Ol-Cpx-Gar [6], 4 - homogeneous composition [7]

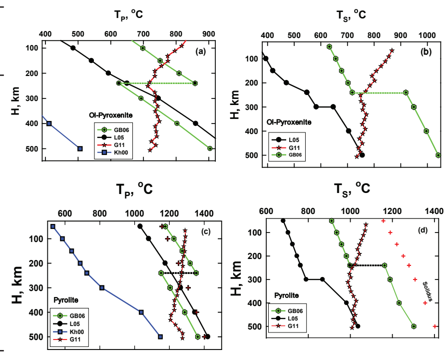

fig. 1. Comparison of the temperature profiles for the upper mantle of the Moon derived from the recent velocity estimates GB06 [1], Kh00 [2], L05 [3], G11 [4] for the Ol-pyroxenite and pyrolite compositions from Table 1. Crosses denote the peridotite solidus.

Our seismically derived T_P and T_S models are much colder than temperatures found by Keihm and Langseth [8]. We get the upper mantle heat flow value of 3.6 mW/m²,

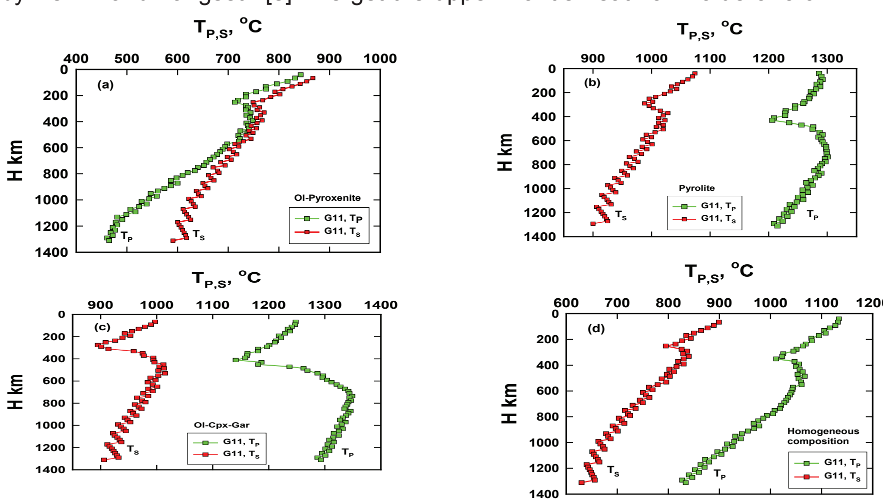

fig. 2. Comparison of *T* estimates for different compositions (Table 1) from the Moon model of Garcia et al. [4]. (a) - Ol-pyroxenite; (b) – pyrolite. (c) – Ol-Cpx-Gar, (d) - homogeneous mantle composition [7].

which is not consistent with heat fluxes in the range of 7-13 mW/m^2 [8]. Temperatures calculated from the very preliminary reference Moon model of Garcia et al. [4] for four different compositions are shown in Fig. 2. Very high T=800-1300^{o}C immediately below the crust are not consistent with the rigid lunar mantle. The large discrepancy between T_P and T_S may be attributed to an inconsistency between V_P and V_S.

Conclusions. (1) The results lend support to a chemically stratified lunar mantle with a change in composition from a dominantly pyroxenite upper mantle depleted in Ca and Al (~2 wt% CaO and Al_2O_3) to a dominantly fertile lower mantle enriched in Ca and Al (~4-6 wt% CaO and Al_2O_3) with larger amounts of olivine, clinopyroxene and garnet. (2) Disagreement between T_P and T_S can be attributed to inconsistency in the absolute velocities of seismic models. (3) Compositional effects play a dominant role in determining the lunar temperatures from seismic models. (4) Upper mantle heat flow is not consistent with that found in [8].

References

[1] Gagnepain-Beyneix, J. et al.: Phys. Earth Planet. Inter., Vol. 159, 140-166, 2006.
[2] Khan, A. et al. Geophys. Res. Lett. 27, 1591-1594, 2000.
[3] Lognonné, P.: Annu. Rev. Earth Planet. Sci., Vol. 33, 571–604, 2005.
[4] Garcia, R.F. et al. Phys. Earth Planet. Interiors, 188, 96-113, 2011.
[5] Kuskov, O.L. and Kronrod, V.A.: Phys. Earth Planet. Inter., Vol. 107, 285-306, 1998.
[6] Kuskov, O.L. and Kronrod, V.A.: Izv. Phys. Solid Earth, Vol. 45, 753–768, 2009.
[7] Khan, A., et al. Geophys. J. 168, 243–258, 2007.
[8] Keihm, S.J. and Langseth, M.G.: Proc. Lunar Sci. Conf. Vol. 8, 499-514, 1977.

SPINEL-ENSTATITE ASSOCIATION OF LUNAR METEORITES.

Nazarov M.A., Demidova S.I., Aranovich L.Ya.,
Vernadsky Institute of Geochemistry and Analytical Chemistry, RAS, Moscow,
Contact: nazarov@geokhi.ru

Rare fragments of Al-rich enstatite associated with Mg-rich spinel, anorthite, olivine were discovered in lunar highland meteorites. Accessory phases in the association are rutile, Ti,Zr oxides, troilite and Fe,Ni metal. The meteorites are impact-melt breccias of troctolitic composition. Similar paragenesis was described in so-called spinel cataclasites from a few Apollo samples. In composition Al-rich enstatites are very different from common orthopyroxenes of lunar highland rocks. They are very enriched in Al_2O_3 (up to 12 wt%), depleted in CaO (<1 wt%) and have a very high MG value (89.5±1.4 at%) which is similar to that of the terrestrial mantle. Thermobarometry and the analysis of phase equilibria showed that the rocks containing aluminous enstatite should be of deep origin and could occur at depths from 25 km to130–200 km at *T* from 800 to 1300°C, i.e., at least in the lower crust and, possibly, in the upper mantle of the Moon. The rocks could form individual plutons or dominate the composition of the lower crust. The most probable source of aluminous enstatite is troctolitic magnesian rocks. The decompression of such rocks must produce cordierite-bearing assemblages. The almost complete absence of such assemblages in the near-surface rocks of lunar highlands implies that vertical tectonic movements were practically absent in the lunar crust. The transport of deep-seated materials to the lunar surface was probably related to impact events during the intense meteorite bombardment >3.9 Ga ago. It can be suggested that the spinel-bearing lithologies detected by the M^3 mapping around Mare Moscoviense and other sites could be of deep origin.

ESTIMATION OF THE AGE OF IMPACT CRATERS ON THE MOON, MERCURY, MARS AND VENUS BASED ON THEIR MORPHOLOGY

A. T. Basilevsky,
Institute of Geochemistry and Analytical Chemistry, Russian Academy of Sciences, Kosygin Str., 19, 119991 Moscow, Russia; atbas@geokhi.ru

Introduction:

Impact craters are observed on and often dominate the surfaces of terrestrial planets, satellites and asteroids. This work is devoted to the problem of determination of the absolute ages of impact craters based on their morphologies. First, we describe our results on the estimation of the ages of small impact craters on the Moon achieved in the era of the the Apollo-Luna-Lunokhod missions. Then we consider the possibility of doing similar work for small craters on Mercury and Mars. And finally we consider the problem of estimating the absolute ages of large craters of Venus.

The Moon

Small impact craters (a few meters to 1-2 km in diameter) are dominant landforms on the lunar surface. They differ in morphology from prominent, with elevated rims, to subdued [e.g., 1] (Fig. 1). Among the craters of the same size, the prominent ones are the youngest while subdued craters are oldest [2].

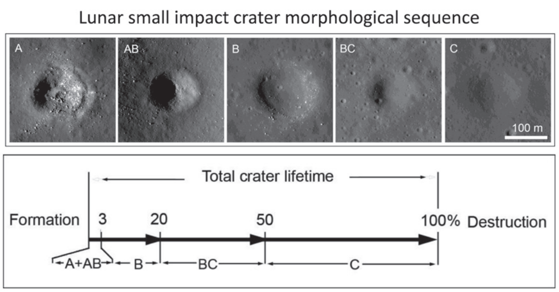

fig. 1. Classification of small impact craters of the Moon into morphological classes A, AB, B, BC and schematic representation of their evolution with time from A to C, and then to complete destruction.,

The relative youth of morphologically prominent craters of approximately the same size is proven by observations exemplified by Fig. 2a. It was also found that the smaller craters morphologically evolve faster than the larger ones (see Fig. 2b). Study of numerous intersections of craters of different morphologies and sizes led to the finding of the dependence of relative age versus crater morphologic class versus crater size, then calibrated by the examples of several isotopically dated craters at the Apollo landing sites (Figs 2c,d) and finally resulted in the interpretation of the dependence of absolute age versus morphologic class versus crater size (Fig. 2e). Now with LROC NAC-based DTMs available for wide areas of the Moon, the crater age-morphology-size dependence can be updated.

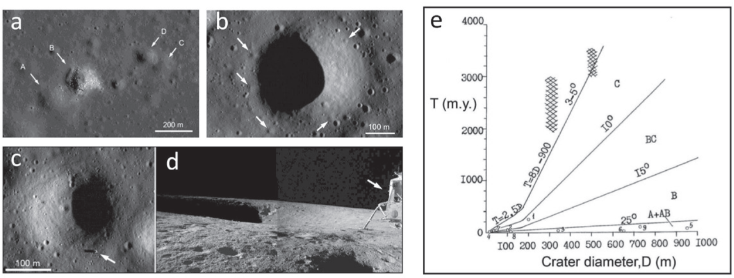

fig. 2. a) intersections of craters of the same size showing that morphologically prominent craters (B and D) are younger than subdued craters (A and C); the Luna 24 landing site. Part of LROC NAC image M119449091RE; b) the 400-m crater Spook at the Apollo 16 landing site; its morphology is transitional from class AB to B while some small craters superposed on its rim represent classes BC and C (arrows). Part of M102064759RC; c) the 200 m crater Surveyor at the Apollo 12 landing site; its absolute age is 200 Ma [e.g., 3]. Part of M117650516RE (arrow shows the landing module); d) the same crater as seen on the photos taken by the Apollo 12 astronauts; e) diagram showing estimates of the age of small lunar craters [2].

Mercury

Mercury like the Moon has no atmosphere, so its surface is also dominated by impact craters and the technique described above of estimating the ages of small lunar craters based on their morphological prominence (Fig. 3) and size seems potentially applicable to small craters on Mercury. Mercury surface gravity is 2.3 times higher than the Moon, it has a flux of impactors 5.5 times greater than the Moon,, and impacts occur at higher velocities there [4]. So craters on Mercury should have shorter lifetimes compared to those of lunar craters of the same size. To approach an estimation of the absolute ages it seems promising to study small impact craters in geologically homogeneous area(s) of Mercury dated by the crater count technique [e.g., 5].

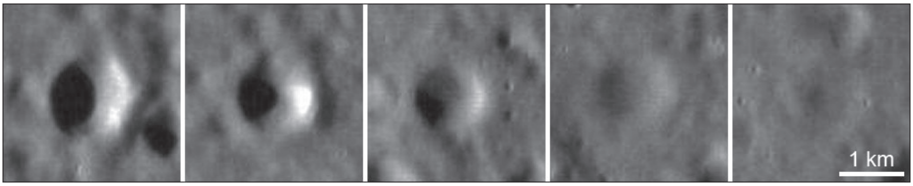

fig. 3. Morphologic sequence of small impact craters on Mercury similar to that of lunar craters (see Fig. 1). Parts of MESSENGER MDIS image 3302953, Lat 28.08° N, long 144.6° E.

Mars

Small craters on Mars also can be arranged in sequences of different morphological prominence obviously having a sense of relative age (Fig. 4). However, different areas of Mars significantly differ from each other in the characteristics of eolian, permafrost and other surface activities, each of which are also changing with time (e.g., 6, 7]; thus, working out the planet-wide dependence of relative/absolute age versus morphologic class versus crater size appears to be impossible, but regional models for certain geologic epochs seem to be achievable. Comparing MOC images of the same areas taken during 7 years of observations led to the discovery of 20 newly-formed craters [8]. Later analysis of HiRISE images extended the number of these very young impacts to 248 [9]. These very young craters have a dark halo (leftmost image in Fig. 4) that makes them readily visible on the images. The halo results from the blowing away of surface dust around the crater-forming event, so this phenomenon is observed mostly in the “dusty” areas of Mars. These observations made it possible to test the calibration curve for small crater formation on Mars [e.g., 10]. The lifetime of the crater dark haloes seems to be of the order of a few years (see e.g., http://www.uahirise.org/images/2012/details/cut/ESP_027806_1700.jpg).

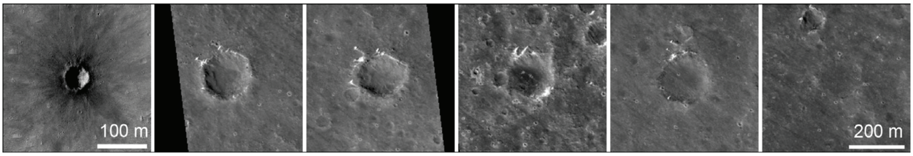

fig. 4. Morphologic sequence of small impact craters on Mars. The leftmost is part of image ESP_011425_1775, and others are parts of image ESP_031816_1835. Lat 3.296o N, Long 138.81o E.

Venus

Venus has a dense atmosphere so impact craters only larger than several kilometers in diameter can be formed on its surface. They are seen on radar images and analysis of the Magellan SAR images discovered specific features associated with them that are indicative of their age. These are radar dark haloes whose shape and prominence (Fig. 5) are indicative of their age [e.g., 11, 12].

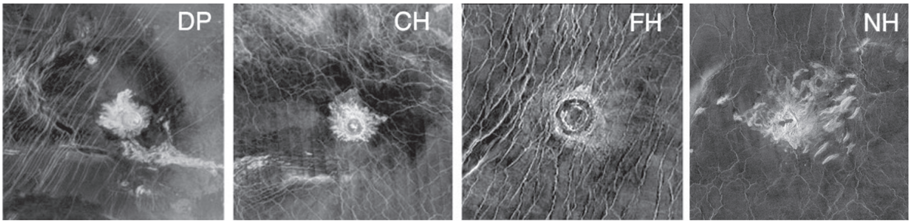

DP crater Stuart, 69 km CH crater Caccini, 38 km FH crater Barrymore, 57 km NH crater Boyd, 22 km

fig. 5. Morphologic classes of Venusian craters: DP, with dark parabola; CH, with clear halo; FH, with faint halo; NH, with no halo.

For craters ≥30 km in diameter it was shown that the DP craters have an age of <0.1-0.15T, CH craters - 0.1-0.15T to ~0.5T, FH and NH - >0.5T, where T is the mean age of the surface of Venus, which is 0.5-1 Ga [12]. Analysis of quantitative radiophysical data for Venusian craters will make this conclusion more accurate and lead to the analysis of craters of smaller sizes.

Acknowledgments: Help of J.Head, B.Ivanov and M. Kreslavsky in preparation of this work is appreciated.

References: [1] Florensky et al. (1972) In: Modern concepts on the Moon, M. Nauka 21-45; [2] Basilevsky (1976) Proc. Lunar Sci. Conf. 7th, 1005-1020; [3] Waenke et al. (1971) Proc. Lunar Sci. Conf. 2nd, 1187-1208; [4] Cintala, (1992) JGR, 97, E1, 947-973; [5] Marchi et al. (2013) Nature, 499, 59-61; [6] Kreslavsky (2009) LPSC-40, abs. 2311; [7] Kreslavsky et al. (2010) LPSC-41, abs. 2560; [8] Malin et al. (2006) Science, 314, 1573-1577; [9] Daubar et al. (2013) Icarus, 225, 506-516; [10] Neukum et al. (2001) Space Sci. Rev., 96, 55-86; [11] Arvidson et al. (1992) JGR, 97, 13303-13317; [12] Basilevsky & Head (2002) JGR, 107, E8, 5061.

CONSTRUCTION OF MARTIAN SEISMIC MODELS. 1. EFFECTS OF TEMPERATURE, ANELASTICITY AND HYDRATION.

V.N. Zharkov, T. Gudkova,
Schmidt Institute of Physics of the Earth, B.Gruzinskaya 10, Moscow 123995, Russia. Contact: zharkov@ifz.ru

Introduction:

Recently several seismic models of Mars have been published [1-5]. Our analysis is based on a four-layer model M7_4 [3], for which all the effects of studied model parameters are considered. This model is based on a geochemical DW model [6]. It consists of a two-layer crust, a mantle and a core. The composition of the crust is derived from the basalts of SNC meteorites and its mineralogy and seismic properties are determined thermodynamically [7]. Crustal thickness is taken to be 50 km. Mantle mineralogy and physical properties are based on the experimental study of [8], where high-pressure experiments are performed on the DW model composition. For M7_4 model [3]: a variable mantle parameter Fe content (Fe/(Fe+Mg) ratio) is 0.22, the Fe-Ni core contains 70 mol % H in addition to 14 wt % S with radius of 1775 km and the bulk Fe/Si ratio is close to chondritic.

In two-component DW model, oxidized component B (40%) contains up to 20 wt % H_2O. Important character of Mars is that under its formation a lot amount of water could be incorporated into the planet. Below we discuss how the admixture of water influences the main minerals (olivine, wadsleite, ringwoodite) of the Martian mantle

Temperature profile:

The problem of temperature distribution (temperature gradient) in the crust of Mars was examined in [7]. The thermal flux is in the range from 30 to 45 erg/cm^2 s, and the mean heat-conductivity coefficient is 2.5 x 10^5 erg/(cm s K). The external layers of the planet have a regional structure. Four trial temperature gradients in the crust 2, 6, 13.5 and 21 K/km were considered. Basaltic models of the crust were determined thermodynamically, while the composition of the crust was derived from four SNC meteorites [7]. The distribution of density and seismic velocities in the crust (Fig. 1) were obtained by numerical modeling. The important point is the presence of reduced velocities zone in the crust when temperature gradient is more then 6 K/km. By analogy with the lunar porous crust, in [7] two-layer seismic model of a porous layer was constructed, in order to smooth the fall of velocity when moving to a consolidated crust.

Whereas the distribution of pressure in Martian interiors is quite reliable, the temperature distribution suffers from the lack of data. This problem was discussed in the publications cited above. At the moment, the line 1 and 2 in the Fig.2 are considered as an upper and a lower limits of the temperature profile in Mars. They correspond to a conductive lid model of Mars. At present it is not clear if a convective regime takes place in the lower part of the silicate mantle extended up to the core. Figure 2 shows two adiabatic curves (line 1 and 2), starting at different depths. Adiabatic gradient in the mantle is about 0.12 K/km. The core of Mars is liquid.

However, the melting temperature can be noticeably reduced due to the presence of substantial amount of the admixture of light elements in the core, as hydrogen for example [3]. In the core the temperature profile is adiabatic.

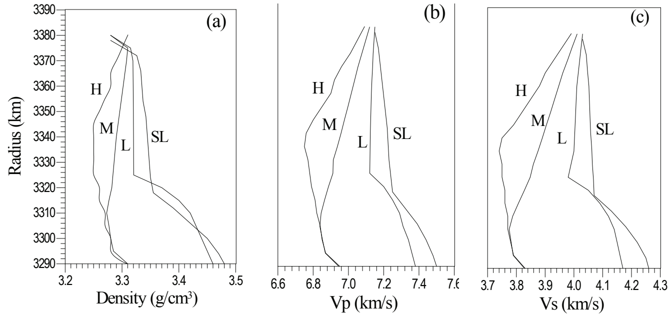

fig.1. Density and velocity profiles of the crust for four different marsotherms tian H (21K/km), M (13 K/km), L (6K/km) and SL (2K/km) corresponding to effective kinetic “freezing”temperature Tf of 8000C. The figure starts at 10 km depth. The data are taken from [7]

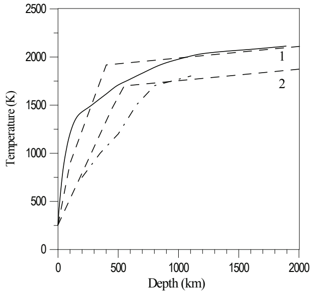

fig. 2. Temperature profiles for Marinteriors as function of the depth. Solid line [3], dashed lines; 1- hot and 2 – cold profiles from [1], dot- dashed line [9].

Dissipative factor:

Based on the data of the secular acceleration of Phobos, the dissipative factor of Mars $Q\mu$ is estimated to be 150-200. Because anelasticity, to use both the data on free oscillations and body waves, it is necessary to introduce a correction of about 5-10 s to travel times of body waves.

Concentration of water:

At present in the geophysics of the Earth, scientists highlight to the study of an effect of water traces in mantle minerals on physical properties of Earth's interiors [10]. It turned out, that olivine can accumulate up to 1 wt % of water, wadesleite – up to 2 wt % of water and ringwoodite up to 1 wt % of water [11-13]. Molecular concentration of Fe in Martian silicates is 2 times higher than in terrestrial minerals. This fact means that, in principle, Martian minerals could accumulate larger amount of water. Below, based on the data from [11-15], we make an attempt to evaluate the effect of trial concentrations of water in olivine, wadsleite and ringwoodite on seismic velocities under conditions of Martian interiors, These partial data were extrapolated, in order to take into account twofold increase of Fe in Martian silicates in comparison with the terrestrial minerals. P-T conditions in Martian mantle were assumed approximately the same as for terrestrial ones. The results are shown in Figs. 3-5.

Acknowledgements: This work was supported by Grant No. 12-02-00378 from the Russian Fund for Fundamental Research.

References: [1] Verhoeven, O. et al. (2005) J.Geophys.Res. 110, E04009, doi: 10.1029/2004JE002271. [2] Khan, A., and Connolly, A.D. (2008), J.Geophys.Res. 113, E077003, doi: 10.1029/2007JE002996. [3] Zharkov, V.N. et al. (2009) Phys.Earth Planet.Int, 172, 324-334. [4] Rivoldini, A. et al. (2011) Icrus.213.451-472. [5] Dehant, V. et al. (2012) Planet.Space Sci., doi:10.1016/j.pss.2011.10.016. [6] Dreibus,G., and Wänke, H. (1985) Meteoritics, 20, 367-381.[7] Babeiko, A.Yu. and Zharkov, V.N. (2000) Phys.Earth Planet.Inter. 117. 421-440.[8] Bertka, C. and Fei, Y. (1997) J. Geophys. Res. 102, 5251-5264. [9] Konopliv, A.S. et al. (2011) Icarus, 211, 401-428. [10] Zharkov, V.N. (2012) Physics of terrestrial interiors, 384 pp. (in Russian). [11] Mao, Z. et al. (2010) Earth Planet. Sci. Lett..293. 250-258. [12] Mao, Z. et al. (2011) Amer. Miner, 96. 1606-1612. [13] Mao, Z. et al. (2012) Earth Planet. Sci. Lett..331-332. 112-119. [14] Zha, C.S. et al. (1997) Earth Planet. Sci. Lett. 147. E9-E15. [15] Liu, W. et al. (2009) Phys. Earth Planet.Int. 174.98-104.

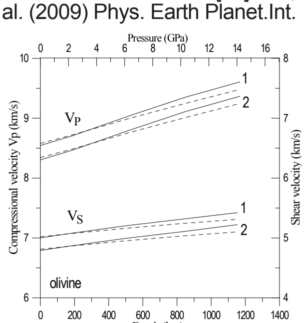

fig. 3. Aggregate compressional VP and shear VS velocities of forsterite (1) and olivine (2) as a function of pressure at 300 K. (1) dotted line – dry; solid – measured data for forsterite with 0.9 wt % H2O,. (2) dotted line – dry; solid – extrapolated data for olivine with 0.9 wt % H2O.

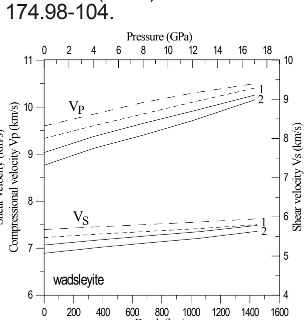

fig. 4. Effect of hydration and Fe on the sound velocities of wadsleite with pressure. Dashed line - Mg2SiO4, wadsleite [14], dotted line = (Mg0.87Fe0.13)2SiO4 wadsleite [15], showing the effect of Fe; solid line - Fe-bearing wadsleite (Fe content 0.1) with 1.93 wt % H20 [12], showing the net effect of Fe and hydration (1), extrapolation for Fe-bearing wadsleite (Fe content 0.2) with 1.93 wt % H20 – solid line (2).

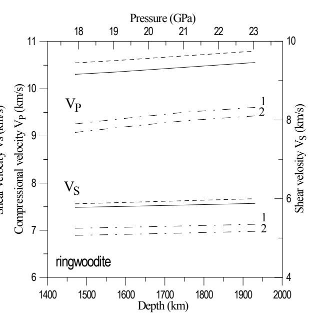

fig. 5. Modeled Vp and Vs of ringwoodite. Dotted line: anhydrouse ringwoodite at 300 K [15]; solid line : ringwoodite with 1.1 wt % H2O at 300K [13] and along the 1400 C mantle geotherm (dot-dashed, 1). Extrapolated data for ringwoodite with 1.1 wt % H2O - Fo80 (Fe content 0.2) dot-dashed line (2) along the 1400 C mantle geotherm.

DEVELOPMENT OF SPACE RESEARCH METHODS IN THE KELDYSH INSTITUTE OF APPLIED MATHEMATICS

Yu. F. Golubev,
Keldysh Institute of Applied Mathematics, Contact: golubev@keldysh.ru

The subject of the report is related to the 60th anniversary of the establishment of the Keldysh Institute of Applied Mathematics. The content of the report is limited to a history of work in this institute associated with the development of space flight practices. The department of the space flight dynamics was created in 1953 on the basis of D.E. Okhotsimskii's group, which was part of the department governed by M.V. Keldysh in the Steklov Institute of Mathematics. In those days this group focused on resolving the difficulties of optimization of rocket flight. The department of space flight dynamics was consequently developed quite harmoniously along with the times of practical space exploration thanks to the productive cooperation between M.V. Keldysh and S.P. Koroliev.

TO THEORY OF VORTICAL DYNAMO IN ASTROPHYSICAL DISK WITH A GYROTROPIC TURBULENCE

A.V. Kolesnichenko,
M.V. Keldysh Institute of Applied Mathematics, RAS, Moscow.
Contact: kolesn@keldysh ru

Introduction:

The problem of formation large and mesoscale coherent vortex structures in a gyrotropic turbulence of the rotaried non-magnetic astrophysical disk surveyed, which one did not yield earlier to examination, as the action of an inverse stage of energy on changes of aircraft attitude of a turbulence of this space object was leave outed. The proposed phenomenological theory of a disk mirror - asymmetrical turbulence has filled a gap due to insert in model of the mechanism vortex dynamo, accountable (at suitable definition of a tensor of shift turbulent stresses of Reynolds) for energy flow from shallow vortexes to large, which one can be interpreted as effect of negative viscosity. The insert of this device in model of a gyrotropic turbulence gives in modification of rheological relations for a turbulent flow of heat and tensor of turbulent stresses, and also to some number of the padding developmental equations for quantities such as turbulent energy, velocity of a dissipation, average vorticity and average vortex helicity. The role of a vortex helicity in origin of an inverse energy stage and bound with it process of oscillation of power-intensive coherent vortex formations incipient in a gyrotropic turbulence at major Reynolds numbers is considered. Is drawn a conclusion, that on a measure of more and more reliable endorsement in numerical experiments of the concept of an inverse stage of energy in a three-dimensional gyrotropic turbulence, registration of effect vortical dynamo, influential on synergetic structuring of space matter in the astrophysical non-magneticdisc, gains the relevant role at its model operation.

ASTROCHEMISTRY OF THE ATMOSPHERE-ICY SURFACE INTERFACE FOR ASTROPHYSICAL OBJECTS.

V. I. Shematovich,
Institute of Astronomy RAS, 48 Pyatnitskaya str., Moscow 119017, Russian Federation. Contact: shematov@inasan.ru

Introduction:

Many astrophysical objects are surrounded by gaseous envelopes. Chemical evolution of the gaseous envelopes of icy astrophysical objects of different masses and sizes (dust particles with icy mantles, icy planetesimals, comets, icy satellites in the Jovian and Saturnian systems, etc.) is determined by the complex influence of a large number of interrelated processes including catalysis on the icy surface of the objects, chemical exchange of the matter between the surface and gas fractions, and chemical changes in the gas composition of the envelope. These chemical processes are initialed by the extreme UV radiation field of either the interstellar medium, or a star, or a star with a planetary system, and characterized by strongly differing time scales and the degrees of non-equilibrium.

Theoretical predictions of the composition and chemical evolution of near-surface atmospheres of the icy astrophysical objects are of great importance for assessing the biological potential of these objects [1]. The water vapour is usually the dominant parent species in such gaseous envelope because of the ejection from the object’s icy surface due to the thermal outgassing, non-thermal photolysis and radiolysis and other active processes at work on the surface. The photochemistry of water vapour in the near-surface atmospheric layer [2] and the radiolysis of icy regolith result in the supplement of the atmosphere by an admixture of H_2, O_2, OH and O. Returning molecules have species-dependent behaviour on impact with icy surface and nonthermal energy distributions for the chemical radicals. The H_2 and O_2 molecules stick with very low efficiency and immediately desorb thermally, but returning H_2O, OH, H and O stick to the grains in the icy regolith with unit efficiency. The suprathermal radicals OH, H, and O entering the regolith can drive radiolytic chemistry.

Chemical complexity of the near-surface atmosphere of the icy astrophysical object arises due to both primary processes of dissociation and ionization by solar/stellar UV radiation and magnetospheric electrons and induced ion-molecular chemistry, and by chemical exchange between near-surface atmospheric layer and the satellite icy surface due to the thermal and non-thermal desorption processes [2]. The standard astrochemical UDFA05 network is usually used to follow the main chemical pathways of photochemistry in the near-surface atmosphere and of diffusive chemistry in the icy regolith.

Achievements and problems of astrochemical kinetics for the atmosphere-icy surface interface with taking into account of both simple and complex networks of chemical reactions characterizing the chemistry of the production of complex molecules are discussed.

This work is supported by the RFBR project No. 11-02-00479a and by the Basic Research Program of the Presidium of the Russian Academy of Sciences (Program 22).

References

[1] Shematovich, V.I. (2012) *Solar System Research,* **46**, 391-407.
[2] Shematovich, V.I. (2008) *Solar System Research*, **42**, 473-487.

SIMULATION OF THE INTERACTION BETWEEN THE EXOPLANET WASP-12B AND ITS HOST STAR

D.V. Bisikalo, *Institute of Astronomy, Russian Academy of Sciences, Moscow, Russia. Contact: bisikalo@inasan.rssi.ru*

Introduction:

WASP-12b is an exoplanet with parameters typical for the so called "hot Jupiters'". However, transit observations, performed in 2009 with COS on board of HST, made it one of the most "mysterious" exoplanet. Indeed, the observations in near-UV showed an early-ingress that, allowing one to assume the presence of optically thick matter located ahead of the planet at a distance of 4-5 planet radii. Any attempts to explain this asymmetry by drawing an outflow of the atmosphere or bow shock, occurring due to the proper magnetic field of the planet, is not able to provide a flow structure which fully corresponds to the observations. Analyzing the results of the 3D gas dynamic simulations of the interaction between WASP-12b and its host star we first managed to obtain a non-controversial flow pattern in this system. In particular it has been shown that the overfilling of the planet Roche lobe leads to the noticeable outflow of the atmosphere in the direction of the L_1 and L_2 points. Due to the conservation of the angular momentum, the flow to the L_1 point is deflected in the direction of the orbital motion of the planet, the flow towards L_2 is deflected in the opposite direction. As a result a non-axisymmetric envelope, surrounding the planet, occurs. The supersonic motion of the planet and its envelope in the gas of the stellar wind leads to the formation of a bow shock, with a complex shape. The existence of the bow shock breaks the outflow through the L_1 and L_2 points and allows us to consider the resulting flow structure to be steady-state and long-living. The parameters of the envelope, obtained as a result of the simulations, correspond to those determined from the observations.

COSMOCHEMICAL RESTRICTIONS ON MODELS OF EVOLUTION OF OUTER SOLAR NEBULA.

V.A. Dorofeeva,
Vernadsky Institute of Geochemistry and Analytical Chemistry, RAS, Moscow.
Contact: dorofeeva@geokhi.ru, venus@umail.ru

Introduction:

During 2005-2012 with help *"Cassini-Huygens"* detailed studying satellite and ring system of Saturn was carried out. Among other results the quantitative data on component, phase and isotope structure of an atmosphere of the Titan, water plumes, open on Enceladus, chemical composition of the main rings A and B were in detail analyzed. The received information in aggregate with the data on structure of atmospheres of the Jupiter and Saturn, substance of comets and parent bodies carbon hondrites allows to reveal system cosmochemical restrictions on models of evolution of matter in the outer solar nebula.

ON TEMPLE 1 COMET’S NUCLEI SURFACE

L. V. Ksanfomality[1],
[1]Space Research Institute, 84/32 Profsoyuznaya str., Moscow 117997, Russia.
Contact: ksanf@rssi.ru

The surface of the nuclei of comet Temple 1 has traces of massive outpourings and displacement of liquid or semi-liquid mass, similar to mudflows. The effusions products solidified and cover a significant part of the nuclei. The center of semi-liquid mass propogation could conceivably be a deep impact crater of relatively small size (tens of kilometers). Based on a comparison of images of the comet Temple 1 nuclei obtained by space missions, an attempt has been made to estimate the total volume of effusions and the corresponding energy released during the formation of an impact crater.

MATHEMATICAL MODELING OF PULSED LASER IMPACT ON SMALL SPACE OBJECTS.

V. I. Mazhukin,
Keldysh Institute for Applied Mathematics of RAS , Miusskaya sq.4, Moscow, Russia.
Contact: vim@modhef.ru

We investigate the problem of generation of recoil momentum at pulsed laser action on condensed media in order to use them to change the orbit of small debris objects. The research is conducted on the basis of numerical solutions of nonstationary two-dimensional axisymmetric radiation gas dynamics problem, which describes the dynamics of the plasma torch formed under the influence of laser pulses with a wavelength of 0.3 ÷ 1.06 μ m, duration of 10 ÷ 100 ns, intensity of $5\times10^{7}\div 10^{9}$ W cm^{-2} and radius of the focal spot of r = r0 [1]. Mathematical modeling also includes a solution of two-dimensional nonstationary problem of laser heating and evaporation of the metal (aluminum) target, Fig.1.

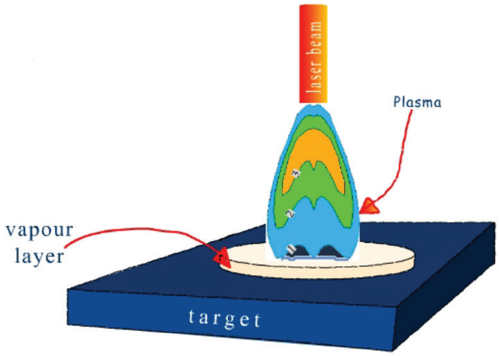

fig. 1. Plasma expansion

The simulation showed that the maximum pressure on the irradiated surface of the target in subplasma modes of evaporation does not exceed 150 bar. Plasma formation in the evaporated material radically changes the picture of the near-surface processes. Dense plasma bunch is characterized by high values of temperature 3 ÷ 15 eV and pressure (0.5 ÷ 5) 103 bar. Typical profiles of the plasma torch is shown in Figure 2.

The pressure in the center of the plasma torch r <r0 may significantly exceed the pressure of saturated vapor, that causes the reversal of vaporized material flow in the opposite direction. On the hot surface of the target in the area r < r0 begins the process of condensation of previously evaporated substance, while in r ≥ r0 continues surface evaporation [2]. The average pressure on the surface of the target undergoing laser - plasma action reaches values of (1 ÷ 2) 103 bar, which is about an order of magnitude higher than the recoil pressure due to surface evaporation.

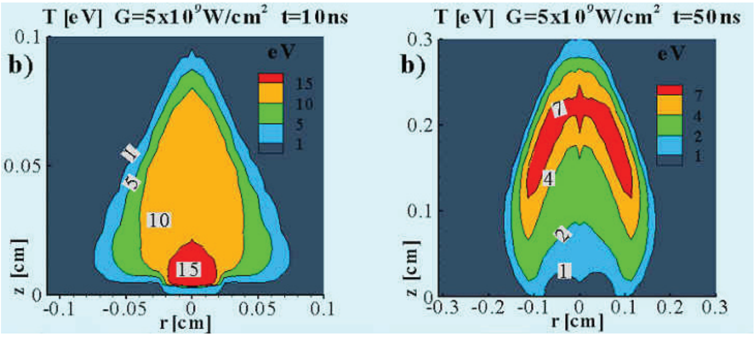

fig. 2. The spatial distribution of thermal fields in the plasma torch.

The methods of optimizing the recoil momentum as a function of wavelength, intensity, and spatial and temporal distribution of energy in the laser pulse are discussed.

References

V.I.Mazhukin, V.V.Nossov, I.Smurov. Modeling of plasma-controlled surface evaporation and condensation of Al target under pulsed laser irradiation in the nanosecond regime. Applied Surface Science, 2007, vol. 253, pp. 7686 – 7691.
V.I.Mazhukin, V.V.Nossov, I.Smurov. Modeling of plasma-controlled evaporation and surface condensation of Al induced de 1.06 and 0.248 μm laser radiations. *J. Applied Physics*, 2007, vol. 101, Issue 2, pp.24922 – 24937.

RESONANCES IN THE SOLAR AND EXOPLANETARY SYSTEMS

I.I.Shevchenko
Pulkovo Observatory of the Russian Academy of Sciences

Resonances, interaction of resonances, and the chaotic behaviour, caused by this interaction, play an essential role in the dynamics of bodies of the Solar and exoplanetary systems. In the Solar system dynamics, some approximate commensurabilities of the orbital periods of planets are well-known: Jupiter-Saturn (the ratio of orbital frequencies ≈ 5/2), Saturn-Uranus (≈ 3/1), Uranus-Neptune (≈ 2/1); not to mention the Neptune-Pluto resonance (3/2). At the end of eighties, Sussman and Wisdom (1988, 1992) and Laskar (1989) made first estimates of the Lyapunov time of the Solar planetary system in numerical experiments. It turned out to be not at all infinite, i.e., the motion of the Solar system is not regular; moreover, its Lyapunov time is three orders less than its age. Murray and Holman (1999) conjectured that the revealed chaos is due to interaction of subresonances in a multiplet corresponding to a particular three-body resonance Jupiter-Saturn-Uranus.

The orbital resonances in celestial-mechanical systems subdivide in mean motion resonances and secular resonances. The first class represents commensurabilities between mean orbital frequencies (of two or even a greater number of orbiting bodies), and the second one represents commensurabilities between orbital precession frequencies. Both kinds often manifest itself in the dynamics of exoplanetary systems. Moreover, resonances determine, in many respects, the observed modern architecture of exoplanetary systems. An increasing attention of researchers is attracted as well by the Lidov-Kozai resonance, which can be regarded as a resonance 1:1 between the frequencies of precession of the pericenter and node longitudes of a perturbed body (Morbidelli, 2002), and which manifests itself when inclination of the orbit is high enough.

Apart from the well-known two-body mean motion resonances, three-body mean motion resonances are often important. In this case, the resonant phase is a combination of angular orbital elements of three bodies. The three-body resonances were investigated in the dynamics of asteroids (Murray et al., 1998; Nesvorný and Morbidelli, 1998, 1999; Smirnov and Shevchenko, 2013) and in the dynamics of major planets of the Solar system (Murray and Holman, 1999; Hayes et al., 2010). With the number of discovered exosystems increasing, the studies of three-body resonances have been extended to exoplanetary systems (Quillen, 2011).

In the Solar system, many planetary satellites form resonant or close-to-resonant configurations. In the Jovian satellite system, the Galilean satellites Io and Europa, as well as Europa and Ganymede, are in the 2/1 mean motion resonance; thus the system of these three satellites is involved in the three-body resonance 4:2:1 (called the Laplace resonance). In the Saturnian system, Mimas and Tethys, as well as Enceladus and Dione, are in the 2/1 mean motion resonance, Dione and Rhea are close to resonance 5/3, Titan and Hyperion are in the 4/3 resonance. In the Uranian system, all resonances are approximate: Miranda and Umbriel are close to resonance 3/1, Ariel and Umbriel — 5/3, Umbriel and Titania — 2/1, Titania and Oberon — 3/2. Captures of satellite systems in orbital resonances are natural stages of tidal evolution of these celestial-mechanical systems. Of particular interest is that the motion of the Prometheus-Pandora system (the 16th and 17th Saturnian satellites — the shepherd satellites of the ring F) is chaotic, as follows from both observation and theory. The Lyapunov time of this system, which resides in the mean motion resonance 121/118, was estimated both in numerical experiments and analytically; it turned out to be only ≈ 3 yr (Goldreich and Rappaport, 2003; Shevchenko, 2008).

Orbital resonances are no less ubiquitous in planetary exosystems, as confirmed in computations of the behaviour of resonant arguments. For many systems, the observational data on planetary orbital elements still suffer uncertainties; however, the occurrence of low-order resonances (such as 2/1 and 3/2) is statistically significant (Wright et al., 2011; Fabrycky et al., 2012), especially in pairs of planets with similar masses (Ferraz-Mello et al., 2006). The presence of mean motion resonances and their interaction implies an opportunity of manifestation of chaotic behaviour in the dynamics of exoplanets, as, e.g., in the case of the Kepler-36 system (Deck et al., 2012). Chaos might emerge not only due to interaction of different mean motion resonances, but as well due to interaction of subresonances (forming a multiplet) of a single mean motion resonance: the form and orientation of planetary (or asteroidal or satellite) orbits usually suffer slow variations, including the monotonous (secular) precession; the splitting of orbital resonances into subresonances is caused by this precession.

Modern classifications usually attribute the exosystems exhibiting mean motion resonances to the first, i.e., basic, dynamical class of planetary systems (Ferraz-Mello et al., 2006; Ollivier et al., 2009). One of the most widespread planetary resonances is the 2/1 resonance. It is a natural outcome of the primordial dynamical evolution of planets, as numerical simulations of the planetary migration show (e.g., Wang et al., 2012). The migration leads to both resonant and non-resonant final orbital configurations, in which the lines of apses are aligned; this phenomenon is observed in a number of actual planetary systems and thus serves as a confirmation that the migration took place indeed. The well-known systems with planets in the 2/1 resonance are Gliese 876 and HD 82943; in the 3/1 resonance — the 55 Cnc system. Moreover, Gliese 876 is an example of a system where three planets are involved in two different 2/1 resonances, thus forming the Laplace resonance 4:2:1 (Martí et al., 2013); recall that, in the Solar system, the Laplace resonance governs the dynamics of three Galilean satellites.

Apart from the mean motion resonances, a major role in the dynamical evolution of exosystems is played by secular resonances (Ferraz-Mello et al., 2006; Barnes, 2008). Some systems seem to exhibit both apsidal and mean motion resonances; a prototype (though not yet confirmed) is HD12661 (e.g., Goździewski, 2003). In what concerns the Lidov-Kozai effect, it might be widespread in systems with highly inclined planetary orbits; in particular, it was shown to be possible in the γ Cephei system (Haghighipour et al., 2010). Moreover, it has been invoked to explain the production of hot Jupiters (Lithwick and Naoz, 2011).

More than a half of all observed main-sequence stars reside in multiple (mostly double) star systems (Duquennoy and Mayor, 1991; Mathieu et al., 2000). A recently discovered circumbinary planet Kepler-16b orbits around a system of two main-sequence stars (Doyle et al., 2011). Though in a dangerous vicinity to the chaotic region around the central double, Kepler-16b survives, because its orbit is close to a half-integer orbital resonance 11/2 with the central double. In the Solar system, the given phenomenon is similar to the survival of Pluto and plutinos in the half-integer orbital resonance 3/2 with Neptune, or to the survival of the Kuiper belt objects in the 5/2 resonance with Neptune (Popova and Shevchenko, 2013). The dynamical behaviour of circumbinary planets in the Kepler-34 and 35 systems is qualitatively similarly to that in the Kepler-16 system.

In this report, dynamical problems on the resonances, including mean motion resonances (both two-body and three-body ones) and secular resonances, are considered in application to the dynamics of the Solar and exoplanetary systems. The analyzed systems include multiplanetary (those with two or more than two planets) systems and planetary systems of double stars. Theoretical methods and criteria for revealing stability or instability of various planetary configurations are described.

References:
Barnes, R., 2008, in: Exoplanets: Detection, Formation, Properties, Habitability. Mason, J.W. (Ed.). Springer: Berlin. P. 177
Deck, K.M., Holman, M.J., Agol, E., et al., 2012, Astrophys. J., 755, L21
Doyle, L.R., Carter, J.A., Fabrycky, D.C., et al., 2011, Science, 333, 1602
Duquennoy, A., and Mayor, M., 1991, Astron. Astrophys., 248, 485
Fabrycky, D.C., Lissauer, J.J., Ragozzine, D., et al., 2012, Architecture of Kepler's multi-transiting systems: II. New investigations with twice as many candidates. ArXiv:1202.6328
Ferraz-Mello, S., Michtchenko, T., Beaugé, C., et al., 2006, in: Chaos and Stability in Extrasolar Planetary Systems. Dvorak, R., Freistetter, F., and Kurths, J. (Eds.). Springer: Heidelberg. P. 171
Goldreich, P., and Rappaport, N., 2003, Icarus, 166, 320
Goździewski, K., 2003, Astron. Astrophys., 398, 1151
Haghighipour, N., Dvorak, R., and Pilat-Lohinger, E., 2010, in: Planets in Binary Star Systems. Haghighipour, N. (Ed.). Springer: Dordrecht. P. 285
Hayes, W.B., Malykh, A.V., and Danforth, C.M., 2010, MNRAS, 407, 1859
Laskar, J., 1989, Nature, 338, 237
Martí, J.G., Giuppone, C.A., and Beaugé, C., 2013, MNRAS, 433, 928
Mathieu, R.D., Ghez, A.M., Jensen, E.L., et al., 2000, in: Protostars and Planets IV. Mannings, V., Boss, A.P., and Russell, S.S. (Eds.). Univ. Arizona Press: Tucson. P. 703
Morbidelli, A., 2002, Modern Celestial Mechanics. Taylor and Francis: Padstow.
Murray, N., and Holman, M., 1999, Science, 283, 1877
Murray, N., Holman, M., and Potter, M., 1998, Astron. J., 116, 2583
Nesvorný, D., and Morbidelli, A., 1998, Astron. J., 116, 3029
Nesvorný, D., and Morbidelli, A., 1999, Celest. Mech. Dyn. Astron., 71, 243
Ollivier, M., Encrenaz, T., Roques, F., et al., 2009, Planetary Systems: Detection, Formation and Habitability of Extrasolar Planets. Springer: Berlin.
Popova, E.A., and Shevchenko, I.I., 2013, Astrophys. J., 769, 152
Quillen, A.C., 2011, MNRAS, 418, 1043
Shevchenko, I.I., 2008, MNRAS, 384, 1211
Smirnov, E.A., and Shevchenko, I.I., 2013, Icarus, 222, 220
Sussman, G.J., and Wisdom, J., 1988, Science, 241, 433
Sussman, G.J., and Wisdom, J., 1992, Science, 257, 56
Wang, S., Ji, J., and Zhou, J.-L., 2012, Astrophys. J., 753, 170
Wright, J.T., Veras, D., Ford, E.B., et al., 2011, Astrophys. J., 730, 93

RECENT RESULTS AND FUTURE ACTIVITIES OF VENUS EXPRESS.

H. Svedhem[1], C. Wilson[2],
[1]ESA/ESTEC, PB 299 Noordwijk, The Netherlands, *[2]Oxford University, Oxford, UK.*
Contact: H.Svedhem@esa.int

After having orbited our sister planet for more than seven Earth years Venus Express has collected a very large data set allowing a great number of fundamental scientific questions to be addressed and answered. Most of the questions formulated as a part of the mission's science requirement, as formulated in the mission proposal have been answered. These include topics in atmospheric dynamics, structure and chemistry, clouds and hazes, surface and interior, radiation balance and greenhouse, induced magnetosphere and plasma environment, and planetary evolution. Solid results have been achieved in all these fields but with some weakness in the radiation balance measurements, mostly due to the early loss of the planetary Fourier spectrometer providing data at the mid infrared wavelengths. Naturally, due to the limited scope and budget of the Venus Express mission a number of important questions had to be left unaddressed and to be taken up by future missions.

The fuel needed for maintaining the orbit and avoid entering the atmosphere is running out in 2014 or 2015. Plans for the operations for the last year of the mission are no being established. It is intended to do a sequence of aerobraking passes during the end of the mission. During this experiment significant scientific data will be gathered from a part of the atmosphere that s not accessible to remote sensing instruments. In addition experience in operating the spacecraft in aerobraking configuration will be gathered and studies of spacecraft resistance to heat and dynamical loads will be made.

This talk will summarise the major results of Venus Express and discuss a number of options for the operations for the final phase of the mission.

NIGHTTIME PHOTOCHEMICAL MODEL AND NIGHT AIRGLOW ON VENUS

Vladimir A. Krasnopolsky[1,2],
[1]CUA, Washington, DC 20064, USA; [2] PhysTech, Moscow, Russia.
Contact: vlad.krasn@verizon.net

The photochemical model for the Venus nighttime atmosphere and night airglow (Krasnopolsky 2010, Icarus 207, 17-27) has been revised to account for the SPICAV detection of the nighttime ozone layer and more detailed spectroscopy and morphology of the OH nightglow. Nighttime chemistry on Venus is induced by fluxes of O, N, H, and Cl with mean hemispheric values of 3×10^{12}, 1.2×10^{9}, 10^{10}, and 10^{10} cm^{-2} s^{-1}, respectively. These fluxes are proportional to column abundances of these species in the daytime atmosphere above 90 km, and this favors their validity. The model includes 86 reactions of 29 species. The calculated abundances of Cl_2, ClO, and $ClNO_3$ exceed a ppb level at 80-90 km, and perspectives of their detection are briefly discussed. Properties of the ozone layer in the model agree with those observed by SPICAV. An alternative model without the flux of Cl agrees with the observed O_3 peak altitude and density but predicts an increase of ozone to 4×10^{8} cm^{-3} at 80 km. Reactions $H+O_3$ and $O+HO_2$ that may excite the OH nightglow have equal column rates. However, the latter is shifted to 92-94 km, and the models agree better with the nightglow observations if $O+HO_2$ does not contribute to the OH excitation. Schemes for quenching of the OH vibrational quanta by CO_2 are chosen to fit the observed band distribution in the $\Delta v = 1$ sequence at 2.9 µm. The models agree with all observational constraints for the mean nighttime atmosphere. Analytic relationships between the nightglow intensities, the ozone layer, and the input fluxes of atomic species are given. The model results are compared with those of three-dimensional models for the Venus thermosphere.

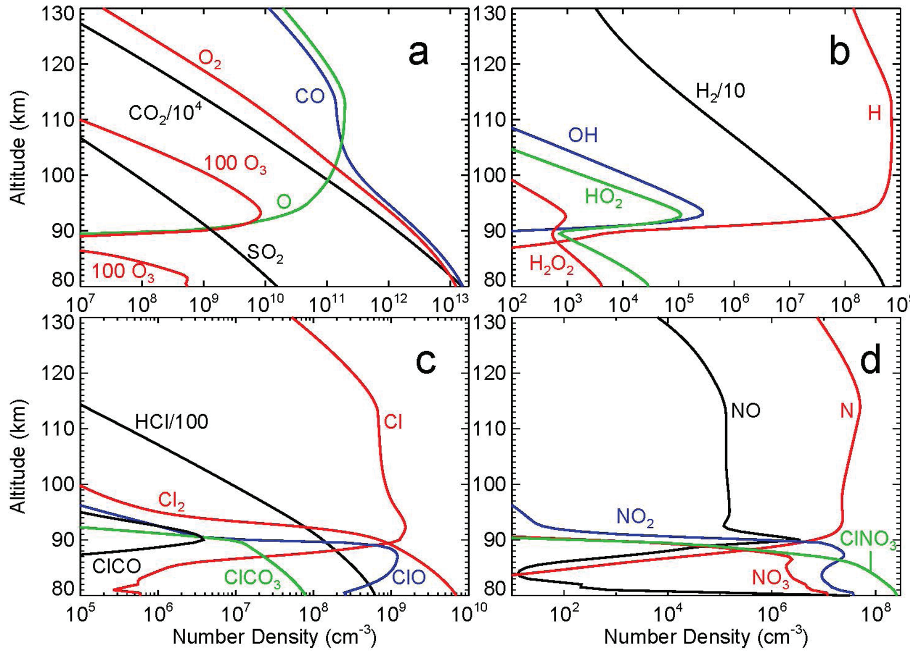

fig. 1. Vertical density profiles of species in the mean nightside atmosphere of Venus.

GRAVITY WAVE DETECTION IN THE TERRESTRIAL PLANETS' ATMOSPHERE THROUGH O2 AIRGLOW.

F. Altieri[1],
[1]IAPS-IANF, Via del Fosso del Cavaliere 100 – 00133 Rome, Italy.
Contact: francesca.altieri@iaps.inaf.it

Gravity waves (GWs) are mesoscale atmospheric oscillations related to the buoyancy restoring force, which play a key role in the circulation of planetary atmospheres. GW propagation induces fluctuation in both temperature and density fields, they can thus affect also the intensity of the airglow emissions. Here we report on the detection of GWs through the oscillations they produce in the intensity of the O2 singlet delta molecule airglow in the atmosphere of Mars and Venus. Data used in this study were carried out by the imaging spectrometers OMEGA and VIRTIS, on board the ESA missions Mars Express and Venus Express respectively. In order to model and derive the GWs properties, a well-known theory used to study terrestrial airglow fluctuations caused by the GWs propagation has been applied.

UPPER HAZE ON THE NIGHT SIDE OF VENUS FROM VIRTIS-M / VENUS EXPRESS OBSERVATIONS.

N. I. Ignatiev[1,2], L. Zasova[1,2], D. Gorinov[1,2], G. Piccioni[3], P. Drossart[4],
[1]Space Research Institute of Russian Academy of Sciences, Profsoyuznaya 84/32, 117997 Moscow, Russia; [2] Moscow Institute of Physics and Technology, Institutskiy per. 9, 141700 Dolgoprudny, Russia; [3]Istituto di Astrofisica e Planetologia Spaziali, INAF, Rome, Italy; [4]LESIA, Observatoire de Paris, Paris, France. Contact: ignatiev@iki.rssi.ru

Introduction:

VIRTIS-M is a mapping spectrometer on Venus Express [1]. It worked on orbit around Venus from 2006 to 2009 years. Night side limb images show existence of scattering radiation above the main cloud layer up to 85-90 km indicating for existence of haze above the clouds. The haze scatters the thermal radiation of the lower atmosphere in the spectral windows from 1 to 2.3 μm. In the 4-5 μm spectral range we observe both scattered thermal emission of the upper clouds and thermal emission of the haze. De Kok et al. [2] have analyzed observations from only 4 orbits and obtained number density vertical profiles of mode 2 particles at 75-90 km from the spectral range 4.3-5 μm in 2 narrow latitudinal bands 20-30° and 47-50°. We are going to considerably extend this first study using several wavelengths in the windows from 1 to 2.3 μm.

Observations:

Polar orbit of Venus Express with pericenter at 75N latitude allows carrying out limb measurements in the northern hemisphere. From the distance of 15 000 km from the planet, the haze vertical profile is obtained with vertical resolution of 2.5 km. Local maxima of intensity are observed often in the 1.74 and 2.3 μm spectral windows on altitudes of 75-85 km, but only in some cases at 1.18 μm. They may be explained by the existence of the detached layers of small particles (mode 1) as well as the horizontal non-uniformity of the clouds.

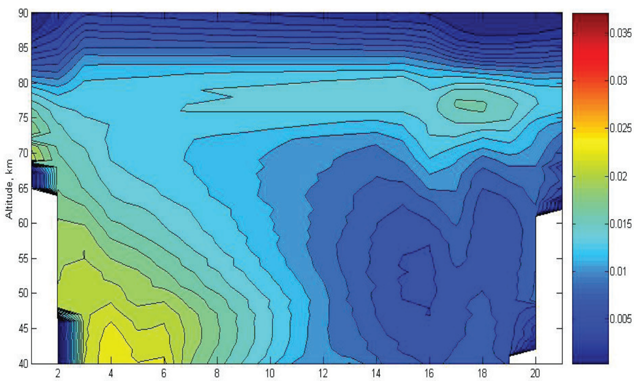

fig.1. Limb intensity at the wavelength 1.74 μm as a function of latitude and altitude, orbit 718.

Modeling of limb spectra: Our radiative transfer model takes into account multiple scattering in a pseudo-spherical geometry: the source function is calculated for a plane parallel atmosphere and then integrated along the optical path. Gaseous absorption is calculated with the line-by-line code [3] with a number of recent improvements for the continuum absorption [e.g. 4]. We first calculated vertical profiles of limb intensity for a number of models of Venus atmosphere and clouds with detached layers with different parameters. The shape of vertical profile of limb intensity in different spectral windows depends on the shape of aerosol vertical profile (detached layer), its optical depth, and particle size distribution.

Inverse problem solution and first results: Haze density can be retrieved by inverting the vertical limb intensity profile by means of standard inverse methods for atmospheric sounding [5, 6]. Vertical extinction or number density profile is obtained using a single window, but particle size distribution can be evaluated only by considering several windows. The retrieval process is extremely time consuming since it requires a huge number of monochromatic multiple scattering calculations. Kernels of the inverse problem (Fig.2a) shows a specific shape of the sensitivity of the vertical profile of limb intensity to variations of the vertical profile of the cloud density, which has an evident interpretation: emission coming from the lower atmosphere is attenuated by the main cloud deck (negative values below cloud tops ~70 km) and scattered by the upper haze (positive values above cloud tops). Fig.2(b,c) provides an example of the convergence of the retrieval algorithm and the retrieved number density profile. However, the cloud density below the cloud top retrieved from the limb intensity vertical profile may be quite far from real values as it serves as a formal attenuator of the model intensity of the lower atmosphere, while the retrieved upper haze density seems to be more realistic once it does not depend on the way the outgoing intensity at the lower (i.e. cloud top) level produced by. Thus, to understand the feasibility of the simultaneous retrieval of the number density and the particle size from 3 spectral windows, a vast sensitivity study must be carried out (this work is being done). However, using the result by de Kok et al. [2], who demonstrated that the spectral dependence of the limb intensity in a wide spectral range (1-5 μm) indicates the existence of 1-micron particles (i.e. mode 2), we can do tentative retrievals of the equivalent mode 2 number density vertical profile (Fig. 2c). Although a detailed comparison is not yet possible, at the altitude of maximum sensitivity 85 km our preliminary results agree with those by de Kok [2] by the order of magnitude 0.1-1 cm^{-3}.

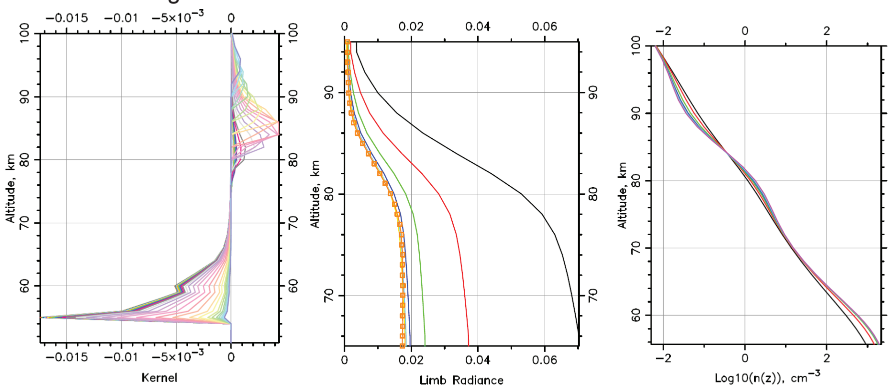

(a) **(b)** **(c)**

fig. 2. Examples of the kernels of the inverse problem (a) and convergence of the retrieval algorithm in terms of radiance (b) and equaivalent mode 2 number density profiles (c). Wavelength 1.18μm, orbit 718, latitudes 15-20° (VI0718_03).

Acknowledgements: The Venus Express is a mission of the European Space Agency. We thank the Agenzia Spaziale Italiana (ASI) and the Centre National d'Études Spatiales (CNES) for the support and funding of the VIRTIS experiment. We thank all members of the Venus Express project and of the VIRTIS technical team. This work is supported by the Ministry of Education and Science of Russian Federation grant 11.G34.31.0074, the Russian Foundation of Basic Research grant 12-02-01280, and the Presidium RAS Program 22.

References: [1] Drossart, P., Piccioni, G., and 29 co-authors: Scientific goals for the observation of Venus by VIRTIS on ESA/Venus Express mission, Planet. Space Sci., Vol. 55, pp. 1653-1672, 2007. [2] de Kok, R., Irwin, P.G.J., Tsang, C.C.C., Piccioni, G., Drossart, P.: Scattering particles in nightside limb observations of Venus' upper atmosphere by Venus Express VIRTIS, Icarus, Vol. 211, pp. 51-57, 2011. [3] Ignatiev, N. I., Titov, D.V., Piccioni, G., Drossart, P., Markiewicz, W. J., Cottini, V., Roatsch, Th., Almeida, M., and Manoel, N.: Altimetry of the Venus cloud tops from the Venus Express observations, J. Geophys. Res., Vol. 114, E00B43, 2009. [4] Bézard, B., Fedorova, A., Bertaux, J.-L., Rodin, A., Korablev, O.: The 1.10- and 1.18-μm nightside windows of Venus observed by SPICAV-IR aboard Venus Express, Icarus, Vol. 216, pp. 173-183, 2011. [5] Ustinov, E.A.: Inverse problem of thermal sounding. III. Determination of the vertical profile of the mixture ratio of a minor gas component, Cosmic Res., Vol. 29, p. 249-256, 1991. [6] Rodgers C.D.: Inverse Methods for Atmospheric Sounding - Theory and Practice: World Scientific Publishing, 2000.Venus Express is a mission of the European Space Agency. We thank the Agenzia Spaziale Italiana (ASI) and the Centre National d'Études Spatiales (CNES) for the support and funding of the VIRTIS experiment. We thank all members of the Venus Express project and of the VIRTIS technical team. This work is supported by the Ministry of Education and Science of Russian Federation grant 11.G34.31.0074, the Russian Foundation of Basic Research grant 12-02-01280, and the Presidium RAS Program 22.

NON-HYDROSTATIC GENERAL CIRCULATION SIMULATIONS OF THE TRANSITION REGION IN THE VENUS ATMOSPHERE.

A. V. Rodin[1,2], I.V. Mingalev[3], K.G. Orlov[3]
[1]Moscow Institute of Physics and Technology, Institutsky Dr., 9, 141700 Dolgoprudny, Moscow Region, Russia; [2]Space Research Institute, 117997 Profsoyuznaya 84/32 Moscow, Russia; [3]Polar Geophysical Institute, Academic Village 26a, 184209 Murmansk Region, Russia. Contact: alexander.rodin@phystech.edu

Introduction:

It is now well established that Venus atmosphere reveals two different regimes of global circulation, dominated with retrograde zonal superrotation (RZS) below and near the upper boundary of cloud layer (65-75 km), and subsolar-antisolar circulation (SS-AS) above the mesopause (90-95 km). In spite of significant progress in general circulation modeling of Venus atmosphere[1], simultaneous simulation of both RZS and SS-AS has not been achieved to date. Here we present the results of non-hydrostatic general circulation model based on the full set of gas dynamics equations and simplified relaxation approximation to the thermal balance and discuss possibile explanations and consequences of the constraints derived from simulations.

The model:

The dynamical core of the model developed at the Polar Geophysical Institute in Apatity, Russia, implements numerical solution to the set of gas dynamics equations for continuous, compressible atmopsheric gas with constant composition[2]. The explicit integration scheme is based on semi-Lagrangian finite volume method, is conservative and monotonous, and reveals no first-order numerical viscosity. We used uniform grid with 250 m step in altitude, and in spherical coordinates with 128 nodes in latitude and 256 in latitude. Vertical domain covers altitude range from the planet's surface to 120 km. Subgrid phenomena included in the model are limited by eddy viscosity parameterization based on the local Richardson number. The model has no built-in radiation block; instead, thermal forcing is implemented by Newtonian relaxation approximation. Relaxation thermal profile and its variations in latitude and height, as well as specified dependence on solar zenith angle, is the only input that provides control of the model behavior. Numerical experiments were carried out with different setup of the relaxation thermal profile, in order to guess thermal forcing that would provide circulation pattern close to the observations. The model implementation takes advantage of hybrid GPU calculations by using CUDA technology, that provides about 100-fold acceleration of the code compared to single-thread calculations.

Initial and boundary conditions:

Lower boundary conditions include Venus topography sampled with the grid resolution, with both vertical and horizontal wind components being zero at the planet's surface. Upper boundary condition implies zero vertical wind component, with no additional friction and no sponge layer. As the model remands high computational cost, it is important to start with wind field that relaxes to a steady-state solution within reasonable time. This is why the developed superrotation state, with wind profile increasing linearly from the surface to 50 km up to the maximum speed of 120 m/s, has been selected as initial condition. Initial wind profile is constant within altitude range 50-65 km and then decreases linearly between 65 and 75 km.

Thermal forcing:

First experiments with the model were run assuming solar thermal forcing expressed in the model by adding to the relaxation profile a component dependent on local time and maximizing in the altitude range corresponding to the main cloud layer (55-65 km). In these experiments superrotation pattern was stabilized as soon as within ~2000 hours of simulation, i.e. during one Venusian sol. A subsolar-antisolar circulation was also developed in the upper part of the model domain, but after relaxation of the whole circulation pattern it was superceded by superrotation expanding upwards. To suppress superrotation expansion to higher altitudes, we slightly modified thermal forcing according to the hypothesis of cyclostrophic balance. If horizontal pressure gradient is balanced by centrifugal forces, increasing temperature to the poles would result in the depression of isobaric surfaces to the equator, which in turn requires the decrease of zonal velocity with altitude. Using this approach, relaxation thermal profile was modified in the polar regions, so that additional warming was added above the cloud layer and additional cooling – within the clouds.

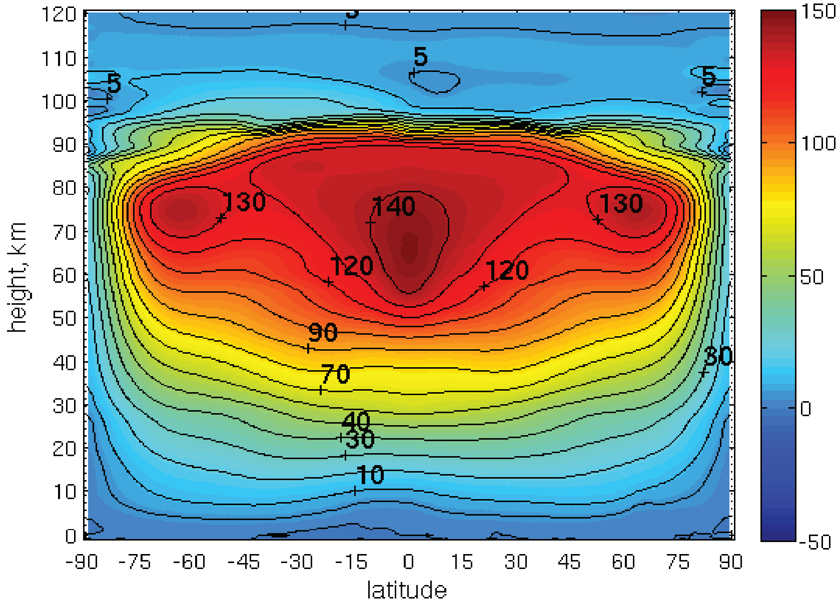

fig. 1. Zonal-mean crossection of zonal velocity field versus latitude and height. Note gravity wave pattern in the polar regions and lowering of the wind pattern to the poles.

Results:

Using the modified thermal forcing described above, we were able to reproduce superrotation pattern consistent with previous models and observations (Figure1). Zonal velocity associated with superrotation decreases above 70 km, which gives a room for the development of subsolar-antisolar circulation at higher altitudes, as shown in Figure 1 (a). In the polar regions, strong wave pattern associated with polar vortex is developed. This pattern reveals localized areas of downward motion in the altitude range 60-70 km, consistent with numerous observations. However, horizontal resolution of the model is far insufficient to reproduce these vortices in detail. It is interesting that forcing modification described above has also resulted in the thermal structure that reveals the depression of cloud layer in the vicinity of the poles and in the inversion of temperature profile at 85-95 km associated with the dynamical heating in the upper part of Hadley cell, also consistent with observations[3].

Temperature distribution at the altitude 95 km shown in Figure 2(a) reveals warm polar regions, with apparent wave-3 structure, which in the lower latitudes is connected with the pattern characteristic of thermal tide. Diurnal and semidiurnal tidal components are revealed as well. This structure is manifested in all simulations resulting in stable superrotation, that implies that thermal tide is an important mechanism of its maintenance.

An example of horizontal wind field at the altitude 95 km shown in Figure 2(a) as a Gaussian-weighted average with vertical smoothing depth of 5 km, demonstrates a competition between fading superrotation and emerging subsolar-antisolar circulation. It is evident that the resulting wind field is not a superposition of these two basic states of the Venus global atmospheric circulation. In contrast, the transition region is affected by a complex combination of waves and vortices of different scales, with several structures associated with either divergent or convergent motion. Figure 2(b) shows that the distribution of tracers, such as oxygen emission at 1.27 micron, should be interpreted with caution in terms of the wind field. For instance, the area of flow convergence, where maximal tracer concentrations are expected, is displaced in the direction of evening, rather than morning local time, as it could be supposed if superrotation impact is taken into account.

Additional cooling of the polar regions within the main cloud deck is consistent with the radiative transfer models, as only negligible portion of solar radiation is able to penetrate optically thick clouds at high zenith angles. Explanation of the assumed additional heating above the clouds is not so evident. Rarified, optically thin mesosphere is transparent for slant propagation of the solar radiation. Due to negligible inclination of Venus' rotation axis, polar mesosphere is exposed to sunlight permanently, without seasonal and diurnal variations. This results in the increase of mean heating rates due to absorption in the UV and NIR spectral bands by a factor of two, compared to lower latitudes. However, the dynamical heating and/or dissipation of turbulent energy according to Gierasch mechanism, may not be ruled out. Thus, the dynamics and thermal regime of the polar regions of the Venus atmosphere may play an important role in maintenance of the transition region between zonal superrotation and subsolar-antisolar circulation at the global scale.

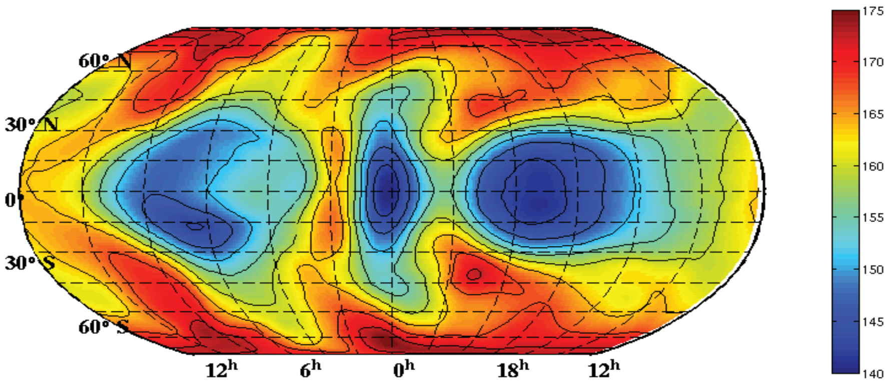

a

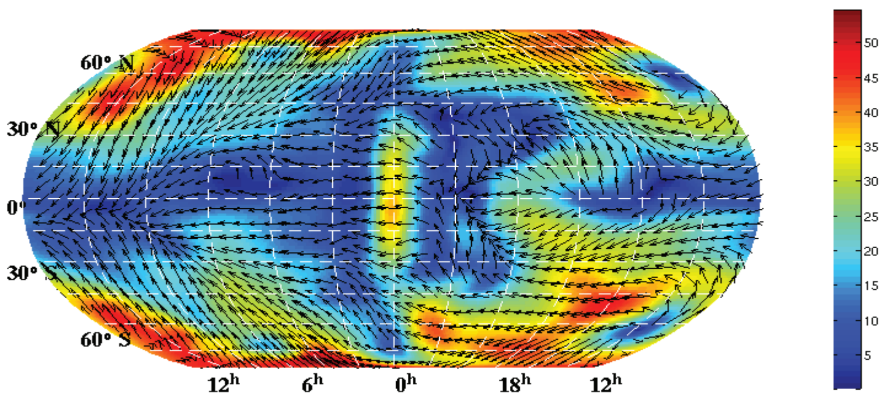

b

fig. 2. (**a**) Temperature distribution in the Venus atmosphere at the altitude 95 km averaged over 5 km with Gaussian weighting function. (**b**) Similarly averaged horizontal wind field.

References:

Lebonnois S., F. Hourdin, V. Eymet, A. Crespin, R. Fournier, and F. Forget Superrotation of Venus atmosphere analyzed with a full General Circulation Model. J. Geophys. Res 2010. V. 115:E06006, DOI 10.1029/2009JE003458

Mingalev I.V., A.V.Rodin, and K.G.Orlov. A non-hydrostatic model of the global circulation of the atmosphere of Venus. Solar System Res. 2012, V. 46, Issue 4, pp 263-277

Bertaux, J.-L., et al. A warm layer in Venus' cryosphere and high-altitude measurements of HF, HCl, H2O and HDO. Nature 2007, V. 450, Issue 7170, 646-649

Acknowledgement: The work has been supported by the Ministry of Education and Science of Russian Federation, grant #*11.G34*.31.0074

TOWARDS A BETTER UNDERSTANDING OF THE VENUS ATMOSPHERE – OBSERVATIONS NEEDED BETWEEN 65 – 110 KM

S.S. Limaye,
[1]Space Science and Engineering Center, University of Wisconsin, 1225 West Dayton Street, Madison, Wisconsin 53706, USA. Contact: Sanjay.Limaye@ssec.wisc.edu,

Through a half century of exploring Venus with spacecraft, we have learned that the planet and its atmosphere continue to hold many mysteries. The ubiquitous cloud cover absorbs much of the incident solar energy through an ultraviolet absorber whose identify still remains unconfirmed but also lets some of the emitted energy leak through many small and large scale ihomogeneities in opacity in the near infrared region of the spectrum. At ~ 54 km altitude VeGa balloons experienced large updrafts and downdrafts, but the variability of the horizontal winds in the 90-120 km region is even more astonishing. Day-side to night-side circulation predicted before measurements of winds were available is found to exist in this layer, but systematic measurements are lacking and details are very sketchy.

All in situ measurements of the Venus atmospheric composition and dynamics by Venera, VEGA, and Pioneer Venus entry probes were obtained at altitudes below ~ 62-65 km. The two VeGa balloons measured atmospheric properties at a level of about 54 km above the surface. From the few measurements of the cloud properties of Venus on day and night side, it is believed that the bottom of the cloud layer is at approximately 48-50 km. Both remote sensing and entry probe measurements indicate that the cloud top was above the highest altitudes where the measurements were obtained. Analysis of remote sensing observations from Pioneer Venus Orbiter Cloud Photopolarimeter (OCPP) showed that the cloud tops extend to as high as 71 km at latitudes below 70 degrees, and a haze layer of smaller particles extended as high as 90 km above the surface. Observations from the Pioneer Venus Orbiter [2,3] and entry probes [4] indicate that the unknown absorber that causes the cloud-top ultraviolet contrasts is confined within the upper cloud (57.5 – 71 km) and is responsible for absorbing almost half of the solar radiation deposited on the planet [5]. However, its global distribution and temporal variability is not well characterized.

Döppler observations at (emitted) infrared [6] and reflected visible [7] wavelengths and imaging observations at near infrared measurements from the ground and from fly-bys and orbiters [8,9] provide insights into the circulation, above, near and below the cloud tops, but much less is known about the the winds in the lower atmosphere (e.g. the altitude of the peak kinetic energy and angular momentum densities).

Meanwhile, numerical simulations of the atmospheric circulation continue with the goal of reproducing the observed superrotation of the atmosphere with its~4 day period at the cloud top levels. The recent efforts by many groups have been able to achieve some resemblance to the observed circulation, but only by modifying the heating rates in the models. Indeed, one of the dominant problems in further progress of such efforts is the uncertainty in the knowledge of where in the atmosphere is being heated by absorbed solar energy and by the absorption of the thermal radiation emitted from the lower atmosphere and surface [10].

New measurements and observation strategies are required to better characterize the atmospheric circulation above the cloudtops to ~ 120 km from future space missions and Earth based efforts to improve our knowledge. In-site sampling may be necessary to confirm the identity of the ultraviolet absorber(s) in the clouds to better understand the global energy deposition and loss from the Venus atmosphere.

References:

[1] Knollenberg. et al. (1980) *JGR,85,* A13, 8039-8058. [2] Travis, L. D., et al., (1979) *Science*, 203, 781–784; Lane and Opstbaum, 1983, *Icarus, 54, 48-58.* [3] Tomasko et al. (1980) *JGR,85,*A13, 8167-8786. [4] Tomasko et al. (1985) *Adv. Space Res. 5*, 71-79. [5] Crisp, D., (1986) *Icarus, 67,* 484-514. [6] Limaye, S.; Rengel, M.; Atmospheric circulation and dynamics - Observations and knowledge gaps. In “Towards understanding the climate of Venus: Applications of terrestrial models to our sister planet”, International Space Studies Institute, Bern, Switzerland, Report # 11, 55-72 (2012), [7] Machado, P., Luz, D., Widemann, T., Lellouch, E., Witasse, O. 2012, Mapping zonal winds at Venus’ cloud tops from ground-based Doppler velocimetry, Icarus 221, 248-261. [8] Taylor et al., (1997) Venus II, 325–351. [9] Sánchez-Lavega et al., (2008) Geophys. Res. Letters, 35, L13204, doi: 10.1029/2008GL033817. [10] Lebonnois et al. (2010), JGR, 115, E06006, doi:10.1029/2009JE003458.

SURFACE EMISSIVITY RETRIEVAL FROM VIRTIS/VEX DATA IN THE QUETZALPETLATL QUADRANGLE ON VENUS BASED ON THE NEW MSR MULTI-SPECTRUM RETRIEVAL TECHNIQUE

G. Arnold[1], D. Kappel[1], R. Haus[2], S. Ebert[2],
[1]Institute of Planetary Research, DLR, Rutherfordstr.2, 12489 Berlin, Germany;
[2]Institute for Planetology, WWU, 48129 Münster, Germany.
Contact: Gabriele.Arnold@dlr.de

Surface emissivity is difficult and error-prone to retrieve from VIRTIS measurements of Venus' nightside. A detailed radiative transfer forward model simulation is used to generate synthetic spectra for given atmospheric and surface parameters. The new MSR multi-spectrum retrieval technique is applied to retrieve atmospheric and surface parameters that allow the synthetic spectra to fit the measurements. The incorporation of expected spatial-temporal correlations between parameters describing a selection of contiguous measurements leads to much more reliable parameters, as does the retrieval of surface emissivity of a surface bin as a parameter that is common to measurements that repeatedly cover that bin, thereby neglecting geologic activity.

The method is applied to Quetzalpetlatl quadrangle including the Lada Terra rise and the Quetzalpetlatl corona. This area combines corona-dominated rises, rifted volcanic rises, and large coronae structures [1]. Retrieved emissivity at 1.02 µm is related to regional geologic units.

Introduction:

Venus' surface properties are not well known except from a few *in situ* measurements and from RADAR mapping. Surface emissivity in the infrared (IR) is more specific to surface materials and textures than RADAR data. The only global data source at high spatial, spectral, and temporal resolution are the IR nightside emissions acquired by the IR Mapping channel of the Visible and InfraRed Thermal Imaging Spectrometer (VIRTIS-M-IR) aboard ESA's spaceprobe Venus Express (VEX) [2, 3]. At each exposure, the range 1.0 - 5.2 µm is sampled by 432 spectral bands for 256 spatial pixels, and many successive exposures yield a carefully calibrated [4] spectrally resolved two-dimensional image of a target on Venus. Such a target can repeatedly be covered by several images recorded over the duration of the mission, providing an excellent data base for surface emissivity retrieval [5].

The hot surface (735 K at 0 km according to VIRA) emits surface temperature, composition, and texture dependent radiation that is, along with deep atmospheric emissions, multiply scattered and partly absorbed by the overlying atmospheric and cloud layers. On Venus' dayside, sunlight is scattered by the clouds and strongly outweighs the relevant surface emissions as well as sunlight reflected at the surface. On the nightside, the dense CO_2 atmosphere and the thick H_2SO_4 clouds completely black out several spectral ranges and leave only a few narrow spectral transparency windows that probe down to the surface and deep atmosphere.

For given atmospheric and surface parameters, these mechanisms are simulated by a detailed radiative transfer forward model [6]. A single-spectrum retrieval algorithm compares a simulated with a measured spectrum and modifies the parameters until the simulation well fits the measurement. The resulting parameters then adequately describe the measured spectrum and are interpreted as the underlying state of atmosphere and surface that led to the measured spectrum. Due to the limited spectral information content, different state vectors may describe the same spectrum equally well, and incorporation of expected mean values and standard deviations for all parameters serves to regularize the retrieval. While this already decreases the probability to determine unlikely parameter values, the surface emissivity retrieval error is still too large to obtain reasonably reliable surface data.

The MSR technique:

The drive to compensate thermodynamic disequilibria yields a certain continuity of atmospheric parameters. Thus, contiguous measurements are likely to originate from spatially-temporally correlated single-spectrum state vectors. Such *a priori* correlations are usually neglected in retrieval algorithms. The new Multi-Spectrum Retrieval technique MSR [7] takes them into account and thus decreases the probability to determine unlikely spatial-temporal state vector distributions as well as noise effects. Parameters with more different correlation lengths or times can be better disentangled. The extreme case is the disentanglement of parameters with finite from those with infinite correlation length or time. The latter can be treated as common to a suitable selection of measurements. MSR's reduction of the effectively available size of the state vector space decreases the uncertainty of retrieved parameters and thus improves their reliability.

MSR enables the retrieval of surface emissivity in the first place. When geologic activity is neglected, surface emissivity of a surface bin is common to all measurements that cover this bin. The surface emissivity map of a target on Venus can be retrieved as parameter vector that is common to a suitable selection of spectrally resolved two-dimensional images that repeatedly cover that target.

Results:

MSR is applied to a geologically interesting region in the Quetzalpetlatl quadrangle (V-61, [8]). The study area is bounded by 335°-360° longitude and 65°-50° southern latitude. It is situated in the region most frequently measured by VIRTIS-M-IR, allowing to take a high number of repetitions into account. The surface target is divided into 250 equal-area bins of roughly 100 km x 100 km. Each bin is covered by 16 measurements, yielding 4000 spectra. With no least-square residual exceeding 5% of its measured spectrum's least-squares norm, the quality of the fits is uniformly excellent (Fig. 1).

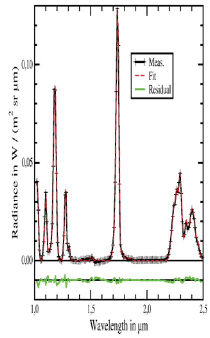

fig. 1. Comparison of VIRTIS-M-IR measurement and fitted simulation.

A single-spectrum retrieval error analysis was performed to identify the main interfering parameters aside from CO_2 opacity uncertainties: surface elevation, deep atmosphere lapse rate, H_2O mixing ratio, and H_2SO_4 concentration of cloud droplets.

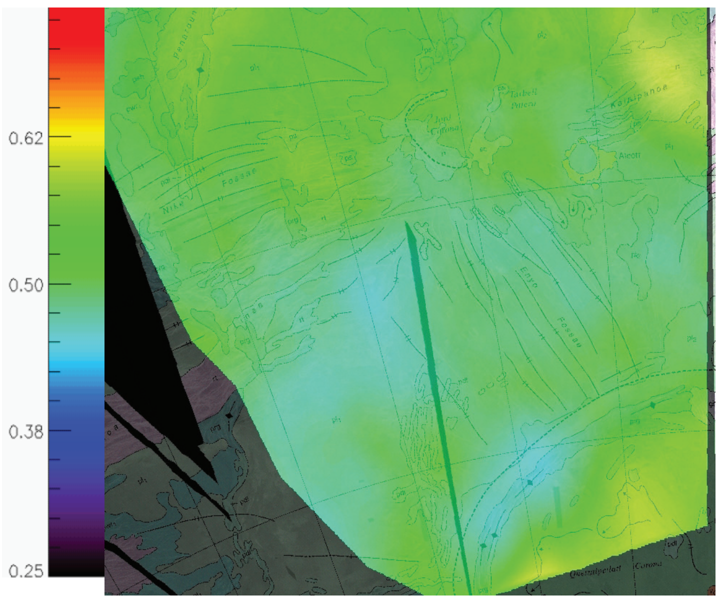

fig. 2. Retrieved 1.02 µm emissivity at Quetzalpetlatl corona rim (overlaid to geologic map).

Fig. 2 shows one example of the retrieved 1.02 µm emissivity near the Quetzalpetlatl corona. Variations of the emissivity are not primarily correlated to topography and therefore not to surface temperature. They are rather linked to the surface geology. Like parts of the corona rim (ridge), lower units of the lobate plains Enyo Fossae can be related to lower emissivity. Higher emissivity values in the south of the corona rim are correlated to the youngest lava flows (lobate plains, upper unit).

References:

[1] Ivanov M.A. and J.W. Head, *Planet. Space Sci.* **58**, 1880-1894, 2010.
[2] Drossart P. et al., *Planet. Space Sci.* **55**(12), 1653-1672, 2007.
[3] Piccioni, G. et al., ESA Spec. Publ. SP-1295, 1–27, European Space Agency, Paris, 2007.
[4] Kappel D. et al., *Adv. Space Res.* 50, 228-255, 2012.
[5] Arnold G. et al., *J. Geophys. Res.* **113** (E5), E00B10, 2008.
[6] Haus R. and G. Arnold, *Planet. Space. Sci.* **58** (12), 1578-1598, 2010.
[7] Kappel, D., «The MSR multi-spectrum retrieval technique for spatially-temporally correlated or common Venus surface and atmosphere parameters», *JQSRT*, accepted for publication, 2013.
[8] Ivanov, M.A. and J.W. Head, «Geologic map of the Mylitta Fluctus Quadrangle (V-61), Venus», US Geological Survey, 2006.

EVOLUTION OF TECTONICS ON VENUS.

M. A. Ivanov[1], J.W. Head[2],
[1]GEOKHI, Kosygin-19 Moscow, Russia[2], Brown Univ., Providence RI, USA.
Contact: mikhail_ivanov@brown.edu

Introduction: Large-scale tectonic deformation of planetary surfaces is often related to mantle circulation patterns and represents one of the manifestations of the process of global internal heat loss [e.g., 1]. The surface of Venus displays several tectonized terrains in which the morphologic characteristics of the original materials are almost completely erased by superposed tectonic structures whose dimensions (100s to 1000s of km) suggest formation related to the mantle convection. The characteristics of these tectonized terrains are in contrast to volcanic units in which tectonic structures are less significant or absent and thus do not hide the volcanic character of the units. Here we describe the temporal distribution of tectonized terrains, their stratigraphic relationships with volcanic units, and how these outline the major episodes in the geological evolution of Venus.

Major tectonized units: The following five tectonized units are the most important on Venus and make up ~20% of its surface [2]. (1) Tessera (t, 7.3% of the surface of Venus, Fig. 1) displays intersecting sets of contractional and extensional structures [e.g., 3]. High-standing occurrences of tessera (Fig. 1) vary in size from a few tens of kilometers up to a few thousands of kilometers [4]. (2) Densely lineated plains (pdl, 1.6%, Fig. 1) are dissected by numerous densely packed parallel fractures. Occurrences of pdl are slightly elevated relative to the surroundings. (3) Ridged plains/Ridge belts (pr/rb, 2.4% Fig. 1) are deformed by broad and long ridges that often form elevated belts. In this paper, mountain belts around Lakshmi Planum are included into the pr/rb unit as a topographically specific facies of ridge belts. (4) Groove belts (gb, 8.1%, Fig. 1) are swarms of extensional structures that completely obscure the characteristics of underlying materials at the scale of the mapping. (5) Rift zones (rz, 5.0%, Fig. 1) consist of numerous parallel fissures and troughs that usually completely erase the morphology of underlying terrains. On average, structures of rz are broader, longer, and less densely packed than structures of gb. Rift zones preferentially occur within the dome-shaped rises. The hypsograms of all tectonized units are shifted toward higher elevations (Fig. 1).

Age relationships with volcanic units: Clear relationships of relative age are often seen among the tectonic and volcanic units at the global scale [2]. Structures of pdl and pr/rb usually cut tessera but in some places they appear to be incorporated into the tessera structural pattern. Graben of gb cut occurrences of tessera, pdl, and pr/rb. Vast expanses of mildly deformed plains units (shield- and regional plains) embay all occurrences of t, pdl, and pr/rb and the majority of groove belts. Structures of rift zones cut the vast plains and are contemporaneous with the younger lobate plains.

Discussion: The majority of tectonized terrains (t through gb) are the products of tectonic resurfacing and are embayed by the vast volcanic plains and, thus, are older. There are no units with either mildly- or non-tectonized surfaces that interleave the tectonic terrains, which would be expected if the tectonic resurfacing operated only during specific phases in discrete regions. The major tectonized terrains thus define a tectonically dominated regime of resurfacing that occurred at the global-scale near the beginning of the observable geological history of Venus.

This ancient tectonic regime began with formation of the oldest unit, tessera. Both contractional (ridges) and extensional (graben) structures form tessera and the relative age relationships between thse strucutres are usually ambiguous [5,6]. In some areas, however, volcanic plains embay the tessera ridges and are cut by the graben [7]. This provides robust evidence for the relatively old age of the ridges and suggests that formation of tessera was due to large-scale compression that resulted in regional thickening of the crust [8,9].

Tectonic units such as pdl and pr usually occur away from tesserae, preventing consistent determination of their exact stratigraphy. In places where t, pdl, and p are in contact, two situations occur: (1) more often, materials of pdl and pr embay tessera and their tectonic structures cut tessera [10]; (2) in a few places, pdl and/or pr are additionally deformed and their surfaces resemble that of tessera (the tessera transitional terrains, ttt, [11]). These relationships suggest that formation of tessera was mostly completed prior to emplacement and deformation of pdl and pr. In some areas, formation of tessera continued and affected surrounding units but it did not last long because the areas of ttt are usually small and occur sporadically.

Ridged plains often represent pronounced belts of contractional structures. This suggests that the belts formed under compressional stresses applied within relatively narrow but very extensive zones [12,13]. These characteristics of rb resemble those of terrestrial thrust-and-fold belts that occur over large thrust faults and may be related to plate tectonics. If ridge belts formed due to shortening of crustal materials, it may indicate lateral movements of lithospheric blocks on Venus. The relatively low relief of ridge belts (hundred meters high [14]) suggests that these movements and related contraction were rather limited and may correspond to immature (arrested) stages of plate tectonics. The distinctive exceptions to this are the mountain belts [15]. The belts are high and their relationships with the surroundings provide evidence for large-scale collision and underthrusting [16,17]. The mountain belts exist only around Lakshmi Planum, which suggests that even if the belts formed by the processes akin to subduction, they were fairly restricted on Venus.

Groove belts are the youngest features of the ancient tectonic regime. In contrast to ridge belts, they are abundant and pervasive (Fig. 1), and mark zones of extension. The contractional structures/zones that are spatially and stratigraphically complementary to groove belts are absent. Instead, branches of groove belts compose the tectonic components of many coronae [18] suggesting that these features are genetically related (e.g., mutual development of mantle diapirs and zones of extension [e.g., 19]) and that coronae may have punctuated the final stages of the ancient tectonic regime.

This regime was followed by emplacement of the vast volcanic plains, such as shield and regional plains, the surfaces of which are extensively deformed by the global network of wrinkle ridges [20]. Emplacement of the plains has defined the second, volcanically dominated regime [21], representing a time when surface tectonic deformation related to the mantle convection waned.

Rift zones are the stratigraphically youngest manifestations of regional-scale tectonic deformation on Venus. Rifts are spatially and temporarily associated with the youngest lava flows and often cut the crest areas of large, but isolated, dome-shaped rises. Structures of rift zones always cut the surface of the vast plains, which means that rifts are separated in time from the ancient tectonic regime, post-date the regional plains, and represent a new phase of tectonism that was contemporaneous with the late volcanism of lobate plains. Rift zones and lobate plains define the third, volcano-tectonic, regime of resurfacing that was related to late stages of evolution of the dome-shaped rises.

Summary: (1) The observable geologic history of Venus appears to consist of three contrasting regimes of resurfacing. The majority of the tectonized terrains that may be related to regional/global mantle convection patterns define the first, tectonically dominated, regime. During this time, large regions of thickened crust (tesserae) were formed; a limited contraction and possible underthrusting along specific zones resulted in formation of ridge and mountain belts. The later phases of the ancient tectonic regime were manifested by the mutual development of groove belts and many coronae. All tectonized terrains of the first regime represent local- to regional topographic highs in the background topography (Fig. 1). (2) During the second, volcanically dominated regime, the vast plains preferentially covered the surface in regional lows. This suggests that the principal topographic features of Venus (i.e., regional plateau-like highlands and broad lowlands) were formed by the end of the ancient, tectonic regime. (3) The density of craters on regional plains suggests that the first two regimes (tectonic and volcanic) operated during about the first one-third of the observable history. (4) Contemporaneous rift zones and lobate plains define the third, volcano-tectonic regime. This regime dominated the last two-thirds of the observable geologic history and likely was linked to the later stages of evolution of the dome-shaped rises.

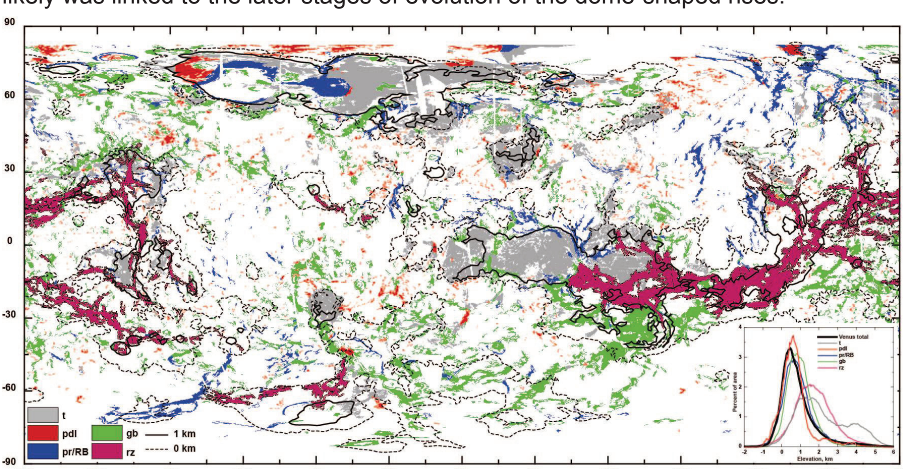

fig. 1. The geological map of Venus [2] with tectonized units highlighted.

References: 1) Solomon, S.C. and J.W. Head, JGR, 87, 9236, 1982; 2) Ivanov, M.A., and J.W. Head, PSS, 59, 1559, 2011; 3) Sukhanov, A.L. In: Venus GGG, Barsukov et al., eds, 82, 1992; 4) Ivanov, M.A. and J. W. Head, JGR, 101, 14861, 1996; 5) Hansen, V.L. and J.J. Willis, Icarus, 132, 321, 1998; 6) Gilmore, M.S. et al., JGR, 103, 16813, 1998; 7) Ivanov, M.A. and J.W. Head, LPSC 31, #1233, 2000; 8) Head, J.W., et al., PSS, 42, 803, 1994; 9) Bindschadler, D.L. et al., JGR, 97, 13563, 1992; 10) Basilevsky, A. T. and J.W. Head, PSS, 43, 1523, 1995; 11) Ivanov, M.A. and J. W. Head, JGR, 106, 17515, 2001; 12) Frank, S.L. and J.W. Head, EMP, 50/51, 421, 1990; 13) Kruychkov, V.P. In: Venus GGG, Barsukov et al., eds, 96, 1992; 14) Young, D.A. and V.L. Hansen, JGR, 110, E03001, 2005; 15) Pronin, A.A. In: Venus GGG, Barsukov et al., eds, 68, 1992; 16) Head, J.W., Geology, 18, 99, 1990; 17) Vorder Bruegge, R.W. and J.W. Head, Geology, 19, 885, 1991; 18) Stofan, E.R. et al., JGR, 97, 13347, 1992; 19) Jackson, M.P.A. and B. C. Vendeville, GSAB, 106, 57, 1994; 20) Bilotti, F. and J. Suppe, Icarus, 139, 137, 1999; 21) Ivanov, M.A., and J.W. Head, LPSC 43, #1037, 2012.

GEOLOGY OF FORTUNA TESSERA: INSIGHTS INTO THE BEGINNING OF THE RECORDED HISTORY OF VENUS.

M. A. Ivanov[1], J.W. Head[2],
[1]GEOKHI, Kosygin-19 Moscow, Russia[2], Brown Univ., Providence RI, USA.
Contact: mikhail_ivanov@brown.edu

Introduction: The V-2 quadrangle (50-75oN, 0-60oE) shows a large portion of Fortuna Tessera, which is among the largest tesserae on Venus [1] and is a good representative of this class of terrain. Tesserae are laterally extensive areas of dense tectonic deformation [2-4] that occurred near the beginning of the observable portion of the geologic history of Venus [5-9]. As such, tesserae provide clues for understanding the broad-scale tectonic regimes at these times and, thus, put important constraints on a variety of geodynamic models of Venus [10-14].

The geological mapping in the V-2 quadrangle is aimed to address several questions about the tessera formation. *Age:* (1) When did tessera form and what are its upper and possible lower stratigraphic limits? (2) Does tessera continue to deform after its fundamental structure is established? *Morphologic and topographic characteristics:* (1) What are the major facies and units of tessera? (2) How do they correlate with topography and can it be related to crustal thickness? (3) What do the boundaries of tessera tell us about the origin of this terrain? *Mechanisms of formation:* (1) What is the sequence of contractional and extensional structures in tessera? (2) What processes, convergent or divergent (or both), played the major role in tessera formation? (3) What is the evidence for formation of tessera by accretion of crustal blocks?

In this study we address some of these questions through investigation of the regional setting of Fortuna Tessera and characterization of its topographic configuration, internal structure, and relationships with the surrounding terrains.

Stratigraphic framework and regional settings: Global survey of relationships among the major units on Venus [15] reveals their consistent relative ages. Tessera appears as the oldest unit, ridge belts and groove belts postdate it. Vast plains units (the older shield plains, psh, and the younger regional plains, rp) superpose the tectonized units and are embayed by younger lobate plains. Tessera Fortuna and the belts form regional highs and separate basins that are filled by the vast plains. Shield plains are exposed closer to the basin edges and regional plains occur in the basin interiors. This correlation of stratigraphy and topography of the units implies that the major topographic features (the highs and the basins) formed before emplacement of regional plains and that the principal topographic pattern has not changed significantly since that time.

Topographic characteristics: A topographic map of the V-2 quadrangle shows that Fortuna Tessera is divided into three major regions. (A) Western Fortuna near Maxwell Montes forms a very broad and high standing (3-4 km) arc-like plateau around the eastern edge of Maxwell. A zone of lower topography occurs at the transition from Maxwell to Western Fortuna. The plateau shows significant (~1 km) high-frequency topographic variations and is disrupted by several topographic depressions that correspond to closed basins. The N edge of Fortuna represents a high (~1.5. km) regional scarp between the tessera and the lowlands of Snegurochka Planitia. (B) Zone of Chasmata displays deep (1-2 km) canyons that outline the western and eastern edges of the zone and separate the western and eastern regions of Fortuna. (C) Eastern Fortuna represents a lower (1-2 km) plateau with less prominent high-frequency topographic variations. The surface of Eastern Fortuna is slightly tilted northward.

Variations of the structural pattern: Near Maxwell Montes, ridges of the tessera (15-20 km wide) are sub-parallel to each other and to the eastern edge of Maxwell (N-S direction). At the E edge of Western Fortuna, the structural pattern of the tessera consists of shorter ridges and mounds that frequently change their width and orientation. Chaotically oriented ridges characterize the Zone of chasmata. Large regions within Eastern Fortuna consist of relatively narrow (5-10 km), long (a few hundred km), straight or curvilinear ridges that are oriented parallel to elongation of the tessera (W-E direction).

Structural facies and plains units: In Western Fortuna there are angular blocks with crisp-looking short and narrow ridges and scarps. A tessera matrix with softer morphology completely surrounds the blocks and overlaps their structures. This pattern resembles the augen-like structure of gneiss and suggests that the blocks may represent older fragments of more resistant materials involved in the formation of tessera. Elongated features with rounded edges in Western Fortuna represent shallow topographic depressions, the interiors of which display stacks of imbricated slabs. The surface of the slabs is morphologically smooth suggesting that they represent fragments of deformed lava plains. Zone of chasmata shows a series of troughs covered by plains that morphologically resemble those outside the tessera region. The plains are mildly deformed and embay structures of the tessera suggesting that they formed in topographic depressions on a tectonically stabilized region.

Relationships of structures and structural zones: In places where relatively old intratessera plains occur, they firmly establish age relationships between contractional (ridges) and extensional (graben) structures of tessera. The plains embay tessera ridges and are cut by a variety of extensional structures, which mean that the ridges are older.

Narrow (10-20 km) and long (100s km) zones divide Fortuna Tessera into a number of structural domains with different structural patterns. The zones usually represent prominent topographic depressions. The easternmost portion of Fortuna Tessera displays a large structure outlined by a series of bent troughs and ridges. The structure consists of two tongue-like features oriented in opposite N-S directions and extending for ~300 km. The syntaxis-like structure in Eastern Fortuna is similar by the structural pattern and the scale to the structures on Earth on both sides of the Indian plate where it collides with the Eurasian plate.

Northern edge of Fortuna: Segments of short ridges that are arranged en-echelon occur on the floor of Snegurochka Planitia to NW of Fortuna [16]. The edges of the segments are bent and turned to each other. This pattern of deformation suggests a strong shear component and may indicate lateral movements of lithospheric slabs relative to each other. Along the N edge of Fortuna there are several places where ridge belts within Snegurochka Planitia are terminated by the edge of the tessera. In some instances, the ridges are bent near the contact with the tessera suggesting stresses oriented parallel to the strike of the ridges. Vast plains units (rp) are not deformed and broadly embay both the tessera and the ridges. These relationships indicate that the deformation of the ridges ceased before emplacement of the plains.

Summary and Conclusions: The results of our study show the following.

(1) Fortuna Tessera formed as a large crustal block before emplacement of vast plains units (shield and regional plains) in the surrounding lowlands.

(2) There is little evidence for contemporaneous formation of the short-wavelength tessera structures and structures of groove and ridge belts along the S edge of Fortuna. At the N edge fragments of ridge belts may have been accreted to the main block of Fortuna.

(3) The surface of regional plains along the S edge of Fortuna is mostly tilted away from the tessera. The same is observed along the N edge of the Eastern Fortuna. Along the NW edge of Western Fortuna the adjacent plains display a moat-like topographic depression. The tilt of the plains can be attributed to a passive, long-wavelength epeirogenic uplift due to gravitational readjustment of a large crustal block of the tessera. The moat at the NW edge of Fortuna may be related to either recent or continued dynamic process (e.g., underthrusting [17]).

(4) Ridges and graben form the surface of tessera [3,4,18,19]. In places where local stratigraphic markers exist (the older intratessera plains [20]) they provide unambiguous evidence that the ridges are primary structures that have been cut and disrupted by the graben.

(5) The topographic characteristics and variations of the structural patterns in Fortuna indicate that the tessera consists of three major sub-regions with different arrangements of major structures: Western Fortuna, Zone of chasmata, and Eastern Fortuna. Four features of Western Fortuna indicate its possible mode of origin. (a) In this region, both the tessera-forming ridges and broader structural domains are aligned parallel to the outer edge of Maxwell Montes and are elongated in a N-S direction. (b) The N portion of Western Fortuna contains augen-like relicts and imbricated basins. (c) The relationships of the relicts with the surrounding tessera indicate that they are fragments of older and more resistant blocks incorporated into the tessera. (d) The topography and structure of the imbricated basins suggest that they represent deformed regions of intratessera plains. These features suggest that Western Fortuna may represent a site of convergent processes.

In the S half of Eastern Fortuna, both the short-wavelength tessera ridges and the larger structural domains are elongated in the same (E-W) direction. The syntaxis structure occurs at the easternmost edge of Fortuna and a series of elongated and triangle-shaped domains characterize the N edge of the region. The orientation and arrangement of structures in Eastern Fortuna is consistent with a model in which the southward displacement of the northern domains imparted stresses toward the southern portions of Eastern Fortuna and caused formation of long parallel ridges there. The structure of the syntaxis is consistent with such a model and may represent a feature similar to those that form on both sides of the India plate [21-23].

Deep troughs that interrupt the tessera structures characterize Zone of chasmata. The trough, thus, are younger structures that cut the crustal block of Fortuna. Mildly deformed plains on the floor of the troughs indicate that little deformation occurred since the emplacement of the plains.

(6) The abruptly terminated and bent ridges at the contact of Snegurochka Planitia with Eastern Fortuna the may suggest that the ridges have been partly underthrust under the crustal block of Fortuna Tessera. Sets of structures and units and their topographic configuration at the NW edge of Fortuna were interpreted as evidence for the underthrusting of the floor of Snegurochka Planitia under Western Fortuna [24]. These observations and interpretations are supported by the unusual arrangements of ridges on the floor of Snegurochka Planitia, which suggest the lateral displacement of lithospheric slabs within the Planitia. Thus, Western Fortuna and Eastern Fortuna probably were affected by the southward displacements of lithospheric blocks of Snegurochka Planitia and their underthrusting under Fortuna.

In summary, our study of Fortuna Tessera reveals evidence for significant lateral displacement of crustal/lithospheric slabs, which may be related to either the upwelling [e.g., 4] or downwelling models [e.g., 12] of tessera formation.

References: 1) Ivanov, M.A. and J.W. Head, JGR, 101, 14861, 1996; 2) Sukhanov, A.L. In: Venus GGG, Barsukov, et al. eds., UAP, 82, 1992; 3) Solomon, S.C., et. al., JGR, 97, 13199, 1992; 4) Hansen, V.L. and J.J. Willis, Icarus, 123, 296, 1996; 5) Ivanov, M.A. and A.T. Basilevsky, GRL, 20, 2579, 1993; 6) Basilevsky, A.T. and J.W. Head, EMP, 66, 285, 1995; 7) Basilevsky, A.T. and J.W. Head, PSS, 43, 1523, 1995; 8) Basilevsky, A.T. and J.W. Head, JGR, 103, 8531, 1998; 9) Ivanov, M.A. and J.W. Head, JGR, 106, 17515, 2001; 10) Parmentier, E.M. and P.C. Hess, GRL, 19, 2015, 1992; 11) Turcotte, D.L., JGR, 98, 127061, 1993; 12) Head, J.W., et. al., PSS, 42, 803, 1994; 13) Phillips R.J. and V.L. Hansen, Science, 279, 1492, 1998; 14) Brown, C.D. and R.E. Grimm, Icarus, 139, 40, 1999; 15) Ivanov, M.A. and J.W. Head, PSS, 2011, submitted; 16) Hurwitz D. and J.W. Head, USGS Map V-1, 2011, in edit; 17) Solomon, S.C. and J.W. Head, GRL, 17, 1393, 1990; 18) Gilmore, M.S., et. al., JGR, 103, 16813, 1998; 19) Ghent, R. and V. Hansen, Icarus, 139, 116, 1999; 20) Ivanov, M.A. and J.W. Head, LPSC131, #1233, 2000; 21) Grosfils, E.B. and J.W. Head LPSC-21, 439, 1990; 22) Tapponier, P., et. al., In: Collision Tectonics, Coward and Reis, eds., Geol. Soc. Spec. Pub., 19, 115, 1986; 23) Tapponnier, P., et. al., Science, 294, 1671, 2001; 24) Ivanov, M.A. and J.W. Head LPSC 38, #1031, 2007.

DYNAMIC PROCESSES IN THE SOLAR WIND AS THE CAUSE OF VENUS IONOSPHERE DISTURBANCES AND LOSS OF MASS.

O. L. Vaisberg, A. Yu. Shestakov,
Space Research Institute RAS, Moscow, Russia. Contact: olegv@iki.rssi.ru, sartiom@iki.rssi.ru

Upper atmosphere and ionosphere of Venus are not shielded from the solar wind flow due to absence of the planetary magnetic field. Mass-loading of the solar wind flow past Venus by exospheric photo-ions leads to loss of atmospheric constituents and to formation of induced or accreted magnetosphere. Other important ionospheric effects caused by the solar wind include intermittent magnetization of ionosphere and strong ionospheric convection from the dayside to the night-side whose magnitude reaches supersonic velocity at the terminator.

The tail of induced magnetosphere is filled with escaping planetary ions making solar wind-induced mass loss an important fraction of total mass losses. Due to existence of dense atmosphere these losses are of not very important factor of atmospheric evolution at Venus. However, predominate loss of lighter atmospheric constituents and lighter isotopes may be important for change of atmospheric composition during the lifetime of the solar system.

Usually solar wind-induced losses are calculated from the set of measurements obtained along the spacecraft trajectories in the tail with some assumptions about distribution across the cross-section of the tail. In calculating average loss rate it is assumed usually that these losses are relatively stable in time. However, observations of cometary plasma tail suggest that non-stationary interplanetary phenomena like coronal mass ejections may cause dramatic one-time loss of cometary ionized material. Some cometary "tail disconnection" events suggest that that sporadic interplanetary phenomena can cause very large cometary plasma losses. These events exemplify similar phenomena at Venus and Mars, and require estimation of transients to total mass loss balance.

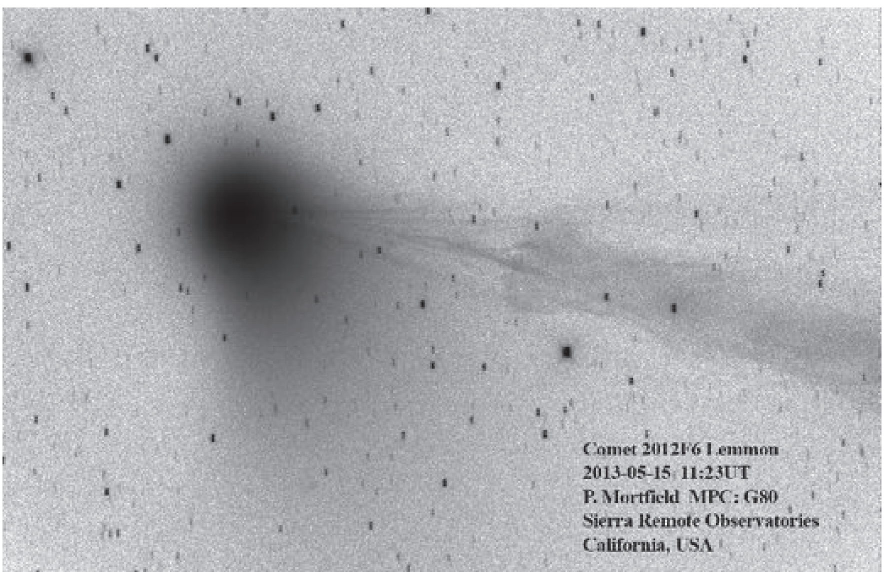

So called "tail disruption" suggesting sudden increase of interplanetary plasma pressure and removal of significant part of cometary plasma mantle.

Another cause of transient induced mass losses at Venus (and Mars) may be Hot Flow Anomalies that form as a result of interplanetary current sheets. These phenomena were studied at the Earth, and were also observed at Venus and Mars. These HFAs lead to very strong disturbances of flow within magnetospeath / ionosheath of Venus with dramatic variations of dynamic pressure on planetary scale. Like CME-associated disturbances, HFA-associated variations of plasma flow should very strongly influence ionosphere of Venus and may lead to additional mass loss of its atmosphere. We show examples of magnetosheath variations associated with HFAs and emphasize the importance of investigations of similar phenomena at Venus as possible source of atmospheric losses.

IONOSPHERIC MAGNETIC FIELDS AND CURRENTS AT VENUS.

Dubinin E.,
Max-Planck-Institute for Solar System Research, Katlenburg-Lindau, Germany

Venus Express spacecraft have provided us a wealth of in-situ observations of characteristics of induced magnetospheres of Venus at low altitudes during solar minimum conditions. At such conditions large-scale magnetic fields are observed deeply in the ionospheres (magnetized ionospheres). The observations again raise a long-standing question about the origin of these fields. The problem is intimately related to the issue of electric current system and their closure. Analysis of the data reveals a lot of features which require a more sophisticated view at the origin and the topology of the ionospheric magnetic fields. Differing perspectives at this problem will be discussed.

STRATIFIED MULTI-LAYER STRUCTURES OF THE VENUS IONOSPHERE FROM VENERA 15 AND 16 RADIO OCCULTATION MEASUREMENTS.

A.L.Gavrik, T.F. Kopnina, E.A. Kuleshov, A.A. Smislov,
Kotel'nikov Institute of Radio Engineering and Electronics, RAS, Fryazino branch, V. A. Vvedensky sq, 1, Fryazino, Russia. Contact: alg248@ire216.msk.su

Since 1975, Venus-orbiting spacecraft have carried out more than 750 two frequency radio occultation measurements of the vertical electron density structure of the ionosphere of Venus: 441 of these have been produced by the Pioneer Venus orbiter between 1979 and 1991; Venera 9 and 10 provided 34 measurements in 1975; Venera 15 and 16 made 155 measurements between 1983 and 1984; Magellan made 20 measurements in 1994 and Venus Express provided 118 measurements between 2006 and 2007. The high coherence and stability of radio signals of Venera 15 and 16 at wave lengths 32 cm and 8 cm, along with the fact, that the refractive amplification at 32 cm in the ionosphere exceeds by factor 6 the refractive amplification at 13 cm used by others researches, have allowed to perform analysis of radiophysical parameters in the Venus ionosphere more accurate. We offer the new technique of the data analysis that allows us to separate influence of noise, ionosphere and atmosphere on the radio occultation results. We report here the presence of stratified multi-layer structures in the electron density from the day side and night side ionosphere of Venus.

From the geometrical optics the linear relation between signal energy and frequency deviation was derived for the spherically-symmetric medium: $X_f(t)=1+\lambda LV^{-2}df(t)dt$, where λ– the wave length, L– distance from the spacecraft to the planetary limb, V=dh/dt is the ray velocity, f– the deviation of the signal frequency caused by the ionosphere, X is the refraction attenuation. Good agreement between the calculated attenuation $X_f(h)$ with observed X(h) has been registered in many occultation events. Coincidence between variations of refraction attenuation X(h) and $X_f(h)$ is indicative of the influence of the plasma stratified layers under investigation. The absence of this correspondence is an indication of the influence of any factors that are not taken into account.

We point out that significant gradient variations in the vertical distribution of the electron density are observed in the region of maximum electron density of the daytime ionosphere at altitudes of 150-175 km. That testifies layered structure of this part of the Venus ionosphere. The results of data analysis reveal the regular existence of the ionospheric layers in the bottom daytime ionosphere at altitudes from 80 up to 115 km. The bottom part of the ionosphere is more variable, than overlying area of the main maximum of the daytime ionosphere. The bottom border of the dayside ionized region can vary in the range of 80-100 km, and gradients of the electron density show strong variability.

In the night-time ionosphere of Venus, variations in the refractive attenuation X(h) coincide with calculated data $X_f(h)$. We observed only one minimum attenuation $X(h) = X_f(h)$ in a single-layer night-time ionosphere, and two minima $X(h) = X_f(h)$ in the two-layer night-time ionosphere of Venus. Below the level of h=115 km ionization on the night side of Venus is absent, since no variations in refraction attenuation X(h).

We observed the bottom ionosphere in all 19 occultations at solar zenith angles between 56° and 87° and in 6 out of 9 occultations near the planet's terminator, but the effect were comparable with noise. In the night ionosphere, none of 25 occultations revealed the bottom plasma layer. Thus, the bottom layers of the daytime Venus ionosphere are permanent and its properties depend on the solar zenith angle. Considerable variations in the bottom layers properties of the Venus daytime ionosphere can be associated with some wave processes in the top atmosphere and in the bottom ionosphere.

The work is partially supported by the RAS Presidium Program № 22 "Fundamental problems of the research and exploration of the Solar system".

RADIO OCCULTATION STUDIES OF INTERNAL GRAVITY WAVES IN THE EARTH'S AND PLANETARY ATMOSPHERES

V.N. Gubenko, A.G. Pavelyev, I.A. Kirillovich, V.E. Andreev, R.R. Salimzyanov,
Kotelnikov Institute of Radio Engineering and Electronics RAS, Vvedenskogo sq. 1, 141190 Fryazino, Moscow region, Russia; Contact: vngubenko@gmail.com

Internal gravity waves (IGWs) modulate the structure and circulation of the Earth's atmosphere, producing quasi-periodic variations in the wind velocity, temperature and density. Similar effects are anticipated for the Venus and Mars since IGWs are a characteristic of stably stratified atmosphere. In this context, an original method for the determination of IGW parameters from a vertical temperature profile measurement in a planetary atmosphere has been developed [1–4]. This method does not require any additional information not contained in the profile and may be used for the analysis of profiles measured by various techniques. The criterion for the IGW identification has been formulated and argued. In the case when this criterion is satisfied, the analyzed temperature fluctuations can be considered as wave-induced. The method is based on the analysis of relative amplitudes of the wave field and on the linear IGW saturation theory in which these amplitudes are restricted by dynamical (shear) instability processes in the atmosphere. When the amplitude of an internal gravity wave reaches the shear instability threshold, energy is assumed to be dissipated in such way that the IGW amplitude is maintained at the instability threshold level as the wave propagates upwards.

We have extended the developed technique [1] in order to reconstruct the complete set of IGW characteristics, including such important parameters as the wave kinetic and potential energy per unit mass and IGW fluxes of the energy and horizontal momentum [2]. We propose also an alternative method to estimate the relative wave amplitudes and to extract IGW parameters from an analysis of perturbations of the Brunt-Vaisala frequency squared [2,4]. An application of the developed method to the radio occultation (RO) temperature data has given the possibility to identify the IGWs in the Earth's, Martian and Venusian atmospheres and to determine the magnitudes of key wave parameters such as the intrinsic frequency, amplitudes of vertical and horizontal wind velocity perturbations, vertical and horizontal wavelengths, intrinsic vertical and horizontal phase (and group) speeds, wave kinetic and potential energy per unit mass, vertical fluxes of the wave energy and horizontal momentum. The results of the wave studies found from temperature data of the RO missions CHAMP and COSMIC (Earth), Mars Global Surveyor (Mars), Venera 15 and 16, Magellan, Venus Express (Venus) have been presented and discussed.

The work is carried out under partial financial support of the RFBR grant №13-02-00526-a and Program №22 of the RAS Presidium.

References:

1. Gubenko V.N., Pavelyev A.G., Andreev V.E. Determination of the intrinsic frequency and other wave parameters from a single vertical temperature or density profile measurement // J. Geophys. Res. 2008. V. 113. № D08109, doi:10.1029/2007JD008920.
2. Gubenko V.N., Pavelyev A.G., Salimzyanov R.R., Pavelyev A.A. Reconstruction of internal gravity wave parameters from radio occultation retrievals of vertical temperature profiles in the Earth's atmosphere // Atmos. Meas. Tech. 2011. V. 4. № 10. P. 2153–2162, doi:10.5194/amt-4-2153-2011.
3. Gubenko V.N., Pavelyev A.G., Salimzyanov R.R., Andreev V.E. A method for determination of internal gravity wave parameters from a vertical temperature or density profile measurement in the Earth's atmosphere // Cosmic Res. 2012. V. 50. № 1. P. 21–31, doi: 10.1134/S0010952512010029.
4. Gubenko V.N., Kirillovich I.A., Pavelyev A.G., Salimzyanov R.R., Andreev V.E. Characteristics of internal waves in the Martian atmosphere obtained from an analysis of vertical temperature profiles of the Mars Global Surveyor mission // Solar System Res. 2013. V. 47. № 5 (in press).

CONTINUED STUDIES OF THE ATMOSPHERE OF VENUS ON THE BASIS OF THE DEVELOPMENT OF LONG-LIVED BALLOONS. / NEXT STEP FOR VENUS INVESTIGATION WITH LONG-LIVING SUPERPRESSURE BALLOONS- AEROBOTS.

Gotlieb V.M., Lipatov A.N., Linkin V.M., Makarov V.S., Khlyustova, L.I., Ekonomov A.P.,
Space Research Institute of RAS, Moscow. Contact: gotlib@iki.rssi.ru, slip@iki.rssi.ru

In this presentation we validate the possibility of long-time in-situ studies of the Venusian atmosphere with the overpressure balloon in terms of technical feasibility, but we also discover new scientific opportunities at flight much longer compared with a unique Vega balloon.

From this point of view, the basic scientific problems are considered that can be raised during the long flight in the atmosphere of Venus and we propose experiments to solve them.

SELECTION OF LANDING SITES FOR THE VENERA-D MISSION.

M.A. Ivanov[1], A.T. Basilevsky[1],J.W. Head[2], L.V. Zasova[3], and E.N. Guseva[1],
[1]GEOKHI, Kosygin-19 Moscow, Russia[2], Brown Univ., Providence RI, USA,[3]SRI, Profsouznaya-84/32 Moscow, Russia[2]. Contact: mikhail_ivanov@brown.edu

Introduction: The record of time when the Earth took shape and began its geological and geochemical evolution has long since been destroyed. The smaller terrestrial planets (the Moon, Mercury and Mars) retain this record and show that principal processes in these times were impact cratering and volcanism. Missing from these planets is the transition from the stable impacted lithosphere to the mobile recycled lithosphere consisting of continents and ocean basins seen on Earth today.

Venus is similar to the Earth in size, bulk density, and position in the Solar System and possesses rich volcanic and tectonic records. The impact craters on Venus suggest that the observable portion of its geologic history extends for about a half-billion years into the geological past. Thus, in contrast to the smaller terrestrial planets, Venus provides an example of the late parts of the spectrum of evolution of terrestrial planets. Nevertheless, conditions on the surface and the global pattern of the volcanic and tectonic landforms indicate that the mode of geological activity on Venus differs radically from that on Earth. The most important difference is the absence of compelling evidence of modern plate tectonics on Venus.

Thus, the two largest terrestrial planets demonstrate different ways of their late geological evolution. The fundamental problem is then: why the geologic histories of Venus and Earth are different and what are the causes of this difference?

Major issues in geology of Venus: The Earth-based studies and interplanetary missions to Venus have resulted in abundant data sets on the surface morphology, global topography and gravity fields, and chemical composition of both the upper portion of the atmosphere and rocks on the surface. These data allowed understanding of the principal details of the Venus geology. However, a variety of fundamental problems remain. Here we formulate a dozen of them and sort them by type of missions oriented to address specific problem. (1) Does non-basaltic crust exist on Venus and where can it be found? (2) What is the variety of the crustal rocks on Venus? (3) What are the composition and the temperature profiles of the lower 10 km of the atmosphere? (4) What additional (to the high D/H ratio) evidence suggests the presence of free water on the surface of Venus in its geological past? (5) How does the near-surface atmosphere interact with the regolith? (6) What is the lithology of the regolith on Venus? (7) What are the types of the tessera precursor materials? (8) How many craters on Venus are truly volcanically embayed? (9) How did volcanism on Venus evolve and what types of volcanic activity have operated on the planet? (10) How did tectonic activity on Venus evolve? What is the evidence for plate tectonics on Venus? (11) What is the history of the long- and short-wavelength topography on Venus? (12) What is the distribution of mass in the crust/lithosphere of Venus?

Answers to these problems are necessary to address the fundamental questions of Venus geology: How did the planet evolve and is Venus geologically (i.e., volcanically and/or tectonically) active now? These problems that encompass the morphological, geochemical, and geophysical aspects of the geologic history of Venus can be addressed by missions of different types, such as landers and a variety of orbiters.

Selection of the terrain type for the Venera-D mission: The Venera-D mission consists of an orbiter, a balloon and a lander and can potentially help to constrain more than half of the above problems, specifically, from 1 through 7. Because measurements of the atmosphere composition and temperature can be done on the way to the surface, the selection of specific landing point will address the problems 1, 2, 5, 6, and 7. Among these, the problems of the possible non-basaltic crust (1), diversity of the crustal rocks (2), and the nature of the tessera precursor material (3) appear to have higher priority.

Landing on tessera permits collection of data that are required to address all three of these major issues of Venus geology.

Tessera (~8% of the surface of Venus [Ivanov and Head, 2011]) was discovered during the Venera-15/16 mission [e.g., Barsukov et al., 1986; Bindschadler and Head, 1991; Sukhanov, 1992] and represents one of the most tectonically deformed types of terrain on Venus. The materials that form the bulk of tessera are heavily deformed tectonically and the surface of the unit is characterized by several sets of intersecting contractional and extensional structures that largely obscure the nature of the preexisting materials at available resolution. Images taken from the lander during its descent and on the ground will improve this situation drastically. A very important characteristic of tessera is that the boundaries of its massifs provide compelling evidence for embayment by materials of the other units. These relationships indicate that tessera represents one of the stratigraphically oldest units on Venus. Both the relatively old age and higher elevation of tessera massifs [Ivanov and Head, 1996] are consistent with the hypothesis that tessera may represent outcrops of the non-basaltic crustal material [e.g., Nikolaeva et al., 1992]. This hypothesis seems to agree with analysis of the orbital NIR observations of the Venus surface [e.g., Hashimoto et al., 2008; Gillmore et al., 2011; Basilevsky et al., 2012]. Thus, tessera appears to be the most important “window” into the geological past of the planet and measurements of composition of the tessera materials may significantly extend our understanding of the geochemical history of Venus.

Unfortunately, a diagnostic characteristic of tessera is its high radar backscatter cross section, which is noticeably higher than that of the surroundings [e.g., Bindschadler et al., 1990]. The radar brightness implies that the surface of tessera is rougher at all scales compared to most other units and landing on this type of terrain may cause failure of the mission.

The vast volcanic plains represent the terrain type that appears to be more permissible for the landing from the engineering point of view. The plains are mildly tectonized and, in general, represent flat, slightly undulating surfaces. Three types of the plains are the most abundant on Venus (cover ~60% of the surface): shield plains, regional plains and lobate plains. The stratigraphically older shield plains are characterized by abundant small (< 10 km across) shield-like features that are interpreted as volcanic edifices [Aubele and Slyuta, 1990; Head et al., 1992; Guest et al., 1992]. The great abundance of the constructs implies that their sources were fairly pervasive and nearly globally distributed while the small sizes of the shields suggest that supply of magma in their sources was restricted. Regional plains that occupy the middle stratigraphic position have generally a morphologically smooth surface with a homogeneous and relatively low radar backscatter. These features strongly suggest that regional plains formed by voluminous volcanic eruptions from broadly, near global, widely distributed sources. The stratigraphically youngest lobate plains consist of numerous radar- bright and -dark flow-like features that can reach hundreds of kilometers in length. The interleaving darker and brighter flows suggest that when lobate plains formed the duration of individual voluminous eruptions and the eruption rates have changed from one episode of activity to the other.

Thus, formation of the vast plains on Venus indicates the progressive change of styles and abundance of volcanic activity on Venus [Ivanov and Head, 2013]. These types of plains have been analyzed during the Soviet Venera landers campaign [Surkov, 1983; Surkov et al., 1984, 1986; Abdrakhimov, 2005] and the collected data have been interpreted in different ways in numerous papers [e.g., Nikolaeva, 1990; Nikolaeva and Ariskin, 1999].

Two major shortcomings of the data collected by the Venera landers largely prevent their robust interpretation. First, the set of detected components was rather small: K, U, and Th only for four landers (Venera-8, 9, 10, and Vega-1) and eight major petrogenic oxides (without Na2O) and S for the Venera-13, 14 and Vega-2 landers. Second, the errors of the measurements are too large (relative errors can reach about 85% e.g., MnO in the data from Vega-2 lander) and introduce great uncertainties in the interpretations (Fig. 1b).

Conclusions: Tessera and three major types of volcanic plains represent the set of appropriate target terrains for the Venera-D mission. Because of its unique morphologic and topographic characteristic and stratigraphic position, tessera has the highest scientific priority. From the engineering point of view, however, this target is the most difficult to reach and a pre-landing analysis of the tessera potential danger must be done by the images taken from a separate descending probe equipped by a high-resolution camera. The major volcanic units appear to be much less dangerous to land on, but the varieties of the plains already have been sampled. The quality of the measurements made on the surface of the plains is not high and re-analysis of the plains at the modern level of measurements may provide key information for unraveling of volcanic history of Venus.

References: 1) Ivanov, M.A., and J.W. Head, PSS, 59, 1559-1600 2011; 2) Barsukov, V.L. et al., JGR, 91, D399-D411, 1986; 3) Bindschadler, D.L. and J.W. Head, JGR, 96, 5889-5907, 1991; 4) Sukhanov, A.L., in: Venus GGG, 82-95, 1992; 5) Ivanov, M.A. and J. W. Head, JGR, 101, 14861-14908, 1996; 6) Nikolaeva, O.V., et al., in: Venus GGG, 129-139, 1992; 7) Hashimoto, G.L., et al., JGR, 113, 2008; 8) Gilmore, M.S., et al., LPSC-42, #1498, 2011; 9) Basilevsky, A.T., et al., Icarus, 217, 434-450, 2012; 10) Bindschadler, D.L., et al., GRL, 17, 171-174, 1990; 11) Aubele, J.C. and E.N. Slyuta, EMP, 50/51, 493-532, 1990; 12) Head, J.W., et al., JGR, 97, 13153-13197, 1992; 13) Guest, J.E., et al., JGR, 97, 15949-15966, 1992; 14) Ivanov, M.A., and J.W. Head, PSS, 84, 66-92, 2013; 15) Surkov, Yu.A., in: Venus 1, 154-158, 1983; 16) Surkov, Yu.A., et al., Proc. LPSC 14th, B393-B402, 1984; 17) Surkov, Yu.A., et al., Proc. LPSC 17th, E215-E218, 1986; 18) Abdrakhimov, A.M., PhD thesis, pp. 143, 2005; 19) Nikolaeva, O.V., EMP, 50/51, 329-341, 1990; 20) Nikolaeva, O.V., A.A. Ariskin, JGR, 104, 18889-18898, 1999.

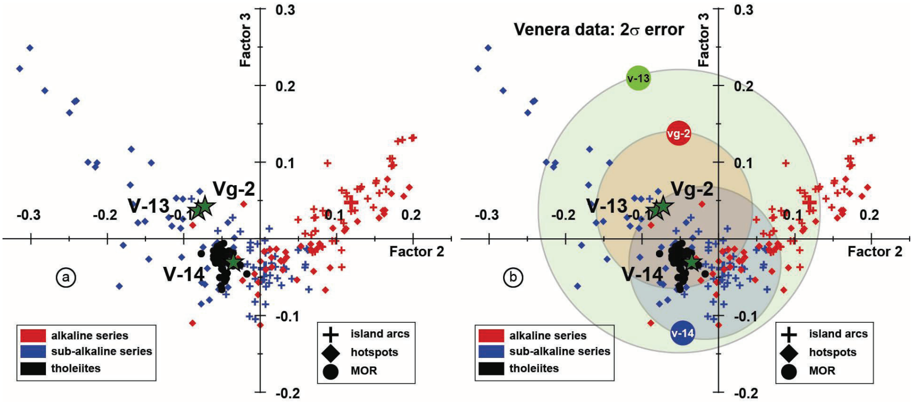

fig. 1. Results of classification of terrestrial basalts from different geodynamic situations by the mean of Q-mode factor analysis. V-13, V-14, and Vg-2 are points for the Venera-13, 14, and Vega-2 landers, respectively, superposed on the factor diagram. a) The points of the Venera data correspond to specific geochemical types of basalts from specific geodynamic situations. b) When the 2-sigma error bars of the Venera data are introduced, the interpretation of the data becomes strongly uncertain.

HYPOTHETICAL LIFE FOUND AT THE VENERA-14 LANDING SITE

Leonid Ksanfomality,
Space research institute of the RAS. 84/32, Profsoyuznaya str., Moscow 117997, Russia. Contact: ksanf@rssi.ru

The hypothesis on possible life on the surface of the planet Venus at high temperatures (735 K) is quite a new subject. It is possible that we shall find an answer to the question about the existence of extraterrestrial life not in other worlds located at a distance of tens of parsecs but on the surface of the closest planet in the Solar system – on Venus. Such opinion was formed after processing of the results of television experiments performed on the surface of Venus by the landers VENERA in 1975 and 1982. In the absence of new landing missions to Venus the study of their panoramas made after their new processing demonstrates many unusual features (Ksanfomality, 2013 a). Despite a possibility of formation and existence of the only known Earth' amino-nucleic acid form of life is excluded on Venus, some details in panoramas of the VENERA television experiment point at the presence of the objects reminiscent of some life forms. The report presents new results obtained and analyzes signs suggesting reality of these entities at the VENERA-14 landing site.

An important question is that of energy sources for life on Venus. In panoramic pictures of the VENERA-14 lander few hypothetical entities of the planet's flora have been found (Figure). Possible pattern of Venus flora were first noted in (Ksanfomality, 2013 b). An interest to the Venusian flora arose due to the relatively numerous objects of the hypothetical fauna found in the processed panoramas of the VENERA landers (1975 and 1982). Even in a non-oxidizing atmosphere of the planet, one can imagine some mechanisms supplying energy for their hypothetical metabolism. As to the energy sources, photosynthesis might be of paramount importance. Direct solar beams, as a rule, do not reach the surface of the planet, but there is sufficient light for photosynthesis. It is most natural to assume that the autotrophic flora of the planet should be a source of energy for its heterotrophic fauna.

Movements of Venusian fauna are much more slowly than that of terrestrial fauna. The objects under consideration are sufficiently large. It is natural to assume that, similarly to that of the Earth, the fauna of Venus is heterotrophic, while a source for its existence is hypothetic autotrophic flora.

Ksanfomality L. V., 2013a. Possible Signs of Life on the Planet Venus. *International Journal of Astronomy and Astrophysics*, 3 (2013) 57-79. doi:10.4236/ijaa.2013.31007.
Ksanfomality L. V., 2013b. Hypothetical life detected on the planet Venus. *International Letters of Chemistry, Physics and Astronomy* 10(1) (2013) 76-89. ISSN 2299-3843.

THE EXOMARS PROGRAMME

O. Witasse[1], J.L. Vago[1], and D. Rodionov[2]
[1]ESA, ESTEC, PO Box 299, 2200 AG Noordwijk, the Netherlands; [2] IKI, Moskow, Russia. Contact: owitasse@rssd.esa.int

The ExoMars Programme is a full cooperation between ESA and ROSCOSMOS ,with some NASA contributions. ExoMars includes two missions, one in 2016 and one in 2018. ExoMars is a preparatory step for the future realisation of an international Mars Sample Return (MSR) campaign during the second half of the next decade. The 2016 mission includes two elements: an orbiting satellite (Trace Gas Orbiter, TGO) devoted to the study of atmospheric trace gases and sub-surface water, with the goal to acquire information on possible on-going geological or biological processes; and an Entry, Descent, and landing Demonstrator Module (EDM) to achieve a successful soft landing on Mars and demonstrate technologies for the 2018 lander. TGO will also provide data communication services for surface missions landing on Mars, nominally until end 2022. The mission will be launched in January 2016, using a Proton rocket, and will arrive to Mars in October 2016. The 2018 mission will deliver a 300-kg-class rover and an instrumented landed platform to the surface of Mars. The mission will pursue one of the outstanding questions of our time by attempting to establish whether life ever existed, or is still present on Mars today. The rover will explore the landing site's geological environment and conduct a search for signs of past and present life, collecting and analysing samples with the Pasteur payload suite from within rocky outcrops and from the subsurface, down to a depth of 2m, using a drill. The platform will carry out scientific environmental measurements at the landing site. This presentation will describe the present status of the ExoMars project, the science objectives, the missions' profile, the instrumentations, and the major upcoming milestones.

THE DREAMS EXPERIMENT FOR THE EXOMARS 2016 MISSION

F. Esposito[1], S. Debei[2], C. Bettanini[2], C. Molfese[1], I. Arruego Rodríguez[3], G. Colombatti[2], A-M. Harri[4], F. Montmessin[5], C. Wilson[6], A. Aboudan[2], M. Zaccariotto[2], S. Abbaki[5], V. Apestigue[3], G. Bellucci[7], J-J. Berthelier[5], J. R. Brucato[8], S. B. Calcutt[6], F. Cortecchia[1], F. Cucciarrè[2], G. Di Achille[1], F. Ferri[2], F. Forget[9], E. Friso[2], M. Genzer[4], P. Gilbert[5], J-P. Goutail[5], H. Haukka[4], J. J. Jiménez[3], S. Jiménez[10], J-L. Josset[11], O. Karatekin[12], G. Landis[13], R. Lorenz[14], J. Martinez[3], L. Marty[1], V. Mennella[1], D. Möhlmann[15], E. Palomba[7], M. Patel[16], J-P. Pommereau[5], C.I. Popa[1], S. Rafkin[17], P. Rannou[18], N.O. Renno[19], P. Schipani[1], W. Schmidt[4], E. Segato[2], F. Simoes[20], A. Spiga[9], F. Valero[21], L. Vázquez[21], F. Vivat[5], O. Witasse[22], S. Yahi[5], R. Mugnuolo[23], S. Pirrotta[23]
[1]INAF - Osservatorio Astronomico di Capodimonte, Napoli, Italy, [2]CISAS - Università degli Studi di Padova, Padova, Italy, [3]INTA, Spain, [4]Finnish Meteorological Institute (FMI),Helsinki, Finland, [5]LATMOS - CNRS/UVSQ/IPSL, France, [6]Oxford University, Oxford, United Kingdom, [7]INAF - Istituto di Fisica dello Spazio Interplanetario (IFSI), [8]INAF-Osservatorio Astrofisico di Arcetri, [9]CNRS, LMD, France, [10]Universidad Politécnica de Madrid, Spain, [11]Space Exploration Institute, Switzerland, [12]Royal Observatory of Belgium,Belgium, [13]NASA, GRC, USA, [14]JHU Applied Physics Lab (JHU-APL), USA, [15]DLR PF Leitungsbereich, Berlin, Germany, [16]Open University, UK, [17]SwRL, Switzerland, [18]GSMA, France, [19]University of Michigan, USA, [20]NASA, GSFC, USA, [21]Universidad Complutense de Madrid (UCM), Spain, [22]ESA-ESTEC, Noordwijk, The Netherlands, [23]Italian Space Agency, Italy.
Contact: Francesca.esposito@na.astro.it

The ExoMars mission is carried out by European Space Agency (ESA) in cooperation with the Russian federal Space Agency (Roscosmos). It is a two-steps mission. It includes an orbiter, the *Trace Gas Orbiter*, and an Entry Descent and Landing Demonstrator Module (EDM), that will be launched on January 2016, and a descent module and surface platform, plus a rover, to be launched in 2018.

The mission will allow Europe to acquire the technologies necessary for the entry, descent and landing of a payload on the surface of Mars, to move on the Martian surface with a rover, to penetrate into the subsurface and acquire samples, to distribute the collected samples to on-board instruments for analysis. From the scientific point of view, the mission will search signs of extant or extinct life forms, will monitor the trace gases in the atmosphere of Mars and their sources, will study the Martian environment during the dust storm season and will perform the first ever measurement of electric field on Mars. The last two represent the scientific objectives of the DREAMS payload on-board the EDM 2016.

DREAMS (*Dust characterization, Risk assessment and Environment Analyzer on the Martian Surface*) is a meteorological station with the additional capability to perform measurements of the electric field close to the surface of Mars. It is an autonomous system that includes its own power supply and control system. It is constituted by the following subsystems (see Figure 1): MarsTEM (thermometer), DREAMS-P (pressure sensors), DREAMS-H (humidity sensor), MetWind (2-D wind sensor), MicroARES (electric field sensor), SIS (Solar Irradiance Sensor), a CEU (Central Electronic Unit) and a battery. All systems in DREAMS have a solid heritage from other missions and have very high TRL.

The ExoMars 2016 EDM mission is foreseen to land on Mars during the statistical dust storm season. DREAMS will have the unique chance to make scientific measurements able to characterize the Martian environment in this dust loaded scenario. DREAMS will perform:

• Meteorological measurements

- The measurement of pressure, temperature, wind speed and direction, humidity and dust opacity will supply the needed parameters to characterize the basic state meteorology and its daily variation at the landing site. Such information will directly be ingested by climate models.

- Characterization of the Martian boundary layer in dusty conditions.

• Hazard monitoring

- DREAMS will provide a comprehensive dataset to help in quantifying hazards for equipments and human crew: velocity of windblown dust, electrostatic charging, existence of discharges, and E.M. noise potentially affecting communications, intensity of UV radiation.

• The first ever investigation of atmospheric electric phenomena at Mars

- A global atmospheric electrical circuit is likely to exist on Mars, between the surface and the ionosphere, with similarities and differences with the Earth's circuit. Atmospheric ionization should be similar to that of the Earth's stratosphere but impact charging through collisions between dust particles moved by the wind and the surface, or between dust particles themselves, is expected to be the dominant charging mechanism. Intense electric fields, possibly capable of producing electrical breakdown, are expected at the time of dust storms and in the vicinity of dust devils.

- Atmospheric electricity is also involved in several processes that have a noticeable impact on the surface and atmosphere. At times of dust storms, electrostatic forces on fine electrically charged dust grains may become larger than aerodynamic forces due to the wind. They are expected to play a significant role in the dynamics (including lifting) of suspended dust particles and their interaction with the surface, thus on the processes that contribute to the erosion and long-term evolution of the surface.

- By energizing the free electrons, the atmospheric electric fields control their interaction with both the surface and the atmospheric gases. They have thus a definite role in the chain of physical and chemical processes that govern the chemical state of surface materials and the production of oxidized constituents in the atmosphere with consequences on the sustainability of proper conditions for life.

DREAMS is an international experiment with hardware contribution from Italy (system, CEU and MarsTEM), Finland (DREAMS-P&H), UK (MetWind), France (microARES), and Spain (SIS). It is in an advanced stage of development. The Flight Model will be delivered to ESA on February 2014.

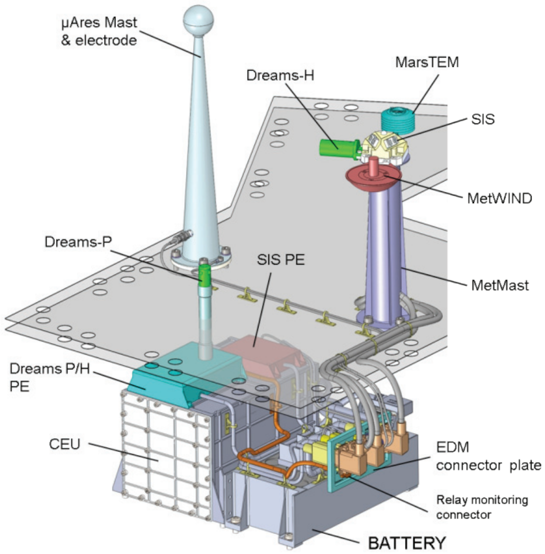

fig. 1. DREAMS payload accommodated on the EDM.

SCIENCE INVESTIGATIONS AT THE EXOMARS 2018 LANDING PLATFORM

D. Rodionov, O.Korablev et al,
Space Research Institute, Moscow, Russia. Contact: rodionov@iki.rssi.ru

The ExoMars Project consists of two missions to Mars launched in the 2016 and 2018 launch opportunities. The missions are part of large international cooperation between ESA and with Roscosmos. In 2018 Descent module produced by Lavochkin Association will land ESA Rover with Pasteur science payload. After Rover egress remaining platform will serve as long-lived stationary science surface platform.

Preliminary payload of surface platform was evaluated. It consists of several instruments, including meteopackage, Fourier spectrometer for atmospheric studies, radiometer, neutron spectrometer/dosimeter, dust suite, set of cameras. Also, robotic arm with sampling device and set of instruments to analyze soil samples is proposed, including gas chromatographer, mass spectrometer with laser ablation, laser gas spectrometer.

SEISMIC EXPLORATION OF MARS WITH VBB SEISMOMETERS.

P. Lognonné[0], D. Giardini[1], S. de Raucourt[0], W.B. Banerdt[2], T.Gudkova[3], D. Mimoun[4], T.Nebut[0], U. Christensen[5] and the VBB-SEIS team,
[0]IPGP-Sorbonne Paris Cité, Univ Paris, France Diderot, lognonne@ipgp.fr, [1]ETHZ, Switzerland, [2]JPL, USA, [3]Institut of the Earth, Moscow, Russia [4]ISAE, France, [5]MPS, Germany

Introduction: A very-broad-band (VBB) seismometer, core of the SEIS experiment (Figure 1), is expected will be deployed on Mars in September 2016 by the NASA/ INSIGHT mission. Such an instrument might also be considered on the Russian lander of the EXOMARS lander-rover mission. The goal of SEIS is to determine the interior structure and seismic activity of the planet. We summarize the instrument performance, present the science goals of INSIGHT and discuss the benefit of deploying a second sensor on Mars.

SEIS noise requirement: Performance and installation quality of VBB seismometer are the most critical parameters to ensure success in terms of seismic signal detection, as negatively demonstrated by the Viking Lander seismometer which was dominated by wind during the day and was weakly sensitive to ground motion during the night (due to emplacement on the lander deck). The InSight seismometer will be robotically installed of the instrument on the ground and include a Wind/Thermal Shield. The improvement of the InSight-VBB requirement over the Viking capability is 1000× for body waves (1 sec) and 65000× for surface waves (20 sec), equivalent to 2 and 3.2 body wave (m_b) and surface wave (m_s) magnitudes respectively.

Seismic and impact signal amplitude estimation: Theoretical estimates from thermoelastic cooling and calculation of the seismic moment release from observed surface faults predict a level of activity ~100× greater than observed shallow moonquake activity. This level would provide ~50 quakes of seismic moment ≥10^{15} Nm (roughly equivalent to terrestrial magnitude m_b=4) per (Earth) year, and ~5× more quakes for each unit decrease in moment magnitude. A few large quakes with moment in the range 10^{17}– 10^{18} Nm might also be expected during the full Mars year nominal mission duration, enabling the detection of free oscillations on the vertical component (Figure 2).

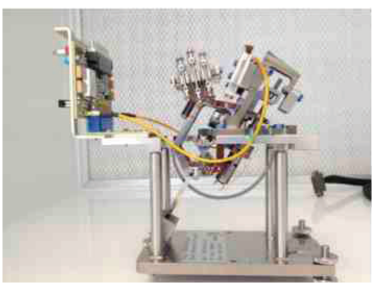

fig. 1. VBB5 sensor with its Earth compensation mass, with its proximity electronics. Two or three such oblique sensors can be used for recomposing a 2 axis (Z+H) or 3 axis (3+2H) VBB seismometer. INSIGHT will deploy a 3 axis VBB, with a complementary 3 axis SP. Both sensors are operated by a 24 bits data logger.

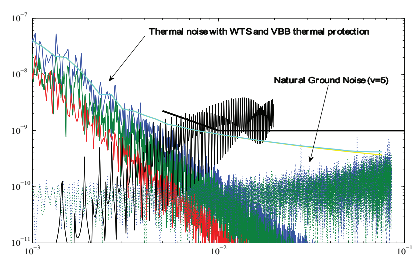

fig. 2. Amplitude of a 3x10^{17} Nm marsquake free oscillation signal compared to instrument noise (black curve is SEIS requirement, cyan is expected capability) and environment noise (left, temperature, right, pressure, for day, sol, night in blue, green, red respectively). One or two such quakes are expected to occur every 2 years.

From InSight to a 2 VBB network: As only one seismic station is available with INSIGHT, structure inversion will be performed using: (i) Secondary seismic data which do not depend on the event location: e.g., free oscillation frequencies for the largest quakes constraining the interior down to 200 km and receiver functions constraining the crust-mantle discontinuity below the landing site; (ii) Seismic impact data from impacts post-located by a Mars orbiter; (iii) Seismic data associated with events with more than 3 different wave arrival time determinations (for V_s inversion with constant V_p/V_s) or more than 4 (for full V_p, V_s inversions).

A second VBB will greatly improve the science return and will allow to address new science objectives, in addition to extending the coverage of the seismic monitoring of the planet. By providing 2 sets of P,S, and Rayleigh arrival times, plus azimuth, it will allows to locate quakes, to better determine the event depth and to study the deep interior structure with phases recorded, for the same quake, at different epicentral distances, which will give access not only to the mantle body waves, but also to the core reflected and refracted phases. At longer period, cross-correlation will be possible, in order extract from noise records the surface green function between the two locations, which will allows a very precise sounding of the Martian upper mantle.

DIODE LASER SPECTROSCOPY FOR MARTIAN STUDIES.

I. Vinogradov[1,2], A. Rodin[2,1], O. Korablev[1], V. Barke[1], A. Klimchuk[2,4], M. Gerasimov[1], N. Ignatiev[1,2], A. Fedorova[1,2], A. Stepanov[1], I. Filatov[2], A. Titov[3], A. Venkstern[1], M. Barke[1], A. Sapgir[1], M. Zaitsev[1], O. Roste[1], Yu. Lebedev[1], A. Kalyuzhnyi[3], O. Grigoryan[3], A. Nadezhdinskii[4,2], M. Spiridonov[4], Ya. Ponurovskiy[4], G. Durry[5], L. Joly[5], J. Cousin[5], N. Amarouche[6],
[1]Space Research Institute (IKI), 117997, 84/32 Profsoyuznaya Str., Moscow, Russia;[2]Moscow Institute of Physics and Technology, Institutsky Dr. 9, Dolgoprudny, Moscow Region, Russia, [3]Special Design Bureau of Space Device Engineering of the Space Research Institute, 249100, Tarusa, Kaluga Region, Russia, [4]Prokhorov General Physics Institute, 119991, Vavilov Str., 38, Moscow, Russia; [5]GSMA, UMR CNRS 7331, Université de Reims, BP 1039, 51687 Reims, Cedex 2, France; [6]Division Technique de l'Institut National des Sciences de l'Univers, CNRS, 92195 Meudon Cédex, France. Contact: imant@iki.rssi.ru

A conception of Martian atmosphere and soil volatiles studies have been developed on the basis of tunable diode laser spectroscopy by collaboration including IKI RAS, MIPT, GPI RAS and University of Reims, France. An experiment, named as M-TDLAS, have been proposed for the Landing Platform scientific payload of the coming soon ExoMars-2018 mission.

The M-TDLAS apparatus is intended for long-term studies of:

- chemical and isotopic composition of atmosphere near the Martian surface, and its diurnal and seasonal variations,
- chemical and isotopic composition of Martian soil volatiles at the location of the Landing Platform, and its diurnal and seasonal variations,
- integral chemical and isotopic composition of Martian atmosphere at low scales of altitude at the Landing Platform location area, and its variations in respect to local time at the light time of a day,
- thermal and dynamic structure of the Martian atmosphere at low scales of altitude at the Landing Platform location, and its variations in local time at the day-light time.

The M-TDLAS studies are based at series of regular periodic measurements of molecular absorption spectra along the M-TDLAS optical path trajectories, which include:

- active measurements in a Herriot multi-pass optical cell, which is directly linked to the outer atmosphere,
- active measurements in a closed optical capillary cell, which is linked to a pyrolitic cell of the Martian Gas Analytic Package (MGAP), in a similar way as it have been designed earlier for the Phobos-Grunt Lander mission,
- passive heterodyne measurements at the Solar occultation open path, which is co-directional with the open optical path of the FAST experiment (Fourier spectrometer for Atmospheric Components and Temperature).

Measurements will take place at series of narrow-band intervals of 2 cm^{-1} wide, with spectral resolution of ~3 MHz (~0.0001 cm^{-1}), which provides for detailed contour resolution of spectral lines. Taking into account high precision of relative absorption measurements in the line contour, being of order $10^{-4..-5}$ ($10^{-3..-4}$ for measurements at the Solar occultation open path), this method provides for realization of:

- monitoring content variations of CO_2, H_2O, CH_4 and of several other molecules,
- measurements of isotopic ratio D/H, O^{18}/O^{16} in water vapor and of C^{13}/C^{12}, O^{18}/O^{16} in CO_2 with precision of 0.1..1.0%%,
- measurements of temperature and pressure vertical profiles, of water vapor contents and of wind velocity projection to the direction of Sun.

Based on the M-TDLAS measurements, we expect to receive data essential to specify physical and chemical interactions between surface and atmosphere for Mars by measurement of diurnal and seasonal variations of H_2O and CO_2 main molecules and of their isotopes, of soil volatiles H_2S, NH_3, C_2H_2 and others. Data related to seasonal variations of H_2O and CO_2 vertical profiles, as well as other atmospheric parameters, will be obtained by detailed recording of molecular absorption line contours during one Martian year. Continuous long-term measurements near the surface and in the atmospheric column at the fixed point of landing will provide contribution into campaign on search of methane in the Martian atmosphere.

This work is supported by the Presidium RAS Program 22

INVESTIGATION OF ATMOSPHERE-MAGNETOSPHERE CONNECTIONS AND ATMOSPHERIC LOSSES AT MARS

Vaisberg O.L.[1], Chernouss S.A.[2], Kirillov A.S.[2], Sosonkin M.G.[3], Ivanov Yu.S.[3], Shefov N.N.[4], Moiseev P.P.[5], Rodionov I.D.[6], Semenov A.I.[4], Berthellier J.-J.[7], Leblanc, F.[7], Syniavskyi I.I.[3] , Fred Sigernes[8], Koynash G.V.[1], Shestakov A.Yu.[1], Zhuravlev R.N.[1], Moiseenko D.A.[1], Fedorenko Yu.V.[2], Roldugin A.V.[2], VictorovA.I.[5], Mityurin M.V.[5], Moryakin S.A.[5], Zherebtsov E.A.[5], Kozura A.V.[5],

[1]Space Research Institute RAS, [2]Polar Geophysical Institute KSC RAS, [3]Main Astronomical Observatory of Ukraine, [4]Institute of Atmospheric Physics, RAS, [5]NPP Astron-Electronics, [6]Institute of Chemical Physics RAS, [7]LATMOS, France, [8]Kjell Henriksen Observatory, UNIS, Norway

We are describing an optical experiment for investigation of nightglow of Mars, aeronomic phenomena, helium fluorescence, magnetospheric tail, and escape of planetary ions. Specifically, proposed experiment aimed to investigation of outer envelope of Mars: upper atmosphere and association of its connections with processes in accretion magnetosphere, including atmospheric losses induced by the solar wind. It includes: **1.** Registration of spatial distribution of night-side atmospheric glow on Mars in order to determine spatial and temporal properties of electron precipitation for investigation of source regions of these electrons, **2.** Registration of spectra of night-side glow for estimation of the energy of precipitation electrons and for analysis of kinetics of electron-excited molecules at different altitudes at Mars, **3.** Registration of helium emission 1083 nm at dusk and down for determination of He number density, its height distribution and its variations, and **4.** Measurements of CO^+ (O^+, O_2^+, CO_2^+) emission at night-side for determination of atmospheric losses through magnetospheric tail.

To study mentioned phenomena we propose the set of instruments that may be used in mission to Mars. Experiment includes 4 optical sensors: all-sky camera, spectrograph, and two photometers.

For investigation of spatial and spectral characteristics of night-side upper atmosphere we have chosen spectral interval 200-230 nm. Observations of Martian night glow will be performed with two instruments: all-sky camera (2π field of view), that measures emission in 200-230 nm band (CO) and narrow-angle spectrograph with 1800 – slit in spectral range 200-230 nm with resolution ~ 0.5 nm. This spectral range almost completely free of absorption by O3 and CO2 Recorded spectrum is attributed to specific emitting regions with help of all-sky camera.

He emission at 1083 nm is observed with narrow-angle (~ 50) fast-lens photometer. 1083 nm emission of He depends not only on He number density but also on content of the atoms and molecules with provide 20-25 eV photoelectrons due to their ionization by solar 30.4 nm emission. Therefore the measurements of He emission will provide information on excitation mechanisms and altitude composition of Martian upper atmosphere.

Observations of escaping ions through the flanks of the tail will be performed with spectrophotometer of emissions of O^+, CO^+, O_2^+ or CO_2^+ ions of that scatter solar light. With observations along the tail it is possible to use increased optical thickness and study the acceleration of these ions along the tail.

This suite of 4 instruments uses one electronics box. Total estimated mass is about 1.7 kg. Instruments can be installed on satellite, rower or stationary platform. Satellite provides better coverage while rower or stationary platform gives opportunity to increase the signal to noise ratio through longer accumulation of the signal and register temporal variations of intensity, Instruments can be used for investigation of other planets, specifically the Venus. Prototypes of 4 instruments exist.

MOURA MAGNETOMETER AND GRADIOMETER FOR PLANETARY MAGNETIC MINERALOGY

Marina Diaz-Michelena[1], Rolf Kilian[2],
[1]INTA, Torrejon de Ardoz, Spain; [2]Trier University, Trier, Germany.
Contact: diazma@inta.es

MOURA magnetometer and gradiometer is a miniaturized and compact instrument (72 g total mass: sensor head + electronic box) devoted to the measurement of the magnetic field and its spatial derivative on the surface of Mars. The instrument is conceived to measure the spatial variations of the magnetic field in the frame of MetNet Precursor Mission, where the instrument is deployed in the inflatable structure of the lander.

However, the maximum potential of this kind of instrument lies on the capabilities they have when they are provided with some mobility, i.e. on board spacecrafts, aircrafts, balloons, rovers, etc. Amongst these, magnetometry on board rovers is of particular importance in planetary magnetic mineralogy because it provides high spatial resolution surveys (HSRS).

In this work it is presented the potential of MOURA magnetometer as a high spatial resolution instrument with several Mars analogous on Earth.

RADIATION INVESTIGATIONS FOR EXOMARS AND LUNA-GLOB MISSIONS

J. Semkova[1], T. Dachev[1], St. Maltchev[1], B. Tomov[1], Yu. Matviichuk, [1] P. Dimitrov[1], R. Koleva[1], I. Mitrofanov[2], A. Malahov[2], M. Mokrousov[2], A. Sanin[2], M. Litvak[2], A. Kozyrev[2], V. Tretyakov[2], D. Golovin[2], S. Nikiforov[2], A. Vostrukhin[2], F. Fedosov[2], N. Grebennikova[2], V. Benghin[3], V. Shurshakov[3], V. Petrov[3],
Space Research and Technologies Institute, Bulgarian Academy of Sciences, Sofia, Bulgaria; Space Research Institute, Russian Academy of Sciences, Moscow, Russia, State Scientific Center of Russian Federation, Institute of Biomedical Problems, Russian Academy of Sciences, Moscow, Russia. Contact: jsemkova@stil.bas.bg

Deep space manned missions are already a near future of astronautics. Radiation risk on such a long-duration journey, the greater part of which takes place in interplanetary space, appears to be one of the basic factors in planning and designing the mission. The radiation field in the interplanetary space is complex, composed by galactic cosmic rays, solar energetic particles, and secondary radiation produced in the spacecraft materials and in the biological objects. The paper relates to scientific objectives and experiments for investigation of the radiation environment to be carried out during the missions under development ExoMars and Luna-Glob. Described are the: 1) 2D particle telescope Liulin-MO for measurement the radiation environment onboard the ExoMars TGO around Mars as a part of the Russian FREND instrument and 2) Liulin-L experiment for measurement the radiation doses and particle fluxes in 3 detectors located in perpendicular directions along the axes of the Luna-Glob Orbiter.

CHANG'E-3/4 LUNAR LANDING MISSIONS AND LUNAR RADIO SCIENCE EXPERIMENTS.

J. Ping[1,2], M. Wang[1], C. Li[1,2], X. Lu[1], Z. Wang[1,2], Y. Yang[1,2], and W. Li[1]
[1]National Astronomical Observatory, CAS (20A Datun Rd., Chaoyang, Beijing, 100012, China; [2]University of Chinese Academic of Sciences ,Beijing, China. Contact: jsping@bao.ac.cn

Overview:

China will launch the 1st lunar landing mission with a rover this year. A backup sister landing and rover mission, Chang'E-4, with identical payloads of Chang'E-3 will be launch and landed at different area of the Moon. They compose the main part of the 2nd phase of Chinese lunar scientific exploration projects. Together with the various in-situ optical observations around the landing sites, missions will also carry out 4 kinds of radio science experiments, cover the various lunar scientific disciplines as well as lunar surface radio astronomy studies.

Chang'E-3/4 lunar landing missions[1,2]:

After the successful lunar orbiting missions of Chang'E-1/2, China will launch the Chang'E-3 lunar landing and rover mission at the end of 2013. Launching mass of the Chang'E-3 is ~3.7 ton, lander mass is ~1.2 ton, rover mass is 120kg with scientific payloads of 20 kg. Some important techniques will be realized, including lunar soft landing, lunar surface rover exploration and surviving over lunar night, deep space communications and remote control operation, rocket directly launched into the earth-moon transfer orbit and other key technologies. The real-time radio altimeter and laser altimeter system onboard the spacecraft platform will support the autonomous soft landing operation. This mission is the key one of Chinese lunar landing exploration phase. Figure 1 shows the configuration of landing mode and rover mode.

fig. 1. Chang'E -3/4 mission 1:1 modes: lander (Left) and rover (right). (Follow Xinhua News)

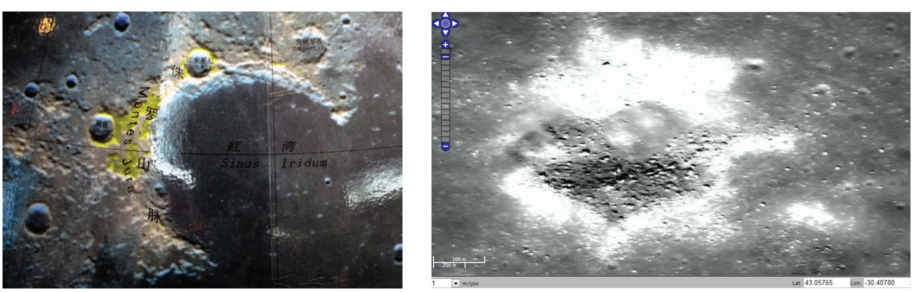

fig. 2. Image of Sinus Iridum taken by Chang'E orbiter (Left) and a younger crater in it (Right).

The key payloads onboard the lander and rover include the near ultraviolet telescope, extreme ultraviolet cameras, ground penetrating radar, very low frequency radio spectrum analyzer, which have not been used in earlier lunar landing missions. Optical spectrometer, Alpha Paticle X-ray spectrometer and Gama Ray spectrometer will also be used this time. The mission will use extreme ultraviolet camera to observe the sun activity and geomagnetic disturbances on geo-space plasma layer of extreme ultraviolet radiation, study space weather in the plasma layer role in the process; also will carry the first time lunar base optical astronomical observations, research extrasolar planetary systems, and active galactic nuclei starquake and AGC. Most importantly, the topography, landforms and geological structure will be explored in detail. 5 candidate landing areas have been selected, including Mare Nectaris, Mare

Humorum, Copernicus crater area, Kepler crater area and Sinus Iridum as the priority choice. Figure 2 shows the images of Sinus Iridum with an average young crater inside it. Chang'E-4 mission will be the full state backup mission of Chang'E-3, landed at different area.

Radio Sciences in Chang'E 3/4:

4 kinds of radio science experiments have been planned in Chang'E 3/4 landing missions: 1) HF and VHF duel-band penetrator radar on the rovers; 2) very low frequency through HF radio astronomy on the surface of Moon; 3) same-beam X-band VLBI for precise positioning of rover; 4) precise radio phase ranging for lunar rotation and dynamics.

HF and VHF duel-band penetrating radar: the radar has center frequencies at 30MHz and 50MHz with bandwidth of 15MHz for each, linear polarized antenna to study the subsurface structure of landing area. In the mission LRS of SELENE/KAGUYA project, Japanese researchers obtained the lunar subsurface structure of 5~10 KM deep with resolution of dozens meters, where the igneous lunar basalt filling at mare area was firstly measured with the maximum thickness of 500~600 meters. Lunar regolith and lunar crust subsurface of shallower than 3km will be firstly studied by using the duel-band GPR on the rover with very high resolution. The thickness of regolith of the soft landing area will be measured [3].

Very low frequency radio astronomy: frequency from several KHz through 10MHz, single polarized dipole antenna, with a spectra analyzer. Due to the frequency truncate by ionosphere of the earth, cosmic radio signal with frequency below 10MHz will be absorb and reflect back to the space. We cannot receive the natural cosmic signal of this band on the ground. To overcome this problem, two sets of antenna and spectra receiver system are installed on the two landing missions separately. The spectra analyzers have frequency resolution better than 1KHz. This instrument is a kind of proto type or path finder for lunar surface low frequency radio network array, or for lunar far side low frequency array in the future. On the surface of the Moon, this payload will be first time to carry the studies of extra-terrestrial solar space VLF radio observations for solar radio burst, space particle flow, kilometric wave radiation, coronal mass ejections and planetary low frequency noise.

Same beam VLBI tracking: Two VLBI beacon transmitters with high stable oscillators are installed on the Chang'E 3/4 landers and the rovers separately. Beacons will transmit X band DOR wave or single carrier wave back to the Earth. The Chinese VLBI network and the new developed Chinese deep space tracking station will observe the DOR signal from two beacons simultaneously by the main lobe of each antenna. In the differential DOR observables, the effects due to the tracking station, the atmosphere and the ionosphere of the earth, as well as the effects due to the lunar rotation, tides and liberation can be cancelled dramatically. Then, the high precise relative position of the rover to the lander of the same mission will be obtained at each observation point of the rover. Based on a simulation results, the precision of relative positioning can reach about 10m or higher [4].

Lunar Radio Phase Ranging: Since early Luna and Apollo missions set 5 optical corner reflector systems on the surface of the Moon, Lunar laser ranging have been played key role on measuring the lunar rotation, Physical liberation and surface solid tides. However, the bad weather on laser site, the full Moon and new Moon phase may block the optical observation. Similar to Luna-Glob landers, together with the VLBI radio beacons, the radio transponders are also set on the Chang'E-3/4. Transponder will receive the uplink S/X band radio wave transmitted from the two newly constructed Chinese deep space stations, where the high quality hydrogen maser atomic clocks have been used as local time and frequency standard. The clocks between VLBI stations and deep space stations can be synchronized to UTC standard within 20 nanoseconds using satellite common view methods. In the near future there will be a plan to improve this accuracy to 5 nanoseconds or better, as the level of other deep space network around world. Radio science receivers have been developed by updating the multi-channel open loop Doppler receiver developed for VLBI and Doppler tracking in Yinghuo-1 and Phobos-Glob Martian missions. This experiment will improve the study of lunar dynamics [5], by means of measuring the lunar physical liberations precisely together with LLR data. Above method may be used in the next Chinese Martian mission.

References:

[1] http://baike.baidu.com/view/2241905.htm
[2] http://scitech.people.com.cn/GB/11965565.html
[3] Zhang Q. and Fang G. (2011), Journal of Electronics and Information Technology, V33(2): 424-428
[4] Liu L. (2011), Master Degree Thesis, Shanghai Astronomical Observatory, CAS, Shanghai.
[5] Ping J. et al. (2012), 3M-S3, Moscow, Russia.

MOON GEODETIC VLBI SYSTEM

A. Gusev[1], O. Titov[2],
[1] Kazan Federal University, 18 Kremlevskaya str., Kazan, 420008, Russia, Contact: Alexander.Gusev@ksu.ru ; [2] Geoscience Australia, PO Box 378 Canberra 2601 ACT Australia. Contact: oleg.titov@ga.gov.au

Geodetic VLBI network managed by the International VLBI Service provides high accurate positions of the reference radio sources, radio telescope coordinates, Earth Orientation Parameters (EOP), etc. A small radio telescope being installed on the Moon surface and incorporated to this existing network will help to improve these traditional IVS products by a factor of ten or even more. In addition, this new instrument will be able to detect some known effects with an unprecedented accuracy, and new effects which are not available for other ground-based instruments or space missions.

RAMAN CHARACTERIZATION OF MINERALS IN THE RECENTLY FALLEN MARTIAN METEORITE TISSINT.

S. Voropaev[1], K. Lorenz[1], A. Eliseev[2], D. Petukhov[2],
[1]GEOKHI RAS, Moscow, Russia; [2] M SU, Chemical Department, Moscow Russia.
Contact: voropaev@geokhi.ru

Introduction:

Martian meteorite Tissint, the subject of this study, was found in the Morocco desert, near village Tissint, in 2011. It is one of a group of meteorites thought to be from Mars on the basis of glass inclusions that contain rare gas and nitrogen isotope compositions matching those of the Martian atmosphere as determined first by the Viking spacecraft. It is a 'shergottite', a basaltic rock generally similar to the Martian meteorite Shergotty [1]. Pigeonite, augite and maskelynite (plagioclase made isotropic by shock due to impact) are the major minerals in Tissint. It contains coarse crystals (xenocrysts) of olivine and orthopyroxene that are more magnesian than their counterparts in the finer grained basaltic matrix [2]. Using the Raman map procedure, we have identified and characterized the major, minor and trace mineral phases in rock chips of the Tissint. Raman spectra are shown for pyroxene, olivine, maskelynite (shocked, isotropized feldspar), magnetite, ilmenite, merrillite, apatite, an Fe sulfide, calcite and hematite.

Experimental setup:

Renishaw InVia Reflex Spectrometer System was used for all of the Raman measurements reported here. High power near infrared diode laser, 300 mW at 785 nm, was used as the excitation source for most measurements; DPSS laser radiation, 100 mW at 532 nm, was used for a few. The Raman spectrometer has a spectral resolution of 1–2 cm^{-1}. Extremely high efficiency 250 mm focal length spectrograph (>30% throughput in spectrograph) was used for all Raman measurements. It provides a laser spot size continuously variable from 1 to 300 µm in diameter at the focal plane (objective and excitation wavelength dependent) with fully optimized beam path.

Scanning electron microscopy (SEM) and energy dispersive X-Ray microanalyses (EDX) were performed on a Leo Supra 50VP microscope equipped with Oxford-Instruments X-Max detector. Measurement parameters of the microscope system during analysis were: low vacuum (N_2, 40 Pa), 15 kV electron beam, working distance 7 nm. VPSE detector and magnifications from 200x to 2500x. The X-Ray microanalyses were done by taking EDX spectra from selected areas and by mapping of sample area. Identification and quantification of the elements were done after ZAF-correction. Energy resolution of the EDX detector was 129 EV for the K-alpha Mn (5,898.8 EV).

Results and Discussion:

Raman spectra provide us with information on compositional variations of pyroxene, olivine and Fe–Ti–Cr oxides and modal proportions of the Tissint's rock. Compositions and variations in compositions of major silicate minerals (pyroxene and olivine) on the basis of Raman peak positions are consistent with those obtained in studies by SEM-EDX analyses. The variations in composition of the silicate minerals represent different stages of crystallization during the formation of this rock near the Martian surface similar to the analyses of another Martian SNC-meteorite EETA79001[3].

During planetary surface exploration, a high priority is to identify and characterize surface materials, especially to do definitive mineralogy, in order to understand Mars's evolutionary history. We determinate mineral and chemical composition of Tissint and make estimation of the relative proportions of different minerals in a Martian rock. Because we know the chemical and physical conditions under which individual minerals form, we will learn about past Martian environmental conditions from such detailed mineralogical information. The mineralogical record in surface rocks is expected to reach back in Martian history from relatively recent alteration of rock surfaces to past stream and lake environments, potentially to hydrothermal settings within the upper martian crust and to the planet's early igneous chemical differentiation. With better knowledge of Mars' past and present environments, we can speculate more rationally on the possible development of life on that planet.

References: [1] F. Rull et al.. 2004. J. Raman Spectrosc. 35: 497–503. [2] H. Chennaoui Aoudjehane et al. 2012. Science, 338 (6108): 785-788. [3] A. Wang et al. 2004. J. Raman Spectrosc.35: 504–514.

RESURFACING EVENTS ON MARTIAN OUTFLOW CHANNELS: A CASE STUDY OF HARMAKHIS VALLIS IN THE EASTERN HELLAS RIM REGION.

S. Kukkonen, V. –P. Kostama, A. I. Rauhala and J. Raitala,
Astronomy, Department of Physics, P.O. Box 3000, FI-90014 University of Oulu, Finland. Contact: soile.kukkonen@oulu.fi

Introduction:

Harmakhis Vallis is one of the four large-scale outflow channel systems (Dao, Niger, Harmakhis and Reull Valles) which cut the eastern rim region of the Hellas impact basin on Mars. It is ~800 km long and located ~450 km south of Hadriaca Patera and ~1100 km southwest of Tyrrhena Patera cutting the surrounding suites of sedimentary and volcanic material, and thus being one of the youngest features on the area. Due to the close proximity to the volcanic features, Harmakhis Vallis is likely to have been formed by the mobilization and releasing of subsurface volatiles by volcanic heat as the other close outflow channels [1–7]. Thus it is in a key role when we are timing the volatile-driven activity on the region.

Previously, the Harmakhis Vallis region has been mapped based on the Viking imagery [3, 8–9]. There are also several works which focus on different geological events [e.g., 10–13] or only on some limited regions [i.e., 14] of the area. In our work [see also 15] we map and date by the crater counting method [e.g., 16–18] the Harmakhis Vallis region in detail by using MRO's high-resolution CTX and HiRISE images. The purpose of this study is to outline the events which formed the geologic features and units observed in the region of Harmakhis Vallis and by doing so provide further understanding of channel evolution.

Characteristic and morphology of the channel:

Harmakhis Vallis resembles the other outflow channels in the eastern Hellas rim region in many aspects. It is a deep (~0.3-1.6 km), steep-sided, relatively wide (~9-25 km) and morphologically prominent feature along its entire extent. One of the most prominent features of Harmakhis Vallis is that it is not a continuous channel. Based on the morphologic characteristics, Harmakhis Vallis can be divided into four segments: 1) the head depression, 2) the barrier surface, 3) the main channel and 4) the terminus (Fig. 1a).

Head depression. Harmakhis Vallis starts as a full size structure with a broad (~38 km wide, ~90 km long and in places even ~1.6 km deep), flat-floored, steep-walled and closed depression close to the end of another channel, Reull Vallis. Except for a few blocks which might be remnants of the original depression collapse, the surface is covered at least by three lateral and possible ice-rich flows, which originate from the interior walls and in places from the surrounding pitted plains and debris aprons (Fig. 1b). Based on the crater counting, the age of the covering flows varies from 179 Ma to 1.12 Ga, which are (due to the ice sublimation and thus the crater erosion) the younger age limits for the formation of these features. All of the units have also suffered from the later resurfacing processes.

The barrier surface. After a well-defined head depression, Harmakhis Vallis ends abruptly and starts again after an ~83 km distance to southwest. This significantly shallower part of the channel, "the barrier surface", separates Harmakhis Vallis' head depression from its main valley (Fig. 1c). It has been suggested that this part of the channel formed by sinking and partly collapsing due to the subsurface flowing [e.g. 14]. The small and shallow valleys (from 1 km to 10 km wide) which cut the barrier surface represent the channel's on-surface connection. These valleys are also mainly covered by a viscous flow for which we dated an age of 353 Ma. At least two resurfacing events were also found.

The main channel. The main channel starts as an ~4 km deep and ~27 km wide valley. When it runs towards the Hellas basin, the channel becomes shallower and shows evidence of the flooding levee. In the main channel, too, the original surface seems to be covered due to the younger resurfacing processes. In addition, in places the channel's walls have collapsed so that the floor is difficult to recognize (Fig. 1d). On the main channel, we mapped four large-scale later ice-related flow-units which seem to originate from the channel walls, but the flows are also partly parallel to the channel. Based on the crater counting, these units are clearly younger than the units in the head depression or on the barrier surface. In places, the biggest craters do not fit to the isochrones at all, but where they fit, the oldest observed age is only ~75 Ma. In addition to this, three resurfacing periods were dated. The incorrect fitting might indicate that the duration of the geological events has varied in the different parts of the units, or like in the case of the possible ice-content flows in the Harmakhis Vallis head depression, the sublimation has caused the original crater eroding.

The channel terminus. Harmakhis Vallis becomes shallower and wider upon reaching the floor of the Hellas basin. Eventually it disappears in the topography. The units on the terminus are clearly smoother and there are no large-scale flow-units similar to those found on the other parts of the channel.

Summary and conclusion:

The preliminary results of the crater counting have been summarized in Fig. 1e. The Harmakhis Vallis fluvial system has been modified throughout by the younger geological events, which are now seen as the channel covered in ice-facilitated flows. However, the age of these flows clearly varies in different parts of the channel.

On the head depression and barrier surface, the crater counts give us systematically older (>170 Ma) ages than for the flows in the main channel (<70 Ma). This does not necessarily mean that the flows have formed at different times or due to different events, but that the duration of the ice sublimation processes, and thus the crater erosion rate, has varied. Instead, the ages of the later resurfacing processes seem to be the same throughout the channel.

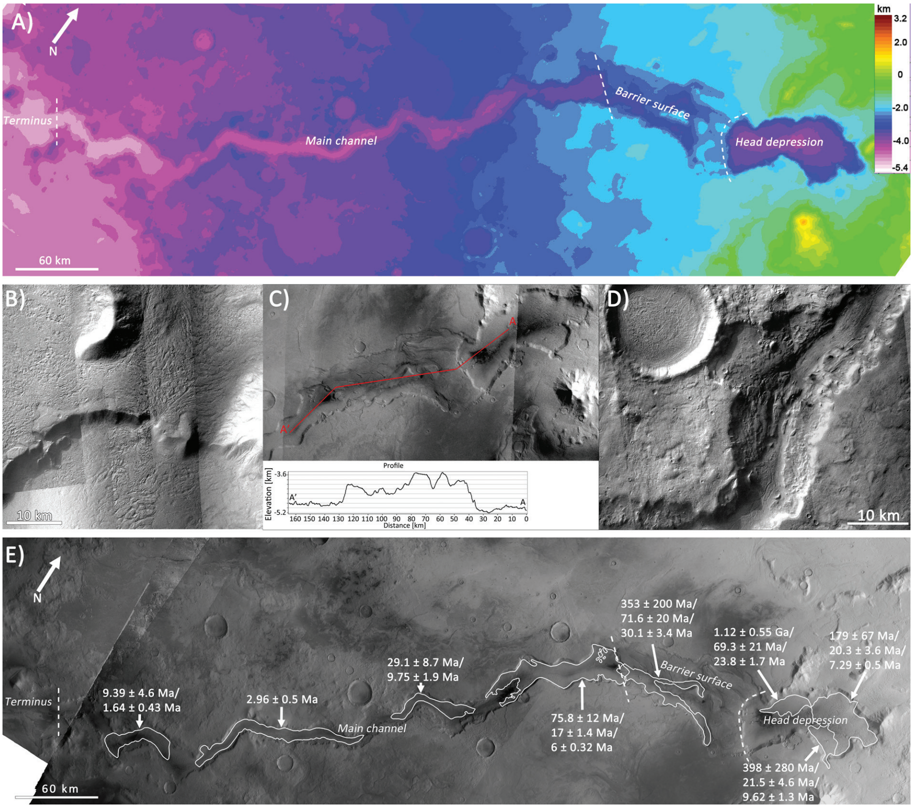

fig. 1. A) Harmakhis Vallis and its four parts in a Mola topography, B) a CTX detail from the ice-related flows originating from the north which cover the Harmakhis head depression, C) a HRSC detail and a Mola profile show the significantly shallower "barrier surface" which separates the Harmakhis Vallis head depression from its main valley, D) a CTX detail from the wall collapses into the Harmakhis Vallis main valley and E) a HRSC mosaic with the mapped flow-units and the summary of crater counts.

References: [1] Greeley R. and Guest J. E. (1987) *USGS Misc. Invest. Ser. Map I–1802–B*. [2] Crown D. A. and Greeley R. (2007) *USGS Misc. Invest. Ser. Map 2936*. [3] Price K. (1998) *USGS Misc. Invest. Ser. Map I-2557*. [4] Crown D. A. et al. (1992) *Icarus, 100,* pp. 1-25. [5] Crown D. A. et al. (2005) *JGR, 110,* E12S22. [6] Harrison K. P. and Grimm R. E. (2009) *JGR, 114,* E04004. [7] Kostama V. -P. et al. (2010) *EPSL, 294,* pp. 321-331. [8] Leonard G. J. and Tanaka K. L. (2004) *USGS Misc. Invest. Ser. Map I-2964*. [9] Bleamaster III, L.F. and Crown D.A. (2010) *USGS Misc. Invest. Ser. Map 3096*. [10] Korteniemi J. et al. (2010) *EPSL, 294,* 466-478. [11] Costard F. et al. (2002) *Science, 295,* 110-113. [12] Head J. W. et al. (2003) *Nature, 426,* 797-802. [13] Mest S. C. and Crown D. A. (2001) *Icarus, 153,* 89-110. [14] Glamoclija M. et al. (2011) *PSS, 59,* 1179-1194. [15] Kukkonen S. et al. (2013) LPSC XLIV, p.2140. [16] CATWG (1979) *Icarus, 37,* 467-474. [17] Ivanov B. (2001) *Space Sci. Rev. 96,* 87-104. [18] Hartmann W. K. and Neukum G. (2001) *Space Sci. Rev. 96,* 165-194.

CALCULATION OF TRAVEL TIMES FOR MARTIAN INTERIOR STRUCTURE MODELS

S. Raevskiy, T. Gudkova,
Schmidt Institute of Physics of the Earth, B.Gruzinskaya 10, Moscow 123995, Russia; Contact: rs1989@rambler.ru

Introduction: Two future missions include seismic experiments on Mars - projects “InSight” of NASA (National Aeronautics and Space Administration) [1] and “MISS” (Mars Interior Structure by Seismology) [2] in the frame of ExoMars of RSA (Russian Space Agency) and ESA (European Space Agency). The main instrument for these seismic experiments is a broadband seismometer [3]. At the moment Martian interior structure models are constrained by the satellite observational data (the mass, the moment of inertia factor, the Love number k_2) [4] and high pressure experimental data [5]. Seismological observations could provide unparalleled capability for studying Martian interiors. When seismic measurements are not yet available, physically consistent interior models, characterized by properties of relevant minerals, make possible to study of the seismic response of the planet.

Software product:

We have developed software product for estimating travel times for direct P, S, core reflected PcP, ScS and core refracted PKP body waves as a function of epicentral distance and hypocentral depth, as well as their amplitudes at the surface for a given marsquake. As the MatLab software is popular tool in data processing, we use it for travel time calculations. Moreover MatLab encompasses many plotting routines that plot resulting travel times and ray paths. The computational results have been compared with the program TTBox [5]. Our code computes seismic ray paths and travel times for a one-dimentional spherical interior model (density and seismic velocities are functions of a radius only). We consider a model as composed of a large number of thin homogeneous spherical shells. The theory is given in [6]. To simplify calculations, we carry out our calculations in Cartesian coordinates, i.e. we transform spherical coordinates into flat ones using formulas from [7]. For a wave at 90 degree another approach is used: a ray path is subdivided into many thin layers with constant velocity. Since such waves don’t have reflections, we calculate directly the path of a wave in each layer until it reaches the center of the planet.

Travel times: Calculations of travel times for direct P, S, core reflected PcP, ScS and core refracted PKP waves as a function of epicentral distance and hypocentral depth are carried out for a trial seismic model of Mars M7_4 from [8]: the core radius is 1775 km, the thickness of the crust is 50 km. The interior structure model M7_4 is shown in Fig.1. Figure 2 demonstrates ray paths of P, PcP and PKP waves. The travel times of P, S, PcP, Scs and PKP waves, computed for a focus at 200 km depth and the seismic model M7_4 from [8] are plotted as a function of epicentral distance in Fig.3. Direct and core reflected P and S waves are recorded to a maximum epicentral distance equal to about 100^0, and PKP arrivals can be detected for epicentral distances larger than 150^0.

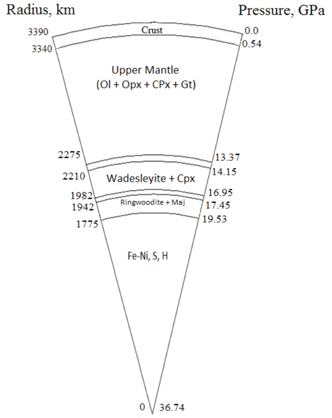

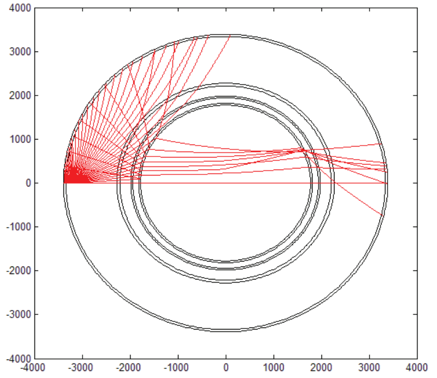

The shadow zone is getting wider in comparison with previous results [10], as the core size of the seismic model under consideration is larger. In the frequency domain, the amplitude of ground acceleration recorded in the far-field at a frequency ω, either on the vertical (P wave) or horizontal (SH-wave) component, can be written as [11]

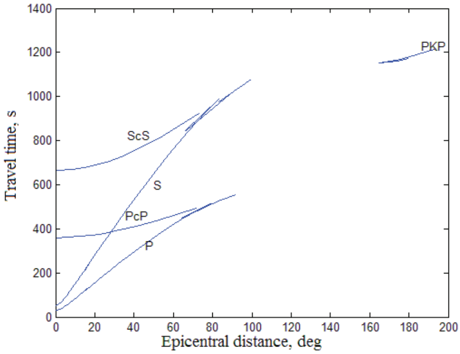

fig. 3. Travel-times of direct (P and S), core reflected (PcP and ScS) and core refracted (PKP) body waves arrivals as a function of epicentral distance for a surface focus, using a trial model M7_4 from [8].

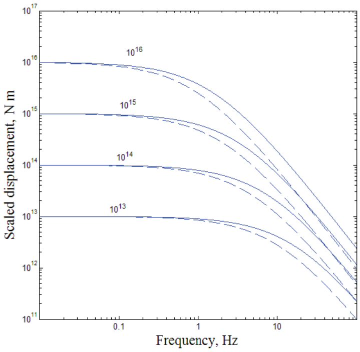

fig. 4. Far-field source displacement spectra M(ω), where ω is the angular frequency of P (solid lines) and S-(dashed lines). Four cases are shown, namely M(0)= 1013, 1014 , 1015 and 1016 Nm.

$$\left|a_j(r,r_\eta,\omega)\right| \approx \frac{\omega^3}{4\pi\sqrt{\rho c_j}} \frac{M_j(\omega)}{\sqrt{\rho_\eta c_{\eta j}^5}} \frac{F_j(r,r_0)}{R_j(r,r_0)} A_j(r,r_\eta,\omega)\ ,\ M_j(\omega) = \frac{M(0)}{\left[1+(\omega/\omega_0)\right]^2}\ ,$$

where ρ is the density, c is either the P- or S-wave velocity. The subscript *j* refers to the wave type under consideration (P or S), and subscript η indicates that the value is evaluated at the source.

The factors M, R and A are the frequency dependent scalar seismic moment, the geometric spreading and the correction due to attenuation, respectively. Seismic source displacement spectrum $M_j(\omega)$ is plotted in Fig.4. The corner frequencies ω_0 are empirically defined following the scaling laws in [12]. As the constants in equations in [12] are very rough estimates, it is expected that seismic events due to the lithospheric cooling of Mars will display similar relationships. The value of the seismic moment *M* (0) is varied from 10^{13} to 10^{16} Nm.

Acknowledgements: This work was supported by Grant No. 12-02-00378 from the Russian Fund for Fundamental Research.

References: [1] Lognonné, P., et al. (2012) Abstract, 3MS³-1-7. [2] Gudkova, T.V. et al., (2013) Sol. Syst. Res, 47, 1. [3]. Robert, O. et al (2012). Abstract LPSC, XXXXIII, 2025.pdf. [4] Konopliv, A.S. et al. (2011) Icarus, 211, 401-428, [5] Bertka, C. and Fei, Y. (1997) J. Geophys. Res. 102, 5251-5264. [6] Bullen, K.E. and Bolt, B.A. (1985) An introduction to the theory of seismology, Cambridge Univ. Press. [7] Muller, G. (1977) J. Geophys., Res. 42, 429-436. [8] Zharkov, V.N. et al. (2009) Phys.Earth Planet.Int, 172, 324-334.[9] Mocquet, A. (1999) Plan. Space Sci. 47, 397-409. [10] Knapmeyer (2010) Planet. Space Sci. , doi: 10.1016/ j.pss. 2010. 03. 016. [11] Aki,K., Richards, P. G. (1980) Quantitative seismology. [12] Sato, T., Hirasawa, T. (1973) J. Phys. Earth. 21, 415-431.

CALIBRATION OF SUBSURFACE RADAR «MARSIS» WITH MARTIAN IONOSPHERE.

V. M. Smirnov, O. V. Yushkova
Kotel'nikov Institute of Radio Engineering and Electronics of RAS, Fryazino Branch, Russia; Contact: vsmirnov@ire.rssi.ru

The subsurface radiolocation is one of the distance investigation methods of the surface properties and the structure of the soil layer. Radar system, located on board the orbiter, allows getting necessary information about the space body for a relatively short period of time. In this the layer thicker is estimated by the lower frequency range of the radar.

The technique for reconstructing depth distribution of the dielectric parameters of inhomogeneous soil is based on analysis of phase and amplitude changes of emitted signal compared with received one. Such method of solving the problem requires accurate calibration of the emitted signal, which is own complicated problem.

Parameters of radar (type of signal, its duration and frequency range) are chosen especial for space object, altitude spacecraft, goals and technical capacity (weight, allowable radiated power).

Calibration of the orbital radar in terrestrial conditions is impossible, because the signal with duration about 0.1 ms must be formed in free space and reflected from extended dielectrically uniform surface. Simulation of such processes is possible, but its results must be verified by physical experiments.

If the body has its own ionosphere, the necessary calibration measurements can be carried out in the time of the main experiment. The ionosphere may serve reflected surface, if the critical frequency is higher than the emitted frequency of the radar. In this case, the reflection of signal from the ionosphere will be dominant.

This report presents:

- height distribution model of the dielectric permittivity of the ionosphere, built on the base of the vertical profile of the electron density of the Mars ionosphere which depends from the solar zenith angle;
- the results of modeling the reflection of the radar MARSIS signal («Mars Express»);
- the results of a comparative analysis of simulation and the processing data of radar measurements MARSIS.

This work was partially supported by the Program 22 of the Presidium of RAS “Fundamental Problems of research and exploration of the Solar System.”

EJECTA MOBILITY OF EXCESS EJECTA CRATERS ON MARS: ASSESSING THE INFLUENCE OF SURFACE SNOW AND ICE DEPOSITS.

D. K. Weiss[1], J. W. Head[1],
[1] *Department of Geological Sciences, Brown University, 324 Brook Street, Providence, RI 02912, USA. Contact: David_Weiss@Brown.edu*

Introduction: Martian impact craters often exhibit unique ejecta morphologies relative to ballistically-dominated ejecta observed in lunar and mercurian impact craters [1,2]: martian lobate ejecta deposits frequently have distinctive ejecta deposit boundaries rather than an ejecta deposit of gradational thickness, and appear to have been fluidized during their emplacement, although there is no consensus on the mode of fluidization [1-7]. It has been noted that there exist major differences among the ejecta mobility values of layered ejecta craters (EM; ratio of ejecta facies radius from the rim/crater radius) (Fig. 1; 2a) [1,4,8-10]. Understanding the nature of the EM of layered ejecta craters may provide some insight into the conditions in which the impact occurred. The large values and variations in the EM of layered ejecta craters have been variously explained as being due to 1) variations in volatile-rich target structure [8] 2) volatile abundance variations in the target [3,9], 3) atmospheric drag, differences in ejecta particle size and atmospheric density [11], 4) variations in target softness [12], or 5) a base surge [13-15]. Of the layered ejecta craters, excess ejecta (EE) craters (Fig. 1) are a particularly unusual subclass, consisting of perched (Pr) craters [16], pedestal (Pd) craters (Fig. 1c & d) [17], and more recently proposed, double-layered ejecta (DLE) craters (Fig. 1b) [18]. EE craters are characterized by an ejecta volume in excess of what can fit in the observed crater cavity, by factors of 2.5-28 [17,19], and are interpreted to form in a decameters-thick ice deposit [16-20]. In this study, we test the hypothesis that the fluidized nature and high EM of EE craters can be accounted for by ballistic deposition followed by ejecta sliding on the lubricating icy-substrate target surface; in this scenario, the low friction ejecta-ice interface serves to enhance sliding distances, and thus EM. We begin by investigating the rim diameter, EM, and substrate thickness relationships between the different martian layered ejecta populations, and then attempt to model the ejecta deposition and sliding process.

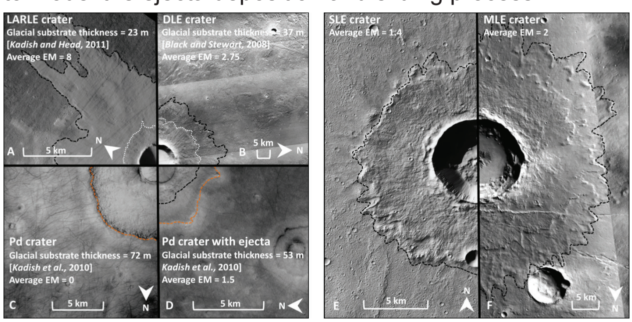

fig. 1. Comparisons of the ejecta deposits of six types of martian craters: A) LARLE crater with DLE morphology, B) DLE crater, C) Pd crater, D) a case of Pd crater exhibiting an ejecta deposit within the pedestal. E) SLE crater, F) MLE crater.

Low-aspect-ratio layered ejecta (LARLE) craters: One class of layered ejecta crater is the low-aspect-ratio layered ejecta (LARLE) crater (Fig. 1a), which displays large and variable EM values (EM=2.5 – 21; average ~8; Fig. 2a & b) and a highly sinuous distal ejecta edge [14,15]. Previous investigators [14,15] report that a LARLE crater can exhibit either SLE or DLE morphology, which is surrounded by the LARLE deposit, and that LARLE crater rim crest diameters are typically larger at higher latitudes. LARLE craters exhibit an identical latitudinal-dependent distribution to that of Pd craters [15]. They [14,15] suggest that LARLE craters are genetically related to Pd craters based on the latitudinal and morphological similarities. As such, LARLE craters are suggested to form in a "fine-grained ice-rich mantle deposit" [14,15], and the high EM and high ejecta sinuosity is attributed to 1) the collapse of the ejecta column, generating a suspension-driven gravity current [13,15], or 2) a base surge [15], in which the primary ejecta re-impacts outside the crater cavity and material surges outward through saltation enhanced by a high volatile component of the ejecta material, in contrast to sliding of the primary ejecta.

We conducted a comprehensive analysis of the global population of LARLE craters in the latitudes equatorward of ~75°N and ~75°S following the description from [14,15] and found a comparable number of LARLE craters, confirming the observations of

[14,15] . Our analysis of LARLE craters indicates that 90% of the 169 craters examined exhibit DLE morphology: we interpret the outer LARLE deposit as the outer ejecta layer of a DLE (Fig. 1a). DLE craters, suggested to form in a surface ice layer and to be EE craters by [18], also have large and variable EM (outer layer EM=1.2 – 10.6; average 3.24; Fig. 2a & b) when compared with SLE craters (EM=0.2 – 6.6; average 1.53; Fig. 1e; 2a & b) and multiple-layered ejecta (MLE) craters (EM=0.3 – 4.7; average 2.17; Fig. 1f; 2a & b) [10].

Some [17, 21] have classified several craters as EE craters, which we classify more specifically as LARLE craters based on their high EM values and ejecta sinuosity. Based on the observation that 1) numerous LARLE craters have DLE morphology, 2) LARLE craters share the same latitudinal-dependent distribution as Pd, DLE craters and other non-polar ice-related deposits, 3) the greater average diameter of LARLE craters at higher latitudes, and 4) our classification of several EE craters as LARLE craters, we suggest that LARLE craters may form in an ice and snow substrate and that they could be a subclass of EE crater. The presence of larger LARLE craters at higher latitudes may indicate impact into a surface icy layer; one might expect thicker ice layers at higher latitudes (a trend observed for Pd craters [22]), and so smaller LARLE craters may not penetrate through a thick ice layer, leading to Pd crater formation. Because the target material is icy, it seems likely that the low friction interface provided by the target material could be responsible for enhancing the runout distances of a surface flow. In this contribution, we test the hypothesis that ejecta sliding on this surface ice layer might be a contributor to the long runout distances observed.

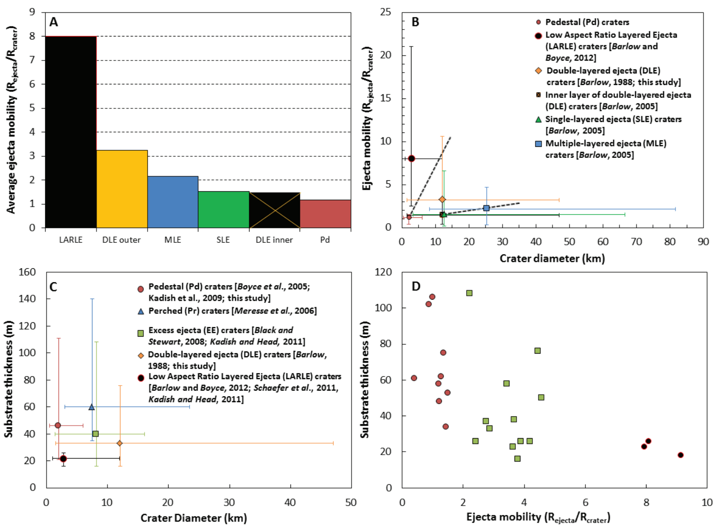

fig. 2. A) Average EM of several martian layered ejecta crater populations [10,14,15; this study]. B) Crater diameter and EM relationship for a number of materian crater populations. C) Crater diameter and icy substrate thickness relationship for a number of materian crater populations. D) Substrate thickness and EM is plotted for Pd craters, EE craters (primarily with DLE), and LARLE craters.

Crater relationships: The LARLE crater rim crest diameter values are quite low (1-12 km), spanning from the low end of Pd craters (1 km) to typical DLE crater sizes (12 km) (Fig. 2c). Pedestal craters impact into an average ~50 m ice sheet (Fig. 2c) and they may occasionally display ejecta within the margins of the pedestal (Fig. 1d). DLE craters impact into a ~40 m ice sheet (Fig. 2c) and display broader ejecta deposits. In contrast, LARLE craters typically form in thinner ice sheets (~20 m on average measured; Fig. 2c) and display laterally extensive ejecta deposits. LARLE ice thicknesses are likely to be thinner than the measured average, as [15] note that LARLE crater ejecta deposits typically appear to be perched only ~10 m above the surrounding terrain. We interpret these relationships to indicate that LARLE craters excavate deeper regolith ejecta material than similarly-sized Pd and DLE craters, due to impact into a thinner substrate.

Differences in EM between crater classes could possibly arise due to ejecta velocity variations. In line with ejecta scaling laws [23-27], ejecta excavated at greater depth will have a lower average velocity than shallower ejecta originating near the surface and the center of the impact. In an impact into a surface ice layer, the near-surface, high velocity material is composed of the surface ice layer, and thus the high velocity ejecta material will experience significantly enhanced vaporization compared to impact into a rocky substrate. Following an impact into a surface ice layer, the vaporized material will be entrained in a vapor plume, which expands in the latter stages of crater

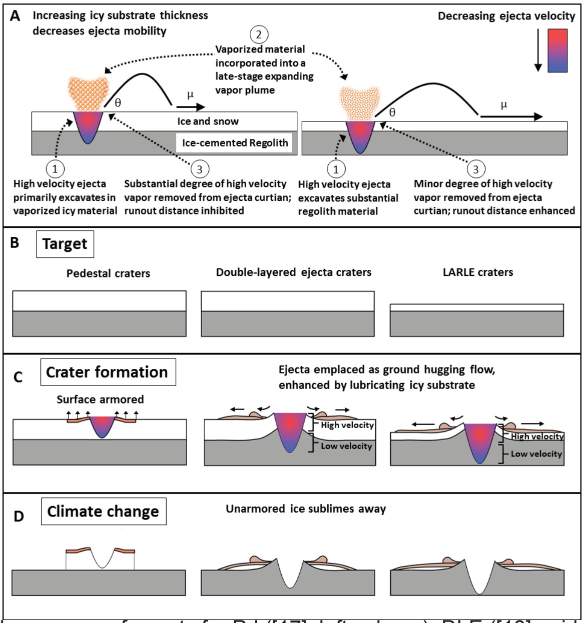

fig. 3. Interpreted sequence of events for Pd ([17]; left column), DLE ([18]; middle column), LARLE craters (right column).

formation [28,29], and thus will not interact with and accelerate ballistically moving ejecta. Hence, enhanced vaporization of ejecta material eliminates the highest velocity ejecta material from the advancing ejecta curtain. Therefore, as the surface ice thickness increases and the depth of penetration below the surface ice is reduced, the volume of vaporized material increases in relation to the volume of excavated regolith material, and more high-velocity ejecta (shallow icy material) is eliminated from the ejecta curtain.

Since the LARLE crater icy substrate is relatively thin, the excavated regolith (that immediately below the icy substrate) will exit the crater cavity at high velocities. In contrast, DLE craters typically form in a thicker ice sheet (~50 m), and so the regolith below the icy substrate is excavated from greater depth relative to the surface, and will exit the crater cavity at a lower velocity, thereby decreasing the EM; in this scenario, a substantial portion of the icy surface layer within the transient cavity is vaporized and entrained in a vapor plume upon impact. Fig. 2d shows that indeed, higher EM values are observed as a function of decreasing icy substrate thickness, which may indicate that with decreasing substrate thickness, more high-velocity ejecta is excavated and will contribute to the ejecta facies runout. We suggest that the thickness of the surface ice layer may be important in controlling the velocity of the ejecta that will contribute to the observed ejecta facies runout.

In this study, we test the idea that the morphologic differences between Pd craters, LARLE craters, and DLE craters (all subclasses of EE craters) might result from gradations in crater diameter and icy substrate thickness. Could the proportion between the volume of vaporized material and the excavated regolith (i.e. depth of penetration below the icy substrate), be a controlling factor on the specific morphology that will be attained upon impact (Fig. 3a)?

References: 1. Carr et al., JGR 82, 4055, 1977; 2. Schultz and Gault, JGR 84, 7669, 1979; 3. Gault and Greeley, Icarus 34, 486, 1978; 4. Mouginis-Mark, JGR 84, 8011, 1979; 5. Mouginis-Mark, Icarus 45, 60, 1981; 6. Woronow, Icarus 45, 320, 1981; 7. Boyce and Mouginis-Mark, JGR 111, E10, 2006; 8. Costard EMP 45, 265, 1989; 9. Barlow and Pollak, LPSC 33, 1322, 2002; 10. Barlow, Large meteorite impacts III, 433, 2005; 11. Schultz, JGR 97, 11623, 1992; 12. Wada and Barnouin-Jha, MPS 41, 1551, 2006; 13. Boyce et al., LPSC 43, 1196, 2012; 14. Barlow and Boyce, LPSC 43, 1253, 2012; 15. Barlow and Boyce, LPSC 44, 1196, 2013; 16. Meresse et al., MPS 41, 1647, 2006; 17. Kadish and Head, Icarus 215, 34, 2011; 18. Weiss and Head, GRL, in press, 2013; 19. Black and Stewart, JGR 113, E2, 2008; 20. Kadish et al., GRL 35, 2008; 21. Schaefer et al., GRL 38, 2011; 22. Kadish et al., Icarus 210, 92, 2010; 23. Wisotski, Planetary and Terrestrial Implications 1, 1101, 1977; 24. Maxwell, Planetary and Terrestrial Implications 1, 1003, 1977; 25. Cooper, Planetary and Terrestrial Implications 1, 11, 1977; 26. Housen et al., JGRL 88, 2485, 1983; 27. Richardson et a;., Space Science Reviews 117, 241, 2005; 28. Melosh and Pierazzo, LPSC 28, 1369, 1997; 29. Pierazzo et al., JGR 103, 28607, 1998;

SNOWMELT MODELING FOR EARLY MARS.

K. E. Scanlon and J. W. Head,
Department of Geological Sciences, Brown University, Providence, RI, 02912 USA.
Contact: Kathleen_Scanlon@brown.edu

Dendritic networks of river valleys dating to the Noachian – Hesperian boundary of the Martian geologic timescale [1] have often been cited as evidence that Mars may have been "warm and wet" enough to support rainfall in the ancient past [e.g., 2-4]. Others have argued that the valleys arose from groundwater sapping, possibly recharged by precipitation [e.g., 5-8], basal melting of snowpack [9], or local hydrothermal melting of ground ice [10-12]. More recent satellite data show that many valley networks are integrated over large areas, have drainage density and basin morphology comparable to terrestrial arid-region valley networks, and head at drainage divides, lending credence to a precipitation origin for the valleys [13-17].

Previous studies have used quantitative geomorphological relationships to determine that most dendritic valley networks were carved by runoff on the order of 0.1 – 1 cm/day [14, 18-19]. Only now, due to the development of three-dimensional climate models for early Mars that include the water cycle [20-23], has it become possible to use these calculated runoff rates to constrain the climate generating the runoff. In order to critically evaluate the hypothesis that the valley networks imply a warm, wet early Mars, we are exploring snowmelt runoff rates as a function of location on Mars and under a variety of climate warming scenarios.

Very few regions of Mars experience annual maximum temperatures above 0°C in modeled thick CO_2 atmospheres, let alone temperatures warm enough for frequent rain, and the warmest regions in these simulations rarely coincide with the main belt of valley networks [20-23]. Rather than experiencing seasonally or continuously temperate conditions, Early Mars may have been icy for most of its history, warmed only intermittently by greenhouse effects from volcanism or impacts [20, 21, 24-28]. We have shown that the local-scale distribution of snowfall on a cold Early Mars is similar to the distribution of valley network tributaries [29], but it remains to be shown whether snow can melt fast enough to create the required fluxes to erode the valleys under plausible Martian climate conditions.

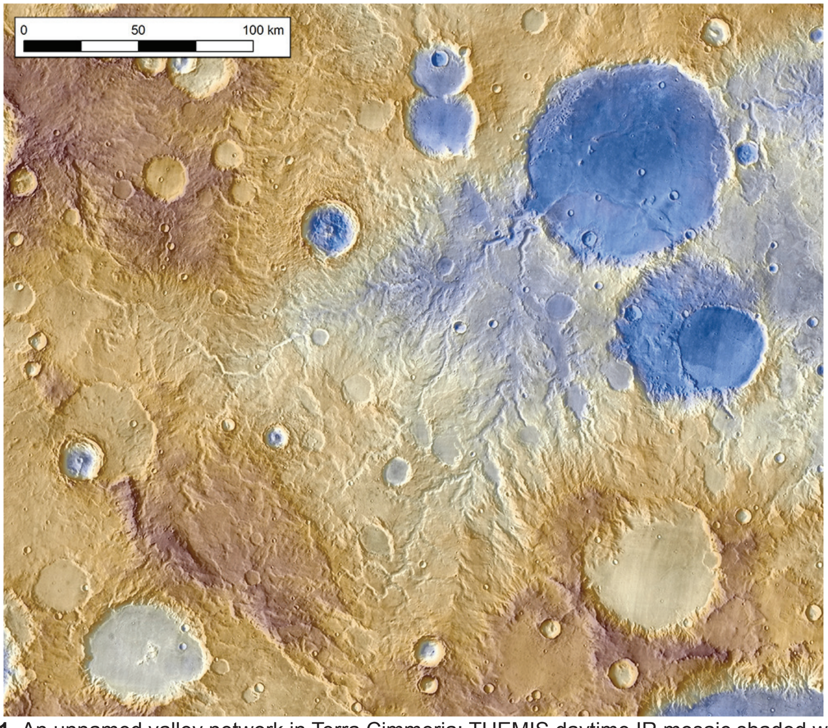

fig. 1. An unnamed valley network in Terra Cimmeria; THEMIS daytime IR mosaic shaded with MOLA topography. Modeling has shown that snowfall amounts on a cold early Mars would have been greatest where the valleys are densest [29], but the capacity of snowmelt to produce the runoff rates that have been inferred from the valleys' geomorphology remains to be determined.

We will present results from an initial phase of work wherein our coupled snowmelt-runoff model is forced with a prescribed time series of surface air temperatures and a set of precipitation rates, atmospheric densities, and near-surface values of relative humidity spanning the plausible range for Early Mars. Using prescribed warming profiles and a wide climate parameter space allows us to consider rapid warming rates that have not yet been demonstrated in the GCM, as well as the possibility of seasonal snowmelt in a moderately cold climate. In the second phase, we are implementing our snow model within the LMD Mars GCM in order to simulate the melt response to changes in greenhouse gases and obliquity variations in a fully self-consistent fashion. This coupled modeling approach will allow us to assess the extent to which the modest greenhouse warming mechanisms currently under study—e.g. impact-generated steam atmospheres [21-22], sulfur dioxide [22, 24, 30], and nitrogen [31]—could meet the liquid water production constraints imposed by the valley networks despite being generally insufficient to allow rain. In addition to our primary aims, and in concert with the GCM's runoff model, this approach may allow novel investigations of the hypothesis that an ocean filled part of the northern highlands.

References

[1] Fassett, C. I., and J. W. Head (2008), *Icarus*, *195*(1), 61-89. [2] Craddock, R. A., and A. D. Howard (2002), *J Geophys Res-Planet*, *107*(E11). [3] Hoke, M. R., and B. M. Hynek (2009), *J Geophys Res-Planet*, *114*(E8). [4] Grant, J., R. Irwin III, S. Wilson, D. Buczkowski, and K. Siebach (2011), *Icarus*, *212*(1), 110-122. [5] Pieri, D. C. (1980), *Science*, *210*(4472), 895-897. [6] Malin, M. C., and M. H. Carr (1999), *Nature*, *397*(6720), 589-591. [7] Carr, M. H., and M. C. Malin (2000), *Icarus*, *146*(2), 366-386. [8] Grant, J. A., and T. J. Parker (2002), *J Geophys Res-Planet*, *107*(E9), 5066. [9] Carr, M. H., and J. W. Head (2003), *Geophys Res Lett*, *30*(24). [10] Gulick, V. C., D. Tyler, C. McKay, and R. Haberle (1997), *Icarus*, *130*(1), 68-86. [11] Gulick, V. C. (1998), *J Geophys Res-Planet*, *103*(E8), 19365-19319,19387. [12] Gulick, V. C. (2001), Origin of the valley networks on Mars: A hydrological perspective, *Geomorphology*, *37*(3), 241-268. [13] Hynek, B. M., and R. J. Phillips (2003), *Geology*, *31*(9), 757-760. [14] Irwin, R. P., R. A. Craddock, and A. D. Howard (2005), *Geology*, *33*(6), 489-492. [15] Luo, W., and T. F. Stepinski (2006), *Geophys Res Lett*, *33*(18), L18202. [16] Mangold, N., C. Quantin, V. Ansan, C. Delacourt, and P. Allemand (2004), *Science*, *305*(5680), 78-81. [17] Stepinski, T. F., and A. P. Stepinski (2005), *J Geophys Res-Planet*, *110*(E12), E12S12. [18] Barnhart, C. J., A. D. Howard, and J. M. Moore (2009), *J Geophys Res-Planet*, *114*(E1), E01003. [19] Hoke, M. R., B. M. Hynek, and G. E. Tucker (2011), *Earth Planet Sci Lett*, *312*(1), 1-12. [20] Forget, F., R. Wordsworth, E. Millour, J.-B. Madeleine, L. Kerber, J. Leconte, E. Marcq, and R. M. Haberle (2013), *Icarus*, *222*(1), 81-99. [21] Wordsworth, R., F. Forget, E. Millour, J. Head, J.-B. Madeleine, and B. Charnay (2013), *Icarus*, *222*(1), 1-19. [22] Mischna, M. A., V. Baker, R. Milliken, M. Richardson, and C. Lee (2013), *J Geophys Res-Planet, 118*(3), 560-576. [23] Urata, R. A., and O. B. Toon (2013), *Icarus 226*(1), 229–250. [24] Halevy, I., M. T. Zuber, and D. P. Schrag (2007), *Science*, *318*(5858), 1903-1907. [25] Phillips, R. J., M. T. Zuber, S. C. Solomon, M. P. Golombek, B. M. Jakosky, W. B. Banerdt, D. E. Smith, R. M. Williams, B. M. Hynek, and O. Aharonson (2001), *Science*, *291*(5513), 2587-2591. [26] Segura, T. L., O. B. Toon, and A. Colaprete (2008), *J Geophys Res-Planet*, *113*(E11). [27] Segura, T. L., O. B. Toon, A. Colaprete, and K. Zahnle (2002), *Science*, *298*(5600), 1977-1980. [28] Toon, O. B., T. Segura, and K. Zahnle (2010), *Ann Rev Earth Planet Sci*, *38*, 303-322. [29] Scanlon, K. E., J. W. Head, J.-B. Madeleine, R. D. Wordsworth, and F. Forget (2013), *Geophys Res Lett*, in press. [30] Kerber, L., F. Forget, and R. Wordsworth (2013), in *LPSC XLIV*, abstract #2296. [31] von Paris, P., J.L. Grenfell, H. Rauer, and J.W. Stock (2013), Planet Space Sci 82–83, 149–154.

TOMOGRAPHIC SIGNAL ANALYSIS FOR THE DETECTION OF DUST-DEVILS IN MARS ATMOSPHERE.

A. Gimenez-Bravo[1], C. Aguirre[1], L. Vázquez[2],
[1]Grupo de Neurocomputación Biológica, EPS, Universidad Autónoma de Madrid, 28049, Madrid, Spain; [2] Departamento de Matemáticas, Facultad de Informática, Universidad Complutense de Madrid, Madrid, Spain. Contact: lvazquez@fdi.ucm.es

Introduction:

The purpose of this work is the implementation of a new method of tomography-based signal analysis for the detection of events in the Martian atmosphere, such as dust devils. These are thought to play an important role in the Martian climate. Dust devils are convective vortices generated due to surface heating, thereby generating convective plumes of rising air with a pressure variation inside. Some of these vortices obtain horizontal wind speeds large enough for dust particles to be lifted off the surface and into the vortex and thus becoming dust devils.

For this study, the pressure data used are those obtained directly by NASA's Phoenix spacecraft, operational since May 25, 2008 through May 2010. The objective is to find pressure drops more or less pronounced, but well localized in time, with a very short duration. Special attention is devoted to non-commutative tomography, which provides very robust strictly positive probability densities in the presence of noise and also provides filtering and to separate signal components. Finally we propose a new technique called Adapted Tomography, where the data itself generate the transform space. Adapted tomography is based on using an operator with the shape of the event we want to extract, and this will be identified as the component of the signal we want. This produces a localized accumulation of energy where the event takes place. With this method several of the available Martian suns are analyzed and the results are shown compared with results obtained in other works.

Tomography and Adapted Tomography for signal analysis:

Recently a new kind of bilinear transforms, called tomograms, have been proposed. Tomograms are strictly positive probability densities and provide a full characterization of the signal. Tomograms are obtained by projecting a given signal ***f(t)*** over the eigenvector set of a linear operator ***B(α)***. One of the most typical Tomograms is the time-frequency tomogram (that is a particular case of the Radon transform). Let's consider the operator where ***t*** is the time operator and is the frequency operator. Using the previously defined operator of the time–frequency operator can be obtained [1] and an explicit expression for the tomogram may be found at [2]. Even when time-frequency tomograms have proven a powerful tool for filtering or component detection at signals, there are situations where the components of the signal we are interested in are not well represented by their frequency spectrum, as is the case of the behavior of a dust-dust inside the Mars atmospheric pressure data. In order to detect appearances of dust devils, represented as brief and sudden drops in the atmospheric pressure level, we have developed a tomographic technique to full characterize such behavior [3].

Consider a matrix where each row of is a typical signal that contains the component we are interested in sampled at intervals. This set of typical signals can be obtained from data or can be artificially generated. Now construct the square matrix. The diagonalization of provides *k* non-zero eigenvalues and its corresponding orthogonal N-dimensional eigenvectors with . The linear operator S constructed from the set of typical signals is

For the tomogram consider now the linear operator where I is the identity matrix. The tomogram adapted to the operator pair (t,S) is obtained from the projection of the signal on the eigenvectors of Usually a one parameter transform is considered just by the simple transform, and therefore.

Mars atmospheric pressure data analysis

Several methods have been proposed for the detection of dust-devils on Mars atmospheric layer, usually these methods use ad-hoc criteria for the detection of the phenomena. In [4] one of such criteria is used for finding dust-devils from the pressure data obtained from Phoenix Mars Lander, in this work, a dust-devil is detected if the signal present a drop of .3 for approximately 20s, the work considers that in the Phoenix working period a total number of 502 vortices were detected.

We have applied the method proposed in the previous section to the same data and a higher number of vortices that were not detected in [4] are now detected. In this example we have used data from SOL 136 as this period showed a higher vortex activity. To construct de data-based operator an artificial database of 167 signals presenting a dust-devil like behavior was generated. Finally, from this database, the data driven tomographic operator is built as indicated in the previous section.

In figure 1 the left panel shows coefficients 8400 to 9000 (segment 15) from the tomographic transform for of the pressure data at SOL 136, showing a clear peak at coefficients 8850-8860, indicating so the presence of a dust-devil at that time instant. The right panel shows the reconstructed signal using only coefficients from 8850 to 8860.

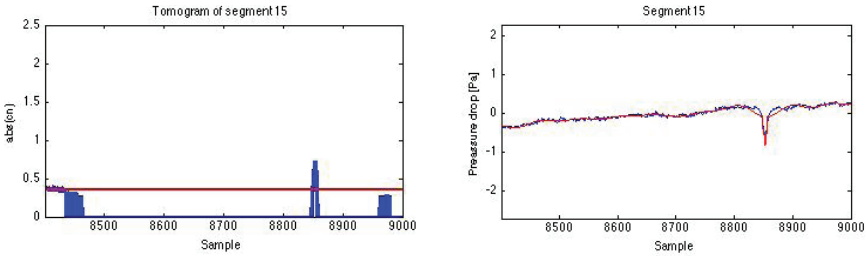

fig. 1. Tomogram of segment 15 (left), signal reconstruction from coefficients, 8850-8860.

A total number of five vortexes were detected at SOL 136, that is a higher number that the vortexes detected in [3] at the same period. Other SOLs were analyzed obtaining in all cases a more accurate number of vortexes.

Bibliography

1. M. A. Manko, V. I. Manko and R. Vilela Mendes, Tomograms and other transforms: a unified view, Journal of Physics A: Math. Gen. 34 (2001) 8321–8332.
2. V. I. Manko and R. Vilela Mendes; Non-commutative time-frequency tomography, Physics Letters A 263 (1999) 53–59.
3. C. Aguirre and R. Vilela Mendes; Signal recognition and adapted filtering by non-commutative tomography, IET Signal Processing. In Press
4. M.D. Ellehoj et al.; Convective vortices and dust devils at the phoenix mars mission landing site, J. Geophys. Res., 115, 2010.

ALTAI SALT LAKES HALOPHILES UNDER SIMULATED EARLY MARS CONDITIONS

A. A. Berezhnoy[1], A. V. Bryanskaya[2], A. S. Rozanov[2], A. A. Peltek[2],
[1] Sternberg Astronomical Institute, Moscow State University, Universitetskij pr., 13, Moscow, 119991 Russia; [2] Institute of Cytology and Genetics, Siberian Branch, Russian Academy of Sciences, pr. akademika Lavrent'eva 10, Novosibirsk, 630090 Russia. Contact: ber@sai.msu.ru

Introduction:

Mars is not hospitable planet for Earth's microbes which can be delivered from Earth to Mars by impacts of meteoroids due to low day and night temperatures, high content of salts, high level of UV-radiation, and low content of organic species. To study the possibility of survival of Earth's microorganisms on Mars, we need to select the most suitable types of them. For this purpose, halophiles are one of the most suitable groups of microorganisms, since saline liquids are more widespread under the Martian surface than pure liquid water.

Extremely halophilic microorganisms are found at various places of our planet, including salt-containing mountain rocks dated 200–250 Ma (Mancinelli et al., 2004), salt surface waters, such as leach in salterns, the Dead Sea, Lake Magadi, and other salt lakes in various arid zones of our planet (Oren, 2002). In the Kulunda steppe (Altai region), with many small drainless lakes characterized by high content of salts, up to saturation, and pH up to 10 extremely halophilic bacteria and archaea have been collected (Sorokin et al., 2005). The purpose of the present study is to study adaptive abilities of bacterial and archaeal strains of salt lakes of the Altai region under extreme simulated early Martian conditions (low temperatures, high salt content). Preliminary results of our experiments are already described by Bryanskaya et al. (2013).

Materials and methods

The strains of bacteria (*Halomonas* sp. H8b, *Halomonas* sp. H12b, *Salicola* sp. H9b) and archaea (*Halorubrum* sp. H2a, *Halorubrum* sp. H3a, *Halorubrum* sp. H4a, *Halorubrum* sp. H7a, *Halorubrum* sp. H11a, *Halorubrum* sp. H13a) were sampled in various salt lakes of the Altai region (lakes Burlinskoe, Bol'shoe Yarovoe, Maloe Yarovoe etc.). Bottom sediments were sampled typically near the shore line at depths of about 0.3 – 0.5 m. Waters of the lakes are of chloride and chloride–sulphate types, with total mineralization ranging from 50 to 250 g/l (Lebedeva et al., 2008). The strains were grown at temperature of 37 °C in the medium containing 50–300 g/l NaCl, 5 g/l $MgCl_2$, 1 g/l KCl, 1 g/l $CaCl_2$, 4 g/l tryptone, 2 g/l yeast extract, and 10 ml/l microelement solution (in mg/l: 700 $FeSO_4$ x $7H_2O$, 234 $CoCl_2$ x $6H_2O$, 24 Na_2MoO_4 x $2H_2O$, 33 $NaWO_4$ x x $2H_2O$, 100 $ZnSO_4$ x $7H_2O$, 5 $CuSO_4$, 10 H_3BO_3, 120 $MnSO_4$ x $5H_2O$). In all solutions examined, pH was brought to 7.5. For exposure experiments cells were placed on solidified growth medium of the same composition and incubated at 22 and 37 °C during 7 days. At least three exposure experiments were performed. Cell numbers were estimated from CFU.

Results

Freezing acts by different ways to survival of strains – low temperatures by itself, crystallization of solid-state fraction, and by stresses arising due to changes of the ice density. To study these effects separately, several experiments were performed.

Study of physic-chemical properties of salt solutions including pH, ice fraction, and composition of solid-state species was performed with usage of the FREZCHEM program described in details by Marion et al. (2003). All studied solutions remain partly frozen at -18 °C with exception of 300 g/l NaCl solution. Temperature was remains constant within ± 1 °C, it corresponds to small changes of the ice fraction.

Images obtained by electron microscope technique show that low temperatures lead to destruction of cell membranes of strains which are just partly survived after freeze-thaw cycles. It was shown that strains H4a are unable to survive due to destruction of cell membranes during freezing while membranes of strains H12b surviving after action of freezing at -70 °C remain unchanged (see Fig. 1).

For studied strains ratio of survival fractions at -70 °C and -18 °C (S(-70 °C) and S(-18 °C), respectively) rapidly increases with increasing of the survival fraction at -70 °C. Survival fractions of strains H4a and H7a are the most sensitive to changes of temperature from -18 °C to -70 °C (for H7a and H4 a S(-70 °C)/ S(-18 °C) = 0.04 and 0.12, respectively), for this reason these strains were selected for additional experiments.

For 200 g/L NaCl solution survival of *Halorubrum* sp. H7a was analyzed at different temperatures (-15, -21, -28, -70 °C). Namely, S(-15 °C) = 0.042 , S (-21 °C) = 0.06, S (-28 °C) = 0.34, S(-70 °C) = 0.09. Thus, survival of this strain is higher for completely frozen solution in comparison with partly frozen solution.

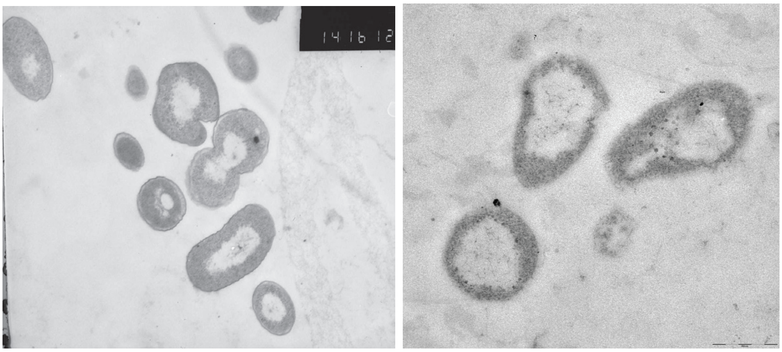

fig. 1. Electron images of strains H12b (left) and H4a (right) after freezing at -70 °C.

The correlation coefficient r^2 between the survival fraction of studied strains after freeze-thaw cycles (1 and 2 cycles) and CFU in the control sample is high, about 0.9. It means that survival fraction increases in solutions more favorite for grow. The highest survival fraction after freeze-thaw cycles at -18 and -70 °C is found for optimal NaCl content and for experiments performed during summer period.

Selected strains were checked for grow in several solutions containing different types of nutrition species. Different results of this biochemical test are obtained only for β -galactosidase and esculin, for other species the results are the same for all studied strains. Among prebiotic molecules which are found in carbonaceous chondrites are amino acids (see, for example, (Glavin et al., 2006)). Glucose is tentatively detected at the 25 ppm level (Kaplan et al., 1963). These species as well as H_2S already detected in comets (Boissier et al., 2007) can be delivered to Earth by impacts of comets and asteroids (Pierazzo and Chyba, 1999). However, studied strains are able to grow only on glucose, but not on H_2S or amino acids lysine, ornithine, and arginine.

Summary

Experiments with survival at different cooling temperatures show that partly frozen solutions are not optimal for survival of microbes. Additional checking of this conclusion is possible by performing of planned experiments with solutions having lower eutectic temperatures. Survival fraction of studied strains after freezing is maximal in solutions which have maximal CFU value at 37 °C and, respectively, are optimal for grow. Studied halophiles are not among the strains which are able to grow on species delivered to Earth by impacts of comets.

Acknowledgments
The financial support by Integration Projects 93 and 94 of the Siberian Branch of RAS, RFBR 11-04-12093-ofi-m is gratefully acknowledged.

Literature

Boissier J., Bockelée-Morvan D., Biver N. et al. Interferometric imaging of the sulfur-bearing molecules H_2S, SO, and CS in comet C/1995 O1 (Hale-Bopp), *Astronomy and Astrophysics*, V. 475, Is. 3, p. 1131-1144, 2007

Bryanskaya A.V., Berezhnoy A.A., Rozanov A.S. et al. Adaptive capabilities of microorganisms of salt lakes of the Altai region under conditions of early Mars, *Paleontological Journal*, V. 47, Is. 9, p. 1-4, 2013

Glavin D.P., Dworkin J.P., Aubrey A. et al. Amino acid analyses of Antarctic CM2 meteorites using liquid chromatography-time of flight-mass spectrometry*, Meteoritics*, V. 41, Is. 6, p. 889-902, 2006

Kaplan I.R., Degens E.T., Reuter J.H. Organic compounds in stony meteorites, *Geochimica et Cosmochimica Acta*, Vol. 27, Is. 7, p. 805-808, 1963

Lebedeva (Verba) M.P., Lopukhina O.V., Kalinina N.V. Specificity of the chemical and mineralogical composition of salts in solonchak playas and lakes of the Kulunda steppe, Eurasian Soil Science, V. 41, Is. 4, p. 416-428, 2008

Mancinelli R.L., Fahlen T.F., Landheim R. et al. Brines and evaporites: Analogs for Martian Life, *Adv. Space Res.,* V. 33, p. 1244–1246, 2004

Marion G.M., Catling D.C., Kargel J.S. Modeling aqueous ferrous iron chemistry at low temperatures with application to Mars*. Geochim Cosmochim Acta*, V. 67, p. 4251-4266, 2003

Oren A. Molecular ecology of extremely halophilic archaea and bacteria, *FEMS Microbiol. Ecol.,* V. 39, p. 1–7, 2002

Pierazzo E., Chyba C.F. Amino acid survival in large cometary impacts, *Meteoritics and Planetary Science*, V. 34, No. 6, p. 909-918, 1999

Sorokin D.Yu., Tourova T.P., Muyzer G. Oxidation of thiosulfate to tetrathionate by an haloarchaeon isolated from hypersaline habitat, *Extremophiles,* V. 9, p. 501–504, 2005

ANALYSIS OF THE LUNAR HYDROXYL ABSORPTION DEPTH BASED ON SIMULATED SURFACE TEMPERATURE DATA

E.A. Feoktistova[1], C. Wöhler[2], A.A. Berezhnoy[1], A. Grumpe[2], V.V. Shevchenko[1]
[1]Sternberg Astronomical Institute, Moscow State University, Moscow, Russia;
[2]Image Analysis Group, TU Dortmund University, 44227 Dortmund, Germany.
Contact: {katk | ber | shev}@sai.msu.ru, {christian.woehler | arne.grumpe}@tu-dortmund.de

Introduction: The widespread distribution of hydroxyl ions on the lunar surface has been analysed based on hyperspectral data acquired by the Moon Mineralogy Mapper (M³) instrument carried by the Chandrayaan-1 spacecraft [1]. Under oblique illumination, especially at the poles of the Moon, the hydrogen content is correlated with topographic features [2, 3]. Based on gamma-ray spectroscopy, hydrogen has also been detected in illuminated regions of the Moon [4]. There the surface temperature is too high for long-term survival of water ice and H-containing compounds, which may comprise hydroxyl-containing minerals as well as implanted hydrogen atoms of solar wind origin (cf. e.g. [2]). In this study we analyse the hydroxyl absorption around 2800 nm based on M³ hyperspectral data [5] for two regions on the Moon comprising small and fresh impact craters associated with impact melt flows, making use of the simulation-based method in [6] for surface temperature estimation.

M³ data processing: Our analysis relies on the M³ level-1B radiance data available at http://pds-imaging.jpl.nasa.gov/volumes/m3.html. A crucial prerequisite for an accurate analysis of the hydroxyl absorption is the removal of the thermal emission component, which requires a surface temperature estimation.

Data-driven surface temperature estimation. As a data-driven approach, we employ the method of [7]. Accordingly, for each M³ spectrum the observed radiance spectrum is modelled in the wavelength range 2377–2936 nm (M³ channels 70–84) as the weighted sum of a reference radiance spectrum, inferred from a linear fit to the reflectance spectrum of sample 62231 returned by Apollo 16 (http://www.planetary.brown.edu/pds/AP62231.html), and a black body spectrum defined by the temperature and the thermal emissivity of the surface. A different data-driven technique is suggested in [8].

Simulation-based surface temperature estimation. A favourable alternative to data-driven thermal emission removal is the simulation-based approach introduced in [6]. We first construct a digital elevation map (DEM) of high lateral resolution using the photometric stereo based approch proposed in [9], which combines M³ image information with a reference DEM of lower effective lateral resolution (here: the GLD100 [10]). It is also possible to use GLD100 data directly. Relying on the illumination angles and mutual orientations of the surface elements of the DEM, the surface temperature of each element is computed based on the direct illumination by the sun, the heat flux from the lunar interior, and the indirect thermal radiation from neighbouring surface elements [6]. The thermal emissivity is set to 0.95 [11]. The size of an element of the temperature map corresponds to 0.01° in longitude and latitude.

Normalisation to standard geometry. The constructed DEM yields the incidence and emission angle for each pixel, such that the photometric model by Hapke [12] can be used to normalise the reflectance of each channel to 30° incidence angle, 0° emission angle, and 30° phase angle [13]. For each pixel and each M³ channel, the single-scattering albedo is estimated, while the remaining parameters of the Hapke model are set according to [14]. The reflectance averaged over the M³ wavelength range and normalised to that of a perfectly white Lambertian surface under identical illumination conditions is used as the surface albedo for the temperature simulation.

Mapping the hydroxyl absorption depth. The depth of the hydroxyl absorption is described by the ratio R_{2817}/R_{2657} between the thermally corrected and normalised reflectances of M³ channels 81 (2817 nm) and 77 (2657 nm) [7]. High values of this ratio correspond to a weak and low values to a strong hydroxyl absorption.

Results and discussion: Crater 1 has a diameter of 3.0 km and is located near Atlas at 49.84° E and 46.75° N. Crater 2 has a diameter of 1.9 km and is located on the lunar farside near Olcott at 121.29° E and 18.69° N. Both craters are associated with dark impact melt flows (Figs. 1a and 2a), which, to our best knowledge, have not been described in previous studies. For crater 2, the illumination is too steep for applying the method in [9], such that GLD100 data were used directly. The results of the data-driven temperature estimation approaches in [7] and [8] are similar to each other (Fig. 1c–d, Fig. 2c–d). For both craters, the surface temperatures obtained based on the simulation method [6] are systematically higher than the values obtained by the data-driven methods (Figs. 1e and 2e). The high simulation-based temperature values are realistic since the M³ data have been acquired 3.3 and 15.9 days after local sunrise, respectively (especially the low temperatures around 300 K inferred by the data-driven methods for the rays of crater 2 less than two days after local lunar noon appear unrealistic). The hydroxyl absorption depth maps shown in Figs. 1g and 2g show that the dark melt flows exhibit a stronger hydroxyl absorption than the surrounding surface. The melt flow of crater 2 is clearly warmer than the surrounding surface. Hence, its increased hydroxyl absorption depth is in contrast to the typical behaviour that warm surface parts, e.g. crater walls inclined towards the sun, have a weaker hydroxyl absorption than cooler parts, e.g. crater walls inclined away from the sun. This “hydrophilic” behaviour is possibly due to the surface structure of the melt, which according to [15] consists of solid rock rather than grainy regolith. Future work will involve a detailed analysis of hydroxyl behaviour in the illuminated regions of the Moon, especially of the hydroxyl adsorption tendency of different types of lunar surfaces.

References: [1] Clark, R., et al. (2010). Proc. Lunar Planet. Sci. XXXXI, abstract #2302. [2] McCord, T. B. et al. (2010) Proc. Lunar Planet. Sci. XXXXI, abstract #1860. [3] Miller, R. S. et al. (2012) J. Geophys. Res. 117(E11), E11007. [4] Boynton, W. V. et al. (2012) J. Geophys. Res. 117, E00H33. [5] Pieters, C. et al. (2009) Current Science 96(4), 500-505, 2009. [6] Berezhnoy, A. A. et al. (2012) Adv. Space Research 50, 1638-1646. [7] Wöhler, C., Grumpe, A. (2013) In: Breuß, M. et al. (eds.), Innovations for Shape Analysis: Models and Algorithms, pp. 467-492. Mathematics and Visualization, Springer-Verlag Berlin Heidelberg. [8] Clark, R. N., et al. (2011) J. Geophys. Res. 116, E00G16. [9] Grumpe, A. and Wöhler, C. (2011) Proc. 7th IEEE Int. Symp. on Image and Signal Proc. and Anal., pp. 609–614. [10] Scholten, F., et al. (2012) J. Geophys. Res. 117, E00H17. [11] Greenhagen, B.T. and Paige, D.A. (2006) Lunar Planet. Sci. XXXVII, abstract #2046. [12] Hapke, B. W. (2002) Icarus 157, 523-534. [13] Pieters, C. M. (1999) Proc. Workshop New Views of the Moon, abstract #8025. [14] Warell, J. (2004) Icarus 167, 271–286. [15] Hawke, B. R. and Head, J. W. (1977) In: Roddy, D. J.et al. (eds.), Impact and Explosion Cratering. Pergamon Press, New York, pp. 815–841.

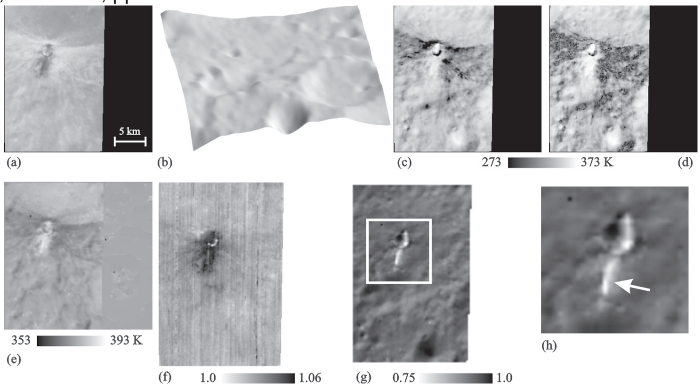

fig. 1: (a) M³ 1579 nm radiance image of crater 1 near Atlas. (b) DEM of high lateral resolution. (c) Temperature map obtained based on [7]. (d) Temperature map from http://pds-imaging.jpl.nasa.gov/volumes/m3.html, computed based on [8]. (e) Temperature map obtained based on the simulation method in [6]. (f) Map of the hydroxyl absorption depth R_{2817}/R_{2657} obtained based on the temperature map in (c). (g) Map of the hydroxyl absorption depth obtained based on the temperature map in (e). Bright pixels correspond to strong hydroxyl absorptions. (h) Enlargement of the melt flow (arrow).

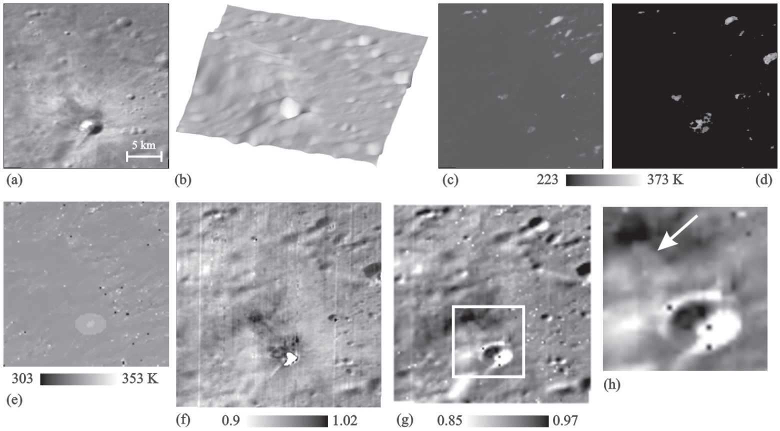

Fig. 2: (a) M³ 1579 nm radiance image of crater 2 near Olcott. (b) GLD100 data. (c)–(h) Analogous to Fig. 1.

EXPERIMENT ARIES-L FOR INVESTIGATION OF LUNAR REGOLITH BY MEANS OF SIMS AND SECONDARY NEUTRAS MASS-SPECTROMETRY

R.Zhuravlev[1], O.Vaisberg,[1], G.Koynash[1], A.Shestakov[1], S.Podkolzin[1], P.Moiseev[2], D.Trufanov[3], V.Kurnaev[3], N.Mamedov[3], D.Sinelnikov[3].
[1] IKI RAS, Moscow, Russia, zhuravlev_roman@iki.rssi.ru, [2] «Astron Electronics», Orel, Russia, [3] National Research Nuclear University "MEPhI", Moscow, Russia

Study of lunar regolith is an important part of investigation of origin, evolution, and properties of the Moon. The purpose of experiment is investigation of solar wind interaction with the surface of the Moon, desorption of surgace layer, and composition of surface layer. Secondary Ion Mass Spectrometry is common methods of analysis solid bodies. The use of specific ion beam allow one to analyze the composition specimen by mass-spectrometry of secondary ions. SIMS as well as analysis of secondary neutrals was already used in space missions Chandrayaan-1 and Kaguya. Space experiment allows one to use the solar wind flux as primary ion beam.

Panoramic ion and neutrals analyzer ARIES-L is an energy-mass spectrometer with field-of-view 2π. Prototype of this instrument DI was developed for ill-fated mission Phobos Soil. Wide viewing angle allows this instrument to measure simultaneously the solar wind flux and characteristics of secondary ion flux sputtered from lunar regolith. Instrument also includes convertor of neutral atoms located within the field of view of instrument. Secondary neutrals sputtered by the solar wind are ionized on the surface of convertor and are measured by the same ion energy-mass analyzer. We describe an instrument and its characteristics. Computer modeling of sputtering regolith and working of neutral-ion converter using codes Scatter and Simion is also presented.

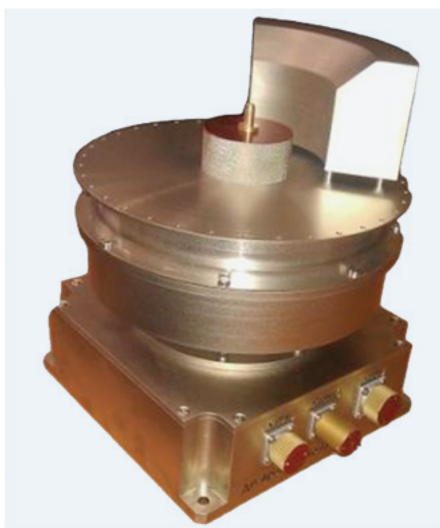

fig. 1. Panoramic ion and neutrals analyzer ARIES-L

GEOLOGICAL REVIEW OF LUNOKHOD 1 AREA.

A. M. Abdrakhimov[1], A. T. Basilevsky[1], I. P. Karachevtseva[2],
[1]Vernadsky Institute, Kosygina 19, Moscow, Russia; [2] MIIGAiK, Gorokhovsky per. 4, Moscow, Russia. Contact: atbas@geokhi.ru

Introduction:

Lunokhod 1 study area (38.2-38.32 N, 35.04- 34.97 W) is covered 1.5 x 2 km^2 in NW part of Mare Imbrium (Fig.1) [1]. The total length of the route Lunokhod 1 is ~ 9400 m. Summarizing the current orbital data of Clementine and LRO, Lunokhod 1 was working on a mare plain, composed of Eratosthenian basalts of 3-2.9 b.y., with a high content of TiO_2 and FeO [2,3].

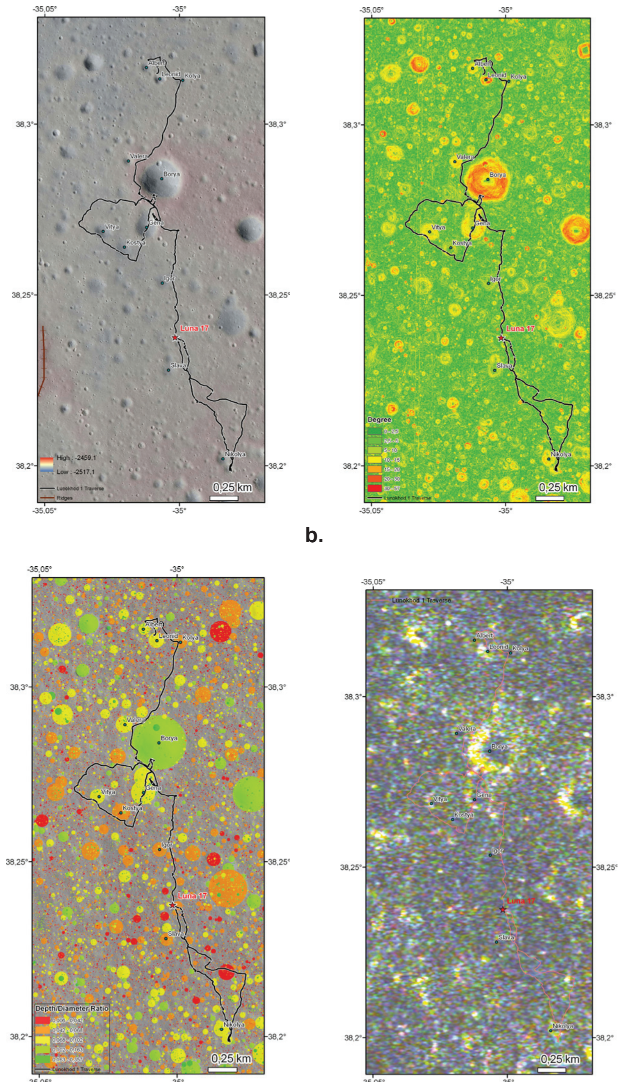

c. d.

fig. 1. Lunokhod 1 study area: a) LROC mosaic with color DTM basing NAC stereo [1], b) slope map [1], c) depth/diameter ratio map (H/D) [4], d) MINI-RF mosaic [5].

The area is weakly affected by the copernican rays (Fig 1d). In general, the surface area is covered with moderately mature regolith. However, it is observed the N-S zoning of homogeneous populations of craters by their size and relative H/D, forming a chain of NE-SW trending (Fig 1c). The chain of large craters (group Boris) in the north section reveals an immature mare material, but is confined to the inner stony slopes of the crater (Fig 1d). Near Luna 17 lander to SW the size of the craters and the H / D decreases, and regolith is more mature. In the south part of the route H / D is growing, there are stony craters, with a larger diameter.

During 12 lunation (17/Nov./1970-11/Oct./1971) 211 TV panoramas was received by the rover [6]. We selected 2 sites as examples of typical geomorphologic environments (Fig 2, 3):

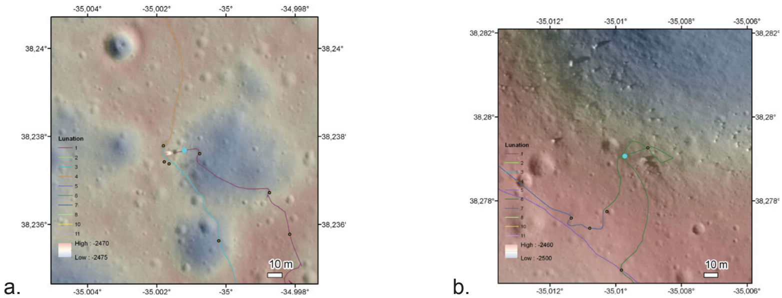

fig. 2. LROC mosaic with color DTM basing on NAC stereo [1]: a) Site 1; b) Site 2.

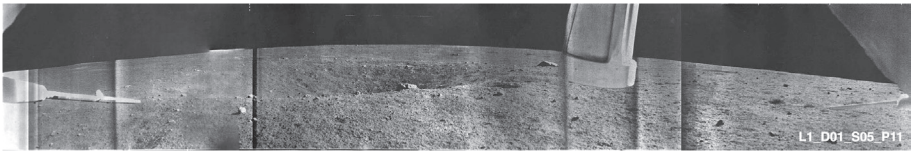

fig. 3. Lunokhod 1 panorama of Site 1.

Site 1 (38.22-38.24 N, 34.98-35.00 W). Near Luna 17 lander. Crater of class B. On a panorama among a flat plain the ~ 3.5 m crater of class B was captured in the left side. Its gentle wall is speckled by small 1-20 cm craters and on the inner slope a concentric heap of cm stones of class 2, form II-III is observed. A horizon is even without any disturbance of relief. The nearest pebbles from the camera are isometric, <10 cm, belong to class 3, the form II. Also <30 cm flattened prismatic stone and farther flattened pyramidal stone <30 cm (class 1, type II) are seen near the crater ring. . On the left side as observed small stones ~ 2-5 cm (class 3, type II) are observed with a density of < 5 stones/m2. Spongy regolith ground is speckled by microcraters, with cellular-plumpy structure.

fig. 4. Lunokhod 1 panorama of Site 2.

Site 2 (38.27-38.28 N, 35.01-35.02 W). A crest of a large regional class A crater Borja. From an orbit this site looks as the rounded wall crest of a large 400 m fresh bowl-shaped crater (Borja) with steep strongly stony internal slopes with high H/D> 0.1 (Fig. 1-2). On the panorama of the inner slope, a dense pile of boulders and pebble is observed. The consisting stones are mainly of angular-rounded irregular and pyramidal forms (a class 1-2, types I, II, III). The sizes vary within 1-50 cm. High density (10-50 stones /m^2) of large stones is observed here. The structure of ground is gravelly with the spots of lumpy-gravelly.

Conclusions:

The considered sites represent typical mare situations. We found the correlation: the smaller crater depth/diameter ratio, less stoniness according Mini-RF, the more gently crater slopes, the more class C craters, meet less and more isometric stones, more loose regolith. Inner slopes of fresh craters are quite steep and stony, as the distance out from them is increasing the density of stones is falling sharply. In the area of the Lunokhod 1 the zonality of crater classes and stoniness degree of NE-SW spreading is found. The regolith around fresh craters is denser, and is less processed by microcraters, than in the area of prevailing of class C craters.

References: [1] Shingareva, K. B., et al. (2012), Lunokhod 1 traverse map, MIIGAiK, DLR, Moscow. [2] Hiesinger, H., R., et al. (2000), J. Geoph. Res., 105(E12), 29239-29276. [3] Lucey, P. G., et al. (1998), J. Geoph. Res., 103, 3679. [4] Gusakova, E. N. et al. (2013), LPSC 44, 1719. [5] McAdam, M. M. et al. (2011), LPSC 42. 2197. [6] Barsukov et al. (1978), Lunokhod 1. Vol. 2. (In Russian). 183 p.

AGES OF CRATER DEPOSITS OF LUNAR SOUTH CIRCUM-POLAR CRATERS CONTAINING EVIDENCE FOR VOLATILES: HAWORTH, SHOEMAKER, AND FAUSTINI

A. R. Tye[1], J. W. Head[1], E. Mazarico[2], A. T. Basilevsky[3],
[1]Brown University, Providence, Rhode Island, USA. [2]Department of Earth, Atmospheric, and Planetary Sciences, Massachusetts Institute of Technology, Cambridge, Massachusetts, USA. [3]Vernadsky Institute 119991 Moscow, Russia. Contact: james_head@brown.edu

Introduction: Lunar craters Haworth, Shoemaker, and Faustini are located in the lunar south circum-polar region and all three have permanently-shadowed (PS) interiors; such craters have been treated as candidate locations for sequestered volatiles[1-6]. Detailed mapping of neutron flux from lunar surface by the Lunar Explorer Neutron Detector (LEND) neutron spectrometer show that although surface deposits of many PS areas do have increased content of hydrogen suggested by a lower flux of epithermal neutrons, in other PS areas this signature of enrichment in hydrogen is not observed[7-8]. Of the three mentioned polar craters, Shoemaker does show enrichment in hydrogen while Haworth and Faustini do not. It has been suggested that hydrogen-poor PS areas are due to the geologically recent downslope movement of surface material leading to destruction and/or burial of the hydrogen enriched deposits[9]. If this is true we would expect to see less downslope movement of material in Shoemaker than in Faustini and Haworth. Here we test this hypothesis by using altimetry data from the Lunar Orbiter Laser Altimeter (LOLA)[10] on board the Lunar Reconnaissance Orbiter (LRO) to assess the distribution of smaller craters in and around Haworth, Shoemaker, and Faustini, model deposit ages, and examine the implications for erosion and deposition within the craters. LOLA data is very dense in the lunar polar regions and has provided a digital elevation model and relief maps of unprecedented detail and unlimited illumination geometries, including in PS regions. Craters of diameter > 250 m on the walls and floors of Haworth, Shoemaker, and Faustini were catalogued, excluding obvious secondary impacts. For Shoemaker and Faustini, deposits from the crater rim outward without major topographic variation or evidence of resurfacing and within one crater diameter were designated as ejecta deposits and their craters were catalogued. For Haworth, a subsection of material extending northwest of the crater rim was designated as ejecta for the purposes of this study.

Results: We compare our crater size-frequency distribution data for each deposit with the global lunar age model to obtain modeled ages for each examined deposit (Table 1). The apparent ages of the walls of the three craters are widely variable; the apparent ages of the floor and ejecta deposits are comparable to one another.

Discussion: *Implications for area geology.* Prior area geologic mapping efforts have been limited by the availability of photographic data in the region[11] (Fig. 1). Crater size-frequency analysis of Shackleton has contradicted existing geologic mapping efforts[6] based on morphological and stratigraphic observations, but has corroborated other, pre-LOLA crater-based ages[12]. Geologic analysis based on a study of superposed craters using AIME and Arecibo image and radar data has yielded Nectarian (~3.9 Ga) ages for the walls and ejecta of Shoemaker and Faustini and pre-Nectarian (>3.9 Ga) ages for the walls and ejecta of Haworth[12] (see their Fig. 3). Our results show all three craters being of Imbrian age (3.2 – 3.85 Ga), though our results do agree that Haworth may be older than Shoemaker and Faustini on the basis of its floor and wall deposits. Prior mapping efforts find a pre-Nectarian age of regional terra material[11, 12]; our study does not address those surfaces.

Slope, deposition, and modeled age. Slope appears to play a major role in determining the crater composition of a surface and, therefore, its modeled age[6]. In Shoemaker and Faustini, the modeled ages of the crater walls are dramatically lower than the modeled ages of the floor and ejecta deposits. These two craters are similar to Shackleton in this way. The wall deposit of Haworth is anomalous in that its modeled age is greater than that of its ejecta deposit. The relationship between slope and crater density is visible in the wall deposit of Haworth (Fig. 2, left panel). Lower slope portions of the wall deposit (the Northwestern portion, South-central portion) show a greater concentration of craters. One explanation for the effect of slope on modeled crater age is that sloping regions have more mass wasting, especially under subsequent impacts, destroying evidence of existing craters[13]. Craters counted in this study of diameter > 250 m would typically be at least 50 m deep upon formation if formed on a low-slope surface[14], and deposition of a layer on the order of at least 50 m thick would be required to erase evidence of such a crater; on a steep slope with a thin, active layer moving downslope eroding and burying underlying topography, it is likely that far less total material is required to erase evidence of a crater. Past efforts to model ages of Shackleton deposits have shown how variable slope and modeled age can be within the floor, wall, or ejecta deposits of a crater[6]. Future efforts around the three craters studied here will need to involve a more precise isolation of deposits to capture the nuances of slope and cratering processes.

Implications for existence and form of volatiles. In Haworth and Faustini, the modeled ages of the crater floors are greater than the modeled ages of the ejecta deposits. Ejecta deposits for this study were chosen to be mostly free of large-scale topographic disruptions and obvious resurfacing; smaller scale variations in slope may have had an effect on the modeled ages of even relatively flat deposits like the floor and ejecta deposits of the three examined craters. To a first order, however, our results suggest that there has not been substantial deposition on the floor of either Haworth or Faustini; such deposition would lower the modeled crater ages of the floor deposits by destroying evidence of past craters[6]. The results for Shoemaker, whose floor deposit is somewhat younger than its ejecta deposit, are less clear and some deposition may have occurred there. This would be consistent with the comparatively lower modeled age of Shoemaker's wall deposit as well, as a higher rate of erosion of material from the wall of the crater would lead to greater deposition on its floor. These results do not agree with what would be expected if the hydrogen enrichment of crater Shoemaker's interior[8] was due to the lower role of downslope movement in this crater compared to the craters Haworth and Faustini. Our age data suggest that there is not a positive correlation between observed crater-based ages and volatile concentration.

Conclusions: The described results show that burial of hydrogen-rich deposits is not likely to be the reason why such deposits are observed in some PS areas and not in others. Hydrogen distribution may be driven by other factors including shallow surficial processes or supply from the lunar interior. Our data show that local slope significantly affects crater presence/preservation, likely through the mechanism of downslope movement, and future study should include crater analysis of smaller, precisely-selected areas to further explore and quantify the relationship between slope and modeled age and find the most accurate deposit ages possible.

References: [1]Watson, K. et al. (1961) *JGR* 66, 3033-3045. [2]Arnold, J. R. (1979) *JGR* 84, 5659-5668. [3]Nozette, S. et al. (1996) *Science* 274, 1495-1498. [4]Stacy, N. J. S. et al. (1997) *Science* 276, 1527-1530. [5]Haruyama, J. et al. (2008) *Science* 322, 938-939. [6] Zuber, M. T. et al. (2012) *Nature* 486, 378-381. [7]Mitrofanov, I. G. et al. (2010) *Science* 330, 483-486. [8]Sanin et al. (2013) LPSC-44, abs 2741. [9]Basilevsky, A. T. et al (2012) *Solar System Research*, 46, 89-107. [10]Smith, D. E. et al. (2010) *Space Sci. Rev.* 150, 209-241. [11]Wilhelms, D. E. et al. (1979) *USGS* Map I-1162. [12]Spudis, P. D. et al. (2008) *GRL* 35, L14201, doi:10.1029/2008GL034468. [13]Howard, K. A. (1974) *Proc. 5th Lunar Sci. Conf.* 61-69. [14]Pike, R. J. (1974) *GRL* 1, 291-294.

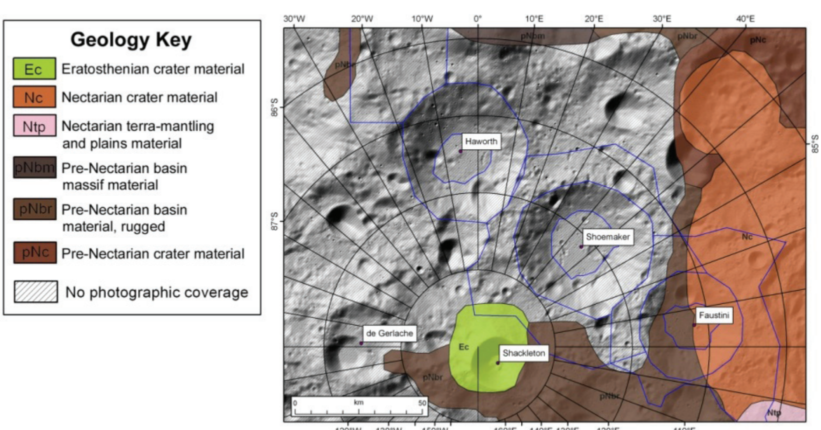

fig. 1. Geologic map[11] of the south circum-polar region study area. Geologic units are plotted in translucent color. Many areas are unmapped due to lack of photographic coverage. Shackleton and associated deposits are mapped as Eratosthenian (1.1-3.2 Ga), while other area deposits are Nectarian (~3.9 Ga) or pre-Nectarian.

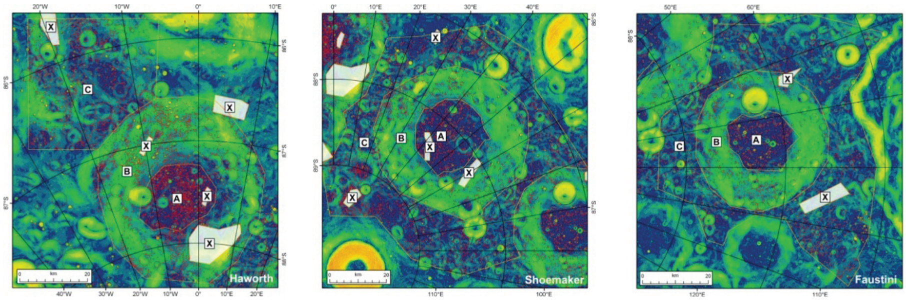

fig. 2. Inset maps of each examined crater and associated deposits. Craters were counted for the following deposits in each figure: floor (marked A), wall (B), and ejecta (C), and the boundaries between deposits are marked in orange. Craters are outlined in red. Secondary clusters are grayed out, marked (X), and not included in the crater frequency data. Craters are plotted over a ~20m baseline slope basemap; see legend. In general, more craters are observed on lower-slope deposits; this can be seen on the Haworth crater wall. Haworth's ejecta blanket was so large that only a subsection of it (deposit (C) in Haworth inset) was included in the study area.

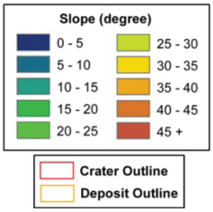

table 1—deposit Ages (**Gyr before present)**

deposit	haworth	shoemaker	faustini
floor (A)	3.57	3.28	3.46
wall (B)	3.4	1.13	1.8
ejecta (C)	3.28*	3.53	3.34

table 1. Ages of observed deposits, based on crater frequency distribution observations. Haworth ejecta is marked with an asterisk (*) because we examine only a subsection of Haworth's large ejecta blanket.

COMPILING THE HYPSOMETRIC MAP OF THE MOON FOR THE ATLAS "RELIEF OF TERRESTRIAL PLANETS AND THEIR SATELLITES"

E.A. Grishakina[1], E.N. Lazarev[1,2],
[1]Lomonosov Moscow State University, Geographical, chair on Cartography and geoinformatics, Moscow, Russia; [2]Sternberg State Astronomical Institute, Lunar and Planetary Research - Moscow, Russia . Contact: orskatya@mail.ru

A large amount of hypsometric maps has been created in the process of moon investigation (Topographic Lunar map, 1964; Lunar Astronautical Chart, 1967; Lunar Map, 1979; Archinal, 2006). After analyzing the most significant achievements corresponding to various stages of moon mapping based on modern and detailed data, obtained by laser altimeter LOLA at LRO spacecraft (Lunar Orbital Data Explorer, 2013), we created a hypsometric map of the Moon at a scale of 1:13 000 000 using the Lambert azimuth equal area Projection (Fig. 1). For calculations a reference sphere with a radius of 1737,4 km was used, as a datum is recommended by the International Astronomical Union (Archinal, 2011). Software of ArcGIS 10 by ESRI Company was used for map creation. One of the primary problems in map compiling was the hypsometric scale generation, what required the primary data used, which quality and detailing was several degrees higher than of the earlier some, to be brought into correlation with a rather rough relief of the nearside and the farside of the satellite. The map is to be included in the "Relief of the terrestrial planets and their satellites" atlas. The separate maps for both Polar regions give possibility to show relief of these very interesting territories in details.

References
Archinal A., Rosiek M.R., Kirk R.L. and Redding B.L. The Unified Lunar Control Network 2005. U.S. Geological Survey: Open-File Report, 2006. 20 p.
Archinal B.A. et al. Report of the IAU Working Group on cartographic coordinates and rotational elements: 2009 // Celestial Mechanics and Dynamical Astronomy. Vol. 109, № 2. 2011. P.101–135.
Lunar Astronautical Chart (LAC), 1:1 000 000. St.Louis/MO/USA: U.S. Air Force Aeronautical Chart and Information Center (ACIC), 1963 – 1967.
Lunar Map (LM), 1:1 000 000. St.Louis/MO/USA: Defense Mapping Agency Aerospace Center (DMAAC), 1978 – 1979.
PDS Geosciences Node Lunar Orbital Data Explorer, 2013. URL: http://ode.rsl.wustl.edu/. (Accessed: 22. Mar. 2013)
Topographic Lunar map (TLM), 1:5 000 000. AMS, Washington: Corps of Eng. 1961-1964.

ANALYSIS OF LUNAR PYROCLASTIC DEPOSITS USING LEND SPECTROMETER DATA.

M. P. Sinitsyn[1], M. L. Litvak[2], I. G. Mitrofanov[2], A. B. Sanin[2]
[1]Sternberg Astronomical Institute MSU, 13 Universitetsky Av. Moscow, Russia; [2] Space Research Institute, 84/32 Profsoyuznaya Str, Moscow, Russia.
Contact: msinitsyn.sai@gmail.com

Introduction:

Lunar pyroclastic deposits (LPD) represent traces of past volcanic activity encountered across the equatorial surface of the Moon. Most of the LPD is located on the near side, both in marine and highlands regions. Quite a lot of these are directly on the boundary mare/highlands areas [3]. Visually, they are regions of low albedo compared to the surrounding areas. Important component of these deposits is the pyroclastic glass, some examples of which were delivered by Apollo 15, 17 [1]. Such deposits contain information about the deep layers of the mantle. Volatile elements enclosed inside the volcanic glass characterize the composition of ancient lunar matter [3]. In the experiments, A. Saal found strong evidence that water and other volatile elements contained within the glass beads, have been voted there just in eruption process [7]. Numerical simulations shows that currently remain some lunar mantle zone, where the concentration of water can reach 600 ppm [7]. The hydrogen content (neutrons count rate) in LPD areas can indicate the amount of water in the lunar mantle beneath these deposits. It should be mentioned that the reduced count rate of epithermal neutrons corresponds to increased hydrogen content [2].Thus it makes sense to look for a correlation between indications of LEND neutron spectrometer [6] and the location of LPD, which are known to about 100 [3,8]. We consider the analysis of neutron flux for the pyroclastic deposits of three areas located on the near side of the Moon.

Mountes Carpatus' Lunar Pyroclastic Deposits :

This LPDs are located on the mountain range, bordering directly to Mare Imbrium (fig.1).

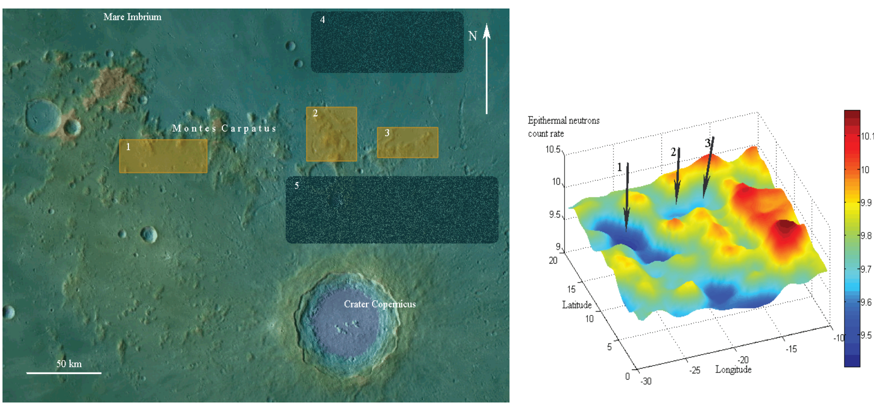

fig. 1. Lunar Pyroclastic Deposits location in the Mountes Carpatus area (left): 1- Montes Carpatus LPD ; 2- Gay-Lussac N LPD ; 3- Gay-Lussac NE LPD ; 4 – mare reference zone; 5 – highland reference zone. Epithermal neutrons count rats of omnidirectional detector (SETN) in the same region (right).The numbers of arrows correspond to the numbers of LPD on the left figure

Calculate the integral average values of the neutron count rates (N_{ex}) in the areas of pyroclastic deposits (1-3 zones) relative to the two reference sites (N_{ref}) (4,5 zones). The reference areas (i.e. the area for comparison) are chosen near the test sites, so that one was in the marine field and the other continental. Comparison neutron fluxes occurs as follows [2,5]:

$\delta = \frac{N_{ref} - N_{ex}}{N_{ref}}$ (1), where δ is called suppression factor.

Clearly, a test section corresponds to reduced hydrogen content compared with the reference for negative delta. Conversely, a positive value of the suppression factor indicates any exceeded concentration hydrogen in LPD area. Calculated values of the suppression factors are shown in Table 1.

From the table it can be concluded that the deposits corresponds to very high values of the suppression factor (2.4-5.3%) with rather convincing degree of reliability.

Table 1. Comparative analysis of LPD areas of Mountes Carpatus with reference zones.

LPD site	reference site	suppression factor (%)	standard error (%)
1	4	4.1	0.93 (4.4 sigma)
1	5	3.6	0.94 (3.8 sigma)
2	4	2.9	0.96 (3.0 sigma)
2	5	2.4	1.0 (2.4 sigma)
3	4	5.3	2.4 (2.2 sigma)
3	5	4.6	2.4 (1.9 sigma)

From the table it can be concluded that the deposits corresponds to very high values of the suppression factor (2.4-5.3%) with rather convincing degree of reliability.

Lunar Pyroclastic Deposits of Apollo-17 landing site and Fra-Mauro crater:

The landing site of Apollo-17 placed in the Taurus-Littrow Valley on the eastern of the Mare Serinitatis. Precisely in this area volcanic glass of red tint has been found and delivered to Earth. Inside the samples of the glass A. Saal subsequently discovered up to 30 ppm water. In this area a large LPD has been identified [3, 8].The suppression factor obtained by collimated epithermal neutron detector (CSETN) is: $\delta = 5.9\% \pm 2.3(2.5\sigma)$ .This indicates a very high content of hydrogen (water) directly at the collection place.

In the area of Fra-Mauro crater the largest neutron depression in the equatorial region is located (fig.2).

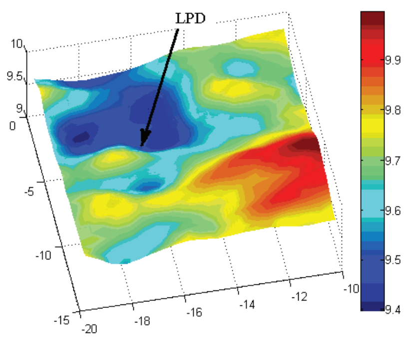

fig. 2. Epithermal neutrons count rate distribution in the Fra-Mauro crater area. The black arrow points to LPD location. The deep blue region corresponds to the neutron depression.

According to the CSETN the suppression factor of LPD is: $\delta = 5.9\% \pm 2.3(2.5\sigma)$. These results for the Fra-Mauro and Taurus-Littrow LPD confirm that analyzed areas can be strong outlet of indigenous lunar water.

Conclusion:

In the present report examined the neutron fluxes from several deposits on the near side of the Moon. It seems very noticeable tendency of suppression the neutron flux. However, in considering the location of various deposits, especially those located on the outside shows a more complex behavior of the neutron flux.

References:
[1] Allen, C.C. et al. JGR, 117, E00H28(2012)
[2] Boynton, G.F. et al. JGR,117,E00H33(2012)
[3] Gaddis, L.R. et al. Icarus, 161, 262-280(2003)
[4] Gustafson, J.O. et al. JGR, 117, E00H25(2012)
[5] Mitrofanov,I.G. et al. Science,330,483-486(2010a)
[6] Mitrofanov,I.G. et al. Space Sci. Rev., 150(1-4),183-207(2010b)
[7] Saal, A.E. et al. Nature, 454(2008)
[8] Moon Pyroclastic Volcanism Project: http://astrogeology.usgs.gov/geology/moon-pyroclastic-volcanism-project

THE TEMPERATURE PROFILE OF THE LUNAR MANTLE AND CONCENTRATIONS OF RADIOACTIVE ELEMENTS IN THE MOON.

E. V. Kronrod, O. L. Kuskov, V. A. Kronrod,
Vernadsky Institute of Geochemistry and Analytical Chemistry, Russian Academy of Sciences, Moscow, Russia, Contact:kendr_ka@bk.ru

Introduction:

In this work we have suggested the probable temperature profile of the lunar mantle that satisfied geophyscal and geochemical constraints and determined possible uranium content in the Moon and surface heat flows.

Computer **simulation and result:**

The following issues have been discussed: (I) Estimation of probable temperature distributions in the lunar mantle, (II) Estimation of heat flows and intensity of radioactive sources.

I. Estimation of probable temperature distribution in the lunar mantle.

1. We determine the probable temperature from seismic velocities [1]. The method of velocity inversion had been discussed in [5], [6].

2. The range of probable temperature variations in the mantle was obtained in the works [5], [6]. We have found the minimal temperature in the upper mantle. The minimal temperature of 500°C at a depth of 150 km satisfies limitations on the mass, moment of inertia and seismic velocities [3], [4].

3. Absence of density inversion is a natural requirement for the hydrostatic equilibrium in the satellite. From numerical modeling temperature profile with gradient ***dT/dH =1,05-0,0006*H, (H – km),*** which satisfies almost zero gradient of density with acceptable accuracy, was selected. The mantle temperature can be described by an equation: $\boldsymbol{T=1.05*H-0.0003H^2+C}$. Temperature gradient at the depth of 150-1000 km accurate within 1°C, $\boldsymbol{\delta T_{1000\text{-}150} = T_{1000} - T_{150} = 600^o}$.

Correlating all of constraints on the temperature profile we find probable temperature profile of the lunar mantle at the depth less than 1000 km: $\boldsymbol{T_{pm}{}^oC = 449+1{,}05*H-0{,}0003H^2}$, **H** – depth in kilometers.

II. Estimation of heat flows and intensity of radioactive sources.

One-dimensional stationary model of thermal conductivity has been used to calculate the radioactive source intensity. We propose the model of the Moon which contains the crust with the depth of 40 km and the density of 2580 kg/m^{-3} [7], the upper mantle with a heat source Q_{up}, the lower mantle with a heat source Q_{low} and the core. The lower boundary of the upper mantle is within the limits of 500-1000 km depth, the radius of the core is 350 km. The aim of the study is to find values of the heat flow sources corresponding to the set of temperature distribution in the mantle. Obtained relations enable to determine the temperature distribution in the mantle. Based on the assumption that Th/U=3.7, K/U=2000 [2], heat conductivity coefficient k=4 W m^{-1}K^{-1}, we have estimated uranium concentration in the upper (C_{Uup}) and lower mantle (C_{Ulow}, C_{Ulow}= C_{Ubulk}), surface heat flow (J_s) (Figs. 1, 2) and the corresponding temperature distributions in the lunar mantle (Fig. 3)

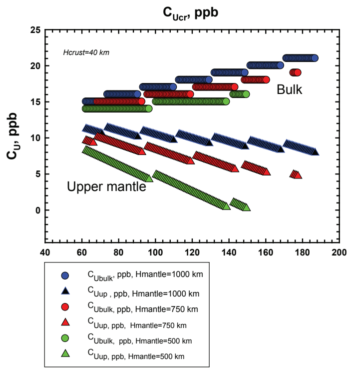

fig. 1. Calculated uranium concentration in the upper mantle (C_{Uup}) and in the lower mantle (C_{Ulow}, C_{Ulow}= C_{Ubulk}). The range of the depth of the boundary between upper and lower mantle H_{mantle} was 500-1000 km, the depth of the crust H_{cr}=40 km, the density of the crust ρ_{cr}=2600 kg/m^3

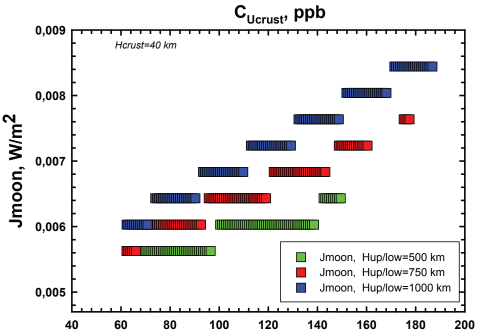

fig. 2. Calculated surface heat flow range. The depth of the crust H_{cr}=40km, the density of the crust ρ_{cr}=2600 kg/m^3

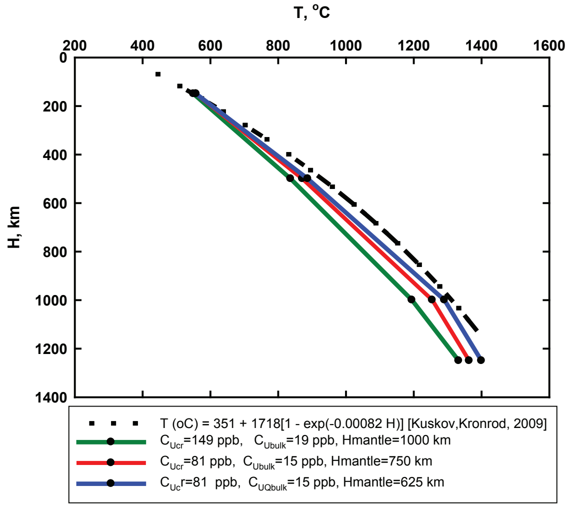

fig. 3. Temperature distributions in the lunar mantle corresponding to calculated surface heat flow

3. Conclusions

1. We have estimated the acceptable temperature distribution in the lunar mantle which satisfy principal geochemical and geophysical constraints.

2. Assuming that the U concentration in the crust is 150-180 ppb, the estimated bulk lunar U_{bulk} abundances range within 19-21 ppb, upper mantle U_{up} abundances range within 4.7-8.9 ppb, surface heat flow J_{moon}=7.6-8.4 mW/m^2.

Acknowledgements
This research was supported by Russian Academy of Sciences under Programs 22 and 28, and by RFBR grant 12-05-00178 and 12-05-00033.

References

[1] Gagnepain-Beyneix, J., Lognonné, P., Chenet, H. et al. (2006). A seismic model of the lunar mantle and constraints on temperature and mineralogy, Phys. Earth Planet. Interiors, Vol. 159, pp. 140-166
[2] Hagermann, A., Tanaka, S. (2006). Ejecta deposit thickness, heat flow, and a critical ambiguity on the Moon, Geophys. Res. Lett. 33, L19203, doi:10.029/2006GL027030.
[3] Kronrod, E.V., Kuskov, O.L., Kronrod V.A. (2012). Geochemical and geophysical constraints for thermal field of the Moon, EPSC Abstracts, Vol. 6, EPSC-DPS2011-16.
[4] Kronrod, V.A., Kuskov, O.L. (2011). Inversion of Seismic and Gravity Data for the Composition and Core Sizes of the Moon, Izv. Phys. Solid Earth., Vol 47, pp. 711-730.
[5] Kuskov, O.L., Kronrod, V.A. (1998). Constitution of the Moon: 5. Constraints on composition, density, temperature, and radius of a core, Phys. Earth Planet. Interiors, Vol. 107, pp. 285-306
[6] Kuskov, O.L., Kronrod, V.A. (2009). Geochemical constraints on the model of the composition and thermal conditions of the Moon according to seismic data, Izv. Phys. Solid Earth., Vol. 45, pp. 753–768
[7] Wieczorek, M.A., Neumann, G.A., Nimmo, F. et al. (2012). The Crust of the Moon as Seen by GRAIL, Sciencexpress /http://www.sciencemag.org/content/early/recent/5 December 2012 / Page 1/ 10.1126/science.1231530.

NEW LUNAR LANDER SITE SELECTION.

Y. Lu[1], J. Ping[1], V. Shevchenko[2],
[1]National Astronomical Observatory, CAS, 20A Datun Rd., Chaoyang, Beijing, 100012, China, [2]Sternberg State Astronomical Institute, MSU, University prospect, 13, Moscow, 119992, Russia. Contact: luyangxiaoyi@gmail.com

Introduction:

In March 2012, China began manufacturing the body and payload of the Chang'e 3 lander, which will perform lunar surface and space studies independently of the mission's mobile rover. Chang'e 3 is scheduled to be the first spacecraft to perform a soft landing on the Moon since the Soviet Union's Luna 24 in 1976, breaking a 37-year gap in lunar surface exploration. The stationary lander will be equipped with a radioisotope thermoelectric generator (RTG) in order to power its operations during its planned three-month mission. The lander has a mass of 1,200 kg (2,600 lb) and will have a scientific payload of seven instruments and cameras. In addition to their lunar scientific roles, the cameras will also acquire images of the Earth and other celestial bodies. The Chang'e 3 mission incorporates a lunar rover, designed to deploy from the lander and explore the lunar surface independently. The development of the six-wheeled rover began in 2002 at the Shanghai Aerospace System Engineering Institute and was completed in May 2010. The rover stands 1.5 m high and weighs approximately 120 kg. With a payload capacity of approximately 20 kg the rover may transmit video in real time, and can dig and perform simple analysis of soil samples. It can navigate inclines and has automatic sensors to prevent it from colliding with other objects. Energy will be provided by a solar panel, allowing the rover to operate through lunar days. The six-wheeled rover is designed to explore an area of 3 square kilometres during its 3-month mission, with a maximum travelling distance of 10 km. The rover will carry a radar unit on its underside, allowing for the first direct measurement of the structure and depth of the lunar soil down to a depth of 30 m, and investigation of the lunar crust structure down to several hundred meters' depth. It will also carry an alpha particle X-ray spectrometer and an infrared spectrometer. Chang'e 3 is scheduled for launch in late 2013 as part of the second phase of the Chinese Lunar Exploration Program.

Landing site:

Topographic data from the Chang'e 1 and 2 orbiters were used to select a landing site for Chang'e 3. The lander is scheduled to land on the Sinus Iridum at latitude of 44° north. The Sinus Iridum is a plain of basaltic lava that forms a northwestern extension to the Mare Imbrium.

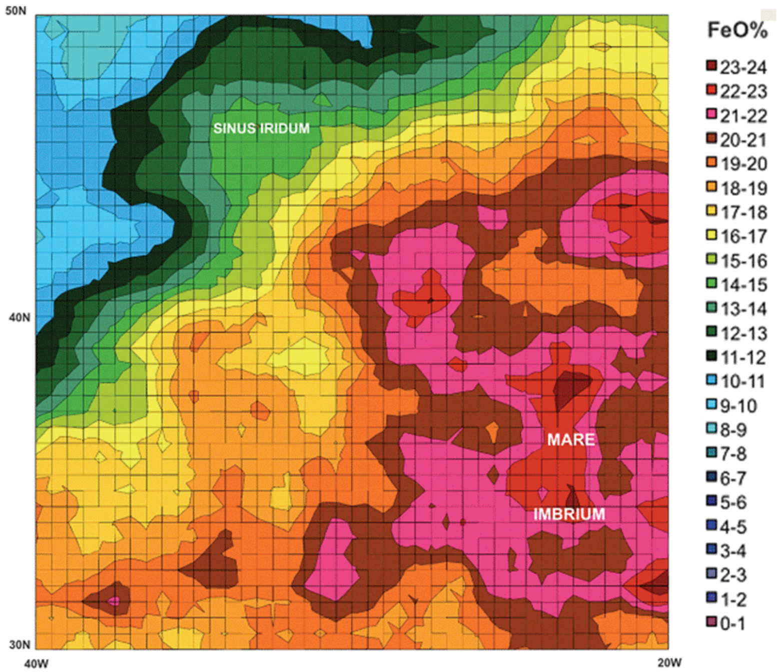

fig. 1

On Figure 1 it's shown the map of iron content inside considered region. These results were obtained by means of the gamma-ray spectrometer data and alpha particle spectrometer data received from **«Lunar-Prospe**ctor» spacecraft. In particular, more accurately able to determine the content of iron (Fe) in the frozen lava of volcanic melts. Their concentration was different for different parts of the surface morphology – Sinus Iridum and northern part of Mare Imbrium. The intermediate zone between both areas is more interesting region for site studies.

Figure 2 shows the variations in the lunar gravity field as measured by the **"**GRAIL**"** mission (image credit: NASA, MIT). Red corresponds to mass excesses and blue corresponds to mass deficiencies.

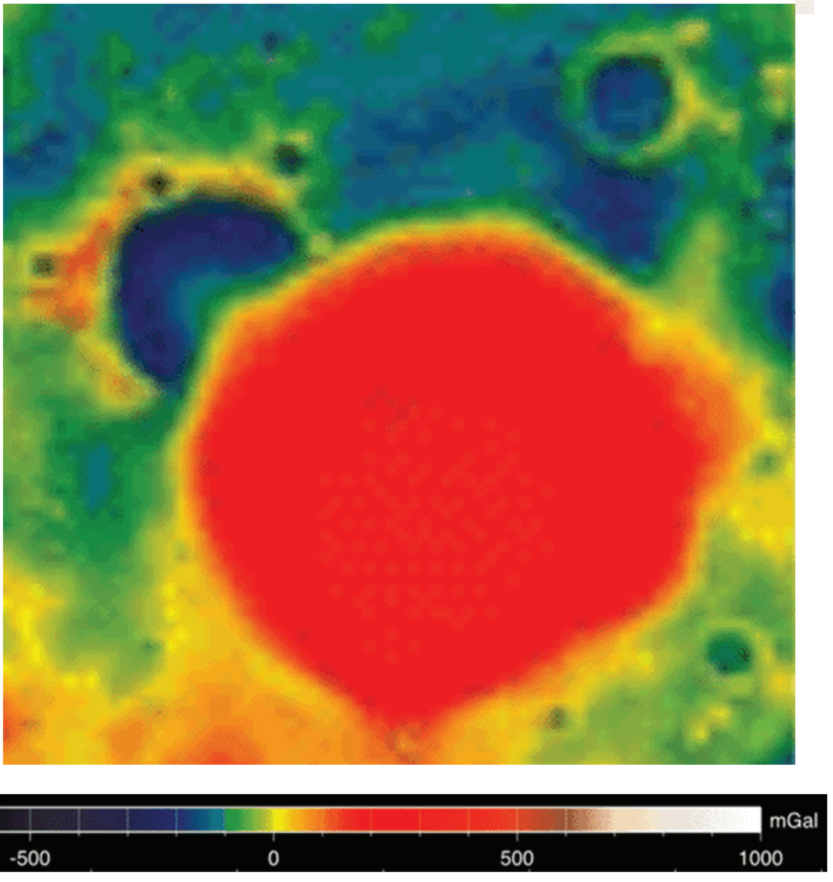

fig. 2

We can see the similar intermediate zone between Sinus Iridum region and Mare Imbrium area on gravity field map. Beneath its heavily pockmarked surface, the Moon's interior bears remnants of the very early solar system. Unlike Earth, where plate tectonics has essentially erased any trace of the planet's earliest composition, the Moon's interior has remained relatively undisturbed over billions of years, preserving a record in its rocks of processes that occurred in the Solar system's earliest days.

Conclusions:

It's known that due to the lunar impact mascon basins have been dominated by an isosdetic processing of the mantle uploading and basalt filling at basin bottom, this evolution is directly connect with igneous activity. Identifying the mascon basins of various features will give more information to uncover the lunar dynamical evolution history.

So, in result of Chang'e 3 mission we can investigate *in situ* such lunar features as structure of impact craters, near-surface magmatism, mechanisms and timing of deformation, cause(s) of crustal magnetization, estimation of upper-crustal density on intermediate zone between Sinus Iridum region and Mare Imbrium area.

IMPACT CRATERS TSIOLKOVSKY AND AITKEN AS OBJECTS OF SEARCH FOR RESIDUAL WATER ON THE MOON.

M.I. Shpekin[1], A.A. Barenbaum[2]
[1]Kazan Federal University, Russia, Kazan, Kremlevskaya str. 18, Michaels1@yandex.ru, [2]Oil and Gas Research Institute RAS, Russia, Moscow, Gubkin str. 3, azary@mail.ru,

Introduction:

The presence of water on the Moon is established by recent research [*Basilevsky et al, 2012*]. In particular, traces of water were found: 1) in igneous rocks delivered from the Moon to the Earth, 2) in the lunar regolith from the IR spectra of the sunlit portions of the lunar surface, and 3) in craters at the lunar poles on measurements of epithermal neutrons.

At present, three groups of hypotheses are proposed to explain the presence of water on Moon.

1) The inflow of juvenile water from the depths at the peak of lunar volcanism 3.2–3.7 billion years ago [*Head, Wilson, 1979; Gaddis et al, 1985; etc*.], and then later [*Hiesinger et al., 2001*]. It is estimated [*Basilevsky et al., 2012*] that 10^{11}–10^{12} tons of water could stand for the outpouring of basalts.

2) Reaction of solar wind protons with regolith and their subsequent conversion to hydroxyl OH, and then H_2O [*McCord et al., 2010; McCord, Combe, 2011; Burke et al, 2011*]. According to [*Housley et al, 1973, 1974; Arnold, 1979*] solar wind can form on the surface of the Moon annually 50 tons of water. In this case, the lunar surface is saturated with OH for about ~10^3 years. It is noted that protons can also get to the Moon when it gets to the tail of the Earth's magnetosphere. In this case, the saturation is reached for about ~10^4 years.

3) The fall of the Solar system comets on the Moon [*Shevchenko, 1999; etc*.], as well as water-rich C-type asteroids [*Ong et al, 2010; etc*.]. Shevchenko estimated that for the mass of the observed ice deposits on the Moon requires 6×10^4 falls short-period comets or 300 falls of giant comets such as Hale-Bopp. And according to the calculations of Ong and others over the last billion years $(0.13–4.3)\times10^9$ tons comet and 2.7×10^9 tons of asteroidal water could be accumulated. That explains a lot of water ice at the poles, estimated at 2.1×10^8 tons [*Feldman et al, 2001*].

Paper tasks:

In connection with the discovery of the phenomenon of jet expiration of gas and dust material from the galactic center [*Barenbaum, 2002, 2010, 2012b*] the main source of water on surface of the Moon is recognized as comets fall of galactic origin. These comets arise in the areas of gas condensation (star) of galactic branches and enter the Solar system solely at the intersection of moving along the galactic orbit of the Sun jet streams and the spiral arms of the Galaxy. The last such period occurred on 5÷1 million years ago and was due to staying of the Sun in the jet stream of Orion-Cygnus.

According to [*Barenbaum, 2002, 2012b*], these comets had a jet stream velocity relative to the Sun 450 km/s. They consisted primarily of water ice density ≈1 g/cm³, had a diameter of 100–3500 m, weight of $10^{12}\div10^{17}$ g and energy of 10^{20}–10^{25} J. In the last period of "comet shower" mostly they bombarded the southern hemisphere of the Moon [*Barenbaum, 2012*], and their falls density was 3–5 bodies of all sizes to the site 100×100 km² [*Barenbaum, 2012a*]. This frequency of galactic comets falls is at least two orders of magnitude larger than the Solar system comets and asteroids of the same size. With an average weight of galactic comets ~10^{14} g only during the last bombardment 5÷0.6 million years ago ~10^{11} tons of water could be brought to the Moon.

It is assumed that some part of cometary water could be preserved in the rocks of lunar surface [*Shevchenko, 1999; Pierazzo, Melosh, 2000; Artemyev, Shuvalov, 2008; Ong et al., 2010*]. Theoretically estimate the amount of this water is very difficult [*Basilevsky et al, 2012*].

Actual data:

In this paper we show the possibility of bringing to its decision the orbital images of Tsiolkovsky (diameter 180 km) and Aitken (diameter 130 km) craters on the far side of the Moon. Both craters have central peaks, and their bottoms are covered with "fresh" basalt lava. On the high-resolution images of the Tsiolkovsky crater we have discovered pouring lava volcano height of 102 m, located on a small flat oval elevation of plume nature 24-26 km in diameter [*Shpekin, 2009; Barenbaum, Shpekin, 2011, 2012*]. The combination of volcanoes and plume rises is typical of the shallow magma chambers, resulting in the fall of galactic comets [*Barenbaum, 2012a*]. We believe that such a chamber volume of ~10^2 km^3 now exists under the bottom of the crater Tsiolkovsky.

According to our data the craters Tsiolkovsky and Aitken emerged in the period of the last bombardment the Solar System by galactic comets. Tsiolkovsky crater was formed about ~1 million years ago, and crater Aitken, probably, by about 1–2 million years earlier. Judging by the diameter of craters, the galactic comets which had created the first and second craters had masses of ~10^{10} tons and ~3×10^9 tons respectively. If all comet water remained in crater, then layer of ice on the bottom of it would be in the first case, 56 cm, and the second – 35 cm.

It is obvious that the galactic comet is completely destroyed during the crater formation. High resolution images, however, show that the water, which is part of the comet, leaves the crater not completely. Some of the water is captured and frozen in rock walls and bottom of the crater. Over time, thawing, these rocks subsequently recover water, which leads to phenomena previously not discussed in the literature.

Three of these phenomena are discussed below. The first phenomenon is the existence of the moving glaciers on the Moon. In both craters we see separate glaciers that descend in the form of a tongue from the south-western slope of a steep central peaks crater Tsiolkovsky and Aitken.

The second fact we associate with the evidences of the existence of the moving water in the surface layer of the Moon. One of them is a volcano in the crater Tsiolkovsky, pouring “liquid” lava, with a large amount of water that freezes and rapidly sublimates.

We can show also another example. This is portion of the surface of the crater bottom Tsiolkovsky north central peak on which there are ravines and “frozen rivers”. It is likely that these structures could arise earlier under action of mobile water.

The high resolution images illustrate another phenomenon widespread in the Tsiolkovsky crater. It is associated with the roll-down of stones from slopes of the crater in result gradually thawing under them the regolith. The resolution of the image allows you to see the stones of the size of ~1 meter. It is no doubt in that the defrosting of rocks under a layer of regolith occurs nowadays. Expiring in this process stones roll-down the slopes crater, filling the depressions and grooves in relief of the crater slopes, or remain on the high regions of the surface with a zero slope.

Main results and conclusion:

• The main source of water on the Moon, as well as on all the planets [*Barenbaum, 2010*], is cyclic bombardment of the Solar system by galactic comets.

• The amount of water that the galactic comets brought to the Moon during the period from 5 to 1 million years ago, about ~10^{11} tons. This water is sufficiently to explain origin of observed quantity ice on the Moon.

• A significant, but still difficult to define amount of frozen water is present under a layer of regolith rocks in the bottom and sides of large comet craters.

• Our analysis of high-resolution images of craters Tsiolkovsky and Aitken shows this water is slowly released in the modern geological processes proceeding on the Moon.

Two final questions are need special study.

References:

Arnold J.R. (1979), *J. Gephys. Res.* V.84, P.5659-5668.
Artemieva, N.A., V.V. Shuvalov (2008), *Astron. Vestnik*, V.42, №4, P.351-356.
Barenbaum A.A. (2002), *Galaxy, Solar system, Earth: Coordinated processes and evolution*, Moscow, GEOS.
Barenbaum A.A. (2010), *Galactocentric paradigm in geology and astronomy*, Moscow, LIBROKOM.
Barenbaum A.A. (2012), *Vestnik ONZ RAS*, V.4, NZ9001, doi:10.2205/2012NZ_ASEMPG, http://onznews.wdcb.ru/publications/v04/asempg12en/2012NZ_ASEMPGE03.pdf
Barenbaum A.A. (2012a), *Uralian Geology Journal*, № 6 (90), P.3-26.
Barenbaum A.A. (2012b), *Galaxy Centric Paradigm in Natural Science, part I*. APAAS № 2, 2012, Kazan-Daytona Beach. http://www.kcn.ru/tat_en/science/ans/journals/rasj_cnt/12_2_4/12-2-4.html
Barenbaum A.A., M.I. Shpekin (2011), *Vestnik ONZ RAS*, V.3, NZ6011, doi:10.2205/2011NZ000141. http://onznews.wdcb.ru/publications/v03/asempg11en/2011NZ000141.pdf
Barenbaum A.A., Shpekin M.I. (2012), *European Lunar Symp.* DLR, Berlin, 05042012, Abstract 101–104. http://lunarscience.arc.nasa.gov/ELS2012/sites/default/files/Abstracts_volume_05042012_0.pdf
Basilevsky A.T., A.M. Abdrakhimov, V.A. Dorofeeva (2012), *Astron. Vestnik*, V.46, №2, P.99-118.
Burke D.J., Dukes C.A., Kim J.H. et al. (2011), *Icarus*, V.211, P.1082-1088.
Feldman W.C., S. Maurice, D.J. Lawrence et al. (2001), *J. Gephys. Res.* V.106, E10, P.2321-23252
Gaddis L.R., C.M. Pieters, B.R. Hawke (1985), *Icarus*, V.61, P.461-489.
Head J.W., L. Wilson, (1979), *Proc. Lunar and Planet. Sci. Conf*. V.10, P.2861-2897.
Hiesinger H., J.W. Head, U. Wolf, G. Neukum (2001), *Lunar and Planet. Sci.* V.32, Abs. 1815.
Housley R.M., R.W. Grant, N.E. Paton (1973), *Proc. Lunar. Sci. Conf*. V.4, P.2737-2749.

Housley R.M., E.H.Cirlin, N.E. Paton, I.B. Goldberg (1974), *Proc. Lunar. Sci. Conf*. V.5, P.2623-2642.
McCord T.B., J.Combe (2011), *Lunar and Planet. Sci*. V.42, Abs. 1843 pdf.
McCord T.B., L.A. Taylor, T.M. Orlando et al. (2010, *Lunar and Planet. Sci.* V.41, Abs. 1860.
Ong L., E.I. Asphaug, D. Korycansky, R.F. Coker (2010), *Icarus*. V.207, P.578-589.
Pierazzo E., H.J. Melosh (2000), *Meteorit. and Planet. Sci.* V.35, P.117-130.
Shevchenko V.V. (1999), *Astron. Vestnik*, V.33, №5, P.400-408.
Shpekin M.I. (2009), One small step for a man (to the ***40th*** anniversary of man landing on the Moon). http://old.kpfu.ru/f6/k8/bin_files/ols!38.pdf

LARGEST IMPACT CRATERS AT SMALL PLANETARY BODIES – MODELS AND OBSERVATIONS.

B. A. Ivanov,
[1]*Institute for Dynamics of Geospheres RAS, Leninsky prospect 38-1, Moscow, Russia. Contact: baivanov@idg.chph.ras.ru, boris_a_ivanov@mail.ru*

Introduction:

Recent robotic space mission to the Moon (e.g. LRO and GRAIL [1, 2]) and the second largest asteroid Vesta (DAWN [3]) delivered a lot of new observational data including images and gravity anomaly measurements. These data create the new database for planetological analysis including the re-iteration of previously elaborated models. Here we discuss problems we met in the numerical modeling of the largest impact craters on Vesta [43] in comparison with new models of lunar craters published recently [5].

Crater Formation Mechanics:

The specific of largest crater formation on planetary bodies is the compatibility of the crater and the target sizes. The proper numeric model should include all the spherical target body into the computational grid and compute the gravity field departed from a simple radial one due to large mass distortion (see details in [6]). A standard work station allows us get a grid approximately of one million cells (e.g. 1000x1000 cells) and resolve the spherical target with approximately 500 cells per the target radius. Without any supercomputing the parametric study of impacts in 2D is easy and fast provide we limit the spatial resolution with ~0.5 to 0.7 km/cell for Vesta and ~5 km/cell for the Moon.

The typical scenario of a crater formation is illustrated in Figure 1 for one of many available Vesta impact modeling [4]. The vertical impact at 5.5 km/s results in a global shock/stress wave propagation, damaging target.

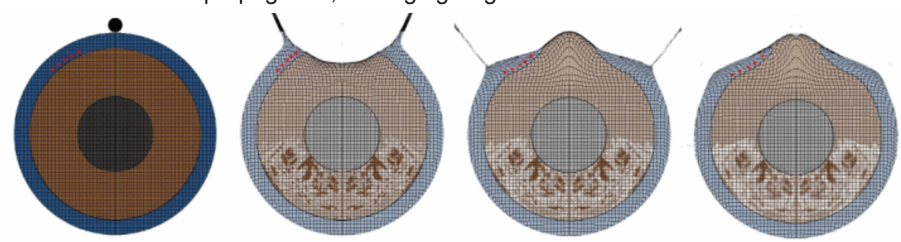

fig. 1. A set of frames illustrated the process of the Rheasilvia impact crater formation on Vesta (the model run B4010045 from [5]: cell size 0.93km, 20 cells per projectile radius, projectile diameter 37.32 km, transient cavity radius 286 km, maximum transient depth 82 km, final rim crater diameter 508 km). Time moments are shown (left to right): 0 s, 500 s, 1500 s, 5000s. Colors outline crust, mantle, and core. Color intensity illustrates the level of damage (for iron core the “damage” means the occurrence of plastic deformations above the elastic limit).

The transient cavity formation is followed with the cavity collapse and the central uplift formation well before the ejecta land back to the target surface. Final state of the target is characterized with the totally fragmented crust and partially damaged mantle in the hemisphere, opposite to the point of impact.

Rotating Vesta: The modern rotational period of Vesta is about 5.3 hours [3]. The close to elastic state of the antipodal mantle hemisphere (the rightmost frame in Figure 1) witnesses in favor of an assumption that the Rheasilvia formation does not result in the extensive inelastic flow approximately in a half of Vesta. Hence, the pre-impact shape of Vesta may be partially preserved [7]. The current estimate is that pre-impact rotation rate of Vesta was about 6% faster than now. Hence the rotation of a target should be implemented in the model.

Rotating Vesta shape. The close to polar location of the Rheasilvia crater allows us to make first steps in the rotation analysis with the same 2D model where centripetal accelerations are added to the gravity accelerations. In this approximation the rotation of Vesta as a solid body may be computed numerically. The general equilibrium solution for a three layer ellipsoid is absent, while partial solutions are available. The direct numerical modeling of the rotational state gives results shown in Fig. 2. Unfortunately only one target structure with only one set of materials (“basalt”, “dunite”, “iron”) was modeled today. The progress in geophysical modeling of Vesta (e.g. [7]) would result in a better initial guess for the future numerical modeling.

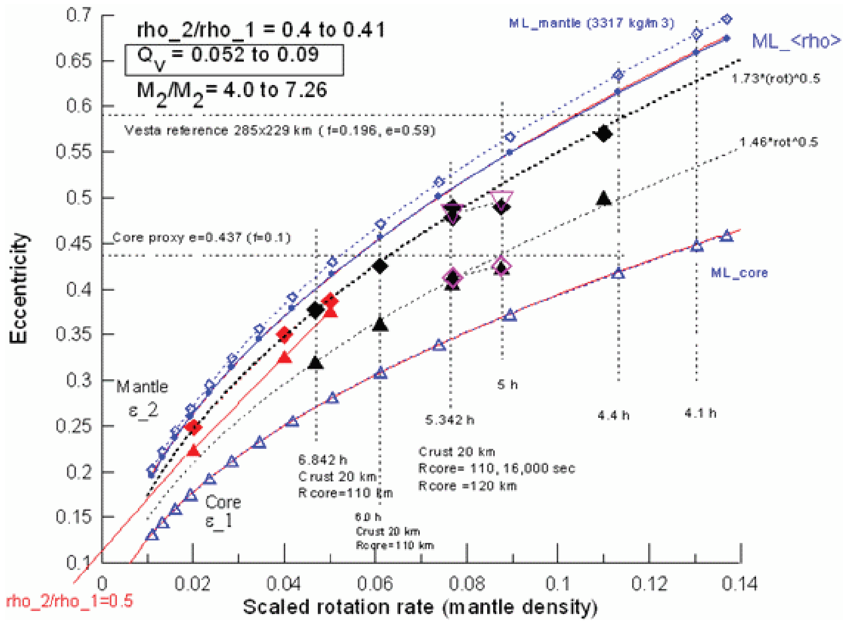

fig. 2. Modeled shape of a 3-layers Vesta rotated with periods from 5 to 6.6 hours (triangles are for the core shape, diamonds are for the surface shape). The rotation velocity is scaled to the mantle density. For comparison blue signs and curves show uniform Maclaurin ellipsoids with mantle density, iron (core) density, and the average density of the layered model Vesta. Red signs illustrate approximate 2-layer rotational ellipsoid shapes from [8]. Density ratio and core/mantle mass ratio in [8] are listed in the upper left corner of the figure. DAWN preliminary estimates [9] are shown as horizontal dashed lines.

Currently the shape of the model Vesta is estimated by the numerical models, where densities of the crust, mantle and core are fixed with the available ANEOS-based equations of state [4]. The next step is to combine new geophysical models of Vesta and more flexible equations of state for the numerical modeling. The current set of densities looks “too heavy” – the model eccentricity is smaller than preliminary DAWN data even for 5 hours rotational period.

Cratering at Rotating Vesta. The few model runs have been done at the elliptic model Vesta rotated with 5.5 hours period. .Two of them resulted in a good representation of the Rheasilvia crater geometry (Figure 3).

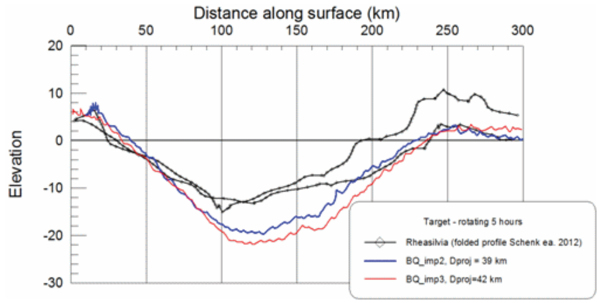

fig. 3. Radial profiles of modeled Rheasilvia crater at the rotating model Vesta (blue curve for 39-km projectile, red curve – for 42-km projectile in comparison with DAWN measurements (black curves).

Discussion and Conclusion: 2D modeling with self-gravity allows us relatively wide (not enough wide yet) parametric study of Vesta’s cratering processes. Direct comparison of model crater profiles with Dawn observations allows us to restrict (not enough well yet) the impact energy corresponding the Rheasilvia formation (D_{proj} ~40±5 km at 5.5 km/s; should be larger for an oblique impact). Impact of this scale on Vesta may result in a minor residual deformation of the core (<~1%) and the vertical offset of the figure center below the center of gravity (0.5 to 1 km). Cratering on rotating Vesta differs only slightly from the spherical target case (at the background of the material model uncertainty). The next step is the study of Vesta’s despinnig.2D parametric study should save some computational time for 3D modelers.

Numerical modeling of giant (in comparison with a planet size) impact craters on Vesta open an important theme of comparative study of giant crater formation on progressively larger bodies (the Moon, Mars, and Earth).

Acknowledgments: The work is supported by the Program 22 “Fundamental Problems of Solar System Research” (Project 8.3).

References: [1] Head J. W. et al. (2010) Global distribution of large lunar craters: Implications for resurfacing and impactor populations. *Science* **329** (5998), 1504-1507. [2] Wieczorek M. A. et al. (2013) The crust of the Moon as seen by GRAIL. *Science* 339, 671-675. [3] Russell C. T. et al. (2012) *Science*, **336**(6082), 684–686. [4] Ivanov B. A. and H. J. Melosh (2013) *JGR-Planets*, v. **118**, doi:10.1002/jgre.20108 (in press). [5] Melosh H. J. et al. (2013) Origin of Lunar Mascon Basins, *Science*, **340**(6140), 1552-1555. [6] B. A. Ivanov et al. (2010) In *Large Meteorite Impacts and Planetary Evolution IV*, W. U. Reimold, R. L. Gibson, Eds. (Special Paper 465, Geological Society of America, Boulder, Colo., 2010), pp. 29–49. [7] Fu R. R. et al. (2013) Early viscous relaxation of asteroid Vesta and implications for late impact-driven despinning. *LPSC 44th*, abs. # 2115. [8] Kong, D. et al. (2010) *JGR-Planets*, **115**, 12003. [9] Jaumann R. et al. (2012) *Science* **336** (6082), 687-690.

TWO EXAMPLES OF NON-TRADITIONAL INTERPRETATION OF PLANETARY FEATURES IN LIGHT OF LATEST COSMIC DATA: 1) MARE ORIENTALE GRAVITY PATTERN; 2) MERCURY'S NORTHERN PLAINS AND ARCTIC OCEAN OF EARTH.

G.G. Kochemasov,
IGEM of the Russian Academy of Sciences, 35 Staromonetny, 119017 Moscow, kochem.36@mail.ru

The wave planetology [1, 3 & others] implies that along with some impact features [2] on planetary surfaces prevail roundish forms of non-impact origin. Intersecting standing inertia-gravity waves, origin of which is related to keplerian non-round orbits with changing accelerations, make them. Warping waves in rotating bodies have four interfering ortho- and diagonal directions (Fig. 2). The NASA' GRAIL mission has provided excellent gravity maps of the lunar marea and basins showing regularly spacing zones of differing gravity and composing them "craters" –beads (Fig. 1). When the most complete and clear this "beads-collar" structure one observes at the Orientale Basin, other Basins of the lunar far sides also have collars with beads (Moscoviense, Freundlich-Sharonov, Dirichlet-Jackson, Hertzsprung). The best explanation of their origin by the wave model is in Fig. 2. It should be mentioned that hints of such wave tectonics were observed already in the Kaguya data. The Kaguya gravity anomalies (Fig. 3) show intersecting chains and grids of even-sized shoulder-to-shoulder "craters" of the wave origin. Titan's icy surface also gives one clear example of such "beads-collar' structure around one tectonic granule (Fig. 4).

A recently published article of H.J. Melosh et al [2] traditionally explains origin of lunar mascons by impacts and develops a model taking into account three major free-air gravity zones of mascons. But more careful analysis of these features reveals their more complex structure, namely the finer division of these superstructures by ring zones (collars) and regularly spaced "beads" adorning them (Fig. 1). Such complex and regular feature is better explained by a lithosphere wave warping then by a random impact (Fig. 2).

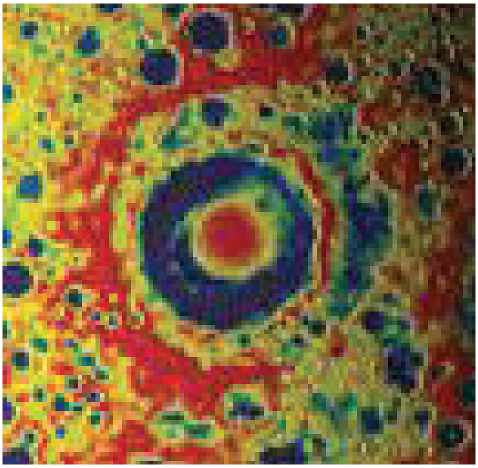

fig. 1. Lunar concentric gravity in Mare Orientale area. Red-high, blue-low (Science, 2013, v. 339, # 6120, book-jacket).

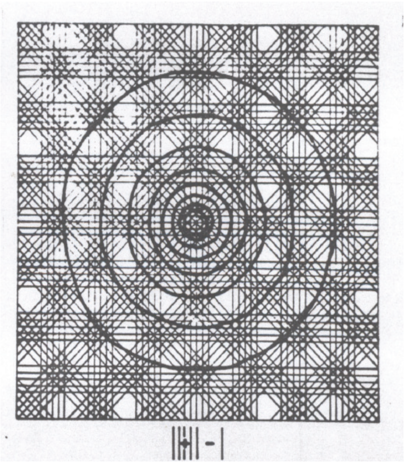

fig. 2. Graphic representation of crossing waves (+ up, - down) producing chains and grids of round forms (craters) and multi-ring structure (better seen from some distance).

The northern volcanic plains occupying considerable low-relief space (Fig. 5) could be compared with the terrestrial Northern Ice Ocean (Arctic) in respect of a relative size and its position on the globe (Fig.6). Strengthening this comparison is an antipodean but uplifted and highly cratered area around the Mercury's South Pole (= terrestrial Antarctic?). This interplanet comparison put question at the plate tectonic origin of the Northern Ice Ocean. Both the terrestrial and mercurian antipodalities are tied to the wave structuring [1,3].

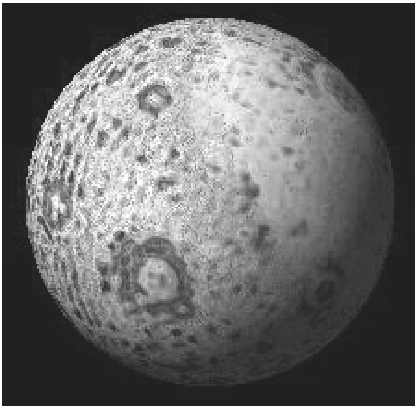

fig. 3. Gravitation anomaly of the Moon measured by Kaguya mission. Credit: forum.worldwindcentral.com.

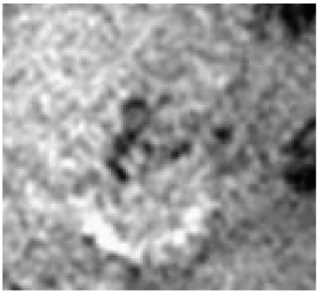

fig. 4. A portion of Titan's surface (PIA06154); the image was taken Dec. 10, 2004 at a distance of 1746000 km by the narrow-angle camera with a special near-infrared filter at 938 nanometers (Credit: NASA/JPL/Space Sci. Inst.). Of particular interest are the regular cross-cutting tight lineations (waves) covering the whole surface of Titan and producing chains and grids of hollows ("craters") with diameters about 70-100 km. This granule size (88 km) was calculated proceeding from the orbital frequency of Titan. These granules are superimposed on much larger blobs-"craters" (500-700 km across) sometimes with multiple concentric rings. One of these features with "beads" on a collar is in the figure.

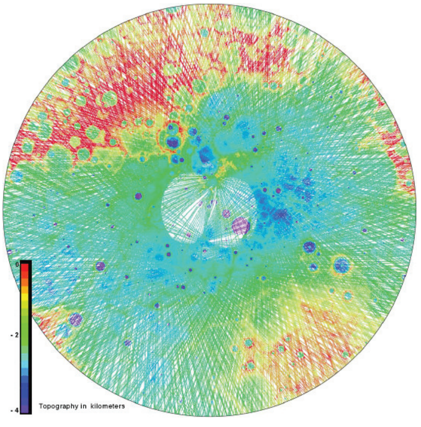

fig. 5 Northern topography of Mercury. PIA16951. Polar stereographic projection, extending southward to 65˚ N, with 0˚ longitude at the bottom. The diameter of this projection is 2130 km.

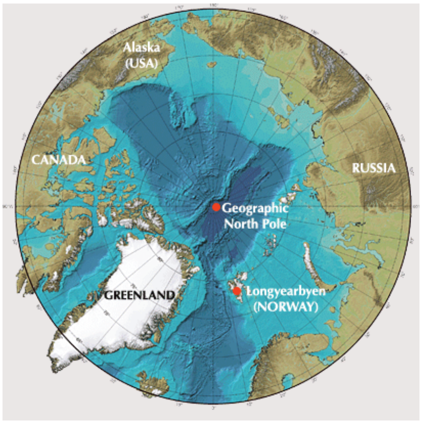

fig. 6. Northern Ice (Arctic) Ocean of Earth

References:

[1] Kochemasov, G. G. (1998) Tectonic dichotomy, sectoring and granulation of Earth and other celestial bodies // "Proceedings of international symposium on new concepts in global tectonics ('98 TSUKUBA)", Tsukuba, Japan, Nov. 1998, p.144-147.

[2] Melosh H.J., Freed A.M., Johnson B.C. et al. (2013) The origin of lunar mascon basins // Science, v. 340, #6140, 1552-1555. DOI: 10.1126/science. 1235768.

[3] Kochemasov G.G. (2003) Coherent structurization of the Earth's geospheres from core to atmosphere and lithospheric weakness zones favourable for concentration of metals // Global Tectonics and Metallogeny, 2003, Vol. 8, # 1-4, pp. 209-212.

CALIBRATION OF SUBSURFACE RADAR «MARSIS» WITH MARTIAN IONOSPHERE.

V. M. Smirnov, O. V. Yushkova
Kotel'nikov Institute of Radio Engineering and Electronics of RAS, Fryazino Branch, Russia; Contact: vsmirnov@ire.rssi.ru

The subsurface radiolocation is one of the distance investigation methods of the surface properties and the structure of the soil layer. Radar system, located on board the orbiter, allows getting necessary information about the space body for a relatively short period of time. In this the layer thicker is estimated by the lower frequency range of the radar.

The technique for reconstructing depth distribution of the dielectric parameters of inhomogeneous soil is based on analysis of phase and amplitude changes of emitted signal compared with received one. Such method of solving the problem requires accurate calibration of the emitted signal, which is own complicated problem.

Parameters of radar (type of signal, its duration and frequency range) are chosen especial for space object, altitude spacecraft, goals and technical capacity (weight, allowable radiated power).

Calibration of the orbital radar in terrestrial conditions is impossible, because the signal with duration about 0.1 ms must be formed in free space and reflected from extended dielectrically uniform surface. Simulation of such processes is possible, but its results must be verified by physical experiments.

If the body has its own ionosphere, the necessary calibration measurements can be carried out in the time of the main experiment. The ionosphere may serve reflected surface, if the critical frequency is higher than the emitted frequency of the radar. In this case, the reflection of signal from the ionosphere will be dominant.

This report presents:

- height distribution model of the dielectric permittivity of the ionosphere, built on the base of the vertical profile of the electron density of the Mars ionosphere which depends from the solar zenith angle;
- the results of modeling the reflection of the radar MARSIS signal («Mars Express»);
- the results of a comparative analysis of simulation and the processing data of radar measurements MARSIS.

This work was partially supported by the Program 22 of the Presidium of RAS "Fundamental Problems of research and exploration of the Solar System."

NEW TECHNOLOGY OF LUNOKHOD'S PANORAMAS IMAGE PROCESSING FOR DETAIL MAPPING AND ANALYSIS OF LUNAR SURFACE

A. E. Zubarev, I. E. Nadezhdina, N. A. Kozlova, L. A. Shishkina and I. P. Karachevtseva,
Moscow State University of Geodesy and Cartography, (MIIGAiK), MIIGAiK Extraterrestrial Laboratory (MExLab), Russia.
Contact: lorencs@mail.ru;i_karachevtseva@mexlab.ru

Introduction:

PRoViDE (Planetary Robotics Vision Data Exploitation) is a project which aims to assemble a major portion of the imaging data gathered from different vehicles and probes on planetary surfaces into a unique database, bringing them into a spatial context and providing access to a complete set of 3D vision products (http://www.provide-space.eu/).

There were several successful Soviet Lunar missions carried out in 1960-70s. MIIGAiK received archive panoramas from State Archive of Russian Federation for research including panoramic images from 5 such missions: Luna 9, 13, 17, 20, 21. Three of them (Luna 9, 13 and 20) were static ones. During these missions only a few panoramas were taken from the point where the modules landed. The other two missions (Luna 17, 21) had rovers – Lunokhod-1 and Lunokhod-2, respectively. They have taken more panoramas which can be useful for geomorphologic and other analyses of different types of lunar surface. Some of them can be precisely pinpointed on LROC NAC images and photogrammetrically processed to obtain a stereo model.

Algorithm:

Data were provided to MIIGAiK by the Russian State Archive in the form of scanned fragments (originally panoramas represented one image) and some description for them. To load the fragments to the database metadata for each fragment is essential. So we have looked through all the fragments and other data we have about the missions and determined parameters for description (camera type, quality, date of surveying, coordinates of the observation points, sun coordinates, etc.).

Then we have developed an algorithm for assembling panoramic images, reconstruction of unknown exterior orientation, and further processing of panoramas that allowed us to obtain a stereo model:

1. Assembling of a panorama from fragments (Fig. A) and resampling it to a real size (scanned panoramas have the size 5 times larger than the real ones).

2. Creation of an LRO orthoimage for the region where the panorama was taken.

3. Orthorectifying of the assembled panorama and determination of exterior orientation (the azimuth, zenith and coordinates of the Lunokhod location) by means of fitting the panorama to an LRO orthoimage iteratively.

4. Re-projecting of the fitted panorama to the central projection to be used for photogrammetric purposes (Fig. B).

5. If there is a stereo-pair for the panoramic image we can obtain a stereo model (tie-points measurements, bundle-block adjustments).

6. Creation of an orthoimage using the stereo model obtained in the previous stage.

All steps but the sixth have been already implemented. Creation of an orthoimage using the stereo model is in progress.

Difficulties:

- As panoramas were obtained by means of the scanning mirror that made oscillatory and rotating motion a panoramic image represents a part of sphere (spherical projection). It is a non-standard model for usual software.

- The processing of panoramas is complicated by lack of some camera parameters and their calibration (principal point and distortion, other parameters are not defined precisely), exterior orientation, parameters of digitizing. Besides that there are some distortions caused by non-uniformity in the rotation of the scanning mirror.

- Unfortunately there is no a publication source describing camera parameters mounted on Lunokhod-2 and we have to use the same parameters as for Lunokhod-1. It is known that cameras for Lunokhod-2 mission were improved but general parameters used for panoramas processing were not modified.

Summary and Results:

To conclude, we have panoramas from five Soviet Lunar missions. In general for all missions we have about 1800 fragments what equals about 340 panoramas. Most of

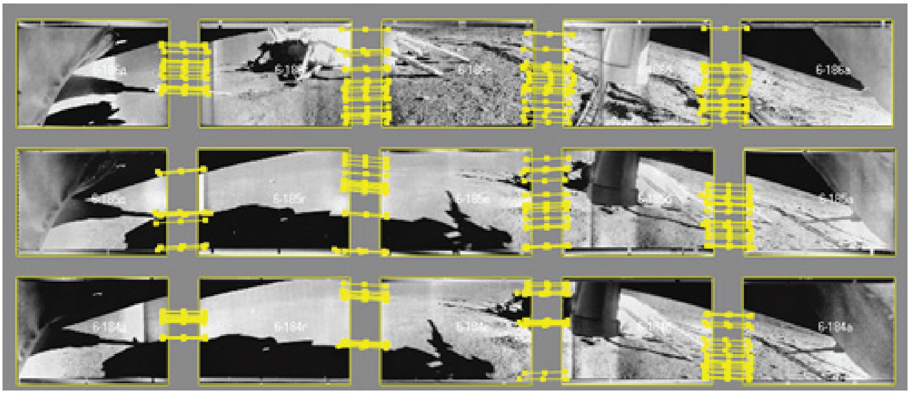

fig. A. Assembling of the panoramic images from fragments using PHOTOMOD software

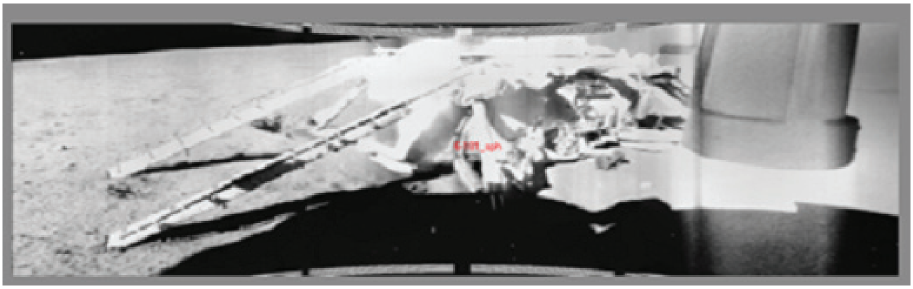

fig. B. Example of a panoramic image in central projection

them (240 panoramas) were taken by Lunokhod-1. We have already created metadata for all of the image fragments, and we uploaded these data for Luna-17 mission into MIIGAiK Geoportal. But these data will be supplemented and refined as the images are processed further. We have developed a unique technology of reconstruction of lost exterior orientation of lunar panoramic images taken during soviet missions Luna which has been implemented using Luna-17 panoramic images. As a result we have determined and improved exterior orientation of panoramas depicting the Luna-17 module and derived a preliminary terrain model to be improved further. The following products are supposed as results of the study:

- assembled panoramas in spherical projection;
- assembled panoramas in central projection (can be used for photogrammetric purposes);
- orthorectified panoramas (Fig. C);
- stereo models or digital terrain models obtained using stereo panoramas.

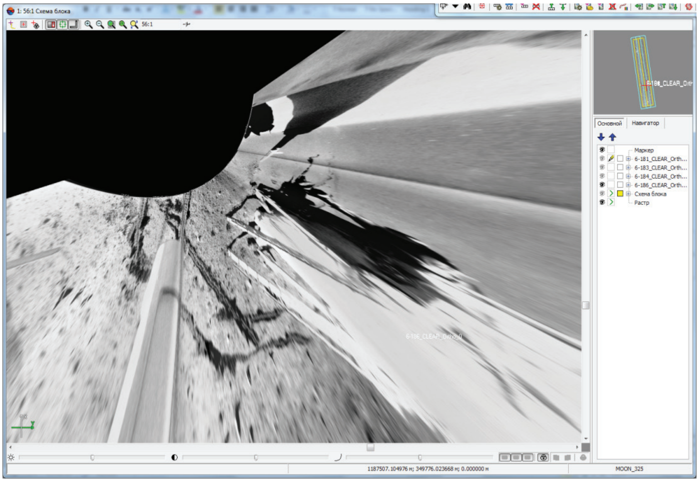

fig. C. Example of orthorectified panorama with a part of module Luna-17 and Lunokhod's track.

Our results will be used for new mapping of lunar surface at high level of detail and geology assessment including morphological analysis of micro-relief and rocks composing it.

Acknowledgments: The research leading to these results has partly received funding from the European Community's Seventh Framework Programme (FP7/2007-2013) under grant agreement № 312377 PRoViDE.

ON THE NATURE OF THE SEISMIC RINGING OF THE MOON. ANALYTICAL MODELING.

Burmin V.Yu.[1], Miroshnikov V.V.[2], Fatyanov A.G.[3],
[1]*Schmidt Institute of Physics of the Earth, RAS, Moscow, Russia;*
[2]*OJSC Sibneftegeophysica, Novosibirsk, Russia;* [3]*Institute of Computational Mathematics and Mathematical Geophysics SB RAS, Novosibirsk, Russia.*

Introduction: Lunar seismograms differ markedly from seismograms obtained on Earth. The most unique feature of the lunar seismograms is a significant duration of the seismic signal. In the paper [*Latem et al*., 1970] provides an explanation of this feature of the lunar seismograms. It is assumed that the "seismic ringing" is due to the high degree of heterogeneity of the environment, which leads to the scattering intensity at a very low absorption of seismic energy in the surface layer. Features of seismic wave propagation in a heterogeneous environment are described by diffusion theory. Shown in the framework of the diffusion theory that most of the scattering takes place in the upper few hundred meters of the Moon, in which the *Q*-factor of about 3000 - 5000. However, the numerical simulation of wave field in a scattering medium was conducted by none

We have carried out mathematical modeling of seismic wave fields for the elastic model of the Moon, in which there is near-surface low-velocity zone (LVZ). Simulation is carried out for the layered medium. The results show that if the elastic medium is no absorption, but there is a zone of low velocities, there is a seismic "ringing", which leads to a significant increase in the recording time of the seismic signal. Thus in the absence of LVZ (regolith) the duration of "ringing" is significantly reduced. The duration of the seismic "ringing" on the moon in the first approximation can be explained by resonance phenomena that occur in the wave field in the presence of a thin LVZ (regolith).

Results: Since the experimental data are given for the significant spatial and temporal scales (range 60 - 600 km., time duration of the registration), it is impossible to model using grid-based approach, even with the use of high performance computing technology. Therefore, for modeling of wave fields for a layered Moon used analytical (not using nets) the method of calculation [*Fatianov*, 1990]. The following are the simulation results for the source type of the normal force, which is located at the free surface, with the dominant frequency of the input signal of 1 Hz. This source is in the first approximation to the impact of a meteorite. The following figure shows the vertical component of the wave field.

The simulation results show a substantial dependence of the duration of "ringing" on the presence of a thin LVZ consisting of regolith. Significant duration of the "ringing" observed in the presence of a thin layer of regolit and models of the upper part of the deep incision of the Moon [*Nakamura et al*., 1975]. If we take the model of the moon without a thin layer of regolith, the wave field has a duration of less than a minute, "ringing" is not observed. It is easy to see that in the case of the presence of a regolith layer model wave field is significantly closer to experiment wave field. In the first approximation the "seismic ringing " on the Moon can be explained by the resonance properties of a thin layer, without the involvement of scattering effects due to the high degree of heterogeneity of the environment.

References

Latham G., Ewing M., Press F., Sutton G., Dorman J., Nakamura Y., Toksoz N., Wiggins R., Derr J., Duennebier F. Apollo 11 passive seismic experiment // Geochim. Cosmochim. Acta. 1970. Vol. 34. Suppl. 1. P. 2309-2320.
Nakamura Y, Dorman J, Duennebier F, Lammlein D, and Latham G. Shallow lunar structure determined from the passive seismic experiment // Moon. 1975. Vol. 13. P. 57-66.
Fatianov A.G. Semi-analytical method for direct dynamic problems in layered media. // DAN. 1990. T. 310. Number 2. S. 323-327.

PROTOTYPE OF THE GAS CHROMATOGRAPH – MASS SPECTROMETER TO INVESTIGATE VOLATILE SPECIES IN THE LUNAR SOIL FOR THE LUNA-GLOB AND LUNA-RESURS MISSIONS.

P. Wurz[1], L. Hofer[1], M. Tulej[1], D. Lasi[1], M. Cabane[2], D. Cosica[2], M. Gerasimov[3] and D. Rodinov[3],
[1]Physics Institute, University of Bern, Sidlerstrasse 5, 3012 Bern, Switzerland; [2]LATMOS, Universite Pierre et Marie Curie, 75252 Paris, France; [3]Space Research Institute, 117810 Moscow GSP-7, Russia

In preparation for the Russian Luna-Glob and Luna-Resurs missions we combined our compact time-of-flight mass spectrometer (TOF-MS) with a chemical chromatographic separation of the species by gas chromatography (GC). Combined measurements with both instruments were successfully performed with the laboratory prototype of the mass spectrometer and a flight-like gas chromatograph. Due to its capability to record mass spectra over the full mass range at once with high sensitivity and a dynamic range of up to 10^6 within 1s, the TOF-MS system is valuable extension of the GC analysis. The combined GC-MS complex is able to detect concentrations of volatile species in the sample of about $2 \cdot 10^{-9}$ by mass.

Introduction:

Since all lunar soil samples available on Earth originate from a restricted area at the lunar near side, close to the equator, the Russian space agency will launch two spacecraft Luna-Glob and Luna-Resurs landing at the lunar poles. For the detection and analysis of the volatile species in the lunar soil, a Neutral Gas Mass Spectrometer (NGMS) was selected as a part of the GC-MS analytic complex. In addition, NGMS will also be operated as a standalone instrument to analyse the composition of the tenuous lunar exosphere after the investigation of the soil samples is completed.

The Neutral Gas Mass Spectrometer:

The Neutral Gas Mass Spectrometer (NGMS) is a time-of-flight type mass spectrometer (TOF-MS) [3]. The neutral gas is ionised by electron impact ionisation. To achieve advanced performance a grid-less ion mirror (reflectron) is integrated in the ion path [5]. The ion optical design of NGMS is based on the P-BACE instrument [1].

A TOF mass spectrometer allows the acquisition of complete mass spectra at once without the necessity of scanning over the mass range. These qualities are combined with high sensitivity and a large dynamic range of up to 10^6 within 1s integration time useful for continuous measurements as they are needed for the analysis of the output of a chromatographic column (GC), which provides sample separation in temporal domain.

Experimental:

GC-MS Setup. In the laboratory a sample valve with a defined sample volume is used as an injection system to load a sample into the chromatographic column. Due to the chemical properties of the chromatographic column and the kind of species to be analysed, the sample is separated in time at GC output. The species of interest, eluted in the carrier gas, are then detected and analysed with NGMS to their composition and structure (see Figure 1).

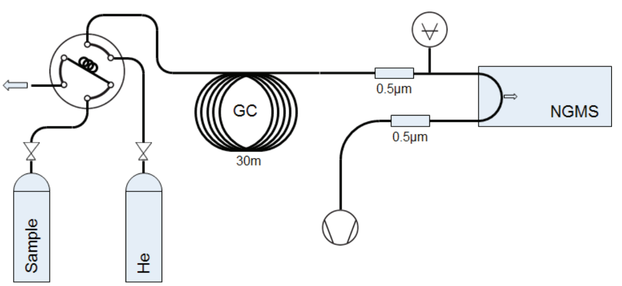

fig. 1. Scheme of the laboratory GC-MS setup with sample valve.

Measurements: Since the GC module we used provides an integrated Thermal Conductivity Detector (TCD), direct comparison between the data recorded by a TCD and NGMS is possible of the same sample.

For testing purposes a gas mixture of several organic compounds (at 1000 and 100 ppm level) with the helium carrier gas is used. A sample of that mixture is injected with the sampling system described in Figure 1. At the output of the chromatographic column the species are detected by a Thermal Conductivity Detector (TCD), non-destructively, and after a short transfer line the same sample is fed into NGMS.

Typical GC-MS data are shown in Figure 2, where the top panel shows TCD data over the full retention time span and the bottom panel shows a part of mass spectrometric data.

As an example, the lower panel in Figure 2 shows the temporal evolution in mass spectrometric data of all six labelled peaks in the TCD data. Shown is the composite signal of the parent molecule and its main fragments arising from the electron impact ionisation. By selecting the most favourable fragments the signal-to-noise ratio can be maximised. Since the fragmentation pattern is characteristic to the molecular structure the fragments can also be used to assist the identification of the chemical nature species.

Typically, mass spectra are recorded at 1s cadence, however, shorter cadences are easily possible (e.g. 0.1 s and shorter) when a difference in retention times of consecutive species makes this necessary.

Due to the high sensitivity and the large dynamic range of NGMS, the instrument is able to detect species in very low concentration, well below the detection limit of the TCD. With the present system it is possible to detect 10 nmol with GC alone (TCD detection) and 10 – 100 pmol with the NGMS. Thus, for a volume of the sample oven of about 5 mm^3 volatile species with a concentration as low as $2 \cdot 10^{-9}$ by mass can be detected.

Summary and Conclusions:

Combined measurements with chemical pre-separation by gas chromatography and analysis by our time-of-flight neutral gas mass spectrometer NGMS were performed successfully. During a GC-MS measurement NGMS acquires continuously complete mass spectra to record the maximum possible chemical information from the sample. Due to the high sensitivity and the large dynamic range of 10^6 of NGMS, we can detect volatile species in the sample at a concentration of about 2 ppb by mass. For comparison, for the SAM instrument on the Curiosity rover a sensitivity for organic compounds of 1 – 10 ppb by mass has been quoted [4].

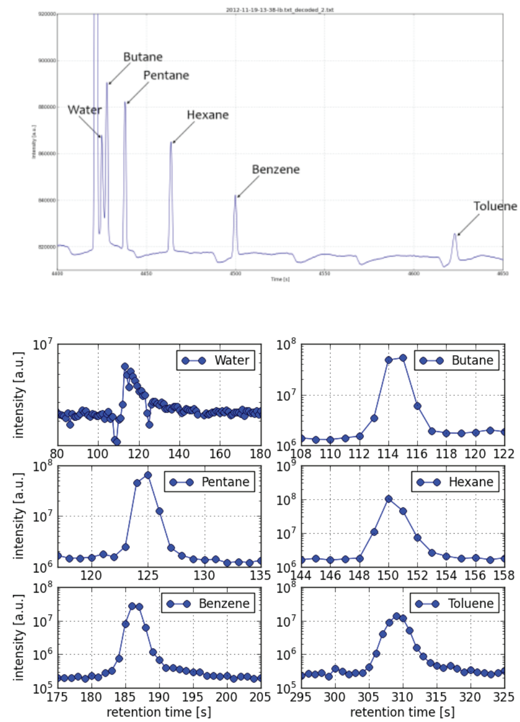

fig. 2. TCD data of a hydrocarbon mix (top) and mass spectrometric analysis of the peaks at GC output by NGMS (bottom).

References:

[1] D. Abplanalp, P. Wurz, L. Huber, I. Leya, E. Kopp, U. Rohner, M. Wieser, L. Kalla, and S. Barabash: A neutral gas mass spectrometer to measure the chemical composition of the stratosphere, Adv. Space Res. 44 (2009) 870–878.

[2] W.V. Boynton, D. W. Ming, S. P. Kounaves, S. M. M. Young, R. E. Arvidson, M. H. Hecht, J. Hoffman, P. B. Niles, D. K. Hamara, R. C. Quinn, P. H. Smith, B. Sutter, D. C. Catling, and R. V. Morris: Science 325 (2009) 61–64.

[3] P. Wurz, D. Abplanalp, M. Tulej, and H. Lammer, A Neutral Gas Mass Spectrometer for the Investigation of Lunar Volatiles, Planet. Sp. Science 74 (2012) 264–269.

[4] P. Mahaffy et al., The Sample Analysis at Mars Investigation and Instrument Suite, Sp. Science Rev., 170 (2012), 401–478.

[5] S. Scherer, K. Altwegg, H. Balsiger, J. Fischer, A. Jäckel, A. Korth, M. Mildner, D. Piazza, H. Rème, and P. Wurz, A novel principle for an ion mirror design in time-of-flight mass spectrometry, Int. Jou. Mass Spectr. 251 (2006) 73–81.

NUMERICAL MODELING THE RADIATION EMITTED AND SCATTERED FROM THE DUST IN THE INNER COMA OF THE COMET 67P/CHURYUMOV GERASIMENKO - A POSSIBLE BASIS FOR SPECTROMETRIC SEARCHES

M. I. Błęcka[1], G. Rinaldi[2], U. Fink[3], F. Cappacioni[2], G.P. Tozzi[4],
[1]Space Research Center PAS; [2]Istituto di Astrofisica e Planetologia Spaziali, INAF, via del Fosso del Cavaliere 100, 00133 Roma, Italy; [3]Lunar and Planetary Laboratory, University of Arizona, Tucson, AZ 85721, United States; [4]INAF - Osservatorio Astrofisico di Arcetri, Firenze, Italy

The work we present deals with the spectrometric measurements of the VIRTIS instrument part of the payload of the Rosetta mission to the Comet 67P/Churyumov-Gerasimenko (C-G).

The dust is an important constituent of cometary environment and is always present on the surface of the nucleus and in the inner coma. The spectra are affected by the processes taking place in the coma and by the structure, composition and the spatial distribution of cometary materials. The particles of the dust, illuminated by solar light, scatter, absorb and emit radiation. The reflected and emitted radiation are transmitted through the coma region before being collected by instruments such as VIRTIS. The reflection, absorption, scattering, and emission processes depend on the Comet-Sun geometry and on the thermal state of the nucleus.

In the present paper we are mainly concentrated on the influence of optical parameters of dust on spectra we expect from the VIRTIS/Rosetta measurements. To this purposes the equation of radiative transfer through the assembly of dust grains and various gases is solved. The number density distribution of the dust grains around the coma and their size distribution are drawn from the recent theoretical models. A few phenomenological scattering phase functions are taken into account.

The work was supported by the grant: 2011/01/B/ST9/05442

DUST LIFTING EXPERIMENT (DLE) : VARIATIONS OF ELECTRIC FIELD AND ELECTRIC RESISTIVITY OF AIR CAUSED BY DUST MOTION

E. Seran[1], M. Godefroy[1], N. Renno[2], H. Elliott[2],
[1]LATMOS, France, [2]SPRL, USA, Elena.Seran@latmos.ipsl.fr

We have been developing an experiment entitled Dust Lifting Experiment (DLE). The main purpose of this experiment is to study the mechanisms of the dust charging and dust transport. The DLE consists of two electric field sensors, a cylindrical Field Mill (FM) developed by SPRL/USA and a Short Dipole Antenna (SDA) developed by LATMOS/France. These two instruments use different principles to measure electric fields. The FM measures the current between the two sections of a rotating cylinder split into two along its axis, while SDA measures the potentials of two spatially separated electrodes. These two principles of measurements cause differences in performance between the two sensors. The FM is capable of measuring DC electric fields ranging from ~few 10 V m-1 to 100 kV m-1. The SDA is capable of measuring electric fields from DC to ~few kHz and have very high sensitivity, about few μV m-1.

We illustrate the instruments performances with few examples of earth's observations made with the DLE package in the desert of Nevada. Further, we show that a combination of the measurements of two instruments allows the estimation of the electric resistivity of air, an important quantity that is extremely difficult to measure near the Earth's surface. The electric resistivity of air is found to vary between 1.5·1013 and 6×1013 Ω m and to correlate with changes in electric field. Vertical DC electric fields with amplitudes up to 6 kV m-1 were observed to correspond to clouds of dust blowing through the measurement site. Enhanced DC and AC electric fields are measured during periods when horizontal wind speed exceeds 7 m s-1, or around twice the background value. We suggest that low frequency emissions, below ~200 Hz, are generated by the motion of electrically charged particles in the vicinity of the SDA electrode and propose a simple model to reproduce the observed spectra. According to this model, the spectral response is controlled by three parameters, (i) the speed of the charged particles, (ii) the charge concentration and (iii) the minimum distance between the particle and the electrode. In order to explain the electric fields measured with the FM sensors at different heights, we developed a multi-layer model that relates the electric field to the charge distribution. For example, a non-linear variation of the electric field observed by the FM sensors below 50 cm is simulated by a near surface layer of tens of cm that is filled with electrically charged particles that carry a predominantly negative charge in the vicinity of the soil. The charge concentration inside this layer is estimated to vary between 1012 and 5·1013 e m-3.

THE LOW-FREQUENCY TURBULENCE IN AN INHOMOGENEOUS DUSTY PLASMA

A.S. Volokitin and B. Atamaniuk

There are many examples of the dusty plasma environment : comets, planetary rings, the lower ionosphere. In the research laboratory, the most important case is the formation of dusty plasma near the walls of the device with magnetic confinement (tokamaks, etc.). Under these conditions, the plasma temperature is not too high, and the impact of neutrals, ions, electrons, and dust with each other as well as the presence of inhomogeneous plasma plays an important role in the development of turbulence in a magnetized plasma. Basing on a linear theory and analysis of the effect of dust particles on the properties of low-frequency waves and unstable conditions, we consider the stabilization of the low frequency waves instability due to nonlinear three-wave interactions. The emphasis is on resistive instability of drift waves, also the results of studies in other cases, including the instability of current-carrying and Farley-Buneman instability, are presented. Because this issue requires consideration of essentially three-dimensional due to the specifics of the nonlinear interaction of waves in a plasma in a magnetic field, it is very difficult to fully 3D numerical simulations. However, given the conditions under which the linear growth rate is lower than the waves, frequency drift, we can assume that the nonlinear interaction also remains weak. Then, the mathematical discreaption original system can be reduced to the set of finite number of non-linear ordinary differential equations, which describing the dynamics of the amplitudes of the waves in the active medium and give a suitable tool to explore different modes of turbulence.

Usually focuses on the study of a well-developed stage of plasma turbulence, but here the case when the turbulent state in active medium can be presented as a set of a finite number of interacting waves. It is supposed that with the important role of the dissipation and not far from the instability threshold, the typically perturbed plasma state can be described as a finite set of interacting interacting waves some of which are unstable and other are more strongly damped. In this case, the number of waves remains finite, but because of the competition between the instability and the damping of the waves when they interact, the dynamics of the wave amplitude is stochastic in nature and so-called Multiple mode turbulence. The analysis conditions of the various types of nonlinear instabilities frequency waves and discussed transition from a quasi-periodic mode to multiple mode of turbulence, and then fully developed turbulence, depending on the density of the dust components and plasma.

MODELING THE INFLUENCE OF LUNAR DUST ON THE PHYSICAL AND BIOLOGICAL SYSTEMS

I. A. Shashkova[1], A. V. Zakharov[1], G. G. Dolnikov[1], I. A. Kuznetsov[1], E. A. Vorobyova[1,2], T. Borisova[3]
[1]Space Research Institute (IKI), 84/32 Profsoyuznaya Str, Moscow, 117997, Russia. Contact: ggd@iki.rssi.ru
[2]Lomonosov Moscow State University, Fac.Soil Sci., Leninskie Gory 1-12, Moscow, 119234, Russia.
[3] Palladin Institute of Biochemistry, NAS of Ukraine, 9 Leontovicha Street, Kiev, 01601, Ukraine. Contact: tborisov@biochem.kiev.ua

Introduction:

One of the problems in the study and exploration of space is the effect of lunar dust on the optical and mechanical systems of the spacecraft, as well as on biological objects [1, 2]. Micrometeorites and secondary particles bombard the moon's surface with forming a dust layer. Ultraviolet radiation from the sun causes the photoemission of electrons, resulting in the surface of the moon is charged to a positive potential. The electric field creates an environment in which dust particles may go up and levitate above the lunar surface [3].

This work presents the experimental simulations of the lunar exosphere influence on the working surface of the scientific device designed to detect the levitating particles [4].

Experimental setup:

Impact effect lunar regolith particles are modeled using a wind tunnel. Air flow in the tunnel is created fan device. Infinitely variable flow rate is in the range of 0,5 ÷ 2,5 m / s and is measured digital anemometer. A piezoelectric sensor device is fixed at an angle of 45 ° to the flow. Particles entering the flow through an injector effect on the sensor surface. For the simulation of particles of lunar regolith, the following materials are used: glass microspheres with a diameter 40 ÷ 100 microns and an analogue of lunar soil LGA-3st, developed in the Vernadsky Institute.

The impact of high energy cosmic rays is recreated in the experiment using laser radiation in the infrared range: the wavelength of 1,06 microns, pulse energy of 3 mJ pulse width of 10 ns. A set of filters used varies the pulse energy of 3 mJ to 0,84 mJ.

Experimental technique is as follows. The working surface of the sensor is subjected to impact or laser irradiation, and then examined under a microscope for the presence of mechanical damage. Also device operation as a whole will be tested.

Along with mechanical systems we intend to investigate the influence of the Moon's exosphere on microorganisms: their survival and interaction with the lunar dust. It is supposed to investigate the interaction of bacterial cultures with granulometric analogues of lunar dust, and assess the impact of the vacuum on the physiological characteristics of immobilized cells. Metabolic properties of tested microorganisms will be compared with identical properties of bacteria immobilized on the lunar regolith analogues and incubated under atmospheric pressure.

The summarized results of upcoming experiments will enable an evaluation of the impact of the lunar exosphere on mechanical systems and terrestrial organisms. Such experiments are important for designing spacecraft, planetary protection solutions and creation of men populated stations on the Moon.

This work is in progress with the support of RFBR grant 13-02-90441.

Duncan N. A., Gruen E., Auer S., Xie J., Sternovsky Z., Drake K., Horanyi M., Robertson S. H. The Electrostatic Lunar Dust Analyzer (ELDA) Instrument // American Geophysical Union, Fall Meeting 2009, abstract #P23C-1263.
Drolshagen G., Dikarev V., Landgraf M., Krag H., Kuiper W. Comparison of Meteoroid Flux Models for Near Earth Space // Earth Moon Planet, 2008,Vol. 102, pp. 191–197.
Golub' A. P., Dol'nikov G. G., Zakharov A. V., Zelenyi L. M., Izvekova Yu. N., Kopnin S. I., Popel S. I. Dusty plasma system in the surface layer of the illuminated part of the moon // Pis'ma v Zh. Èksper. Teoret. Fiz., 95:4 (2012), 198–204.
Popel S.I., Zelenyi L.M., "Future Lunar Missions and Investigation of Dusty Plasma Processes on the Moon", J. Plasma Phys., 79:4 (2013), 405–411

WHAT DETERMINES THE SIZES OF REGULAR SATELLITE SYSTEMS OF JUPITER AND SATURN

A. B. Makalkin,
Schmidt Institute of Physics of the Earth of Russian Academy of Sciences, B.Gruzinskaya, 10, Moscow 123995, Russia. Contact: makalkin@ifz.ru

Why systems of regular satellites of giant planets are so compact? The most distant from Jupiter and Saturn large satellites are orbiting at about 26 Jovian radii (Callisto) and 20 Saturnian radii (Titan). In the models of formation of regular satellites in "gas-starved" accretion disks around Jupiter and Saturn [1,2] it was suggested that the region where the satellites were formed, is determined by the spatial distribution of the mass flux of gas and solids onto the circumplanetary protosatellite disk. Specifically, it was suggested that the parent material of the satellites fell onto the disks inside the "centrifugal" radius, estimated to be about 30 planetary radii [1]. However, recent 3D simulations of accretion of material onto circumplanetary disks [3] show that the fall of gas onto the disks occurs at the distances lower than 15 planetary radii, while the fall of solid particles is probably distributed over the distances much higher than 30 planetary radii. Therefore another mechanism than spatial distribution of infalling material should exist in order to explain the orbital distribution of regular satellites of the gas giants.

We suggest that formation of the regular satellites of Jupiter and Saturn is determined by the combined effect of several processes occurring within their accretion protosatellite disks. We compare the timescale of the accretion of satellites of specific size in the disk of definite density with timescales of two other processes. One of these is the timescale of mass inflow of solid material necessary for the regular satellite formation to the inner region from the outer part of the accretion protosatellite disk. The other timescale is the one for the destructive catastrophic collision of the forming satellite with a large body moving in the planetary Hill sphere. From comparing the above timescales for the disks around Jupiter and Saturn we obtain restrictions on the maximal radii of formation regions of Callisto and Titan, which are in good accordance with their real orbits. The data necessary to make more definite and more confident estimates is the mass distribution of solid bodies. It is still not clear how much mass was contained in dust particles, small bodies and larger planetesimals. However, improvement of estimates of these parameters is necessary to improve the theory.

References: [1] Canup R.M., & Ward W.R. 2002, Astrophys. J., 124, 3404. [2] Makalkin A.B., & Dorofeeva V.A. 2006, Solar Syst. Res., 40, 453. [3] Tanigawa T., Ohtsuki K., & Machida M.N. 2012, Astophys. J., 747, Issue 1, 16p.

A GLOBAL GEOLOGIC MAP OF GANYMEDE.

G.W. Patterson[1], G.C. Collins[2], J.W. Head[3], R.T. Pappalardo[4], L.M. Prockter[1]
[1]Johns Hopkins University Applied Physics Laboratory, Laurel, MD 20723, U.S.A.; [2]Wheaton College, Norton, MA, 02766, U.S.A.; [3]Brown University, Providence, RI, 02912, U.S.A.; [4]Jet Propulsion Laboratory, Pasadena, CA, 91109, U.S.A.. Contact: (Wes.Patterson@jhuapl.edu)

Introduction. We have completed a global geological map of Ganymede that represents the most recent understanding of the satellite on the basis of Galileo mission results (Fig. 1). This contribution builds on important previous accomplishments in the study of Ganymede utilizing Voyager data [e.g., 1-5] and incorporates the many new discoveries that were brought about by examination of Galileo data [e.g., 6-10]. Material units have been defined, structural landforms have been identified, and an approximate stratigraphy has been determined utilizing a global mosaic of the surface with a nominal resolution of 1 km/pixel assembled by the USGS. This mosaic incorporates the best available Voyager and Galileo regional coverage and high resolution imagery (100-200 m/pixel) of characteristic features and terrain types obtained by the Galileo spacecraft. This effort has provided a more complete understanding of: 1) the major geological processes operating on Ganymede, 2) the characteristics of the geological units making up its surface, 3) the stratigraphic relationships of geological units and structures, and 4) the geological history inferred from these relationships.

Material units. Four fundamental geologic materials have been defined for Ganymede; dark, light, reticulate (**r**), and impact material [11,12]. On the basis of our mapping, dark material on Ganymede has been subdivided into three units; cratered (**dc**), lineated (**dl**), and undivided (**d**), while light material has been subdivided into four units; grooved (**lg**), subdued (**ls**), irregular (**li**), and undivided (**l**). Impact material encompasses palimpsest, crater, and basin materials. Palimpsest material is further subdivided into four units; three of these are distinguished on the basis of their stratigraphic relationship with light material units ($\mathbf{p_1}$, $\mathbf{p_2}$ and **pu**) and the fourth is an interior plains unit (**pi**). Five crater units – fresh ($\mathbf{c_3}$), partially degraded ($\mathbf{c_2}$), degraded ($\mathbf{c_1}$), unclassified (**cu**), and ejecta (**ce**)- comprise the crater materials, and two units – rugged (**br**) and smooth (**bs**) - comprise basin material.

Stratigraphy. As part of our global mapping effort, we have identified ~4000 craters >10km in diameter across the surface of Ganymede. This dataset has enabled us to calculate crater densities on a global-scale (Table 1) and compliments previous regional estimates of crater densities calculated utilizing counting areas 10 to 100 times smaller [e.g., 1,13]. These data confirm that dark cratered material is the oldest material on Ganymede and that light materials formed substantially later. Dark lineated material and reticulate terrain have crater densities on the higher end of light material units, suggesting they mark a transition into the formation of light materials. Palimpsests are older than light materials, dark lineated material, and reticulate terrain, but younger than dark cratered terrain. Finally, Gilgamesh basin appears to be younger than light materials.

	10 km^a	20 km	30 km	area (x 10^6 km^2)
light				
grooved	39±2 (44±3)^b	14±1 (14±2)	8±1	9.29 (5.71)
irregular	30±4 (20±5)	13±3 (5±2)	6±2	1.94 (0.992)
subdued	42±2 (39±3)	18±1 (15±2)	9±1	8.24 (4.90)
dark				
cratered	85±2 (97±2)	32±1 (34±1)	15±1	21.9 (16.3)
lineated	67±8 (69±8)	19±4 (20±4)	8±3	1.06 (1.01)
reticulate				
reticulate	39±12 (39±12)	18±8 (18±8)	4±4	0.28 (0.28)
impact				
palimpsest	61±7	23±4		1.37
basin	19±5	11±4		0.80

table 1.

The mapping of groove orientations within polygons of light material and the cross-cutting relationships of those polygons with respect to each other have given us additional insight into the time sequence of their formation [14,15]. To determine this sequence, ~2000 light material polygons were run through a sorting algorithm [16,17]. The results suggested that four episodes of light material formation could describe the observed distribution of the orientations of grooves within polygons of light material. Using this distribution, and the fact that light material appears to form predominantly by extension [1,6,18], a strain history for light material formation was then determined [15]. This history was compared to various proposed driving mechanisms for the formation of light material and it was determined that stresses due to internal differentiation provided the best fit to the data.

Summary. A landed mission to Ganymede will be capable of addressing fundamental questions regarding the surface processes (current and ancient) and potential habitability of icy worlds that are, or have been, geologically activity. Key to such an effort will be choosing scientifically compelling targets. In compiling the first global geologic map of Ganymede, we have been able to integrate valuable insights garnered from the Galileo mission into extensive work done mapping quadrangles of the satellite's surface based on Voyager data [e.g., 3-5]. New map units have been described, important structures and landforms have been classified, a global stratigraphy has been determined, and a driving mechanism for the formation of light material has been proposed. This map reflects the most current understanding of Ganymede's surface and will be an invaluable tool for evaluating such targets.

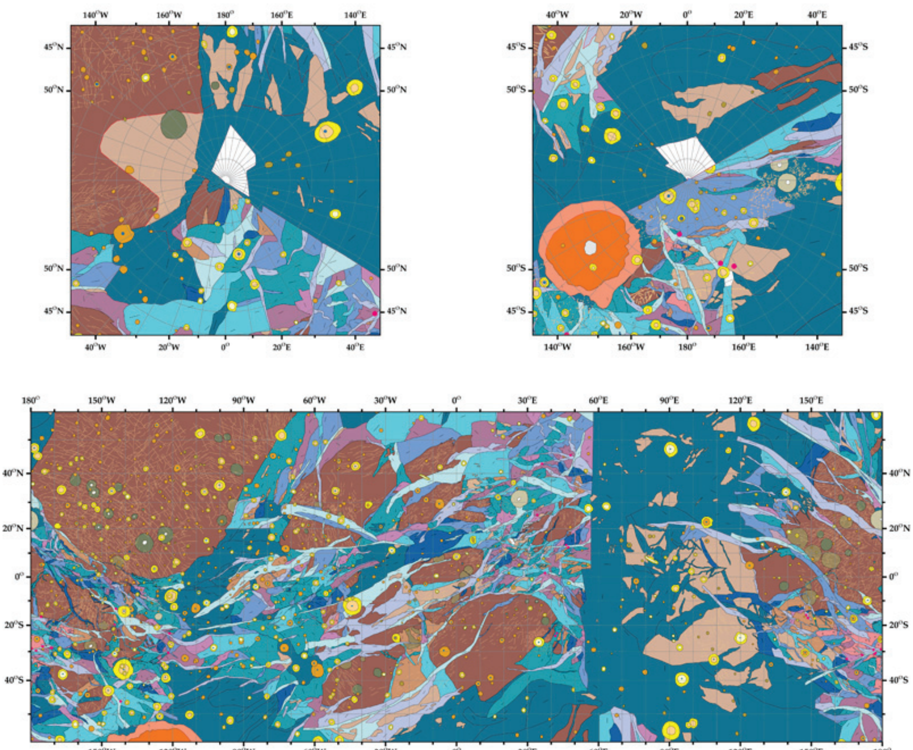

fig. 1. Geological map of Ganymede [19].

References: [1] Shoemaker et al., in The Satellites of Jupiter, 435-520, 1982; [2] McKinnon and Parmentier, in Satellites, 718-763, 1986; [3] J.E. Guest et al., USGS Map I-1934, 1988; [4] D.E. Wilhelms, USGS Map I-2242, 1997; [5] B.K. Lucchitta et al., USGS Map I-2289, 1992; [6] Pappalardo et al., Icarus, 135, 276-302, 1998; [7] Prockter et al., Icarus 135, 317-344, 1998; [8] Prockter et al., JGR 105, 22,519-22,540, 2000; [9] Oberst et al., Icarus 140, 283-293, 1999; [10] Schenk et al., Nature 410, 57-60, 2001; [11] Patterson et al., LPSC XXXVIII #1098, 2007; [12] Patterson et al., USGS Open-File Report 2007-1233, 2007; [13] Murchie et al., Icarus 81, 271-297, 1989; [14] Collins, LPSC XXXVIII #1999, 2007; [15] Collins, LPSC XXXIX #2254, 2008; [16] Crawford and Pappalardo, Astrobiology, 2004; [17] Martin et al., LPSC XXXVII, 2006; [18] Collins et al., Icarus, 135, 345-359, 1998; [19] Patterson et al., Icarus, 207, 845-867, 2010..

THEORETICAL FLUORESCENCE SPECTRA OF PYRENE IN COMETARY COMAE

R. R. Valiev [1, 2], A. Ya. Freidzon[3], A. A. Berezhnoy[4],
[1]Department of General and Inorganic Chemistry, National Research Tomsk Polytechnic University, Tomsk 634050, 43a Lenin Avenue, Building 2, Russia;
[2]Tomsk State University, 36, Lenin Avenue, 634050 Tomsk, Russia; [3] Photochemistry Center, Russian Academy of Sciences, ul. Novatorov 7a, 119421 Moscow, Russia;
[4] Sternberg Astronomical Institute, Moscow State University, Universitetskij pr., 13, 119991 Moscow, Russia. Contact: valievrashid@mail.ru

Introduction:

Polycyclic aromatic hydrocarbons (PAH) are already detected in carbonaceous chondrites (Botta and Bada, 2002). Search for pyrene in interstellar molecular clouds gives only negative results (Salama et al., 2011). However, pyrene was tentatively detected in UV spectra of the comet Halley by Clairemidi et al. (2004). Pyrene nitrile is detected also in dust particles from the comet 81 P/ Wild 2 collected by Star Dust mission (Clemett et al., 2010).

Existence of luminescence continuum in cometary spectra is often explained by the presence of PAH (see, for example (Churyumov et al., 2002)). Identification of individual PAH luminescence features was performed by comparison of high-resolution cometary spectra with laboratory PAH spectra obtained in liquid hydrocarbon solutants by Simonia (2007). In this work we check the suitability of such identification technique by theoretical study of the differences in luminescence spectra of pyrene in water ice matrix and in the gas phase. The absorption and emission spectra of free (gas-phase) pyrene and pyrene in water ice matrix are calculated ab initio together with their vibronic structure.

Results and Discussion

The equilibrium structure of pyrene in the water cluster in its electronic ground state is shown in Figure 1. Our calculations show that the structure of pyrene in the water cluster changes only slightly as compared to the gas phase both in the ground and in the excited electronic states. The transition dipole in the ^1L_b state is very small (i.e., the state is dark) and directed along the short axis of the molecule, while the transition dipole in the ^1L_a state is essentially nonzero (i.e., the state is bright) and directed along the long axis of the molecule.

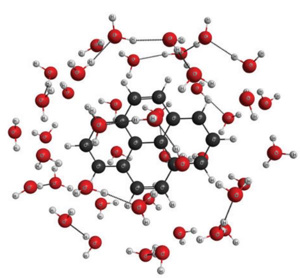

fig. 1. Optimized structure of pyrene in water cluster.

The calculated excitation and emission energies are summarized in Table 1. The agreement of the calculated absorption energies with the experimental data for the gas-phase pyrene is excellent; the agreement of the emission energies for ^1L_b and ^1L_a is good.

Table 1. Calculated excitation and emission energies of pyrene in in the gas phase and in water cluster (oscillator strengths in parentheses) compared to the experiment

	Excitation, nm	Exp., nm	Emission from ^1L_b, nm	Exp., nm	Emission from ^1L_a, nm	Exp., nm
Gas phase	367.8 (0.0002) 317.7 (0.5424)	369 323	392.8 (0.0006)	372	343.2 (0.6369)	327
Water cluster	364.6 (0.0016) 316.7 (0.5266)		389.2 (0.0025)		343.4 (0.5998)	

The calculated absorption spectrum for the five lowest-lying states including vibronic line structure is shown in Figure 2. The agreement with the available experimental spectra of pyrene is very good. The presence of the water cluster has only slight effect on the position and negligible effect on the lineshape of the calculated spectra. This also agrees with the experimental data indicating that the absorption and emission spectra of pyrene in the gas phase and in water are very similar.

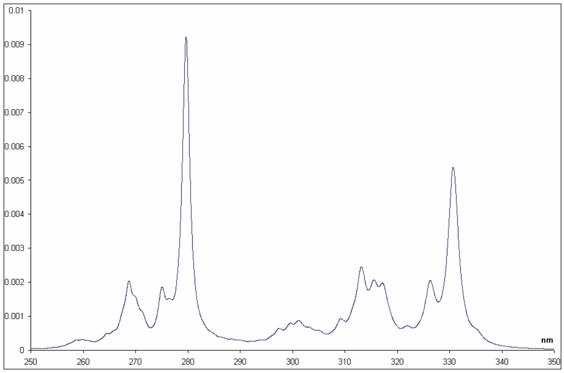

fig. 2. Calculated absorption spectrum of gas-phase pyrene.

The calculated emission spectrum from the bright ^1L_a state is shown in Figure 3. Again, our calculation shows that the presence of water has only slight effect on the position and lineshape of the spectrum. The agreement of the calculated emission spectrum with the experiment, however, is not as good as in the case of absorption. Nevertheless, the similarity of emission spectra of the gas-phase pyrene and pyrene in water agrees well with the experiment. At the same time, careful examination of emission spectra of pyrene in various organic solvents shows that the vibronic structure of these spectra differs substantially from that in the gas phase or in polar media, such as water or methanol. Therefore, identification of vibronic bands of pyrene in cometary spectra on the basis of its spectra in organic solvents is inadequate.

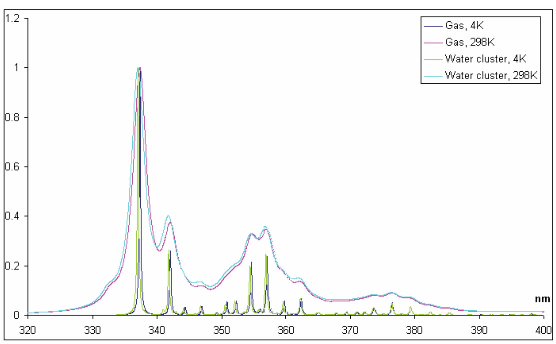

fig. 3. Calculated emission spectrum of gas-phase pyrene and pyrene in the water cluster.

Summary

The absorption and emission spectra of pyrene in the gas phase and in a water cluster are simulated ab initio together with their vibronic lineshapes. Close similarity of pyrene spectra in the gas phase and in water environment is demonstrated. It is concluded that identification of vibronic bands of pyrene in cometary spectra on the basis of its spectra in organic solvents is inadequate.

Literature

Botta O., Bada J.L. Extraterristrial organic compounds in meteorites, Surveys in Geophysics, V. 23, p. 411–467, 2002.

Churyumov K.I., Luk'yanyk I.V., Vlassyuk V.V., Borisov N.V. Spectra of split comet C/1999 S4 (Linear), Earth, Moon, and Planets, V. 90, Is. 1, p. 141-146, 2002

Clairemidi J., Bréchignac P., Moreels G. et al. Tentative identification of pyrene as a polycyclic aromatic molecule in UV spectra of comet P/Halley: An emission from 368 to 384 nm, Planetary and Space Science, V. 52, Is. 8, p. 761-772, 2004

Clemett S.J., Sandford S.A., Nakamura-Messenger K. et al. Complex aromatic hydrocarbons in Stardust samples collected from comet 81P⁄Wild 2, Meteoritics and Planetary Science, V. 45, Is. 5, p. 701–722, 2010

Salama F., Galazutdinov G.A., Krełowski J. et al. Polycyclic aromatic hydrocarbons and the diffuse interstellar bands: a survey, Astrophysical Journal, V. 728, doi:10.1088/0004-637X/728/2/154, 8 p., 2011

Simonia I. On the possible luminescence nature of unidentified cometary emissions, Astrophysics Space Science, V. 312, p. 27–33, 2007

ANCIENT VOLCANIC RELIEF TYPES AT MARS, VENUS, MERCURY AND MOON. ORIGIN, MORPHOLOGY, AGE.

S. G. Pugacheva, V. V. Shevchenko,
Sternberg Astronomical Institute, *Moscow State University, Universitetsky 13, Moscow 119992, Russia, sve-pugacheva@yandex.ru*

Introduction:

The article presents basic features of volcanic surface relief of earth-type planets. Effusive magmatism processes at early stages of planet crust forming come out in structure of solidified relief forms of Mars, Venus, Mercury and Moon. Volcanic relief of planets represents relict ancient line oriented forms, areal and central lava flooding. Linear forms generate shield volcanoes, chains of volcanic mountains and radial-concentric faults.

Mars. Major volcanic edifices you can see on Mars. Shield volcanoes located in the northern hemisphere of Mars, huge shield volcanoes Olympus, Arsia, Pavonis and Alba, represent them. Olympus is the highest in comparison with the volcanoes on other planets. The basal diameter of Olympus Mons is 700 km, its height is 27 km. As a comparison, the largest ancient shield volcano on Earth (Mauna Loa, Hawaiian Islands) has the diameter of 200 km, the height of the volcano above the Pacific Ocean bed is 9 km. Martian volcanoes have peculiar characteristic features: volcano shield, calderas at tops, arched grabens and chains of craters round the calderas. The age of shield volcanoes on Mars comes to $3*10^8$ years. The age of more ancient Martian volcanoes, like Arsia, Ascraens, Pavonis and others, partly buried under lavas of later overflow, comes to $4*10^8$ – $0.9*10^8$ years. Martian volcanic plains are limited to mountainous areas of Tharsis and Elysium, and run vast domain. So, the dimensions of Tharsis volcanic field come to 4000 km northing and 3000 km easting. Huge canyons, flooded with lava, reside on Mars surface. One of them, Mariner valley, is 4.5 thousands kilometers by length, canyon width exceeds 100 kilometers, and depth is about 2-3 kilometers. Nevertheless, images made by spacecraft Curiosity show traces of water-erosion formation in the ancient riverbeds of Mars [1]. It appears that the origin of Mars volcanic relief is connected with ancient tectonics, with movement of huge plates of Martian crust.

fig.1. The ancient extinct volcano Olympus.

fig.2. The texture of surface “Point Lake” is a volcanic or sedimentary deposit. (Rover Curiosity, NASA).

Venus. Images of Venus’s surface made with help of spacecrafts represent volcanic lava fields and some large volcanic edifices in riftzones cutting flats and tesserae. The work of A. Bazilevsky and J. Head represents the model of global Venus stratigraphy with 16 types of locality and planet relief forms [3]. On the surface of Venus one can see a particular type of channels 1-2 km wide, extending for thousands of kilometers. Baltis Vallis channel with length of 6800 km is the most extended object in the Solar system [4]. It is possible that there was water on Venus during first 100-150 million years, it is confirmed also by exploration of ancient rivers and channels, beds of which are very similar to natural rivers, but Venus lost water as a result of increase in solar emissions.

THE WAVE PLANETOLOGY: COMPARATIVE TECTONIC GRANULATION OF TITAN, MOON, AND MERCURY IN RELATION TO THEIR ORBITAL FREQUENCIES.

G.G. Kochemasov,
IGEM of the Russian Academy of Sciences, 35 Staromonetny, 119017 Moscow, kochem.36@mail.ru

The main point of the comparative wave planetology [1-3] is a notion: "Structures of celestial bodies are functions of their orbits" or "Orbits make structures". In more detailed form this notion can be unfolded into four theorems: 1. Celestial bodies are dichotomous; 2. Celestial bodies are sectoral; 3. Celestial bodies are granular; 4. Angular momenta of different level blocks tend to be equal. There is a strict relationship between orbital frequencies and tectonic granulations of celestial bodies: higher frequency – finer granules, lower frequency ,- larger granules. These wave-induced granules are a consequence of an interference of standing waves of 4 directions occurring in rotating celestial bodies due to their movements in non-circular (elliptical, parabolic) orbits with periodically changing accelerations. These changing accelerations evoke in bodies warping inertia-gravity waves having a stationary character. A direct viewing of them now is possible due to excellent "Cassini SC" images of saturnian satellites, a recent image of the Saturnian's D- ring (Fig. 3), MOONCAM (GRAIL project) images of the lunar surface (Fig. 1, 2) Ubiquity of these wave induced granules allowed to formulate the 3rd theorem of the wave planetary tectonics [2, 3]: "Celestial bodies are granular". At first, this law was illustrated by a row of terrestrial planets starting from Sun: Solar photosphere orbiting the center of the solar system has the granule size πR/60, Mercury πR/16, Venus πR/6, Earth πR/4, Mars πR/2, asteroids πR/1. This granulation in Sun is known long ago as famous solar supergranulation with the characteristic size ~30 000 km. At Earth it was observed with help of geological and deeper geophysical data as eight superstructures about 5000 km in diameter in a great planetary circle. But now one can observe them directly due to a "lucky" image of Earth from a distance 1 170 000 km (Image PIA04159 taken by MRO).

Now three celestial bodies of comparable sizes but drastically differing compositions show their tectonic granulations (Fig. 4-6). Mercury, metal-rocky, R= 2440 km, Moon, rocky, R= 1738, Titan, icy, R= 2912. They differ by orbital frequencies: Mercury 1/ 88 days, Moon 1/ 29 days, Titan 1/16 days. The images of fig. 4-6 show that relative sizes of their granulations differ accordingly: πR/16, πR/60, πR/ 91 (in kilometers ~500, 100, 88).


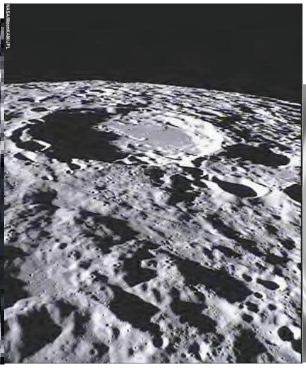
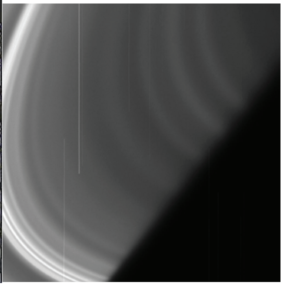

1 **2** **3**

fig. 1. Image of a spacious portion of the lunar surface acquired by the MOONKAM cameras at the twin satellites of the GRAIL mission. Intersecting wave formations are clearly seen. They produce chains and grids of round features ("craters").-20120418_20120419-Ben-Franklin-CO.jpg; Two important things must be underlined. This phenomenon has really planetary scale. At intersections of the waves appear "craters" of non-impact origin. These "crater" chains and grids must be excluded from cumulative frequency-crater size statistics [4]. Theoretical representation of intersecting waves of four directions is in Fig. 7.

fig. 2. Enlarged portion of Fig. 1.

fig. 3. Waving in the saturnian D-ring. PIA14664.

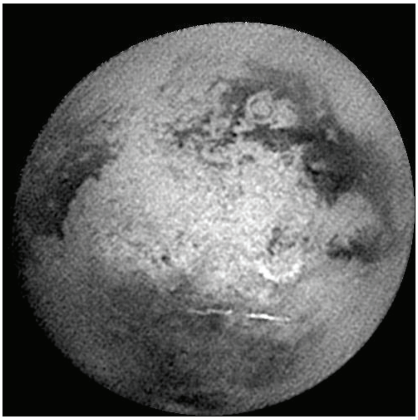

4

5

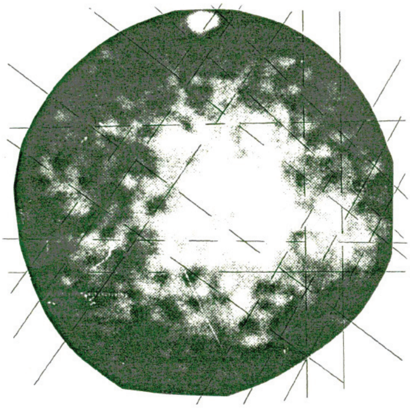

6

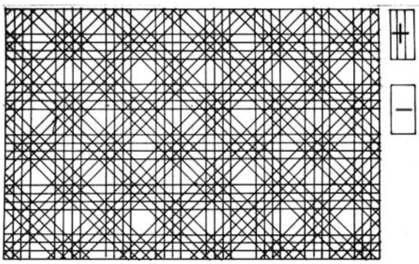

7

fig. 4. Titan (PIA06154); the image was taken Dec. 10, 2004 at a distance of 1746000 km by the narrow-angle camera with a special near-infrared filter at 938 nanometers (Credit: NASA/JPL/Space Sci. Inst.). In the center is a broad bright area Xanadu. Of particular interest are the regular cross-cutting tight lineations (waves) covering the whole surface of Titan and producing chains and grids of hollows ("craters") with diameters about 70-100 km. This granule size (88 km = πR/91) was calculated proceeding from the orbital frequency of Titan. These granules are superimposed on much larger blobs-"craters" (500-700 km across, hardly distinguished at the center) sometimes with multiple concentric rings (collars of "beads").

fig. 5. Gravitation anomaly of the Moon measured by by Kaguya mission. Credit: forum.worldwindcentral.com

fig. 6. Mercury is covered by dark or bright circles of similar sizes evenly distributed through its surface [5]. It seems that the circles are disposed along not random lines (aligned). This regularity is rather caused by a more regular process than random impacts.

fig. 7. Graphic representation of crossing waves (+ up, - down) producing chains and grids of round forms (craters) (better seen from some distance).

References: [1] Kochemasov G.G. (1994) An alternative (not impact) model of ring structure formation: order out of chaos and harmony of nature // 20th Russian-American microsymposium on planetology, Abstracts, Moscow, Vernadsky Inst., (GEOKHI), p. 42-43. **[2]** Kochemasov G.G. (1998) Tectonic dichotomy, sectoring and granulation of Earth and other celestial bodies // Proceedings of international symposium on new concepts in global tectonics ('98 TSUCUBA), Tsucuba, Japan, Nov. 1998, 144-147. **[3]** Kochemasov G.G. (1999) Theorems of wave planetary tectonics // Geophys.Res. Abstr., v. 1, #3, 700. **[4]** Kochemasov G.G. (2013) Lunar global scale crossing wave lineations (GRAIL-MOONCAM) // Microsymposium 54. Lunar farside and poles: new destinations for exploration. The Woodlands, Texas, USA, March 16-17, 2013. **[5]** Slade M.A. et al. (1992) Mercury: the radar experiment from Earth // Science, v.258, 635-640.

INTERNAL STRUCTURE OF TITAN FOR THE MODEL OF THE HOMOGENEOUS ACCRETION IN THE CIRCUMPLANETARY DISK

V. A. Kronrod , A. Dunaeva , O. Kuskov,
Vernadsky Institute of Geochemistry and Analytical Chemistry, Russian Academy of Sciences, Kosygin Str., 19, 119991 Moscow, Russia, Contact:va_kronrod@mail.ru

Abstract

Based of geophysical data on mass, average density and moment of inertia, as well as thermodynamic data on equations of state of water, high-pressure ices, and meteorite matter, we analyzed models of the Titan's internal structure and degree of its differentiation. The new numerical model has been applied. We have been employed constraints from a model of global convection in the mantle and a model of the homogeneous accretion of the satellite. Thickness and aggregate state of water-ice shell, size of the rock-iron cores, ice concentration in the ice-rock mantle, and total H_2O content in the satellite were determined. We found the probable thickness of the water-ice shell ~260-280 km, bulk concentration of H_2O ~ 49%, radius of the rock-iron core is 1080-1120 km

1. Computer simulation

Following [1-4], we consider the main parameters of the Titan internal structure in combination with geophysical observations. Our tasks included: (1) study of differentiation degree of the satellite; (2) determination of thickness and aggregate state of its water-ice shell; (3) determination of ice content in the mantle and total ice concentration in the satellite; (4) revealing constraints on the density distribution in the mantle and sizes of the rock core. Modeling was carried out on the basis of equations of hydrostatic equilibrium, moment of inertia and mass of the satellite, equations of state of water and high-pressure water ices. Density distribution in the interior depends on the ice content in the rock-ice mantle. We have employed that the amount of ice in the rock-ice mantle is constant for all depths. This constraint is a result of global convection in the satellite's rock-ice mantle. According to our model, the satellite was divided into three areas: pure ice or water-ice shell, rock-ice mantle and rock-iron (Fe-Si) core free of ice. The boundaries between the regions were determined by calculations. We assume a conductive heat transfer within the icy crust. The temperature gradient in the water and ice–rock mantle is set equal to adiabatic. We applied the Monte Carlo method for solving the problem. In our calculations we take into account uncertainties in the moment of inertia and mass of the satellite [5]. The density of the satellite's inner rock-iron core was assumed to be 3.62 g/cm^3, the density of the Fe-Si component in the rock-ice mantle was chosen in the range typical for the ordinary L/LL chondrites (3.15 to 3.62 g/cm^3) [1,2,6].

2. Internal structure of Titan

Model with a constant amount of ice in the rock-ice mantle. The heat flux is taken of 7.0 mW/m^2 [7], which corresponds both to its radiogenic and tidal heating. The results of calculations show that Titan may have been formed as a partially differentiated satellite with the water-ice shell maximum thickness of 470 km. The water ocean's depth is about 310 km and the thickness of the outer Ih-crust is equal to 80 km. Ices V and VI located under the ocean have the total thickness of about 120 km. The total H2O content of Titan is 45-52%. The undifferentiated rock-ice mantle has an average density of 1.4 - 2.6 g/cm^3.

Fe-Si core with the density of 3.62 g/cm^3 has a radius which inversely depends on the thickness of Titan's water-ice shell. Maximum allowed size of the inner rock-iron core (1350 km) is achieved at the minimum thickness of the water-ice shell, and this corresponds to the particular case of another two-layer model of the satellite (Fe-Si core + rock-ice mantle). Such a model does not assume the presence of the internal ocean and thus is not considered in this study.

Titan's internal structure for the model of the homogeneous accretion**.** In this section, we assumed that the satellite was formed by homogeneous accretion of planetesimals with small masses. Accretion heating did not lead to the melting of ice and differentiation ice-rock mixture onto the pure ice and silicate mantle. Rock-ice mantle of the satellite consists of an undifferentiated mixture of ice and rock similar to the composition of planetesimals.

Ice crust and a Fe-Si core were created in the last stage of accretion, when the heating of the surface layers was sufficient for partial melting of ice. A heavy stone planetesimals fall to the center of the satellite and form a Fe-Si core. The lighter ice and water formed a water-ice shell.

For this model we have adopted the following constraints:

1. The average ratio of water / rock for planetesimals and for the rock-ice mantle is equal.

2. The average ratio of water / rock for satellite and for the rock-ice mantle is equal.

3. The average ratio of water / rock for ice-water crust + Fe-Si core and for the satellite is equal.

4. The ratios of water / rock in the mantle for all depths are equal.

Estimates for the rock-iron core radius, thickness of the water-ice shell and the amount of bulk H_2O are shown in Fig. 1 and Fig2.

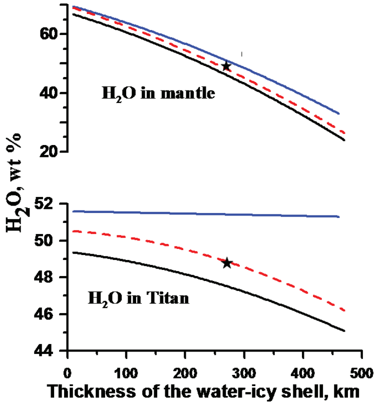

fig. 1. The total content of H2O in the ice-rock mantle and Titan, depending on the density of Fe-Si component in the mantle and the thickness of the outer icy shell. Density 3.62 g/cm3 (upper line) and 3.15 g/cm3 (lower line). The red dashed line is the amount of H2O in ice + hydrous rock. Stars denote a solution for the model of the homogeneous accretion.

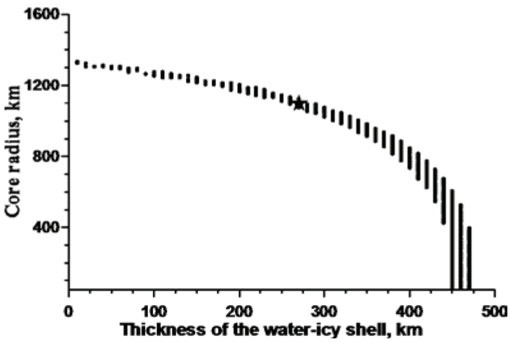

fig. 2. Titan's rock-iron core radius as a function of thickness of the outer water-ice shell. Stars denote a solution for the model of the homogeneous accretion.

Density of Fe-Si component - 3.15 g/cm³. H_2O content in the hydrous silicates was taken account.

The thickness of the water-icy shell is 260-280 km,

bulk concentration of H_2O – 49%, radius of rock-iron core is 1080-1120 km.

Density of Fe-Si component - 3.15 g/cm³. The thickness of the water-icy shell 240-260 km, bulk concentration of H_2O – 49%, radius rock-iron core - 1110-1150 km.

Density of Fe-Si component - 3.62 g/cm³. The thickness of the water-ice shell is 260-280 km, bulk concentration of H_2O – 51.5%, radius of rock-iron core is 1070-1110 km.

Our calculations reflect the possible similarity of the composition and internal structure of Titan and Callisto [4].

Acknowledgements

This research was supported by Russian Academy of Sciences under Programs 22, and by RFBR grant 12-05-00178 and 12-05-00033.

References

[1] Kronrod, V.A., Kuskov, O.L.: Chemical differentiation of the Galilean satellites of Jupiter: 1. An internal structure
of Callisto's water-ice shell, Geokhimiya, № 9, pp. 968-983, 2003.

[2] Kuskov, O.L., Kronrod, V.A.: Internal structure of Europa and Callisto, Icarus, V. 177, pp. 550–569, 2005.

[3] Dunaeva, A.N., et al.: Phase diagram of H_2O: Thermodynamic functions of the phase transitions of high-pressure ices, Solar System Research, Vol. 44, **№ 3**, pp. 202-222, 2010.

[4] Dunaeva A. N., V. Kronrod, Kuskov O.: Rock and H2O content in the satellites Titan and Callisto, EPSC Abstracts Vol. 7 EPSC 2012-498-1, 2012

[5] Iess, L., Rappaport, N.J., Jacobson, R.A., Racioppa, P., Stevenson, D.J., Tortora, P., Armstrong, J.W., Asmar, S.W., Gravity field, shape, and moment of inertia of Titan. Science 327, pp. 1367–1369, 2010.

[6] Kuskov, O.L., Kronrod, V.A.: Core sizes and internal structure of the Earth's and Jupiter's satellites, Icarus. Vol. 151, pp. 204–227, 2001.

[7] Mitri, G. et al.: Thermal convection in ice-I shells of Titan and Enceladus, Icarus, V.193, pp. 387–396, 2008.

DETECTION OF POSSIBLE SPECTRAL SIGNS OF O_2 AND CH_4 ON EUROPA AND O_2 ON GANYMEDE AND CALLISTO.

V. V. Busarev [1],
[1]Moscow Lomonosov State University, Sternberg Astronomical Institute (SAI MSU), 13, Universitetskij pr-t, Moscow 119991, Russian Federation.
Contact: busarev@sai.msu.ru

Abstract: Weak absorption bands with relative intensity ~1-10% are found for the first time in the visible-range reflectance spectra (RS) of Galilean icy satellites of Jupiter, Europa, Ganymede and Callisto. It seems several of the bands are common for the bodies and may be manifestations of adsorbed O_2 for radiation implantation of O^+ ions into the satellite surface in the magnetosphere of Jupiter. Specific ones could be produced by iron ions (Fe^{2+} and Fe^{3+}) in silicates on Ganymede and Callisto and by methane adsorbed in water ice on Europa.

Previous results: As is known, Europa, Ganymede and Callisto have predominant or considerable water-ice component in the surface matter [1-4]. Sings of internal water oceans on the satellites were found by the NASA's spacecrafts Voyager and Galileo. For instance, space images of Europa discovered an extremely low crater density for the atmosphereless body and formations of the «iceberg»-type going on its surface in the relatively recent past (e. g., [5, 6]). Spectral data showed that non-icy materials on the surface of Europa are mostly represented by $MgSO_4$, Na_2SO_4, H_2SO_4 and their hydrates [7-11] filling numerous intersecting cracks in the ice surface of the satellite [11, 12]. As follows from modeling based on reflectance spectra, shares of water ice may be ~50% on Ganymede and up to 10% on the surface of Callisto [9]. Their non-icy materials are similar to carbonaceous chondrites, though they could have more organics and hydrated silicates of serpentine type [9, 13]. Small amounts of SO_2 [14], CO_2, H_2S and H_2O_2 [15, 16] as well as hydrates of sulfuric acid (H_2SO_4•$8H_2O$, H_2SO_4•6, $5H_2O$, H_2SO_4•$4H_2O$) [7] are discovered on the surface of the satellites as possible products of sulfur and other ions implanted from Jovian magnetosphere. It leads to emergence of anions (SO_4^{2-}, HSO_3^-, and HSO_4^-) and cations (H_3O^+ and H_5O^+) having spectral details in the infrared (IR) range [17]. A radiolysis product on the surface of icy Galilean satellites is also molecular oxygen (O_2 and/or O_3) originated from O^+ which may be in an adsorbed state in the water ice [18-21].

Reflectance spectra and their interpretation: The observations were carried out at 1.25-m telescope with a CCD-spectrograph (SBIG ST-6) of the SAI MSU Crimean Observatory in the range of 0.40-0.92 µm with a spectral resolution of ~8Å [22]. HD101177 was used as a standard and a solar analog star. To exclude a noise component emerging in the RS, they were smoothed by a running box average. The methods are the same as used in processing of asteroid spectral data [22]. Relative errors (RMSD) in the central part of the RS do not exceed 1-2% and rise up to 5-7% near the edges of the spectral range. Phase-angles of the Galilean satellites at the observations were small and changing from 3.8 to 4.3º. Normalized (at 0.55 µm) RS 1-3 of Europa, Ganymede and Callisto obtained on three nights of March 2004, 22/23 (1), 23/24 (2) and 25/26 (3), are shown in figs 1-3. The curves are offset vertically for clarity. The RS of Europa (T_{rot}= 3. 551^d, D = 3121.6 km) span a time interval close to the rotational one of the body and, therefore, represent its surface as a whole (Fig. 1). The spectra 1-3 of Ganymede (T_{rot}= 7.155^d, D = 5262.4 km) cover a time close to a half of its rotational period (Fig. 2). The spectra 1-3 of Callisto (T_{rot}= 16. 689^d, D = 4820.6 km) span a quarter of its rotational period (Fig. 3).

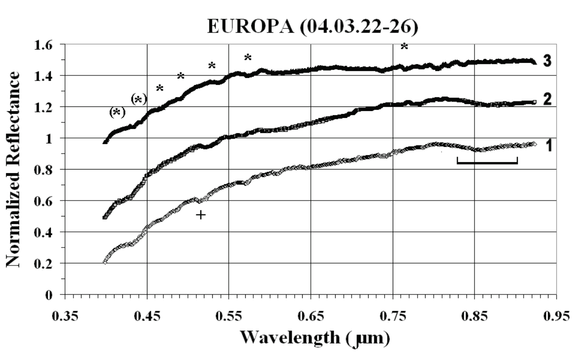

fig. 1.

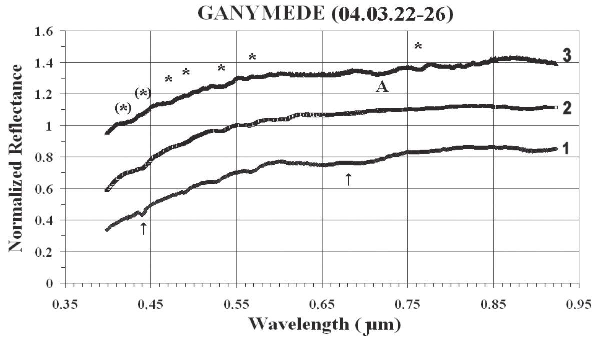

fig. 2.

Some weak absorption bands indicated by marks (see figs 1-3) were registered for the first time in the RS of Europa, Ganymede and Callisto. We are interpreting them with regard to found materials on the surfaces of the satellites. Only molecular oxygen and silicates and/or hydrated silicates have noticeable absorption bands in the visible range among the mentioned compounds (e. g., [23, 24, 25]). Absorption bands of solid O_2 in the range are as follows: at 0.420, 0.445, 0.446, 0.448, 0.475, 0.479, 0.494, 0.532, 0.574, 0.575, 0.576, 0.623, 0.627, 0.751, 0.756, 0.760, and 0.915 µm (the underlined values refer to more intense bands) [23]. At least seven of them or their signs at 0.420, 0.446, 0.475, 0.494, 0.532, 0.576, and 0.760 µm (indicated by asterisks or asterisks in brackets if the feature is overlapping with another one) are provisionally distinguished in the RS of Jovian satellites in question (figs 1-3). As a confirmation, it can be considered discovery of O_2 on the bodies based on absorption bands at 0.577 and 0.628 µm close to listed [18, 20]. However, there is a sizeable discrepancy between the temperatures of solid O_2 (<54 K [23]) and daytime surface of the bodies ~120-170 K (e. g., [26, 27]).

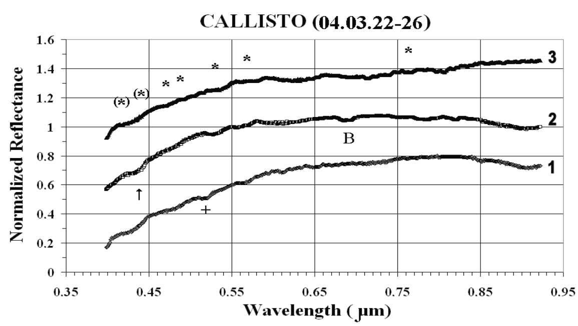

fig. 3.

Nevertheless as follows from laboratory measurements, wavelength positions of absorption bands of solid, liquid and condensed states of O_2 are roughly the same (e. g., [23, 28]). Thus, the found absorption features could be attributed to O_2 on the satellite surface in an adsorbed state, as a type of condensed one.

Two or three of the mentioned absorption bands of O_2 in the RS (figs 1-3) overlap possibly with an absorption feature of Fe^{3+} at 0.44 µm [24] found by us on many asteroids and considered as an indicator of serpentine-type phyllosilicates [22]. Such interpretation is corroborated by the spectrum 1 of Ganymede (fig. 2) with a more narrow absorption feature at 0.44 µm of Fe^{3+} and a wide absorption band of hydrated silicates at 0.67 µm arising probably due to electronic charge-transfere transitions $Fe^{2+}\rightarrow Fe^{3+}$ [25] (indicated by a vertical arrow). The spectrum could be attributed to a Ganymede's side containing a large proportion of hydrated silicates in average and less water-ice. Prevalence of silicates on the surface of Callisto is probably confirmed not only a narrower absorption band at 0.44 µm (Fe^{3+}) [24] (indicated by a vertical arrow, spectrum 2, fig. 3) but also relatively intense absorption features at 0.90 µm (Fe^{2+}, similar to orthopyroxenic one) [25] in the spectra 1 and 2 (fig. 3). A subtle absorption feature at 0.52 µm in the reflectance spectra of Europa (fig. 1, curve 1) and Callisto (fig. 3, curve 1) (inducated by "+") could be ascribed to electronic transitions in Fe^{2+} [25] in salts and/or minerals. Letters "A" and "B" in the RS of Ganymede and Callisto (figs 2 and 3) designate residual telluric absorption bands of O_2.

SIMULATION OF THE INITIAL STAGES OF FORMATION OF PROTO-PLANETARY RINGS IN THE SOLAR SYSTEM.

T. R. Abdulmyanov,
Kazan State Power Engineering University, Krasnoselskaya st., 51, Kazan, Russia,
Contact: abdulmyanov.tagir@yandex.ru

Introduction:

Formation of the Solar system, according to recent research (Zabrodin, et al., 2006), could start with the fragmentation of the proto-planetary disk and the formation of proto-planetary rings. Dynamic structure of the asteroid belt shows (Dermot, Murray, 2009) that the slow growth of bodies in less dense proto-planetary rings could be the cause of the simultaneous formation of many bodies which has heliocentric orbits. In such cases, the mechanism of mutual collisions of bodies is becoming one of the main mechanisms of the orbital evolution of these bodies. Rings with a critical density, by gravitational instability will collapse. The compression will not be local, if and only if the critical density will support by influx of particles from the outer regions of the ring. If the collapse is not local, then in the ring will be formed single planetesimal.

The main mechanisms of growth planetesimals to the size of the planets could be mechanisms of long-period librations near the Lagrange points (Hayashi et al., 1977). For small planets it was near the mean motion commensurabilities $(p + q) / p$ (Abdulmyanov, 2001). The collision mechanism of growth of the planetesimals is seen in (Ida, Morbidelli, 2008). One of the most difficult to modeling is the growth of body size of about 1 m. According to the results of numerical simulations (Yohansen, et al., 2007), the formation and growth of such bodies could occur in areas of turbulent motion of gas and dust particles in the early stages of the evolution of the proto-planetary disk.

This paper presents a model of the surface wave disturbances of proto-planetary disk of the Solar system. The locations of proto-planetary rings are determined with the help of an analytical solution of the wave equation for a circular disk. The mechanism of particle migration from the outer zones in the proto-planetary ring also is considered.

Origin of the surface wave disturbances of proto-planetary disk in the Solar system:

Compression (collapse) dynamics of the proto-stellar cloud was first investigated in 1964 by the Japanese astrophysicists C. Hayashi and T. Nakano (1963). The performed calculations of these scientists show that in a few years from the beginning of a cloud adiabatic compression a hydrostatic equilibrium core is formed in the central part of the star (proto-star). The outer layers of the cloud at the same time continue to fall freely to the center. Due to the collision of outer layers matter with the kernel a shock wave appears at the border of the core and the kinetic energy of the incident gas is converted into heat (Surdin et al., 1992). When the temperature is 1 million K, thermonuclear reactions begin in this area. A convection zone appears at the border of the core, which is associated with the appearance of a magnetic field and a stellar wind.

According to Hayashi - Nakano models at the early stages of formation a gaseous proto-planetary solar system disk had dimensions similar to a modern orbit of Jupiter. As a result of the collapse of the proto-star, it became a star surrounded by a cloud of gas and dust. The dust cloud became an embryo of the future planetary system. The gas-dust cloud, having separated from the star, compacted under the influence of the gravitational interaction. The rotating cloud took the form of a flat disk. Due to the gravitational instability there happened a proto-planetary disk fragmentation into circular formation.

At the stage of rapid compression proto-stellar clouds, which lasts for about 10 years (Shklovsky, 1977), the radius of the proto-star down from 40 AU, to the value of semi-major axis of the orbit of Mercury (about 0.4 AU). That is, the radius of the proto-star dropped a hundred times. Spatial density of the proto-star in this case will increase a million times. This change in density in a relatively short time (about 10 years) will lead to the replacement of the light gases, and emissions from the central proto-star to the periphery and outside of the proto-star. The movement of these gases will be created on the surface of the forming of the proto-planetary disk surface waves. By the beginning of the next stage of the formation of proto-stars (stage Hayashi), the radius of the proto-planetary disk was about 5 AU (Hayashi et al., 1963). According to the simulation results (Abdulmyanov, 2012a, 2012b), under FU Orionis (from 10^2 years to 10^5 years from the beginning of the rapid compression of proto-star) is separated proto-planetary rings of Neptune, Pluto and Uranus. By the end of this stage, the radius of the proto-star is decreased by 10 times and was about 0.04 AU. The density is increased by almost a thousand times. At the stage of T Tauri it is separated the rings of Saturn, Jupiter and the asteroid belt. T Tauri stage is the stage of slow compression proto-star and the longest stage (from 10^5 years to $4 \cdot 10^6$ years from the beginning of the stage of rapid compression). By the end of the stage of T Tauri proto-star radius is decreased by 10 times and came close to the current radius of the Sun (and 0.00465 AU). The density of the proto-star has increased a thousand fold. The value of the radius of the proto-planetary disk at that time was around 0.18 AU. At the early stage of fusion reactions ($4 \cdot 10^6$ to $5 \cdot 10^6$ years from the beginning of the rapid compression) formed proto-planetary ring of the terrestrial planets.

Thus, there is a big difference between the pressure inside proto-star and in the emerging field of the proto-planetary disk. Proto-star and proto-planetary disk, decreasing in diameter, will always remain united hydrodynamic object. The processes occurring in the central part of the proto-planetary disk, will differ from the processes taking place on the periphery. Because of the linear stability of Kepler disks, any random perturbations within these discs will fade over time. However, the difference in density of the proto-star and the surface of the proto-planetary disk will be created on the surface of the proto-planetary disk regular periodic disturbance. These disturbances can not be redeemed due to the stability of Keplerian disks. Such perturbations of the surface of the proto-planetary disk are the most interesting in the study of the mechanism of formation of proto-planetary rings.

The model of surface wave disturbance of the proto-planetary disk:

The most intensive movement of the waves could be even in the early stages of formation of the proto-planetary disk. Wave motion of gas and dust particles are formed mainly by the action of two forces (Safronov, 1969): by the gravitational force $\delta F_g = 4\pi G\rho_0 u$, related to a change $\delta\rho$ density $\rho = \rho_0 + \delta\rho$ and by the gas pressure δF_P:

$$\delta F_P = -\frac{1}{\rho}\frac{\partial P}{\partial x} \approx c_s^2 \frac{\partial^2 u}{\partial x^2},$$

where $u(x)$ - the displacement of gas and dust particles as a result of the forces δF_g and δF_P, c_s – the speed of sound. The equation of wave motion of gas and dust particles in this case will be the following (Safronov, 1969):

$$c_s^2 \frac{\partial^2 u}{\partial x^2} = -4\pi G \rho_0 u.$$

Acceleration of particles for each time point in the polar coordinates (r, φ) can be determined from the following equation:

$$\frac{\partial^2 u}{\partial t^2} = c_s^2\left(\frac{\partial^2 u}{\partial r^2} + \frac{1}{r}\frac{\partial u}{\partial r} + \frac{1}{r^2}\frac{\partial^2 u}{\partial \phi^2}\right) + 4\pi G \rho_0 u. \tag{1}$$

Solving the Eq. (1) we obtain the functions $T(t)$, $\Phi(\varphi)$, $R(r)$ and the desired solution $u(r, \varphi, t)$ of the Eq. (1):

$$u(r,\phi,t) = \sum_{\nu=0}^{\infty}\Phi_\nu(\phi)\sum_{k=0}^{\infty}T_{k\nu}(t)R_{k\nu}(r),$$

were $\Phi_v(\varphi) = \cos(v\varphi + \varphi_0)$, $R_{kv}(r) = J_v(\lambda_{kv} r/R_0)$, J_v – the Bessel function of order v, λ_{kv} – zeros of the Bessel function J_v; R_0 – radius of the proto-planetary disk, φ_0 – the arbitrary constant , a_{kv}, b_{kv} – the coefficients determined by the initial conditions for the equation (1). If the value of the constant $\lambda = [4\pi G\rho_0 - (\lambda_{kv}/R_0)^2] > 0$, then the function T will be equal $T_{kv}(t) = a_{kv}\exp(c_s\lambda^{1/2}) + b_{kv}\exp(-c_s\lambda^{1/2})$. If the value of the constant $\lambda \leq 0$, then $T_{kv}(t) = a_{kv}\cos[c_s(-\lambda)^{1/2}] + b_{kv}\sin[c_s(-\lambda)^{1/2}]$. The initial and boundary conditions for (1) are defined as follows:

$$u(r,\phi,0) = f(r,\phi) = \sum_{\nu=0}^{20}cos(\nu\phi)\sum_{k=0}^{20}a_{k\nu}J_\nu(\lambda_{k\nu}r / R_0),\ u_t(r, \varphi, 0) = 0,$$

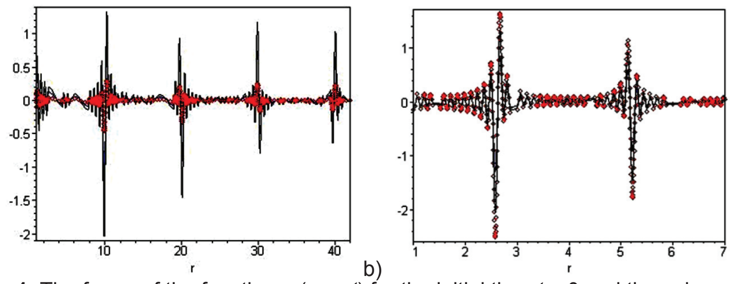

fig. 1. The forms of the function $u(r, \varphi, t)$ for the initial time $t = 0$ and the value of the angle $\varphi = 0$. a) For the parameter $R_0 = 5$ AU, and the values of the parameters $H = H(1, 0) = 0.1081$ (solid line); $H = H(1, 1) = 0.0678$ (solid line); $H = H(2, 0) = 0.024$ (dotted line); b) for the parameter value and $R_0 = 1.3$ AU.

where $f(r, \varphi)$ - the function that defines the shape of the initial surface of the proto-planetary disk. Shape of the surface of the proto-planetary disk is defined using the results obtained by Safronov (1969).

Fig. 1a – 1b shows the characteristics of wave disturbances for the parameter R_0 = 5 and 1.3 AU. According to Fig. 1b – 1b, as a result of addition of the waves on the surface of the proto-planetary disk will form standing waves, the amplitude of which is more than ten times greater than the amplitude of the background waves. In this case, the length of standing waves for R_0 = 5 AU, and will be 10 AU. For the value R_0 = 1.3 AU the wavelength is equal to 2.6 AU.

Conclusion:

Circular waves can occur as a consequence of active star formation processes in the early stages of the proto-planetary disk. Such waves are observed only in supernova explosions of stars. However, around other stars, such waves can exist, but can be optically inaccessible. Circular waves around other stars could be due to the large density gradient in the central part of the disc and its periphery. In this case, the surface of the proto-planetary disk that is in fluid balance, there will always be a good conductor of any central disturbances, even of small amplitude. Broadcast central perturbations in the form of circular waves can occur as long as the proto-planetary disk and its center will be a single gas-dust complex dynamic. Despite the lack of observational data, the effect of circular waves, in the initial stages of the proto-planetary disk, confirmed that observed in the solar system, patterns of distribution of planetary orbits.

According to the astrophysical studies (Shklovsky, 1977) the dust cloud radius from which the solar system was formed, was about 40 AU. The radius of the proto-planetary disk, according to the Hayashi - Nakano model, was about 5 AU. As a result of the gravitational collapse the dust cloud formed a proto-planetary disk, and then the solar system, which measures about 40 AU. The gravitational contraction of gas-dust cloud moved the light gases to the periphery of the cloud. Proto-planetary disk, which is in equilibrium, in the early periods of evolution, may have been a good conductor of radial perturbations arising in the solar interior. Therefore, the movement of the light gases to the periphery may have been in the form of circular waves. According to the wave model of the proto-planetary rings formation we can make the following conclusions:

The modern distances between the orbits of Saturn and Uranus, Neptune and Uranus, Neptune and Pluto show that the initial radius of the proto-planetary disk was 5 AU. This conclusion is consistent with the conclusions of the Hayashi - Nakano theory. The initial radius of the proto-planetary disk is the initial radius of the active region of the Solar wind waves. According to the data on the distances between the planets orbits the forming start of the ring of proto-planetary Neptune coincides with the date of the birth of the Sun. Then, after about half a million years, the proto-planetary rings of Uranus and Pluto begin to form. Proto-planetary rings formation of these planets may have occurred during the greatest solar activity.

This work was supported by RFBR grant № 13 - 02 - 00792.

References:

Abdulmyanov, T. R. Determination of Libration Characteristics of asteroids near Mean Motion Commensurabilities 1/1, 4/3, 3/2, 2/1, 7/3, 5/2 and 3/1 // Solar System Research. 2001. V. 35. № 5. P. 408 – 414.
Abdulmyanov, T. R. The evolution of the Solar activity and planet formation. EPSC2012-75, 2012a. V. 7, Madrid.
Abdulmyanov T. R. Defining characteristics of the wave and thermal effects on structural changes in the environment // Vestnik KSPEU. 2012b. V. 12. № 1. P. 75 - 84.
Hayashi C., Nacano T. Evolution of Stars of small masses in the Pre – Main – Sequence Stage // Progress of Theoretical Physics. 1963. V. 30. № 4. P. 460 – 474.
Hayashi C., Nakazawa K., Adachi I. Long-Term Behavior of Planetesimals and the Formation of the Planets // Publ. Astron. Soc. Japan. 1977. V. 29. P. 163 – 196.
Ida S., Morbidelli A. Accretion and destruction of Planetesimals in turbulent disks. Astrophysical Journal. 2008. V. 686. P. 1292 – 1301.
Johansen A., Oishi J., Mac Low M. – M., et al.). Rapid planetesimal formation in turbulent circumstellar disks // Nature. 2007. V. 448. P. 1022 – 1035.
Murray, K., Dermott S. Dynamics of the solar system. Moscow: FIZMATLIT. 2009. 588 p.
Safronov V. S. Evolution of the proto-planetary cloud and the formation of the Earth and planets. Moscow: Nauka. 1969. 244 p.
Surdin V. G., Lamzin S. A. Protostar. Where, how and from which stars form. Moscow: Nauka. 1992.
Shklovsky I. S. Stars, their birth, life and death. Moscow: Nauka. 1977. 393 p.
Zabrodin A. V. Zabrodina E. A., Legkostup M. S., et al. Some models describe the proto-planetary disk of the sun in the early stages of its evolution. Moscow: Preprint. Keldysh Institute. RAS. 2006. 43 p.

DETERMINATION OF THE INITIAL MOMENTS OF FORMATION OF PROTO-PLANETARY RINGS IN THE SOLAR SYSTEM.

T. R. Abdulmyanov,
Kazan State Power Engineering University, Krasnoselskaya st., 51, Kazan, Russia, Contact: abdulmyanov.tagir@yandex.ru

Introduction:
According to the astrophysical studies (Shklovsky, 1977) the dust cloud radius from which the solar system was formed, was about 40 AU. The radius of the proto-planetary disk, according to the Hayashi - Nakano model (1963), was about 5 AU. As a result of the gravitational collapse the dust cloud formed a proto-planetary disk, and then the solar system, which measures about 40 AU. The gravitational contraction of gas-dust cloud moved the light gases to the periphery of the cloud. Proto-planetary disk, which is in equilibrium, in the early periods of evolution, may have been a good conductor of radial perturbations arising in the solar interior. Therefore, the movement of the light gases to the periphery may have been in the form of circular waves. This paper deals with an analytical model of perturbation motion of the particles of the proto-planetary disk of gas and dust, in the early stages of its evolution (Abdulmyanov, 2012a, 2012b). Using the model it was estimate the date of the formation of proto-planetary rings of the solar system.

Determination of the date of formation of proto-planetary rings: In the model of Hayashi - Nakano considered two phases of changes in the activity of stars. The first stage is short phase of rapid changes in activity of the star. The second stage is the stage of long-term and slow changes in activity of the star. Between these two stages, we note a third, intermediate stage, when there was a rapid slowdown stars. Comparing the mutual distances between the modern orbits of the planets is easy to see that there are three main groups of distances. The first group is the distance of Pluto - Neptune - Uranus - Saturn: d = 9.5; 10.8; 9.7 AU. The second group is the distance of Saturn - Jupiter - Ceres - Mars: d = 4.3; 3.2; 1.2 AU. The third group consists of the distance of Mars - Earth - Venus - Mercury - Sun: d = 0.52; 0.28; 0.33; 0.38 AU. The results of simulation of wave disturbances surface of the proto-planetary disk show that such a division of planetary distances in three groups is not random. These groups may correspond to a specific stage of the evolution of the proto-star. The first group of distances, according to the considered wave pattern begins to form immediately after the stage of rapid compression of the proto-star. The third group of the distances between the orbits of the planets began to form near the end of the T Tauri phase of the proto-star. The second group was formed distances throughout the stages of T Tauri. The existence of a connection between the stages of the evolution of the proto-star and the formation of the distances between the orbits of the planets can be found in the diagram shown in Fig. 1b. If the numbers in this chart the planets placed in reverse order, then this figure will almost repeat graph theoretical dependence of the radius of the proto-star time (Shklovsky, 1977). Fig. 1a shows a graph of the distance D from the radius r. The function $D(r)$ is built using the spline - interpolation of the current observed distances between the orbits of planets in the solar system. On the graph of the function $D(r)$ is easy to see areas of slow change of the function $D(r)$ for small values of the radius r (r <1.5 AU) and for the values of r > 20 AU. The rapid change of the function $D(r)$ is in the intermediate range of values of r and 1.5 AU, up to 20 AU.

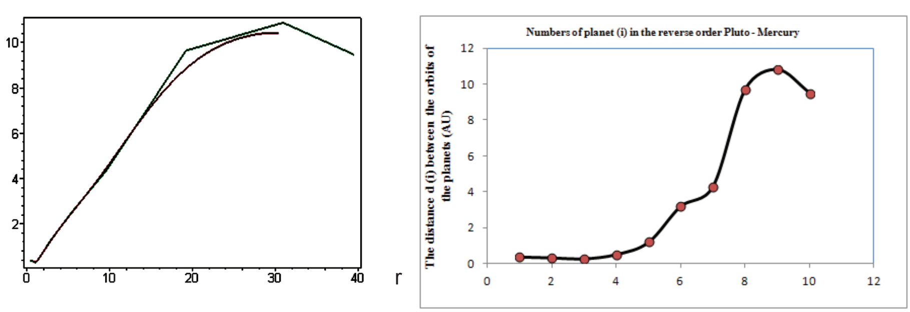

a) b)

fg. 1. (a) Schedule (r, D) depending on the distance D between the orbits of planets in the solar system on the distance r (spline - interpolation of the observed data), (b) the diagram (n, d): number of the planet - the distance between the orbits of planets in the Solar system.

Using the graph of the function $D(r)$, shown in Fig. 1a, we define the initial moments of the formation of proto-planetary rings. For this we consider the polar radius r as a function of time. Differentiating $D(r)$ at time t as a complex function, we get: $dD/dt = (dD/dr)/(dr/dt)$. According to the formulae, for to determine the time of formation of wave-length D, should be known relationship dD/dr and dr/dt. Relationship dD/dr can be determined using the graph of $D(r)$, shown in Fig. 1a. The highest, lowest and average value of the ratio dD/dr, as shown in Fig. 1a power tangent angles 53°, 43° and 33° respectively. The rate of decrease of the proto-planetary disk of radius r, in the theoretical model of compression, is approximately equal to the tangent of the angle of 40° (Shklovsky, 1977). Consequently, when the average value of the ratio dD/dr, for a difference of views differentials we get: $(D_i - D_j)/(t_i - t_j) = \mu = 0.7812$. According to the model of wave disturbances of the proto-planetary disk of proto-planetary rings before anyone begins to form proto-planetary ring of Neptune, having a maximum value of the wavelength $D_0 = 10.876$ AU. Proto-planetary ring of Neptune began to take shape with the birth of the Sun (early stage Hayashi). For the asteroid belt (Ceres) $D_i = 1.243$ AU. Consequently, the time elapsed since the birth of the sun to the beginning of the formation of the asteroid belt will be equal to (10.876 - 1.243) / μ = 12.33 million years. At the lower estimate of the ratio dD/dr beginning of formation equals 17.7 million years. According to the estimates of the age of meteorites, the age of the asteroid belt is about 4 million years after the start of the stage thermonuclear reactions in the sun (4.57 billion years ago). Consequently, the lower estimate of the ratio dD/dr, stage Hayashi began 4.583 billion years ago. The median estimate is 4.5783 billion years ago. That is, the estimate of the start of the stage for the Sun Hayashi 4.59 billion years old, resulting in work (Bonanno, 2002), according to the model is too high. To estimate the age of meteoritic bodies use different methods. With the improvement of these methods are found to be more precise data on the early stages of Hayashi. If you know the date of the beginning of the stage Hayashi, by the age of meteorites can determine the value of the constant μ. For further calculations, we assume μ = 0.5442, that is obtained at the lower estimate. Then the beginning of the formation of proto-planetary rings can be determined using the following formula: $t_i = t_0 - \Delta t_i$, $\Delta t_i = (1 / \mu) \cdot (D_0 - D_i)$, where t_0 - the start date for the proto-star stage Hayashi (about 4.583 billion years ago). Calculating from this formula Δt_i, we get moments of the beginning of the formation of proto-planetary rings for the rest of the planets. Proto-planetary rings of Uranus and Pluto began to take shape 2.02 and 2.388 million years after the start of the Hayashi stage for the Sun respectively. Proto-planetary rings of Saturn, Jupiter, Ceres (asteroid belt), respectively - 11.94, 13.96, 17.64 million years. Proto-planetary rings of Mars, Mercury, Venus and the Earth began to form, respectively, 18.88, 19.14, 19.23, and 19.32 million years after the start of the stage Hayashi.

Conclusions: Comparison of the distances between the standing waves in the wave model (Abdulmyanov, 2012a, 2012b) of the formation of proto-planetary rings with the observed data of distances between the orbits of planets in the solar system shows that in the model the distribution of distances between the orbits of the planets represented the observed pattern of distribution of distances between the orbits of the planets. Therefore, the observed pattern of distribution of the orbits of the planets, according to the wave model, is a result of the circular waves actions. The initial moments of the formation of proto-planetary rings are defined by the observed distances between the orbits of the planets and are consistent with the known theoretical stages of compression of stars. It is received the estimation of the early Hayashi stage for the Sun (4.583 billion years) and the initial date of the formation of proto-planetary rings for planets in the Solar system. These estimate relate to the assessment of the age of chondrites, and in the case of other age estimates of the asteroid belt can be adjusted accordingly using the same formula that has been applied in assessing the beginning of the formation of proto-planetary rings in this paper. Compare the width and positioning of proto-planetary rings shows that the presently observed distribution of the orbits of the planets is characteristic of wave action in the early stages of the evolution of the proto-planetary disk. In this model does not take into account the rotation of the proto-planetary disk. It is assumed that the rotation of the disk affects substantially only the horizontal component of the perturbation and recorded in the main model, the hydrodynamic equations. Rotation of the disk in the resulting solution can be considered using the rotating coordinate system.

This work was supported by RFBR grant № 13 - 02 - 00792.

References:

Abdulmyanov, T. R. The evolution of the Solar activity and planet formation. EPSC2012-75, 2012a. V. 7, Madrid.

Abdulmyanov T. R. Defining characteristics of the wave and thermal effects on structural changes in the environment // Vestnik KSPEU. 2012b. V. 12. № 1. P. 75 - 84.

Bonanno A., Schlattle H., Patern L. The age of the Sun and the relativistic corrections in the EOS // Astronomy and Astrophysics. 2002. V. 390. P. 1115 – 1118.

Hayashi C., Nacano T. Evolution of Stars of small masses in the Pre – Main – Sequence Stage // Progress of Theoretical Physics. 1963. V. 30. № 4. P. 460 – 474.

Shklovsky I. S. Stars, their birth, life and death. 1977. Moscow: Nauka. 393 p.

SUN – EARTH: NEW CHANNEL OF INTERACTION

O.B. Khavroshkin, V.V. Tsyplakov.
Institute of Physics of the Earth. RAS, Moscow, Russia, Contact: khavole@ifz.ru 8499766 26 53

The study of natural radioactivity as an objects which able to change their temporal timing feature is presented in [1]. It is of interest to compare the latest data on the activity of the Sun and the periodicity of solar neutrinos and the temporal characteristics of the radioactive source. That is, to conduct a search for the possible influence of external sources for radioactivity. There are cycles 5 min, 18 min and 53 min found in solar physics. The cycle of 27 days corresponds to the activity of the Sun. During of the solar activity these temporal pulsations are lost in a strong variation of solar wind (Neugebauer, NASA). The Stanford University scientists (P. Starrek, G.Valter and M.Vitlend) have found the cycle of 28.4 days as pulsations of the solar neutrinos. Neutrinos come from the depths of the Sun and it tells about the frequency of oscillations of solar bowels. See also online: Kostyantynivska L.V. Solar activity. Search experiment is better to have a known but modified the experiment. Experiments on monitoring natural radioactivity and the possible influence from the Sun as previously carried out by measuring the variations of the gamma-ray sample of ore from the Trans-Baikal uranium deposit; the characteristics of the sample are known [1].

The spectrum of temporal variations in the activity of the sample Zabaikalskaya radioactive ore contains peaks which coinciding with the period of natural oscillations of the Sun [2].

The capture cross section of the radioactive heavy deformed nucleus in time decay increases by in many orders and is able to interact with the stream of solar neutrinos which are modulated by own oscillations of the Sun.

The picks of spectrum of long-period oscillations of the Earth exceeding its own and contains peaks that match the value with an accuracy of 1-3% with peaks of its own oscillations of the Sun. The mechanism of excitation of these oscillations is similar to the nature of variations in the activity of a radioactive sample of ore.

These effects are included in the mechanisms of interaction of the Earth - the Sun systems and the impact on seismicity; search problem of existing natural nuclear reactor inside Earth core.

References:

Oleg Khavroshkin, Vladislav Tsyplakov. RADIOACTIVITY OF NUCLEI IN A CENTRIFUGAL FORCE FIELD. The Natural Science (NS) Vol.3,No.8,733-737 (2011).
Iben I., Jr., Mahaffy J. Astrophys. J. (Lett.), 1976, v.209, p.L39.

OUTBURSTS AND CAVITIES IN COMETS

S. I. Ipatov, *Space Research Institute, Profsoyuznaya st. 84/32, Moscow, Russia. Contact: siipatov@hotmail.com*

The impact module of the Deep Impact (DI) spacecraft collided with Comet 9P/Tempel 1 in 2005. Based on analysis of the images made by this spacecraft during the first 13 minutes after the impact, Ipatov and A`Hearn [2] concluded that the triggered outburst of small particles and excavation of a large cavity with dust and gas under pressure began at t_e=8 s, where t_e is the time after the DI collision. Schultz et al. [4] analyzed images of Comet Tempel 1 made by the Stardust spacecraft and supposed that the diameter d_{tc} of the transient DI crater was about 150-200 m. Some authors support smaller values of d_{tc} (up to 50 m). Ipatov [1] estimated the distance d_{cav} between the upper border of the cavity excavated at t_e=8 s and the pre-impact surface of the comet. In particular, I supposed that the depth of a growing crater is proportional to t_e^{γ} (where γ is about 0.25-0.4) during the intermediate stage of crater excavation. The most probable estimate of d_{cav} was about $0.1d_{tc}\times(t_e/T_e)^{0.3}+1$ meters, where T_e is the time of duration of ejection (T_e=500 s at d_{tc}=150 m). Using this approach Ipatov [1] obtained d_{cav} to be 5 or 6 meters for d_{tc} equal to 150 or 200 m (d_{cav} is 3 or 4 m for d_{tc} ~ 50-100 m). The obtained values of the depth are in accordance with the depth (4-20 m) of the initial sublimation front of the CO ice in the models of the explosion of Comet 17P/Holmes considered by Kossacki and Szutowicz [3]. Our studies testify in favor of that cavities with dust and gas under pressure located a few meters below surfaces of comets can be common. The porous structure of comets provides enough space for sublimation and testifies in favor of existence of cavities. Natural outbursts were observed for several comets. Similarity of velocities of particles ejected at triggered and natural outbursts shows that these outbursts could be caused by similar internal processes in comets.

[1] Ipatov S.I., *Mon. Not. R. Astron. Soc*., 2012, v. 423, 3474-3477
[2] Ipatov S.I. and A'Hearn M.F., *Mon. Not. R. Astron. Soc*., 2011, v. 414, 76-107
[3] Kossacki K.J., Szutowicz S., *Icarus*, 2011, v. 212, 847-857
[4] Schultz P.H., Hermalyn B., Veverka J., *Icarus*, 2013, v. 222, 502-515

THE ANGULAR MOMENTUM OF COLLIDING RAREFIED PREPLANETESIMALS ALLOWS THE FORMATION OF BINARIES

S. I. Ipatov,
Space Research Institute, Profsoyuznaya st. 84/32, Moscow, Russia.
Contact: siipatov@hotmail.com

Several scientists consider that solid planetesimals were formed by contraction of rarefied preplanetesimals. Ipatov [1] and Nesvorny et al. [3] supposed that trans-Neptunian binaries were formed from rarefied preplanetesimals (RPPs). Ipatov [1] obtained that the angular momenta acquired at collisions of RPPs moving in circular heliocentric orbits could have the same values as the angular momenta of discovered trans-Neptunian and asteroid binaries. Ipatov showed [2] that the angular momenta used by Nesvorny et al. [3] as initial data in their calculations of contraction of RPPs and formation of binaries could be obtained at collisions of two RPPs moving in circular heliocentric orbits. These studies testify in favor of the existence of the stage of rarefied preplanetesimals. The fraction of preplanetesimals collided with other preplanetesimals during their contraction can be about the fraction of small bodies of diameter d>100 km with satellites (among all such small bodies), i.e., it can be about 0.3 in the trans-Neptunian belt. The model of collisions of RPPs explains negative angular momenta of some observed binaries, as about 20% of collisions of RPPs moving in almost circular heliocentric orbits lead to retrograde rotation. Note that if all RPPs got their angular momenta at their formation without mutual collisions, then the angular momenta of minor bodies without satellites and those with satellites could be similar (but actually they differ considerably). In my opinion, those RPPs that formed TNOs with satellites acquired most of their angular momenta at collisions. Most of rarefied preasteroids could turn into solid asteroids before they collided with other preasteroids. Some present asteroids can be debris of larger solid bodies, and the formation of many binaries with primaries with diameter d<100 km can be explained by other models (not by contraction of RPPs). The model of growth of a RPP by accumulation of small objects moved in almost circular orbits does not explain a large difference between angular momenta of single and binary small bodies. For such model, all trans-Neptunian objects formed from such preplanetesimals would have satellites because the angular momentum of the preplanetesimal would be much greater than that for a single trans-Neptunian object.

[1] Ipatov S.I., *Mon. Not. R. Astron. Soc*., 2010, v. 403, 405-414
[2] Ipatov S.I., *Abstracts of 44th LPSC*, 2013, # 1488
[3] Nesvorny D., Youdin A.N., Richardson D.C., *Astron. J.,* 2010, v. 140, 785-793

ANALYSIS OF SULFUR OXIDES CONTENT ABOVE VENUS' CLOUDS.

D.A. Belyaev[1,2], O.I. Korablev[1,2], A.-C. Vandaele[3], A.A. Fedorova[1,2], F. Montmessin[4], E. Marcq[4], J.-L. Bertaux[4], M. Luginin[1,2], D. Evdokimova[1];
[1]Space Research Institute RAS, Moscow, Russia; [2]Moscow Institute of Physics and Technology, Russia; [3]BIRA/IASB, Brussels, Belgium; [4]LATMOS CNRS, Guyancourt, France. Contact: dbelyaev@iki.rssi.ru

Introduction:

Sulfur compounds are key components of Venus' atmosphere because the planet is totally covered by H_2SO_4 droplets clouds at altitudes 50–70 km. Any significant change in the SO_x oxides above and within the clouds affects the photochemistry in the mesosphere (70-120 km). Very recent papers about sulfur dioxide (SO_2) on Venus provoked more questions than gave answers concerning SO_2 behavior above the clouds. Belyaev et al. (2012) reported detection of two SO_2 abundance layers from Venus Express (VEX) solar occultations: 0.02-0.1 ppm at 65-80 km and 0.1-1 ppm at 90-100 km with negligible content at 80-90 km. This structure of vertical profile was confirmed by photochemical models, where existence of the upper layer is described as a result of possible sulfuric acid photolysis (Zhang et al., 2012). Nevertheless, study of H_2SO_4 content above the clouds disputed this version of SO_2 production (Krasnopolsky et al., 2011; Sandor et al., 2012). Another source – oxidation of S_x – is discussed to be less possible. Generally speaking, all measurements (ground based (Krasnopolsky et al., 2010; Sandor et al., 2010); VEX nadir (Marcq et al., 2012); our VEX occultations) show high variability of SO_2 mixing ratios, especially in the lower layer. Goal of the present paper is an analysis of several puzzles that arose as results of SO_2 exploration on Venus. We also present here our recent SO_x results from solar and stellar occultation measurements by SPICAV-SOIR instrument onboard VEX orbiter.

Acknowledgements:
Our work is supported by the Program №22 of RAS, RF President Grant МК-3820.2012.2, and grant of the Russian Government to MIPT. We also thank our colleagues: A. Mahieux (BIRA, Belgium) for SOIR data analysis; and X. Zhang (CalTech, USA) for modeling of SO_x photochemistry.

References:

Belyaev D. et al., 2012. Vertical profiling of SO_2 and SO above Venus' clouds by SPICAV/SOIR solar occultations. Icarus 217, 740–751.
Krasnopolsky V.A., 2010. Spatially-resolved high-resolution spectroscopy of Venus. 2. Variations of HDO, OCS, and SO_2 at the cloud tops. Icarus 209, 314-322.
Krasnopolsky V.A., 2011. Vertical profile of H_2SO_4 vapor at 70–110 km on Venus and some related problems. Icarus 215, 197–203.
Marcq E. et al., 2012. Variations of sulphur dioxide at the cloud top of Venus's dynamic atmosphere. Nature Geoscience, DOI: 10.1038/NGEO1650.
Sandor B.J. et al., 2010. Sulfur chemistry in the Venus mesosphere from SO_2 and SO microwave spectra. Icarus 208, 49–60.
Sandor B.J. et al., 2012. Upper limits for H_2SO_4 in the mesosphere of Venus. Icarus 217, 839–844.
Zhang X. et al., 2012. Sulfur chemistry in the middle atmosphere of Venus. Icarus 217, 714–739.

OBSERVATIONS OF THE NEAR-IR NIGHTSIDE WINDOWS OF VENUS DURING MAXWELL MONTES TRANSITS BY SPICAV IR ONBOARD VENUS EXPRESS

A. Fedorova[1,2], B. Bézard[3], J.-L. Bertaux[4], O. Korablev[1,2], C.Wilson[5],
[1]Space Research Institute (IKI), Moscow, Russia; [2]Moscow Institute of Physics and Technology (MIPT), Dolgoprudny, Russia; [3]LESIA, Observatoire de Paris, section de Meudon, CNRS, Meudon, France; [4]LATMOS-UVSQ, Guyancourt France; [5]Department of Atmospheric, Oceanic, and Planetary Physics, Oxford University, U.K.

One of the difficulties in modeling of Venus' nightside windows is an additional CO_2 continuum opacity due to collision-induced CO_2 bands and/or extreme far wings of strong allowed CO_2 bands. Characterization of the CO_2 continuum absorption at near-IR wavelengths and also search for a possible vertical gradient of water near the surface require observations over different surface elevations. The largest change of altitudes occurs during a passage above Maxwell Montes at high northern latitudes.

In 2011 and 2012 the SPICAV IR performed two sets of observations over Maxwell Montes during 8 and 6 orbits, respectively, in the 1.10-, 1.18- and 1.28-μm windows with a variation of surface altitude from -2 to 9 km. The 1.28-μm window do not probe down to the surface and were used to characterize the cloudiness during the observations. The observations in 2011 were not successful due to the low solar zenith angle during the passage over Maxwell Montes (<95°) and solar light contamination of spectra.

We will present results on the CO_2 continuum absorption for the 1.10- and 1.18-μm windows and an investigation of the H_2O mixing ratio gradient from the SPICAV data.

NOCTURNAL VARIATIONS OF THE VENUS UPPER CLOUD SCALE HEIGHT

A. Longobardo[1], E. Palomba[1], D. Grassi[1], A. Migliorini[1] , G. Piccioni[1], P.Drossart[2]
[1] IAPS-INAF, via Fosso del Cavaliere 100, 00133 Rome, Italy; [2] LESIA, Observatoire de Paris, CNRS, Université Pierre et Marie Curie, 92195 Meudon, France,
Contact: andrea.longobardo@iaps.inaf,it

The infrared spectrum of the Venus nightside is opacity-dominated at wavelengths lower than 3 μm and only some narrow transmission windows are detectable (Meadows and Crisp, 1996). From 3 μm to 5 μm, the continuum thermal emission dominates the Venus spectra. This emission comes from the upper cloud region, located at altitudes between 62 and 73 km (Esposito et al., 1983).

Therefore studies of the 3-5 μm spectral region would help to infer some properties of the upper layer of the Venusian clouds. In particular, the limb darkening effect observed at these wavelengths, i.e. the brightness temperature decrease at increasing emission angle, is related to cloud scale height and mesospheric lapse rate. According to the radiative transfer model developed by Diner (1978), the following relation occurs:

$$T = T_0 + C \ln \cos \theta \qquad (1)$$

where T and the T_0 are the observed and the brightness temperature respectively, θ is the emission angle and C is the product between the lapse rate Γ of the upper cloud region and the cloud scale height H. The application of Eq. (1) to NIMS-Galileo data gave H=4.1±0.6 km at equatorial latitudes (Roos et al., 1993). A similar result was obtained on VIRTIS-Venus Express data (Longobardo et al., 2012).

Otherwise, that no limb darkening has been observed poleward of 60°S, due either to a very low scale height (i.e. <1 km), a very low lapse rate or both (Longobardo et al., 2012). Moreover, the average H value retrieved between 60°S and 50°S is affected by a large uncertainty, because of the strong lapse rate variations in this region, not only with latitude, but also with local time (Grassi et al., 2011; Migliorini et al., 2012).

This work aims to take into account these variations and to monitor the upper cloud scale height during the night-time, by applying Eq. (1) to VIRTIS observations of the Venus nightside at different latitudes and local times.

In particular, 1725 VIRTIS hyperspectral images (Piccioni et al., 2007) at high exposure time (i.e. 3.3 and 8 seconds) have been considered. Prior to analysis, spectra were reduced, by obtaining a more refined spectral calibration and by removing the contribution of scattered Solar light (Longobardo et al., 2012). We focused on observations at

The analysis has been performed on observations taken at two wavelengths in the thermal continuum spectral range, i.e. 3.72 μm and 4.00 μm, at different latitude and local time intervals. The three considered latitude ranges are: near-equatorial latitudes (50°S to 0°), where a constant scale height is expected, middle latitudes (60°S to 50°S), within which scale height could vary, and near-polar latitudes (70°S to 60°S), where it is not expected to observe limb darkening. The three considered local times intervals are: early night (19:30-22:30), middle night (22:30-1:30) and late night (1:30-4:30). Since the parameters of Eq. (1) can change with the atmospheric height (i.e. with brightness temperature), ten brightness temperature intervals were empirically defined (according to the procedure exposed in Longobardo et al., 2012) for each wavelength, latitude and local time. By means of least squares technique, we obtained twenty estimates of the C parameter (ten for every considered wavelength) at every latitude and local time interval considered. Scale height can be obtained dividing C for the lapse rate Γ of the upper cloud region. To infer Γ, a grid of atmospheric thermal profiles at different latitudes and local times has been developed, basing on procedure described in Grassi et al. (2011) and Migliorini et al. (2012).

The scale height retrieval is currently in progress. Linear fits of observed temperature T as function of are very good at near-equatorial latitudes (Figure 1) and no trend of C with local time is observed. At near-polar latitudes Eq. (1) does not work whatever the local time interval considered (Figure 2) Conversely, at middle latitudes, the C value and the goodness of fit decrease from early to late night. In other words, at later local times the upper cloud region at middle latitudes tends to become similar to near-polar latitudes. Since latitudes between 70°S and 60°S are characterised by the presence of a cold collar (Zasova et al., 2007), these results would suggest a cold collar extension toward middle latitudes in the late night, according to observations of Grassi et al., (2011)

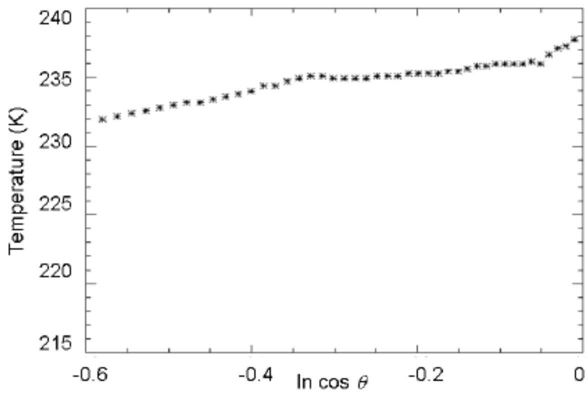

fig. 1. Observed temperature at near-equatorial latitudes, in the early night and at 3.72 μm, as function of . A clear linear relation occurs between the two quantities.

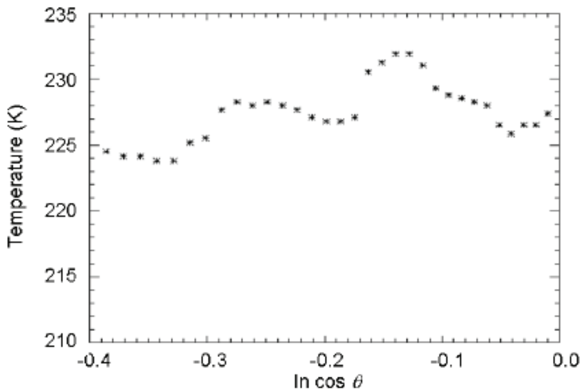

fig. 2. Observed temperature at near-polar latitudes, in the early night and at 3.72 μm, as function of . No dependence of temperature on emission angle arises.

References:

Diner, D. (1978), *J. Atm. Sci.*, 35, 2356-2361
Esposito, L. et al. (1983), In: *Venus*, Univ. Arizona Press, Tucson, AZ, pp. 484-564
Grassi, D. et al. (2011), *Journal of Geophysical Research*, 115, E09007, doi:10.1029/2009JE003553
Longobardo, A. et al. (2012), *Planetary and Space Science*, 69, 1, 62-75
Meadows, V. and Crisp, D. (1996), *Journal of Geophysical Research*, 101, 4595- 4622
Migliorini, A. et al. (2012), *Icarus*, 217, 2, 640-647
Piccioni, G. et al. (2007), *ESA-SP-1295*
Roos, M. et al. (1993), *Planetary and Space Science*, 41, 7, 505-514
Zasova, L.V. et al. (2007), *Planetary and Space Science*, 55, 1712-1728

RESULTS OF COMPARISON OF MORPHOMETRIC PARAMETERS OF THE DOME-SHAPED RISES AND ASSOCIATED RIFT ZONES ON VENUS (ATLA, BETA-PHOEBE) AND EARTH (EAST AFRICA).

E. N. Guseva,
Vernadsky Institute, Moscow, 11999, Russia. Contact: guseva-evgeniya@ya.ru

Introduction: Rift zones of Venus (Atla and Beta-Phoebe) and continental rift zones of the Earth (East Africa) are spatially associated with large regional dome-shaped rises [1-3] and likely related to mantle diapirs [4-6].

The morphometric parameters of the terrestrial domes depend on: 1) the strength of the lithosphere (its flexure stiffness), 2) diameter of the diapir interacting with the lithosphere, 3) their rate of uplift, and 4) the erosion rate [7].

In this study, I compare the morphometric parameters of the rift-bearing, dome-shaped rises on Venus and Earth in attempt to put constraints on characteristics of either thermal or mechanical (elastic) lithosphere of Venus.

Observations and results: The studied rift systems of Venus (Beta, Atla-Phoebe) and Earth (East African rifts) are and comparable in their dimensions (several thousands of kilometers) [8] and consists of structures of the same type and origin: graben and series of complicating secondary faults.

The rifts of Atla (NW, SE and SW branches) are spatially confined to the Atla dome. The height of the dome is estimated to be from ~ 2.5 to ~ 4.2 km (Tabl. 1). The horizontal dimensions of the dome are from ~ 1200 km to ~ 1600 km; the aspect ratio (K=height*1000/diameter) is ~ 3.2 (estimated from topographic profiles). The rifts of Atla often have a complex shape with left-sided asymmetry of the flanks (Tabl. 2). The depth of the rift of Atla Regio is ~ 2.5±1.2 km and an average width of ~ 243.3±94 км.

The height of the rise that hosts the rifts of Beta-Phoebe Regio (N, SW, S branches) varies from ~ 2.1 to 5 km (Tabl. 1) and its horizontal dimensions vary from ~ 2000 to 2500 km; the aspect ratio is ~ 2.2 (estimated from topographic profiles). The rifts of Beta-Phoebe Region, as well as the rifts of Atla region have a complex shape with left-sided asymmetry of the flanks (Tabl. 2). The depth of the studied rift of Beta-Phoebe Region is ~ 2.2±1.4 km and an average width of ~ 212.5±75 км.

Ethiopian rift is spatially confined to the Ethiopian dome. The height of the dome is from ~ 1.8 to 3.5 km according to different estimates (Tabl. 1). Diameter of the dome varies from ~ 690 to 1000 km; the aspect ratio is ~ 2.7 (estimated from topographic profiles). Ethiopian rift has V-shaped profile with left- and right-sided asymmetry of flanks (Tabl.2). The depth of the rift is about ~ 2.3±0.4 km (including sediment thickness of ~ 0.5 to 1 km, [8]), its average width of ~ 127.6±43.5 km.

The height of the Kenyan dome varies from a ~1.5 to 3.7 km (Tabl. 1) and its horizontal dimensions are ~ 416 by 1000 km; the aspect ratio is ~ 4.3 (estimated from topographic profiles). Kenyan rift often has V-shaped profile with a left-sided asymmetry of the flanks, less complex and trough-shaped form (Tabl. 2). The depth of the rift is ~ 3.1±0.5 km (including sediment thickness ~ 3 км [8-9]), its average width of ~ 92.3±33.8 km.

Conclusions: Venusian domes of Atla and Beta-Phoebe Regiones characterized by large diameters and high altitudes compared to the Earth domes – Ethiopian and Kenyan. The aspect ratios of the domes of the Atla Regio and Kenyan rift are higher than the ratios for the domes of the Beta-Phoebe Region and Ethiopian rift. Despite the fact that, the aspect ratios of the Beta-Phoebe and Ethiopian domes are roughly comparable to each other, the diameter of the dome of Beta-Phoebe is twice as much as that of the Ethiopian dome.

The studied domes of Atla and Beta-Phoebe Regiones are about two times larger than the domes of the East African rifts zone. The aspect ratio of the domes is comparable for Atla Regio and Kenyan rift. Thus, formation of the dome-shaped rises and rifting in the Venusian regiones of Atla and Beta-Phoebe probably had occurred in areas where the lithosphere was at least as thick as that on Earth (~ 100 km). Although the studied rifts of Venus and Earth are comparable in their length, shape, and depth of the rift valleys, the width of the rifts on Venus, however, is approximately two times larger than that of the East African rifts. This is consistent with the hypothesis of the absence of the low-viscosity zone (the asthenosphere) in the upper portion of the mantle on Venus (e.g., [4]).

Thus, the morphometric differences of the terrestrial and Venusian dome-shaped rises and associated rift zones can be explained either by thicker lithosphere on Venus than that on Earth in East Africa, or by the larger diapirs interacting with the lithosphere in the Beta-Phoebe and Atla Regions, or both.

These preliminary conclusions require more detailed study and quantification and consideration of the other factors (e.g., lithospheric rigidity, the rate of the uplift, etc.) affecting the formation of the dome-shaped rises and subsequent rifting.

table 1. Morphometric parameters of the dome-shaped rises on Venus (Atla, Beta-Phoebe) and Earth (East Africa).

dome	diameter of dome (km), published data		diameter of dome average (km), estimates from profiles	height of dome (km), published data	height of dome average (km), estimates from profiles	K* estimates from profiles	thickness of lithosphere (km)
	min	max					
atla	1200 [10]	1600 [10]	1290	2.5 [10]	4.2	3.2	?
beta-Phoebe	2000 [11-12]	2500 [10-12]	2253	5 [12] 2.1 [10]	5	2.2	?
ethiopian	1000 [8]		690	2.5-3 [8] 1.8-3.5 [8] >2 [9]	1.9	2.7	100-40 [14]
kenyan	1000 [13]		416	3.7 [8] 3 [8] 1.5 [9]	1.8	4.3	

*K – the aspect ratio (K = height/diameter*1000).

table 2. Morphometric parameters of the rift zones on Venus (Atla and Beta-Phoebe) and Earth (East Africa).

planet	rift region	depth of rift[1], max (km)	width of rift, max (km)	shape of the rift valley	asymmetry of the rift valley
Venus	Atla	2.5±1.2	243.3±94	complex[2]	left-sided
	Beta-Phoebe	2.2±1.4	212.5±75	complex[2]	left-sided
Earth	Ethiopian rift	2.3±0.4	127.6±43.5	V-shaped	left- and right-sided
	Kenyan rift	3.1±0.5	92.3±33.8	V-shaped	left-sided

[1]the depth of the rift valley including sediment thickness [9; 15],
[2]complex shape of the rift valley characterized by a horst uplifts at the bottom and complicated numerous of the scarps on the flanks.

References:

[1] Milanovsky E.E. Continental rift zones. M.: Nedra, 1976. P. 279.
[2] Senske D.A., Schaber G.G., Stofan E.R. Regional topographic rises on Venus: Geology of western Eistla Regio and comparison to Atla Regio and Beta Regio, JGR, 1992. V.97, P. 13395-13420.
[3] Smrekar S.E., Stofan E.R., Kiefer W.S. Large volcanic rises on Venus//in Venus II, S.W.Bougher, D.M. Hunten, and R.J. Phillips eds., Univ. of Arizona Press Tucson, 1997. P. 845-878.
[4] Phillips, R.J. and M.C. Malin The interior of Venus and tectonic implications In: Venus Geology, Geophysics, Atmosphere, and Solar wind environment, D.M. Hunten, L. Colin, T.M. Donahue, and V.I. Moroz eds., Univ. Arizona Press Tucson, 1983. P.159-214.
[5] Nikishin A.M. *Rifting in the geological history of the Earth and the planets of the terrestrial group/ Diss*., 1992, V.2.
[6] Condie K.C. Mantle plumes and their record in Earth history. Cambr. Univ. Press, 2001. P 306.
[7] Withjack M. A convective heat transfer model for lithospheric thinning and crustal uplift, JGR, 1979. V.84, B6, P.3008-3022.
[8] Chorowicz J. The East African rift system. J. of Afr. Earth Sci, 2005. V.43, P. 379-410.
[9] East-African rift system. Beloussov V.V. et al. M.: Nauka, 1974. V.1, P.264.
[10] Stofan E.R. et al. Large topographic rises on Venus: Implications for mantle upwelling, JGR, 1995. V.100, E11, P.23,317-23,327.
[11] Basilevsky A.T., Head J.W. Beta region, Venus: Evidence for uplift, rifting, and volcanism due

to a mantle plume, Icarus. 2007. V.192, P. 167-186.
[12] Campbell D. B. et al. Venus: volcanism and rift formation in *Beta* Regio, *Science*, 1984. V.226, P.167-169.
[13] Saemundsson K. East African Rift Syste–an overview. Presented at Short Course III on Exploration for Geothermal Resources, 2008.
[14] Lobkovsky L.I, Nikishin A.M, Khain V.E Modern problems of geotectonics and geodynamics, M.: Nauchniy mir, 2004. P.*107*-175.
[15] Continental rifts. Ramberg I.B., Neumann E.-R. eds., M.: Mir, V.1, 1981, P.477.

STRUCTURE OF THE MULTI-RAY RADIO WAVE FIELD IN THE VENUSIAN IONOSPHERE: NUMERICAL SIMULATIONS WITH PARABOLIC DIFFRACTION EQUATION.

A.L. Gavrik[1], Ya. Ilyushin[2],
[1]Kotel'nikov Institute of Radio Engineering and Electronics, RAS, Fryazino branch, V. A. Vvedensky sq, 1, Fryazino, Russia., alg248@ire216.msk.su; [2]Moscow State University, Russia 119992 GSP-2 Moscow, Leninskie.
Contact: ilyushin@physics.msu.ru

Radio occultation technique is a very effective tool of remote sensing of planetary atmospheres. Practice of development of new advanced methods of experimental data analysis, suitable for lower ionosphere investigations, has shown the need for high ratio between refractive effects and instrumental errors. To investigate fine structure of the lower ionosphere utilization of decameter wave band is preferable. In this case, an informative variation of the signal parameters in the planetary plasma environment is significantly larger than instrumental phase fluctuations due to limited accuracy onboard local oscillator. However, strong refraction of the lower frequency signal can lead to violation of the geometrical optics applicability conditions, on which radio occultation interpretation techniques are based.

There are presented the results of numerical simulations of radio occultation experiment with ground based transmitter and on-board receiver of coherent signals (e.g. Fig.1.). By direct numerical solution of the parabolic wave equation [1] variations of the wave field parameters along the spacecraft trajectory are investigated. The modeling results are validated with the experimental data from the Venera 15 and 16 spacecrafts. Basic attention is paid to the analysis of radio physical effects caused by the wave diffraction in thin ionized layers near the lower boundary of the Venusian ionosphere.

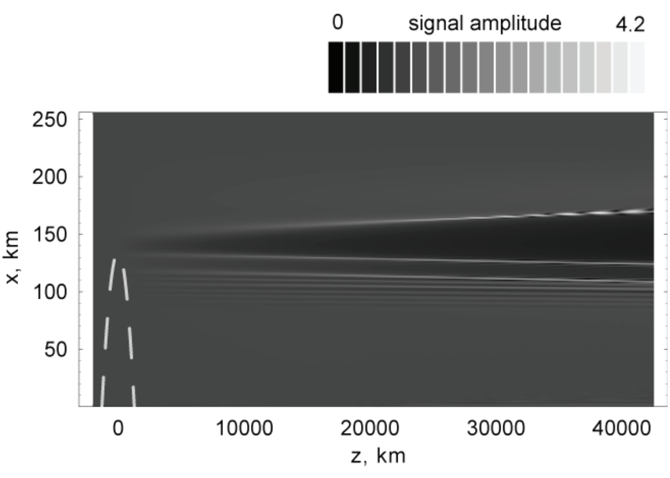

fig. 1. Wave amplitude distribution in the simulation domain. White dashed line marks the maximum of ionosphere of Venus. Focusing regions are clearly seen in the right part of the figure.

Experimental data, acquired with Venera 15 and 16 spacecrafts, suggest the possibility to study multi ray wave propagation and diffraction effects, appearing at 32 cm wavelength in the spherically symmetric ionosphere. Simulation results revealed the criteria, allowing checking validity of geometrical optics approximation from the experimental data of thin ionospheric layer sounding. It has been shown that the linear relation between periodical frequency and energy deviations observed in the experiment of the lower ionosphere sounding, proves the absence of multi-ray wave propagation or diffraction effects, so it is caused by the wave refraction during the wave propagation through the stratified multi-layered periodical plasma structure.

The work is partially supported by the RAS Presidium Program № 22.

References.

[1]. Ya.A. Ilyushin Fluctuations of the GPS signals on the tangential paths in the lower terrestrial atmosphere: influence of the small-scale structure. Journal of Atmospheric and Solar-Terrestrial Physics 70 (2008) 1863-1869. doi:10.1016/j.jastp.2008.05.020

SIZES OF PARTICLES IN THE UPPER CLOUDS OF VENUS FROM THE SPICAV/VEX POLARIMETRY

E. V. Petrova[1], A. A. Fedorova[1,2], O. I. Korablev[1,2], J.-L. Bertaux[3],
[1]Space Research Institute RAS, Profsoyuznaya 84/32, Moscow, 117997, Russia. [2]Moscow Institute of Physics and Technology (MIPT), 9 Institutsky dr., 141700 Dolgoprudny, Moscow Region, Russia. [3]LATMOS – UVSQ/UPMC/CNRS, 11 bd d'Alembert, 78280 Guyancourt, France. Contact: epetrova@iki.rssi.ru

In due time, polarimetric studies of Venus with ground-based telescopes and from the Pioneer Venus orbiter yielded the key information on the sizes, shape, and refractive index of particles in the upper clouds and hazes of the planet. The SPICAV IR instrument onboard the Venus Express orbiter provides the measurements of two components of light polarized in orthogonal directions, i.e., the degree of polarization is recorded in addition to the total flux in the SPICAV IR spectral range (from 650 to 1700 nm). SPICAV observations allow the phase dependences of intensity and polarization scattered by a specified region on the cloud top to be measured.

We considered the phase profiles of intensity and polarization measured by SPICAV at phase angles from 5° to 50° in three wavelengths (λ=756, 982, and 1101 nm) during one of the orbits near the equator at the local noon. We compared these profiles to the models calculated with the vector radiative transfer procedure for different values of radii (1.0-1.4 μm) and real refractive indices (1.43-1.49) of particles in the clouds. The specified ranges of the parameters as well as the spherical shape were chosen according to the results of the previous measurements.

We found that the shape of the phase profile of intensity, especially the angular position of the interference feature at small phase angles, is consistent with the effective radius of cloud particles 1.2 μm. This value well agrees with the estimate obtained from the phase profile of intensity measured by the VMC camera at λ=965 nm in the same region. However, the value of the radius providing the fitting of the phase profiles of polarization in all considered wavelengths is somewhat smaller, 1.0 μm. Since the polarization state is known to be formed in first several scattering events, we may expect that the estimate yielded from the polarization phase curve is referred to the higher cloud layers than that from the intensity phase curve. Thus, the analysis of the simultaneous measurements of intensity and polarization performed by SPICAV allowed us to confirm that the particle sizes decrease with altitude in the upper clouds of Venus. Our modeling also showed that, to provide the agreement with the measured profiles, one should assume the presence of submicron particles within the clouds and/or above them.

THERMAL STRUCTURE OF THE VENUS NIGHT SIDE, RETRIEVED ON VIRTIS/VENUS EXPRESS DATA

A. Migliorini[1], D. Grassi[1], G. Piccioni[1], P. Drossart[2], L. Zasova[3],
[1]INAF-IAPS, Via Del Fosso del Cavaliere, 100, Roma, Italy; [2]LESIA-Observatory of Paris, Place J. Jansen, 5, Paris, France; [3]IKI, Space Research Institute, Russian Academy of Science, Moscow, Russia. Contact: alessandra.migliorini@iaps.inaf.it

Introduction:

Atmospheric temperature of the night side of Venus is investigated using remote sensing data acquired with the VIRTIS (Visible and Infrared Thermal Imaging Spectrometer) instrument on board the European Venus Express mission. The northern and southern hemispheres of the planet are explored in the pressure range from 100 to 1 mbar. In the analyzed data, the same behavior is observed on both hemispheres, though the coverage in the North is sparse. On the other hand, differences between the dusk and dawn sides are observed in the temperature values, the dawn being the coldest quadrant in the pressure range 100 to 12 mbar. The cold-collar feature is detected around 60-70° on both hemispheres. This region is on average 15 to 20 K colder than the temperature at the pole at 100 mbar (about 65 km), also showing a significant thermal inversion. A peculiar pattern of maxima and minima in temperature is observed at 100 and 12 mbar. These features can be interpreted as indication of diurnal and/or semidiurnal thermal tides, as it results from the Venus global circulation model (Lebonnois et al., 2010b) of the Laboratoire de Météorologie Dynamique (LMD). Some results are shown in figure 1, at polar and mid latitudes. Temperature decreases with pressure at the considered latitude values, while some variability is observed at 50°S in the pressure range 10 mbar to 1 mbar.

Thermal variation with respect to local time is also taken into account. The results here presented can provide important hints for an update of the VIRA model, based on in situ measurements by Venera spacecrafts, the four Pioneer Venus probes and the Pioneer Venus Orbiter.

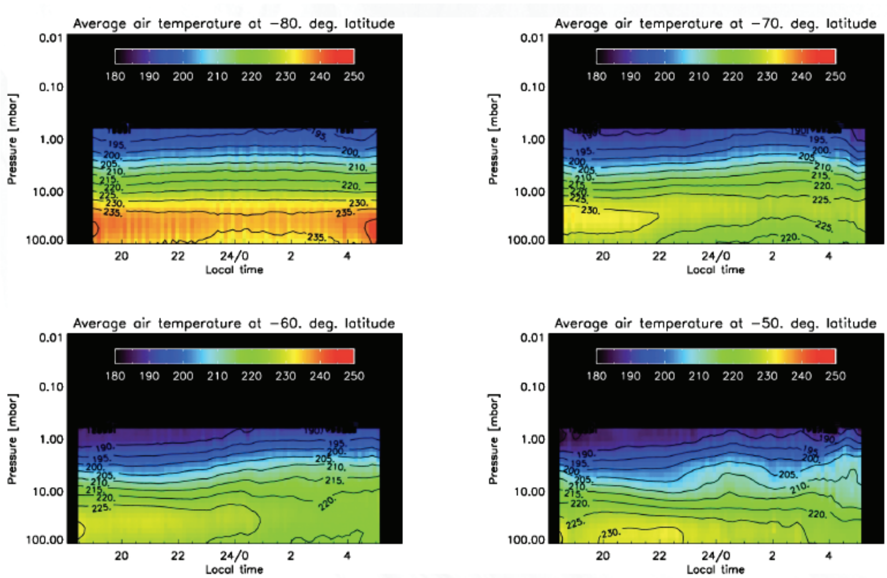

fig. 1. Temperature variation at selected latitude values.

DATABASE OF VENUS-15 AND VENUS-16 RADIO OCCULTATION EXPERIMENTS.

E.A. Kuleshov, A.A. Smislov, A.L. Gavrik,
Kotel'nikov Institute of Radio Engineering and Electronics, Russian Academy of Sciences, Fryazino branch, V. A. Vvedensky sq, 1, Fryazino, Russia., alg248@ire216.msk.su

Introduction

One of the imperative tasks today is building information resources which provide wide access to the experimental data from multiple space missions. European (ESA) and US (NASA) space agencies regularly add new data to their databases, which when modern methods of processing are applied to the data of previous, completed missions, become means of extraction of new knowledge about objects in the Solar system. However existing resources offer almost no results of the double frequency occultaion measurements of the Venus atmosphere conducted by the Soviet Venus-15 and Venus-16 spacecraft in a number of experiments (170 occultaions in 1983-1984). These data allowed us to obtain 73 electron concentration profiles in daytime ionosphere, 20 terminator profiles and 62 nighttime profiles at Sun zenith angles between 50 and 160 degrees [1]. Parameter variations of two coherent radio signals (at wavelenths of 32 and 8 centimeters) offer a unique opportunity for the research into low-density plasma in nighttime ionosphere and in the lower regions of the daytime ionosphere of Venus.

This presentaton will discuss an information system developed in our group, which is based on a relational database containing experimental data from the occultation experiments in Venus-15 and -16 missions and provides a user environment/software for data access, analysis and graphical display.

Structure of the Information System

The database contains the major portion of the experimental data and references to files with raw data for each session in the occultation experiment. Data files are kept in several formats. Processing of these data with modern techniques adds new files expanding the collection. These data will be placed for storage on a remote FTP server, and wide access to it will be granted after the initial testing period is completed. Each occultation experiment/session is described by a number of files which supply full details, i.e.:

1. Describe the data format;
2. Amplitude measurements of the two radio signals at ground stations;
3. Power and frequency of the two radio signals.
4. Ballistic data and other information about details and conditions during the experiment;
5. Data on parameter variations of the radio signals during the session;
6. Calculated electron concentration profiles as a function of altitude;
7. Calculated characteristics of fine structure of the Venus ionosphere;
8. Error ranges for the above data and calculated results.

The supplied user-end software implements a number of standard operations for access to and user interaction with data, such as data search, editing, addition or deletion, copying etc. The software facilitates various processing methods and provides graphical display of data. Program output can be saved in one or several files as text or plots.

Acknowledgements: The work is partially supported by the program No.22 of the Presidium of RAS, “Fundamental problems of the research and exploration of the Solar system”.

Reference

[1]. N.A. Armand et al. Results of solar wind and planetary ionosphere research using radiophysical methods // Physics-Uspekhi. 2010. V. 180. № 5. P. 517-523.

DUST COMPLEX OF THE EXOMARS-2018 PROJECT

A.V. Zakharov[1], G.G. Dolnikov[1], V.N. Barke[1], V.V Afonin[1], I.A. Kuznetsov[1], A.N. Lyash[1], I.A. Shashkova[1], A.V. Yakovlev[1], A.A. Venkstern[1], F. Esposito[2], C. Molfese[2], E. Seran[3], M. Godefrov[3], O.F. Petrov[4], E.A. Lisin[4], S.N. Popel[5], N.D. Borisov[6], E.A. Vorobieva[7],
[1]Space Research Institute (IKI), 117997, 84/32 Profsoyuznaya Str, Moscow, Russia, [2]INAF – Osservatorio Astronomico di Capodimnte, Napoli, Italy, [3]LATMOS, Guyancourt, France, [4]Joint Institute for High Temperatures of the Russian Academy of Sciences (JIHT RAS), Moscow, Russia, [5]Institute of Geosphere Dynamics (IDG RAS), Moscow, Russia, [6]Institute of Earth magnetism, ionosphere and radiowaves propagation named after Nikolay Pushkov of the Russian Academy of Sciences (IZMIRAN), Troitsk, Russia, [7]Moscow State University, Moscow, Russia,
Contact: ggd@iki.rssi.ru

Introduction:

Martian atmosphere contains a significant load of suspended dust. Its amount varies with seasons and with the presence of local and global dust storms, but never drops entirely to zero. Airborne dust contributes to determine the dynamic and thermodynamic evolution of the atmosphere, including large scale circulation processes, on diurnal, seasonal and annual time-scales.

It plays a key role in determining the current climate of Mars and probably influenced the past climatic conditions and surface evolution. Under certain conditions, wind and dust can trigger dust storms on a planetary scale which continuing for 4 - 5 months. Probability of such storms during the Martian year estimated of 1 to 3. Of great interest is also the phenomenon of “dust devils” that generates electric field of intensity, according to various estimates, up to 160 kV/m.

Moreover, wind and windblown dust are the most important currently active surface modifying agents on Mars. They are responsible for erosion, redistribution of dust on the surface and weathering. Wind mobilized particles on Mars range in size from less than 1 μm, for suspended dust, to perhaps as large as 1 cm in diameter. The mechanisms for dust entrainment in the atmosphere are not completely understood as the data available so far do not allow us to identify the efficiency of proposed processes.

Only a model proposed by Renno and Kok [1] and takes into account the possible occurrence of the electric field due to the processes of saltation, showing results which agreed with observations.

Despite the great interest shown in these phenomena and the high scientific and technological importance of these studies, direct measurements of transport of dust on the surface of Mars have not been conducted yet.

An instrument to study dust activities on Mars named Dust Complex (DC) was suggested to be included in the ExoMars payload.

The dust complex is a suite of 3 sensors devoted to the study of Aeolian processes on Mars: 1) an Impact Sensor, for the measurement of the sand grain dynamics, 2) a particle counter sensor, MicroMED, for the measurement of airborne dust size distribution and number density, and 3) an Electric Probe, for the measurement of the electric field at the surface of Mars. Its primary aim is to monitor the dust cycle by direct measurements of dust flux at the surface of Mars.

The presentation tells about the Dust Complex and the specifics of his work. Describes an interaction with other projects from the scientific payload of the ExoMars-2018 mission landing platform. It also describes the possible effects associated with the Martian dust and negative consequences for the study and development of Mars arising from these phenomena.

References:

J. F. Kok and N. O. Renno, J. Geophys. Res. 114, D17204 (2009).

DUST INSTRUMENT FOR THE LUNAR LANDERS

A.V. Zakharov[1], G.G. Dolnikov[1], V.N. Barke[1], I.A. Kuznetsov[1], A.N. Lyash[1], V.V. Afonin[1], A.A. Venkstern[1], I.A. Shashkova[1], A.V. Yakovlev[1], O.F. Petrov[2], E.A. Lisin[2], S.N. Popel[3], N.D. Borisov[4], E.A. Vorobieva[5],
[1]Space Research Institute (IKI), 117997, 84/32 Profsoyuznaya Str, Moscow, Russia, [2]Joint Institute for High Temperatures of the Russian Academy of Sciences (JIHT RAS), Moscow, Russia, [3]Institute of Geosphere Dynamics (IDG RAS), Moscow, Russia, [4]Institute of Earth magnetism, ionosphere and radiowaves propagation named after Nikolay Pushkov of the Russian Academy of Sciences (IZMIRAN), Troitsk, Russia, [5]Moscow State University, Moscow, Russia, Contact: ggd@iki.rssi.ru

Introduction:

One of the most interesting phenomena, located on Moon, is its dusty exosphere. Dusty particles might seriously harm (and even break down!) scientific and engineering systems as well as create a glow whose picture was taken in 1968 by Surveyor 7, and in 70s an astronauts seen it themselves. Estimation of glow intensity increased by ~10^7 times of predicted effect of micrometeorites bombarding the Moon surface. It could be explained by electrostatic particle levitation phenomenon.

Regolith properties (density, temperature, composition, etc.), as well as close to the surface lunar exosphere is strongly dependent on the solar activity, the local lunar time, the position of Moon relative to the Earth’s magnetotail.

The top layer of regolith (a few meters) is an insulator, which is charged by solar UV radiation and the constant bombardment of charged particles and creates a charge distribution on the the lunar surface: positive - on the sunlit side and negative - on the night side. The charge distribution depends on the local lunar time and electrical properties of regolith (the presence of water in the regolith can strongly influence the local distribution of charge).

The increased near-surface electric field strongly influences the dynamics and transport of the dust component of the lunar regolith, creating dusty exosphere near the Moon, which can reach tens of kilometers in altitude. The area of the lunar terminator and irregular surface (craters, rocks) can create peculiarities of the dynamics of dust, so-called “Moon Dust Fountains.”

In addition to medium-sized levitating particles, sources of flying above the lunar surface dust can be high-speed micrometeorites and secondary particles ejected as a result of micrometeorites collisions with surface of the Moon.

Thus, the need to study the lunar dusty exosphere settles by a number of reasons:

- From a scientific point of view - dust is a significant component of the lunar exosphere.
- From the point of technological safety - ubiquitous dust on the Moon. Since the 60’s scientific instruments, solar panels and mechanisms; and of course astronauts experienced by the detrimental effects of charged dust particles. In addition to this, the dust has strong adhesion, and its elimination from the work surfaces is not trivial.

So, we designed dust detector PmL, which is scheduled for launch to the Moon in the mission “Luna-Glob”, as well as the extended version in the mission “Luna-Resource”.

Dust detector includes:

- Impact Sensor to measure the momentum of the dust particles, the speed of their movements and their electrical charge.
- Electric field Sensor (2 pieces) to measure the potential difference of the electrostatic field near the surface of the moon.

Dust detector PmL will allow to measure characteristics of the dust component and its dynamics at the Moon’s exosphere, to estimate of the electric field near the surface of the Moon. Besides, it will allow to registrate of micrometeorites and secondary particles ejected of lunar regolith by micrometeorites, measuring their physical characteristics (weight, speed).

The presentation will describe the principles of development, calibration and operation of the Dust instrument.

VISTA, A MICRO-THERMOGRAVIMETER TO MEASURE WATER AND ORGANICS CONTENT IN PLANETARY ENVIRONMENT

E. Palomba[1], A. Longobardo[1], F. Dirri[1,2], E. Zampetti[3], D. Biondi[1], A.Boccaccini[1], B. Saggin[4], A. Bearzotti[3], A. Macagnano[3]
[1] IAPS-INAF, via Fosso del Cavaliere 100, 00133 Rome, Italy; [2] Dipartimento di Fisica, Università La Sapienza, Piazzale Aldo Moro, 9 , Rome, Italy; [3] IMM-CNR, Rome, Italy; [4] Politecnico di Milano, Milan, Italy,
Contact: ernesto.palomba@iaps.inaf,it

VISTA (Volatile In Situ Thermogravimetry Analyser) is a thermogravimeter developed by a consortium of Italian institutes, which aims to perform planetary in situ measurements. Its specific applications depend on the planetary environment under study, but the main goal is usually related to the water and organics detection in dust or aerosols, that can be linked to the habitability of the planetary body.

It is based on Thermogravimetric Analysis (TGA), a widely used technique to investigate condensation/sublimation and absorption/desorption processes of volatile compounds. The core of a thermogravimeter is a Piezoelectric Crystal Microbalance (PCM), which converts mass in frequency variations. The PCM temperature can be increased by an appropriate heater and when this occur the volatile component of the analysed sample desorbs, resulting in a frequency change. This frequency variation allows to infer the abundance of evaporated compound, whose composition can be inferred by its desorption temperature.

VISTA is based upon a lab-on-chip miniaturised sensor philosophy (Figure 1), since it has very small mass/volume and power requirements and needs a quite small amount of material for the analysis, i.e. less than 1 mg. The main innovation introduced by VISTA concerns the special design of the thermogravimeter, equipped with a built-in heater and a built-in thermistor, both controlled by proximity electronics. The thermistor can act as additional heater in parallel to the other: this special design dramatically reduces the total mass and the power required to perform thermal cycles. The VISTA overall technical characteristics are summarised in Table 1.

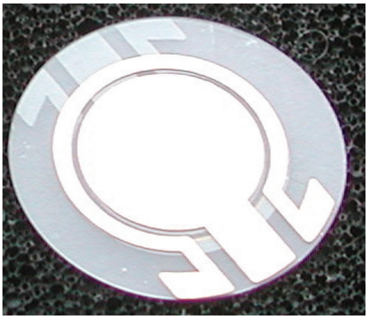

fig. 1. PCM equipped with built-in heater and built-in thermistor produced at IMM-CNR Facility Center.

VISTA technical characteristics	
Mass (g)	40
Volume (cm^3)	7
Resonance Frequency (MHz)	5.8
Accuracy (Hz)	4
Sampling rate (s^{-1})	5
Sensitivity (ng/Hz)	0.3
Saturation mass (μg)	~10
Crystal Diameter (mm)	14
Thickness (mm)	0.2

Table 1. VISTA technical characteristics.

VISTA can have a large range of applications in planetary in-situ measurements. Currently, it has been selected in the scientific payload of MarcoPolo-R, a proposed ESA mission addressed to a primitive asteroid. In this scenario, VISTA plans to measure the volatile content in the asteroid regolith. In particular, it will focus to detect water and organics, in order to give more physical insights about the astrobiologic potential of the primitive asteroid (Palomba et al., 2013)

In addition, it has been studied for Phase A of JUICE (JUpiter and ICy moons Explorer), in the framework of the a Penetrator Consortium, in order to perform in-situ measurements on the Europa and Ganymede surfaces, i.e. composition of non-ice materials, detection of clathrate hydrates and organics (Gowen et al., 2011).

Moreover, VISTA can find application on in-situ missions on Mars, where it can measure dust and ice settling rate, water content in dust, humidity (Palomba et al., 2011), on the Moon, for water ice detection and water/organics content in regolith (Longobardo et al., 2013), on Venus, where it would infer the dew point of cloud condensable species and the composition of refractory component of clouds (Wilson et al., 2011), and on Titan, in order to measure the methane dew point and the organics content in near-surface aerosols.

We developed a laboratory set-up (shown in Figure 2) in order to test the capability of the VISTA breadboard to measure the enthalpy of sublimation **ΔH, i.e. the amount of energy absorbed or released during a che**mical-physical process, of different carboxylic acids (i.e. adipic, oxalic, succinic, azelaic). Because of similar desorption temperatures of several volatile species, to measure this thermal property can necessary to characterize a volatile compound.

The sample and the PCM were placed inside a vacuum chamber, which would simulate an asteroidal environment. Then, the sample was heated and degassed, while the PCM was cooled down to about -72**°C by a cold finger, in order to allow the deposition of the gas molecules produced by the sublimation process. By measuring the rates of deposition on the PCM at different temperatures, it has been possible to infer the enthalpy of subl**imation ΔH of the sample from the Van't Hoff relation. The obtained results are in good agreement with literature, demonstrating the VISTA ability to perform this kind of measurements.

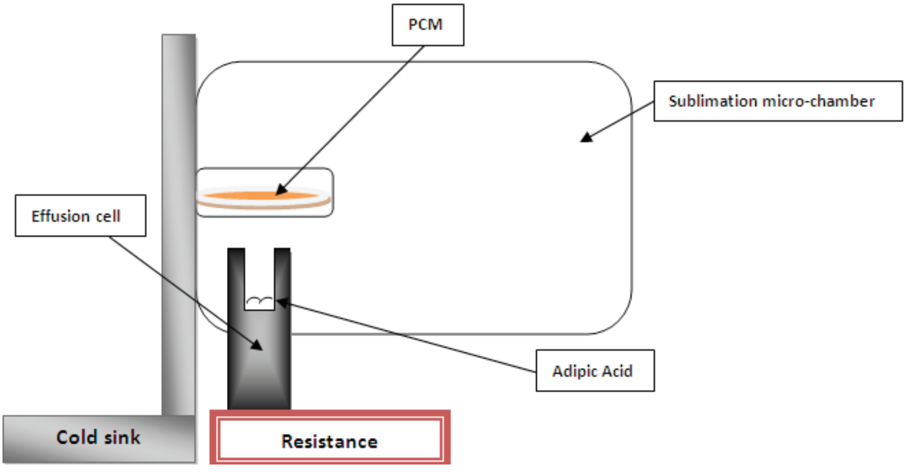

fig. 2. Schematic representation of the set-up used to measure the enthalpy of sublimation of adipic acid.

References
Gowen, R. A. et al. (2010), *Adv. Sp. Res.*, 48, 8, 725-74
Longobardo, A. et al. (2013), *44th LPSC*, 2204
Palomba, E. et al. (2011), *EPSC abstracts*, 87
Palomba E. et al. (2013), *EPSC abstracts*, 8, 619
Wilson, C.F. et al. (2011), *Experimental Astronomy*, 33, 2-3, 305-335;

MICRO-RAMAN SPECTROSCOPY OF A PARTICLE RA-QD02-0035 FROM A COLLECTION OF THE HAYABUSA SPACE PROBE TO THE 25143 ITOKAWA ASTEROID.

S. G. Pavlov [1], C. Alwmark [2], S. Bajt [3], U. Böttger [1], H. Busemann [4], J. D. Gilmour [4], U. Heitmann [5], H.-W. Hübers [1,6], M. M. M. Meier [2], U. Schade[7], N. H. Spring [5], I. Weber [5],

[1] Institute of Planetary Research, German Aerospace Center (DLR),Rutherfordstr. 2, 12489 Berlin, Germany; [2] Department of Geology, University of Lund, Sölvegatan 12, 223 62 Lund, Sweden; [3] Photon Sciences, DESY, Notkestr. 85, 22607 Hamburg, Germany; [4] University of Manchester, School of Earth, Atmospheric and Environmental Sciences (SEAES), Oxford Road, Manchester M13 9PL, UK; [5] Institut für Planetologie, Westfälische Wilhelms-Universität Münster, Wilhelm-Klemm-Str. 10, 48149 Münster, Germany; [6] Institut für Optik und Atomare Physik, Technische Universität Berlin, Straße des 17. Juni 135, 10623 Berlin, Germany; [7] Helmholtz-Zentrum Berlin für Materialien und Energie, Albert-Einstein-Str. 15, 12489 Berlin, Germany. Contact: sergeij.pavlov@dlr.de

The Hayabusa space probe is JAXA's first successful sample return mission (it is the first successful asteroid sample return mission – ever!) to the near-Earth asteroid 25143 Itokawa. By the touch-down landing in 2005 small soil particles have been sampled on the asteroid uppermost regolith layer and returned back to the Earth in 2010 [1]. In 2012 the project "The characterization of the asteroid Itokawa regolith - A correlated study by X-ray tomography, micro-Raman spectroscopy, and high-sensitivity noble gas analysis" led by H. Busemann [2] has passed a competition in "The First International Announcement of Opportunity for *HAYABUSA Sample* Analysis". Seven particles returned by Hayabusa mission have been allocated for the study. We report here results from micro-Raman spectroscopy of particle RA-QD02-0035 (further: #35).

Raman spectroscopy has been used for initial analysis of each of the Itokawa particles, as a nondestructive tool for a mineral phase analysis. The measurements were performed with a confocal microscopic system (WiTec alpha300R) with a spatial resolution of about 1.3 μm and spectral resolution of about 4/cm. Several positions have been selected on the flat-polished side of the particle formed during microtoming (Fig. 1).

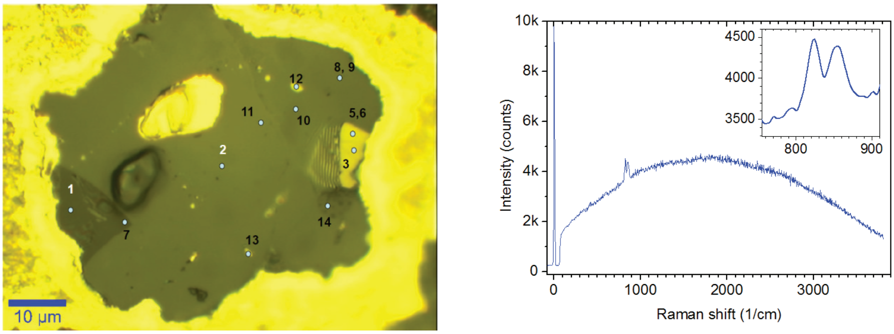

fig. 1. Left: Image of the of the sample #35 with shown locations selected for Raman spectroscopic analysis. Right: Stokes spectrum at the position 11, showing olivine; uncorrected background.

The Raman spectra indicate dominating Mg-rich olivine (when compared with calibration data for olivine [4]). This is consistent with ordinary LL chondrites [1]. The Raman spectra of small inclusions reveal goethite, the origin of which has not been clarified yet. Correlated study by Raman spectroscopy and X-ray tomography [3] allows reconstruction of spatially resolved mineral topographic images of an individual particle.

We thank Dr. Abe and JAXA for the allocation and efficient delivery of the particles.

[1] T. Nakamura et al., Science **333**, 1113-1116 (2011).
[2] H. Busemann et al., LPSC XLIV, Abstract #2243 (2013).
[3] M. M. M. Meier et al. LPSC XLIV, Abstract #1937 (2013).
[4] K. E. Kuebler, Geochimica et Cosmochimica Acta **70**, 6201-6222 (2006).

SOLAR IRRADIANCE SENSOR OF THE DREAMS-EDM EXOMARS 2016

L. Vázquez[1], S. Jiménez[4], M.L. Martín[5], F. Valero[2], A. Vicente-Retortillo[2], J.J. Jiménez[3], F.J. Álvarez-Ríos[3], I . Arruego[3], V. Apéstigue[3], J.M. Oter[3],
[1]Dept. Mat. Aplicada, Facultad de Informática, Universidad Complutense de Madrid, Spain; [2] Dept. Astrofisica y Física de la Atmósfera, Facultad de Ciencias Físicas, Universidad Complutense de Madrid, Spain; [3]Departamento de Cargas Útiles y Ciencias del Espacio, Instituto Nacional de Técnica Aeroespacial (INTA), Madrid, Torrejón de Ardoz, Spain; [4]Dept. Mat. Aplicada, E.T.S.I. Telecomunicación, Universidad Politécnica de Madrid, Spain; [5]Dept. Matemática Aplicada, E. U. Informática, Universidad de Valladolid, Spain. Contact: lvazquez@fdi.ucm.es

Introduction:

The Solar Irradiance Sensor (SIS-DREAMS) is one of the instruments of the meterological station DREAMS of the ExoMars Descent Module [1]. It measures the solar irradiance in three different spectral bands: [315nm - 400nm] (UVA), [700nm - 1100nm] (NIR) and [220nm - 1200nm] (Total illumination). It is based on the Solar Irradiance Sensor (MET-SIS) [2,3] of METNET, the Mars MetNet Mission [4].

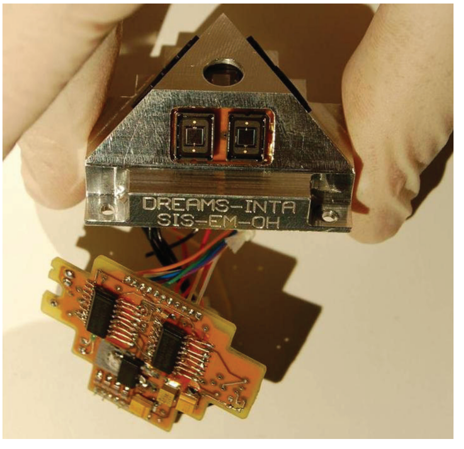

Radiative Transfer:

SIS-DREAMS will provide measurements which will allow us to adjust some radiative transfer codes by using local broadband data of interest. Some goals derived from determining the amounts of solar radiation transferred through the atmosphere on its way to the Martian surface would be useful to gain some insight into the following items under different atmospheric scenarios:

- UV irradiation levels at the bottom of the Martian atmosphere to use them as an habitability index.
- Incoming shortwave radiation and solar heating at the surface.
- Relative local index of dust in the atmosphere.

Measurements:

The instrument is mounted on a truncated tetraedron support with a similar array of two photodiodes for the UVA and NIR bands on each of the three lateral sides, and one sensor for total illumination on the top side covered by a semi-spherical diffusor and a 180º field of vision. With this disposition, the top sensor will measue total irradiance during the whole day, while the other sensors will measure either the direct or part of the diffuse irradiation as the Sun crosses the Martian sky.

The calibration process of the instrument cover the following points:

Responsivity. The sensors will be calibrated for different radiation intensities. A light beam, with a spectral distribution similar to that of the Sun, will incide ortogonally with different levels of intensity, ranging from 100 to 800 W/m**2** .

Angular response. The dependence of the measurements on the angle of the incident radiation will be determined for each of the four faces, with a given illumination power.

Thermal correction. To determine the behaviour under thermal variations, the instrument temperature will be set to cover the range between -110ºC and +35ºC, with a given illumination power.

Interpretations:

From the measurements taken from the sensors, we will reconstruct the signal by classical interpolation methods with Tchebyshev polynomials. These techniques have already being developed for the MSL irradiance sensor [5] both for ideal case (see [6]) and for the case where the sensors can suffer a modification in their response due to dust, alteration etc. (see [7]). We show in the graphic the reconstructed spectra from the ideal measurements of the black-body radiation.

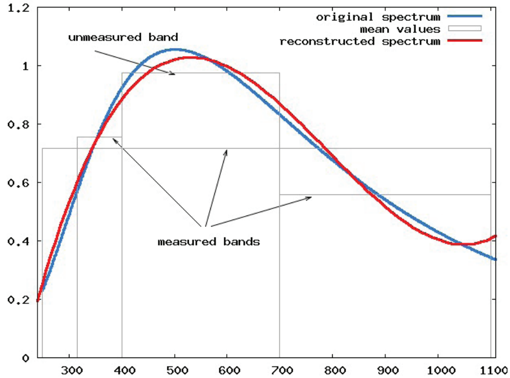

References:

[1] F. Esposito, S. Debei, C. Bettanini, C. Molfese, I. Arruego Rodríguez, G. Colombatti, A.-M. Harri, F. Montmessin, C. Wilson, A. Aboudan, M. Zaccariotto, S. Abaki, G. Bellucci, J.-J. Berthelier, J.R. Brucato, S. B. Calcutt, F. Cortecchia, F. Cucciarrè, G. Di Achille, F. Ferri, F. Forget, E. Friso, M. Genzer, P. Gilbert, J.-P. Goutail, H. Haukka, J.J. Jiménez, S. Jiménez, J-L. Josset, O. Karatekin, G. Landis, R. Lorentz, L. Marthy, J. Martinez, V. Mennella, D. Möhlmann, E. Palomba, M. Patel, J-P. Pommereau, C.I. Popa, S. Rafkin, P. Rannou, N.O. Renno, P. Schipani, W. Schmidt, E. Segato, F. Simoes, A. Spiga, F. Valero, L. Vázquez, F. Vivat, O. Witasse, S. Yahi, R. Mugnuolo, S. Pirrotta, "DREAMS for the ExoMars 2016 mission: a suite of sensors for the characterization of Martian environment", EPSC Abstracts Vol. 8, 2013.

[2] J.J. Jiménez, F. J. ÁLVAREZ-RÍOS, J.M. Oter, I.Arruego, J Azcue, M. González-Guerrero, I. Martín, G. Martínez, J. Moreno-Ventas, M. Reina, J. Rivas, C. Ruiz de Galarreta, L.M Sánchez-Brea J. Sánchez-Páramo, Alberto VALVERDE, L. Vázquez, H. Guerrero. "Sensor espectral de irradiancia solar para estudios atmosféricos planetarios". 7ª Reunión Española de Optoelectrónica – OPTOEL 2011. S1-50. Santander, España, 29 de Junio – 1 de julio 2011.
http://www.teisa.unican.es/optoel2011/images/stories/programa_optoel11.pdf

[3] I.Arruego, M. Díaz-Michelena, J.J. Jiménez, J. Martínez, V. Apéstigue, M. González-Guerrero, J. Azcue, A. Valverde, V. de Manuel, J. A. Domínguez, I. Martín, B. Martín, J. Alvarez, M. Alvarez, C. Hernando, M.F. Cerdán, C. Ruiz de Galarreta, J. Sánchez, G. Martínez, L. Vázquez, H. Guerrero, "Development of miniaturized instrumentation for Planetary Exploration and its application to the Mars MetNet Precursor Mission", Proceeding of the European Geosciences Union – 7th General Assembly, Vienna, Austria 02-07 May 2010. Geophysical Research Abstracts Vol. 12, EGU2010.
http://meetingorganizer.copernicus.org/EGU2010/EGU2010-13330.pdf

[4] See: http://metnet.fmi.fi

[5] J. Gómez-Elvira, C. Armiens, L. Castañer, M. Domínguez, M. Genzer, F. Gómez, R. Haberle, A.-M. Harri, V. Jiménez, H. Kahanpää, L. Kowalski, A. Lepinette, J. Martín, J. Martínez-Frías, I. McEwan, L. Mora, J. Moreno, S. Navarro, M.A. de Pablo, V. Peinado, A. Peña, J. Polkko, M. Ramos, N.O. Renno, J. Ricart, M. Richardson, J. Rodríguez-Manfredi, J. Romeral, E. Sebastián, J. Serrano, M. de la Torre Juárez, J. Torres, F. Torrero, R. Urquí, L. Vázquez, T. Velasco, J. Verdasca, M.-P. Zorzano, J. Martín-Torres, "REMS: The Environmental Sensor Suite for Mars Science Laboratory Rover", *Space Sci. Rev.* (2012) **170**:583-640.

[6] L.Vázquez, M.-P. Zorzano, S. Jiménez, "Spectral information retrieval from integrated broadband photodiode Martian ultraviolet measurements", *Opt. Lett*. **32**, 2596-2598 (2007).

[7] M.-P. Zorzano,L.Vázquez, S. Jiménez, "Retrieval of ultraviolet spectral irradiance from filtered photodiode measurements", *Inverse Probl.* **25**, 115023-115032 (2009).

USING *IN SITU* NEUTRON AND GAMMA-RAY SPECTROSCOPY TO CHARACTERIZE ASTEROIDS

J. G. Bodnarik[1,2], A. M. Parsons[3], J. S. Schweitzer[4], K. G. Stassun[1],
[1]Vanderbilt University, Dept. of Physics and Astronomy, 6301 Stevenson Center Ln., Nashville, TN 37235, USA; [2]University of Arizona, Lunar Planetary Laboratory, 1629 E. University Blvd, Tucson, AZ 85721, USA (contact author's current address); [3]NASA Goddard Space Flight Center, Code 691, Greenbelt, MD 20770, USA; [4]University of Connecticut, Laboratory for Nuclear Science, 2152 Hillside Road, U-3046, Storrs, CT 06269, USA. Contact: bodnarik@lpl.arizona.edu

Introduction:

Asteroids are the remnants of the formation of the Solar System and provide insight into its formation, evolution and how life may have begun. An important issue is determining which meteorite composition is representative of which asteroid class and type. *In situ* composition measurements would be one way to resolve this issue.

This research contributes toward the developing and testing of a neutron/gamma-ray spaceflight instrument for subsurface regolith composition measurements for landed asteroid missions. The Probing In situ with Neutrons and Gamma rays (PING) instrument was tested at an outdoor test facility on well-characterized granite, basalt, and asteroid simulant monuments with a variety of different layering configurations. PING utilizes a 14 MeV pulsed neutron generator to probe the subsurface, and uses neutron and gamma-ray spectrometers to detect the resulting moderated neutrons and gamma rays. The neutron and gamma-ray energy spectra are used to determine bulk properties and material composition.

The experimental spectra were compared both to Monte Carlo simulations and to independently verified elemental assays in order to establish a benchmarked Monte Carlo model. This comparison shows that PING can quantitatively determine bulk asteroid properties, but more sophisticated MCNPX models are needed to

Properly model PING experiments. The benchmarked Monte Carlo model can then simulate PING measurements on asteroids, which could be used to determine bulk asteroid properties, differentiate between asteroid types, and thus strengthen their connection to meteorite compositions.

This research firmly establishes that PING can obtain important geochemical information on asteroids from neutron transport and elemental analysis. A future asteroid mission with PING will have substantially increased science return providing a direct subsurface regolith description, without needing to drill or disrupt the surface. It has been demonstrated that compositions for specific asteroid types can be fabricated in large volume structures on Earth permitting experiments, with a benchmarked Monte Carlo program, to predict responses to optimize the science return prior to launch.

THERMAL INFRARED SPECTROSCOPY OF MERCURY FROM ORBIT: POTENTIAL OF, AND PREDICTIONS FOR, BEPICOLOMBO MERTIS

W. M. Vaughan[1], J. W. Head[1],
[1]Department of Geological Sciences, Brown University, Providence, RI, USA.
Contact: William_Vaughan@brown.edu

Introduction: In late 2023, the BepiColombo Mercury Planetary Orbiter (MPO) is scheduled to enter Mercury orbit, where its Mercury Radiometer and Thermal Infrared Spectrometer (MERTIS) instrument will map Mercury in the thermal infrared (TIR) wavelength range of 7-14 μm at a spatial resolution of 500 meters [1-2] in order to characterize the mineralogy of the surface. Spectral characterization of mercurian mineralogy may seem unpromising: spectra of Mercury at UV-vis wavelengths show no clear absorption features and provide little information about surface mineralogy [3], even when acquired ~10^2-10^3 km from Mercury with the Visible and Infrared Spectrograph (VIRS) aboard NASA's MESSENGER orbiter [4]. The natural question is thus: Will TIR spectra collected by MERTIS be more revealing than UV-vis spectra collected by VIRS?

In this abstract, we argue that the answer to this question is "yes". We review what is known (and what is suspected) about the mineralogy of Mercury's surface, and we demonstrate the potential of thermal infrared spectroscopy for the characterization of likely mercurian minerals. We also consider spatially-resolved Earth-based TIR measurements, which, in retrospect, agree with MESSENGER observations and again demonstrate TIR spectroscopy's potential. In the poster accompanying this abstract, we additionally predict what MERTIS ought to observe at Mercury. We focus on the Christiansen feature (CF), which is likely to be the most prominent TIR spectral feature of the mercurian surface. We model the wavelength of the CF for the major geologic units on Mercury and consider how the position of the CF might be controlled by variations in temperature, both in mantle source regions and on Mercury's surface. Finally, we develop a method for determining the sodium content of plagioclase on Mercury's surface from the position of the CF and the local Mg/Si ratio.

We hope that a careful comparison between our predictions (first committed to the scientific record at 4M-S³ in 2013) and MERTIS observations (which the authors hope to discuss at 14-M³ in 2023, ten years hence) will throw into relief what we understand—and, more importantly, what we *do not* understand—about the mineralogy of the surface of Mercury.

Potential of BepiColombo MERTIS:

Review of mercurian mineralogy. UV-vis reflectance spectra of Mercury show no Fe^{2+} absorption feature [3-4], suggesting that mercurian silicates contain only minor FeO. If there is indeed little FeO in surface silicates (an inference also supported by the high microwave transparency of Mercury's regolith [5]), then either (1) Mercury's surface has *no* FeO-bearing *mafic silicates*, or (2) Mercury's surface has mafic silicates *bearing no FeO*. Both possibilities are superficially plausible. Possibility (1) was supported by [6], who suggested that Mercury has an anorthosite flotation crust like that of the Moon. (This interpretation also provides a reasonable explanation for Mercury's unfrozen core: a thick anorthosite crust might suppress volcanism and keep Mercury's interior warm [5].) Possibility (2) was supported by [7], who suggested that Mercury's silicate fraction is similar to, though more Fe-rich than, certain reduced meteorites (*i.e.*, meteorites with little FeO in their mafic silicates) known as enstatite chondrites and achondrites. In this interpretation, Mercury is covered by a basaltic crust of magnesian orthopyroxene and sodic plagioclase feldspar; sulfur, abundant in these meteoritic materials, depresses the freezing point of the core and also occurs in the crust and mantle.

Which interpretation is correct? Recent measurements of the chemistry of Mercury's surface made by X-ray and gamma-ray spectrometers aboard the MESSENGER spacecraft have put the question to rest. The results [8-10] indicate clearly that Mercury's surface is not anorthosite. (This is supported by high-resolution orbital imagery of Mercury's surface acquired by MESSENGER, which suggest extensive basaltic volcanism [11].) Rather, as suggested by [7], Mercury's surface resembles enstatite chondrite and achondrite material chemically. Mercury is a reduced planet: Fe partitions into the core, rather than the mantle, and cations such as Ca are apparently associated with sulfur, not oxygen. Normative calculations [12] suggest that magnesian orthopyroxene and sodic plagioclase feldspar are the major minerals; high abundances of sulfur (up to 4 wt. % [8]) indicate that minor sulfides (<10 vol. %) probably also occur. Mercury's surface can be divided into two units: (1) relatively young (<4 Ga) volcanic smooth plains, which infill large basins and cover much of Mercury's north polar regions, and (2) older intercrater plains and heavily cratered terrain. Spatially resolved chemical measurements [10] indicate that the intercrater plains are rich in Mg, Ca, and S, whereas the smooth plains have abundant Na and Al. Normative calculations [12] suggest that the recipe for intercrater plains silicates is ~2 parts magnesian orthopyroxene to ~1 part moderately calcic feldspar (labradorite); smooth plains silicates have ~1 part magnesian orthopyroxene to ~2 parts sodic plagioclase feldspar (albite?).

Mercurian minerals in the UV-vis and TIR. Laboratory reflectance spectra [7] and thermal infrared emissivity measurements [13-14] demonstrate that the major mercurian surface minerals, magnesian enstatite and plagioclase, are spectrally featureless in the UV-vis but spectrally featureful at TIR wavelengths. This is predicted by spectroscopic theory: silicate absorption bands in the UV-vis are due to of Fe and Ti cations, which are nearly absent in low-FeO mercurian silicates. On the other hand, absorption bands and spectral features at TIR wavelengths are the result of Si-O stretching; such TIR spectral features are intrinsic to all silicates, regardless of FeO content. TIR spectroscopy is better able to characterize mercurian surface minerals than UV-vis spectroscopy.

Earth-based TIR spectroscopy of mercurian silicates. The potential of TIR spectroscopy for characterizing mercurian surface minerals has been demonstrated in practice by Earth-based thermal infrared spectroscopic measurements of Mercury, summarized in [15]. TIR spectra of Mercury were taken to indicate the presence of albite, labradorite, and magnesian pyroxene on Mercury—interpretations fully consistent with MESSENGER measurements. (Not all inferences from TIR spectra have been borne out by MESSENGER data. Suggestions of rutile, garnet, and potassium-rich feldspar in [15] are contraindicated by MESSENGER XRS and GRS measurements showing that Mercury's surface is too poor in Ti, Al, and K for such phases to be present in any abundance. This may be the result of spectral libraries comprising thermal emissivity measurements made at atmospheric pressure; [13-14] show the dramatic effect of very low pressure on thermal infrared emissivity measurements. Spectral libraries used for unmixing mercurian TIR spectra into mineral abundances should consist of thermal infrared emissivity measurements made at mercurian surface conditions [1-2].)

Earth-based TIR spectra of Mercury have been collected at a wide range of mercurian longitudes. This presents another test of the potential of TIR spectroscopy for characterizing mercurian silicates, as the proportion of Mercury's surface covered with volcanic smooth plains varies markedly with longitude (Figure 1) from a maximum near the volcanically-flooded Caloris basin at approximately 180° east longitude to a minimum between 270° and 300° east longitude. Since the smooth plains and the intercrater plains are mineralogically distinct, Earth-based TIR spectra ought to record mineralogical variation with longitude. Indeed, Figure 1 shows that TIR spectra recorded near 180° east longitude suggest Na-rich plagioclase and minor Mg-rich orthopyroxene, as anticipated for a region flooded in smooth plains, whereas TIR spectra recorded between 270° and 300° east longitude suggest labradorite and Mg-rich orthopyroxene, as anticipated for a region covered with intercrater plains.

In summary, TIR spectroscopy is able to characterize mercurian mineralogy and spatial variations in that mineralogy at ~10^8 km (from Earth)—we therefore anticipate that MERTIS, once sited ~10^2-10^3 km from Mercury, will be extremely capable of characterizing silicate minerals on Mercury.

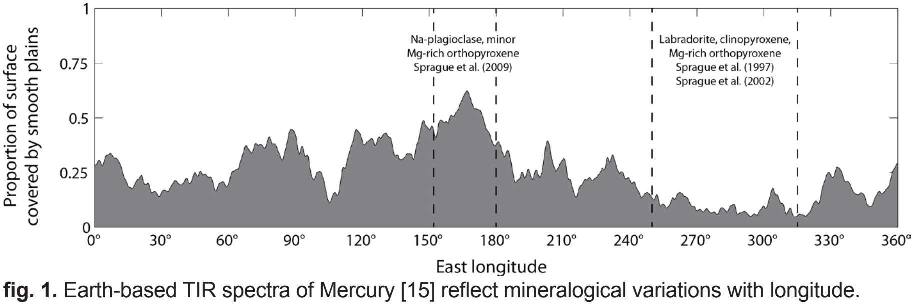

fig. 1. Earth-based TIR spectra of Mercury [15] reflect mineralogical variations with longitude.

References: [1] Arnold G. E. et al. (2008) *J. Appl. Remote Sens.*, 2. [2] Hiesinger H. and Helbert J. (2010) *Planet. Space Sci.*, 58, 144-165. [3] Vilas F. (1988) in *Mercury*. [4] McClintock W. E. et al. (2008) *Science*, 321, 92-94. [5] Jeanloz R. et al. (1995) *Science*, 268, 1455-1457. [6] Blewett D. T. et al. (2002) *Met. Planet. Sci.*, 37, 1245-1254. [7] Burbine T. H. et al. (2002) *Met. Planet. Sci.*, 37, 1233-1244. [8] Nittler L. R. et al. (2011) *Science*, 333, 1847-1850. [9] Peplowski P. N. et al. (2011) *Science*, 333, 1850-1852. [10] Weider S. Z. et al. (2012) *JGR*, 117. [11] Head J. W. et al. (2011) *Science*, 333, 1853-1856. [12] Stockstill Cahill K. R. et al. (2012) *JGR*, 117. [13] Donaldson Hanna K. L. et al. (2012) *JGR*, 117. [14] Donaldson Hanna K. L. et al. (2012) *JGR*, 117. [15] Sprague A. L. et al. (2009) *Planet. Space Sci.*, 57, 364-383.

MODEL OF 3D-GPR FOR SPACE APPLICATIONS

V. N. Marchuk[1], O. A. Byshevski-Konopko[1], A.S.Bazhanov[2],
[1]FIRE RAS, Fryazino, Russia, [2]SDB IRE RAS, Fryazino, Russia.
Contact: Marchuk@ms.ire.rssi.ru

Introduction:

In this article an example of creation of the model of multichannel 3D-GPR for space application is reviewed. Bases of its designing proceeding from the main solved scientific objectives are offered. Possible types of antennas and their placement for an offered design are considered.

Now more and more broad application was received by multichannel GPR (3D-GPR). They showed outstanding results when using in archeology, construction and municipal services [1-3]. In work [4] possibility of application 3D-GPR for research of space bodies is considered and possible characteristics of such device are provided. This device can take place on the mobile device moving on a surface of a studied space body.

Development of the 10-channel 3D-GPR model is begun by joint efforts of FIRE RAN and SDB IRE RAN. This model consists of the following units: antenna system with 5 transmitting (Tr) and 6 receiving (Rs) antennas, switching unit (SU), signal generation unit (SGU), amplifiers and ADC unit (AAU), collection and storage of data unit (DSU). Block diagram of the model of 3D-GPR for space applications is showed on Fig.1. The emitted signal represents one period sine wave duration of 0.5 ns; this corresponds to the center frequency of the broadband signal 2.GHz. The choice of frequency range is caused by the requirement of high resolution (5-10 cm) in the assumption of weak absorption of a radio signal in the studied environment. Sweep duration of a received signal in the simplest case is 13 ns that provides sounding depth of about a meter; if needed, this value can be increased by 2 - 4 times.

Principle of operation of the instrument: short pulse is emitted serially by each of the transmitting antennas, penetrates into the environment and reflects from discontinuities in it goes to the nearest receiving antenna, amplified, digitized and stored for further processing and analysis. After processing of the accepted signals the three-dimensional data file by which analysis it is possible to receive idea of internal structure of the studied environment is formed.

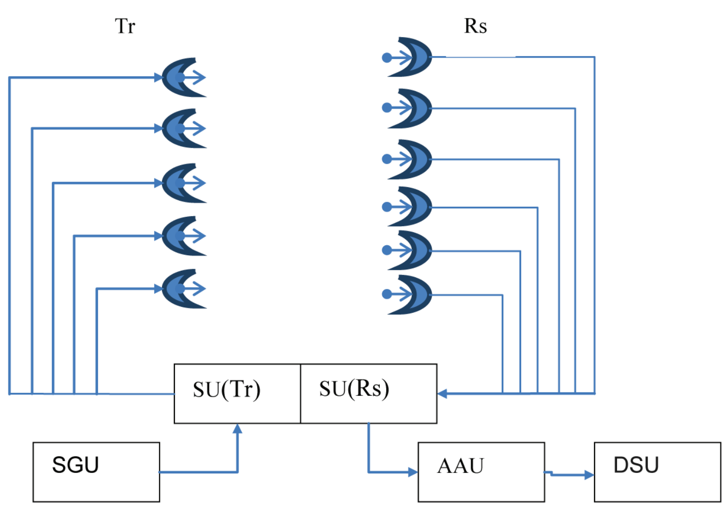

fig.1. Block diagram of the Model of 3D-GPR for space applications

At the first stage for radiation and reception of a signal it is supposed to use Vivaldi's antennas, as the most compact broadband antennas providing the optimum directional pattern. Different types of polarization of a signal (in the direction of movement and across) by the corresponding orientation of transferring and reception antennas will be tested. Besides, it is alternatively supposed to test other types of antennas: spiral, slot-hole, flat biconical vibrator.

Referenses

1. Linford, N., Linford, P., Martin, L. and Payne, A. Stepped frequency ground-penetrating radar survey with a multi-element array antenna: Results from field application on archaeological sites. Archaeological Prospection, 17: 187–198. doi: 10.1002/arp.382, 2010.

1. Dean Goodman, Alexandre Novo, Geostudi Astier, Gianfranco Morelli, Geostudi AstierSalvatore Piro, Doria Kutrubes, Henrique Lorenzo. Advances in gpr imaging with multi-channel radar systems from engineering to archaeology // SAGEEP 2011 Charleston, South Carolina USA
2. Immo Trinks, Jaana Gustafsson, Jesper Emilsson, Christer Gustafsson, Bernth Johansson et Johan Nissen. Efficient, large-scale archaeological prospection using a true 3D GPR array system // ArcheoSciences, suppl. 33, 2009, pp. 367-370
3. Marchuk V. N. , Smirnov V. M., Byshevski-Konopko O. A. Multi-channel ground penetrating radar for space applications / The third Moscow Solar System Symposium (3M-S³), Moscow 8-12 October 2012 abst 270-271.
4.

EXPLORATION OF SOLAR SYSTEM: ACTIVE SEISMOLOGY

Aleksandr V. Bogdanov[1], Oleg B. Khavroshkin[2]
[1]Moscow Technical University (former Emperor), [2]Institute of the Physic of the Earth. RAS, khavole@ifz.ru

Existing methods of seismic exploration of the Moon, the planets and moons of the giants planets are severely limited by temporary and weight limits which makes obtaining the necessary key information about the internal structure of a celestial body is almost impossible. So, for a detailed study of the Moon including the central zone is necessary to conduct seismic profile relevant observations and / or the creation of seismic small aperture groups. Seismic equipment for the duration of effective work on Mercury, Venus, Jupiter's satellites, and many do not exceed a few hours. In addition actual demand from new expeditions simultaneous geological - geophysical monitoring and delivery of the soil sample to Earth. For all of the above requirements for operation and to achieve these scientific goals are ballistic Barrel System (BBS) of different modifications: the block light mortars, central trunk with service equipment and special purpose penetrators, propellant loading of store. Propelling charges for seismic profile measurements performed by the scheme resilient compact body capable of repeatedly reflected from the surface of a celestial body devoid of atmosphere. Depending on the type and scientific tasks expedition circuit formed ballistic system (see Fig. 1). For example, BBS based on light mortars can provide a short-examination of the internal structure of Europe for 40 - 50 min from the moment of landing. Another option BBS can ensure the delivery of the penetrator with the lunar soil to Earth, and / or throw a special type mikrorover to any area of the moon. For the implementation of the existing layout of the installation on the basis of mortars and / or BBS obtained the calculated ratios and working formulas for the conceptual design and operation of ballistic systems. The proposed system is reliable, anti-shock performance, easy to use, requires substantial investment.

At centrums of fig.1 the barrel general similarity of gun is placed. Short barrel mortals fixed on circus periphery of the barrel general.

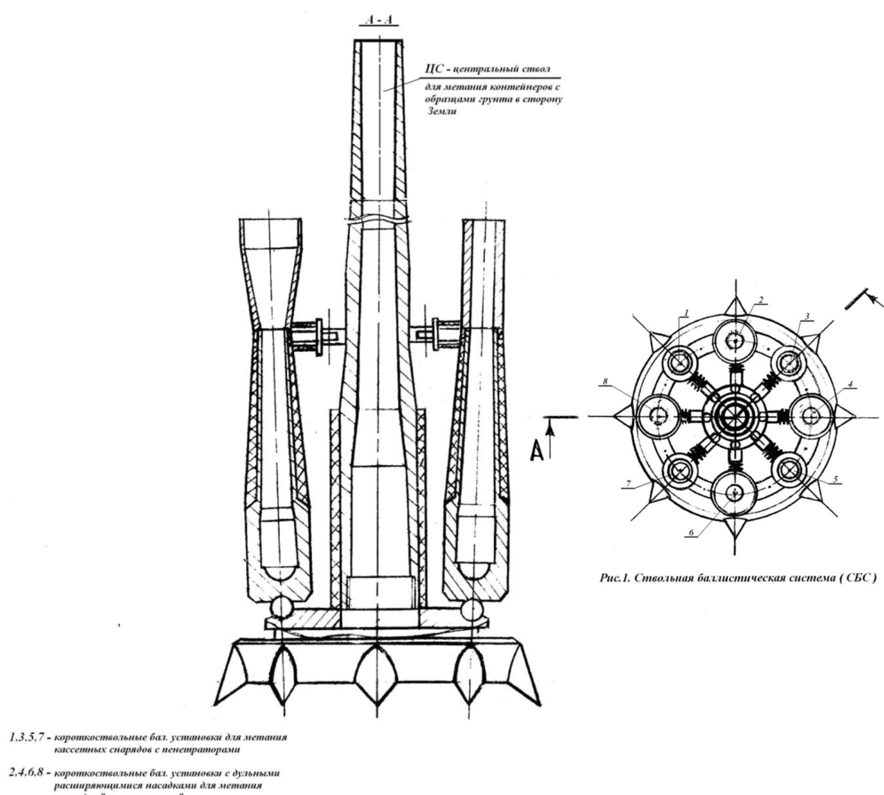

fig.1. Barrel ballistic system (BBS).

POLYATOMIC IONS MASS ANALYSIS USING COMPACT LASER DESORPTION/IONIZATION TOF-MS

K. A. Luchnikov[1], G. G. Managadze[1], P. Wurz[2], A. E. Chumikov[1], A. I. Kuznetsov[1], A. L. Bondarenko[1], G. Z. Saralidze[1], N. G. Managadze[1].
[1]RAS Space Research Institute (IKI), 117997, 84/32 Profsoyuznaya Str, Moscow, Russia; [2]University of Bern,, Sidlerstrasse 5, CH- 3012 Bern, Switzerland.

Introduction:

At present experiments dedicated to the study of the habitability of Mars and other planets became actual. One of the tasks is to determine elemental and isotopic composition of the surface material. A compact laser ablation mass-spectrometer LASMA is able to implement this research. It can measure local elemental composition of regolith extracted from any possible depth. These measurements do not require any sample preparation. LASMA is a part of scientific payload of LUNA-RESURS and LUNA-GLOB missions.

However, there are many questions regarding mineralogical and chemical composition of regolith, particularly organic compounds analysis. Instruments for solving these tasks exist (MSL, ChemCam) or still developing (MOMA). Therefore, our group set the goal to expand the functionality of LASMA for future missions without a considerable sacrifice of size and weight of the instrument. We have modified existing instrument and named a modification ABIMAS.

Instrument modification and results:

ABIMAS a possibility of polyatomic ions analysis. Laser irradiance was reduced and ion optics system modified for the ability of ion pre-acceleration. Spectra of polyatomic ions of inorganic samples were obtained in the first experiments. Furthermore, spectra of some organic salts (IR-1061 and Malachite green G dyes) were obtained too and fragmentation degree dependency from laser irradiance was studied. These results give us hope that the range of the detectable substances can be considerably extended. This instrument has been selected for EXOMARS mission.

Moreover, it’s possible to create miniature MALDI-like TOF-MS instrument using UV range laser. Such instrument can be able to detect microorganisms by direct measurements after proper sample preparation on the board of spacecraft.

ENERGY-MASS SPECTROMETER FOR PLASMA MEASUREMENTS AT GANYMEDE

D. Moiseenko[1], O. Vaisberg[1], G. Koynash[1], A. Shestakov[1], R. Zhuravlev[1], A.J. Coates[2], G.H. Jones[2], C.S. Arridge[2], D.O. Kataria[2],
[1] Space Research Institute, Russian Academy of Sciences, Russian Federation, Profsouznaya str, 84/32; [2]Mullard Space Science Laboratory, University College London, UK. Contact: modaldi@iki.rssi, olegv@iki.rssi, ajc@mssl.ucl.ac.uk

Introduction:

Ganymede, which is composed of rock and ice and possessing intrinsic magnetic field, is an exciting object for investigation. Its plasma environment consists of Jupiter's magnetospheric particles and ions originated from the surface of Ganmede. Interaction of Ganymede's and Jovian magnetospheres leads to acceleration of ions and complicated transport.

Analysis of ion flux, composition and velocity distribution provides important tool for investigation of Ganymede's soil composition and characteristics, not only on local scale but also on planetary scale, due to transport within Ganymede's environment.

The goals of experiment also include:

- Ganymede's magnetosphere and its interaction with Jovian magnetosphere
- Ganymede's atmosphere/exosphere and its loss to Jovian magnetosphere
- Flux and composition of magnetospheric ions hitting the surface of Ganymede
- Sputtering of the surface and implantation of energetic ions.

Proposed instrument is energy-mass-analyzer using combination of electrostatic and magnetic analysis (fig.1). Estimated characteristics are presented in table below. Prototype of instrument was flown on Prognoz-2 satellite.

The proposed instrument consist of three cylindrical electrostatic analyzers with scanners, covering different fields of view, wedge magnet with drift tube for m/q analysis, and position-sensitive detector. Trajectories of the following ions are shown for the solar wind mode measurements: from Fe^{+6} to Fe^{+12}, and O^{+6} and O^{+7}.The instrument is under development for solar wind studies on Interhelio-Probe mission; it can be used for analysis of secondary ions from surface of solid body.

We present the results of computer simulation of the analyzer.

characteristics	value
energy range, keV	1…20
mass range, M/Q	2…9
mass resolution, M/ΔM	10-40 for E/Q = 1 keV
field of view	till ±45^0 for each direction
size of analyzer, mm	230x170x120
mass with electronics, kg	3.5

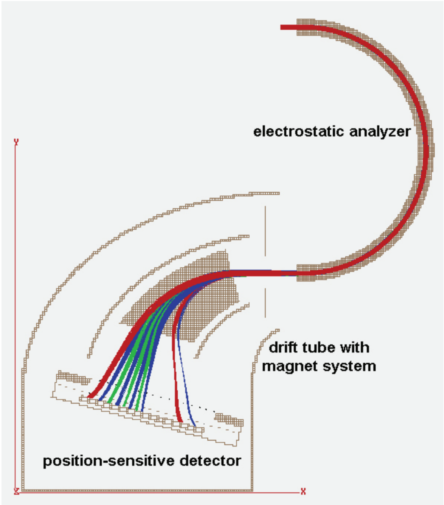

fig.1. Structure of electronic optics

QUASI PERIODIC ORBITS IN THE VICINITY OF THE SUN-EARTH SYSTEM L_2 POINT AND THEIR IMPLEMENTATION IN “SPECTR-RG” AND “MILLIMETRON” MISSIONS.

I.S.Ilin, A.G.Tuchin[1],
[1]Keldysh institute of Applied Mathematics, Moscow, Miusskaya sq, 4, Russian Federation; Contact: is.ilin@physics.msu.ru

Introduction:

This work considers quasi periodic orbits in the vicinity of the Sun-Earth system L_2 libration point that could be used for the upcoming “Spectr-RG” and “Millimetron” missions, presupposing deployment of a space telescope on some quasi-periodic trajectory in the vicinity of the Sun-Earth system L_2 point. The classification of periodic motions in the vicinity of the collinear libration points is presented along with the visualization of the described manifolds with the help of Poincare section.

Different types of halo orbits are proposed for “Millimetron” and “Spectr-RG” missions – in the first case it is a halo orbit, going 1 mln km away from the ecliptics plane, and in the second one, on the contrary it is a halo orbit, lying in a close vicinity of the L_2 point. To construct these halo orbits, the method and mathematical algorithm, providing the ballistic design of the spacecraft transfer to the vicinity of the Sun-Earth system L_2 point and halo orbit motion in this area has been developed and implemented. The developed method provides halo orbits with given geometrical dimensions in the ecliptics plane and in plane orthogonal to it.

For calculation of one impulse flights from Earth to the selected halo orbit (with the help of a Moon swing by maneuver or without it) the initial approximation construction algorithm has been implemented. These approximations are calculated by means of two variables’ function isolines construction and analysis. The transfer trajectory pericentre height above the Earth surface is considered to be such a function. The arguments of this function are the special parameters describing the halo orbit.

The motion in the vicinity of the collinear libration points is unstable, that presupposes some station keeping strategy to keep the spacecraft in the selected halo orbit. An algorithm, calculating stationkeeping maneuver impulses and providing stationkeeping strategy for the whole spacecraft lifetime has been developed. The characteristic velocity costs needed for the stationkeeping have been evaluated.

The halo orbits calculated with the help of the methods described above and presented in this study meet all ballistic requirements and restrictions of the “Spectr-RG” and “Millimetron” missions.

TO THE ORBIT DESIGNING OF THE JOVIAN'S MISSIONS USING REDUCING GRAVITY ASSIST MANEUVERS FOR THE LANDING.

Yu.F., Golubev[1], A.V. Grushevskii[1], V.V. Koryanov[1], A.G. Tuchin[1],
[1] Keldysh Institute of Applied Mathematic, Moscow, Russia.
Contact: golubev@keldysh.ru

Introduction:

The new Phase Beam method of Orbit Designing [1] is developed. It uses a quasi-singular semi-analytic construction of the trajectories for the design of the spacecraft flight in the Jovian sphere of influence with multiple flybys close to it's natural satellites. The Phase Beam method and the Tisserand-Poincare graph forms the basis of the analysis. Some kinds of orbital Jovian tours received classification. Criteria are fuel expenses, mission duration and jovian radiation doze. A variants of realization for general classification types of such spacectaft projects are given.

References:

[1] Golubev, Yu.F., Grushevskii, A.V., Koryanov, V.V., Tuchin, A.G., 2012. A Method of Orbit Designing Using Gravity Assist Maneuvers to the Landing on The Jupiter's moon Ganymede. In: Third Moscow Solar System Symposium, Moscow, 2012. URL: http://ms2012.cosmos.ru/presentations.
[2] Golubev, Yu.F., Grushevskii, A.V., Koryanov, V.V., Tuchin, A.G.,2013. A Method of Orbits Designing Using Gravity Assist Maneuvers To The Landing on the Jovian's Moons. In: International Colloquium and Workshop Ganymede Lander: scientific goals and experiments, Moscow, March 4-8, 2013. URL: http://glcw2013.cosmos.ru/presentations.

TEMPERATURE CHANGE UNDER ADIABATIC CONDITIONS IN H_2O CONTAINING INTERIORS OF TITAN.

A. N. Dunaeva, V. Kronrod, O. Kuskov,
Vernadsky Institute of Geochemistry and Analytical Chemistry, Russian Academy of Sciences, Kosygin Str., 19, 119991 Moscow, Russia, Contact: dunaeva@kmail.ru

Introduction:

One of the key issues in constructing of the models of internal structure of the large ice satellites of Solar System is to determine the thermal regime of their internal regions. Contemporary theories consider that at least two main different zones exist in the satellites: the outer ice crust composed by ice Ih and characterized by conductive heat transfer and lower H_2O layers characterized by convection. Temperature distribution in the outward conductive Ih-ice crust is described with the steady-state equation of conductivity [1], and in convective zones the temperature distribution governed by adiabatic laws.

This paper considers temperature distribution in Titan in context of well-developed substance convection occurring in the satellite inner regions and assuming the changes in phase composition and aggregate state of its water-containing phases.

Theory and calculations:

Within the proposed models of Titan internal structure, the satellite was assumed to consist of three major structural domains: 1) the outer water-ice shell including the icy polymorphs Ih, III, V, VI and a layer of the liquid water (internal ocean), 2) the rock-icy mantle, and 3) rocky core. The core size inversely depends on the thickness of the satellite's outer H_2O-shell and has minimum values (up to a core absence in a satellite at all) at maximum allowable thickness of Titan water-ice shell 470-490 km.

The following regions was classified to Titan's convective zones as being the study subject of this paper: internal ocean beneath the ice-Ih crust, underlying high pressure ices III, V, VI, and the rock-ice mantle.

In convective inner satellite zones, the temperature profile of the satellite varies adiabatically, with the gradient of adiabatic curve determined according to thermodynamic formula:

$\frac{dT}{dP} = \frac{T \cdot \alpha}{\rho \cdot C_{p,w}}$, were *α* – is the coefficient of thermal expansion: $\alpha = \frac{1}{V}\left(\frac{\partial V}{\partial T}\right)_P$,

T, P, $C_{p,w}$, ρ, V – respectively: temperature, pressure, heat capacity, density and volume of the substance (H_2O).

Using equations of states (EOS) of water and water ices, and necessary data for their heat capacity [2-6], the *α* values were calculated for temperatures and pressures corresponding to the conditions of Titan's internal ocean (T= 255-300K, P=0.1-10 kb), and for the ices III, V, VI, VII.

The obtained values of *α* coefficient were then used in calculation of adiabatic temperature gradients in water layer and in high pressure ices in Titan (Fig. 1).

The results of performed calculations show that adiabatic gradients in the Titan's water layer are modest on the whole (average value being 1.94 K/kb), therefore adiabatic temperatures of Titan's internal ocean are low and do not exceed 280 K.

Equation of states of water ices available in the literature gives significant spread of ice density values calculated using these equations (up to 20-30%) which affects values of resulting *α* coefficients and accuracy of dT/dP values. However, for preliminary estimates the value of adiabatic gradient in high pressure ices (as calculated using various EOS) may be assumed in the range of 2.4-2.9 K/kb.

From the hydrostatic equilibrium condition: $dP = -\rho \cdot g \cdot dr$, and hence: $\frac{dT}{dr} = \frac{\alpha \cdot T \cdot g}{C_{p,w}}$ (dr – is the depth).

Providing that relation $\alpha / C_{p,w}$ in the Titan ices varies slightly with depth (for ices VI, VII it is of the order of 10^{-7} kg/J), the average adiabatic gradient value in Titan's ices (at T = 300K) may be estimated as $dT/dr \approx 0.035$ K/km.

It should be noted that the above estimates (similar to adiabatic curves shown on Fig. 1) were calculated for a purely water system, i.e., strictly speaking, may be directly applied for simulation of Titan' water-ice shell only. The underlying rock-ice mantle contains a significant admixture of the rocky components which the higher, the larger is the thickness of the satellite outer H_2O-shell. Taking into account maximum thickness of water-ice shell ~ 500 km and the satellite lacking the internal core, the internal regions of Titan are composed of ice/rock mixture in quantities of 25 and 75 mass %, respectively. Such significant amount of rock component which is different in its properties from water ices should significantly change thermodynamic properties of the mantle's medium. Since in our model the rock component of the mantle has been assumed as incompressible, the change of the mantle properties is mostly contributed by heat capacity of rock ($C_{p,r}$) which in general may be assumed equal to 0.9 $kJ \cdot kg^{-1} \cdot K^{-1}$ [7] as different from heat capacity of ices varying in the range 2.1-2.7 $kJ \cdot kg^{-1} \cdot K^{-1}$ [3].

The heat capacity of rock-ice mantle ($C_{p,m}$), according to additive rule, may be represented as follows:

$C_{p,m} = C_{p,w} \cdot \chi_{H_2O} + C_{p,r} \cdot \left(1 - \chi_{H_2O}\right)$, were χ_{H2O} – mass fraction of H_2O in mantle.

The calculation shows that that addition of rock component may lower specific heat capacity of the mantle almost 2-fold, thus resulting in respective increase adiabatic gradient of the mantle and significant increase of temperature with depth. At the same time, maximum divergence of adiabatic curves with depth (between profiles in pure ice and in rock-ice mixture) which is achieved closer to the satellite center will be in the stability zone of ice VII. The equation of state of this ice phase is such [6] that at maximum spread of temperatures of 200 K the resulting difference in ice density will not exceed 5% which is within calculation accuracy and do not affect the internal structure of the satellite.

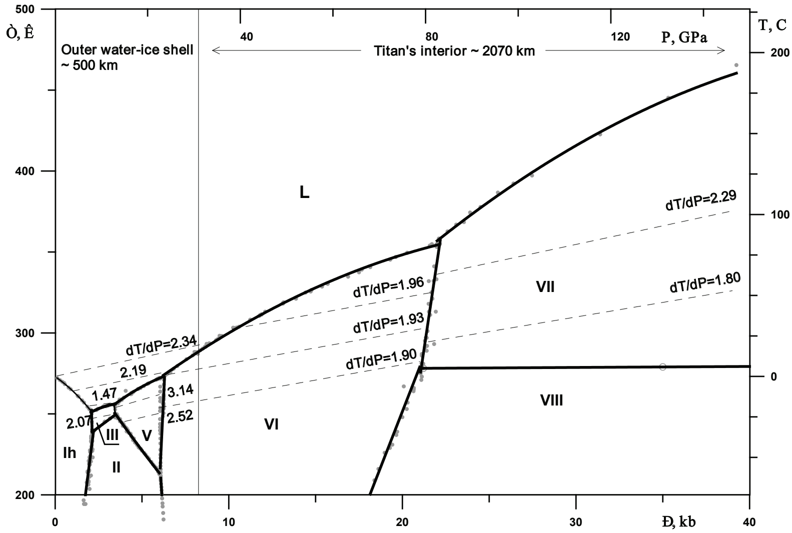

fig. 1. Adiabatic temperature gradients in water-ice system at Titan conditions.

Dashed lines are shown adiabatic temperature profiles and their average dT/dP values. Gray points represent experimental data on phase transitions in water-ice system.

Acknowledgements:
This work was supported by RFBR grants 05-00178 and 12-05-00033 and by the grant of the Russian academy of sciences Presidium Program 22: "Fundamental problems of research and exploration of the Solar system".

References:

[1] Kuskov, O.L., Kronrod, V.A.: Internal structure of Europa and Callisto, Icarus, V. 177, pp. 550–569, 2005.
[2] Wagner, W., Pruß, A.: The IAPWS Formulation 1995 for the Thermodynamic Properties of Ordinary Water Substance for General and Scientific Use, J. Phys. Chem., V. 31, pp. 387-535, 2002.
[3] Tchijov, V.E.: Heat capacity of high-pressure ice polymorphs, Journal of Physics and Chemistry of Solids, V. 65, Issue 5, pp. 851-854, 2004.
[4] Tchijov, V. et al.: Kinetics of Phase Transitions Induced by Shock-Wave Loading in Ice, J. Phys. Chem. B, V. 101, pp.6215-6218, 1997.
[5] Noya, E.G., Menduiña, C., Aragones, J.L., Vega, C.: Equation of State, Thermal Expansion Coefficient, and Isothermal Compressibility for Ices Ih, II, III, V, and VI, as Obtained from Computer Simulation, J. Phys. Chem. C, V. 111(43), pp. 15877, 2007.
[6] Fei, Y., Mao H.-K., Hemley, R.J.: Thermal expansivity, bulk modulus, and melting curve of H_2O-ice VII to 20 GPa, J. Chem. Phys., V.99 (7), pp. 5369-5373, 1993.
[7] Grindrod, P.M., Fortes, A.D., Nimmo, F., Feltham, D.L., Brodholt, J.P., Vocadlo, L.:The long-term stability of a possible aqueous ammonium sulfate ocean inside Titan, Icarus, V. 197, pp. 137-151, 2008.